Theoretical models for quantum simulators of novel materials and devices

Tymoteusz Salamon

Quantum Optics Theory Group
Supervised by Dr. Debraj Rakshit and Prof. Maciej Lewenstein
November 3, 2023

To all the people — my parents, grandparents, and public education teachers— who understood the value of knowledge long before I did, and who invested their time, money, and patience in educating me, often facing resistance. Tears fill my eyes every time I reflect on the faith they had in me, far greater than the faith I had in myself. This thesis is for them, a faint evidence that their time was not entirely wasted.

And to my sister Hania, to my GF Luisa Figeireido Lopes Alves, and to my dear friends. For keeping me sane - with their jokes, love and care.

And to Maciej of course. For being the best boss one could dream of.

Contents

Chapter 1

Introduction

Quantum simulation refers to the process of using quantum systems, to simulate and study the behavior of other quantum systems, usually more complex. It involves creating a controllable and understood model of a quantum system of interest and then realizing this model by running it in an experimental set-up or quantum computer (a.k.a. digital quantum simulator). Going one step down one should reflect on what the quantum systems actually are. All the matter is built from quantum particles, but what makes one system quantum and other classical? One of the measures to distinguish these two regimes might be a temperature. Quantum phenomena can be observed when the system is in, or close to, its ground state, i.e close to absolute zero. Increasing the temperature excites the constituents of the system resulting with the state being an incoherent statistical mixture of configurations that is described by Fermi-Dirac, Maxwell, or Bose-Einstein statistics, depending on the species of the constituents. The other issue that should be clear already at this point is, what systems are we talking about. Depending on the internal degrees of freedom (let's call them X) of the constituents, the system of N constituents will have X^N possible states. For the simplest non-trivial constituents of two internal degrees of freedom (like spins), the system with $N = 20$ will already be on the edge of being classically computable. Therefore, the systems that are usually considered in the quantum simulation are the systems that exceed the computational power of the classical computers and, therefore, offer a unique way of analysing the many particle (or many-body) quantum systems. Needless to say, basically all condensed matter systems will fall into this category.

This thesis focuses on quantum simulation of complex many-body systems in

three different scenarios. The first one is simulation of 2D electronic materials 1.3 i.e simulation of fermionic systems. The second scenario is quantum simulation of dynamics of spin systems in context of quantum batteries. The last one is the quantum simulation of bosonic systems with dipolar excitons. All these systems reveal the behaviour at which, due to interactions between particles, the constituents (electrons, bosons, spins) are not independent of each other, but rather form a correlated phase. The details of correlated phases are explained in the next section.

1.1 Correlated phases of matter

In general, correlated phases of matter refer to states of matter where the behavior of particles or constituents is strongly influenced by interactions and exhibits collective behavior that extends over a large number of particles. In these phases, the properties of individual particles are intertwined and interconnected, leading to emergent phenomena that cannot be understood by considering the behavior of each constituent in isolation. Correlations can arise due to various interactions, such as electromagnetic, gravitational, or quantum mechanical interactions, among others. These interactions can lead to the emergence of novel phenomena and properties that are not present in the individual constituents.

Traditionally, the condensed matter physics orbited around the Fermi Liquid Theory (FLT), which expands the description of non-interacting Fermi gas into the system of interacting electrons [1]. According to FLT the interactions between particles lead to the new, "dressed", quasi-particle states altering its effective mass, specific heat etc. but with retained independent behaviour legitimizing the validity of the band theory. This however, works only if the dispersion (bandwidth) is big enough comparing to electronic interactions, i.e in the FLT regime. Remarkably, some materials, generally these with d and f atomic orbitals, have vastly reduced dispersion of electrons due to smaller orbital overlap between the sites, and therefore, smaller hopping amplitude (smaller possibility of an electron jumping from one atom to the other and, therefore, moving within the material). This leads to regime out of the scope of FLT, where Coulomb interactions are the leading mechanism responsible for collective behaviour of the whole system, while kinetic movement of constituents is reduced.

The band theory defines the allowed energies for non-interacting electrons, as well as the forbidden energy regions, known as gaps. The energy gaps in materials are a

consequence of the discrete energy spectrum of the individual atoms (constituents) of the material. The transport properties of the material depend on the filling of the highest bands. If the highest band is fully filled with electrons, then the material is considered to be an insulator. However, when the highest band is only partially filled, then the excited electrons can access it. In such case the material is a metal. In the presence of strong, repulsive Coulomb interactionsm the material can be an insulator even with only partially filled highest bands. Such material, which should conduct, but due to interactions does not, is called a correlated (Mott) insulator and is one of the most prominent correlated phases, which we will discuss in detail in 6.

Another well-known example of a correlated phase of matter is a ferromagnet. In a ferromagnetic material, the magnetic moments of individual atoms align in the same direction, resulting in a macroscopic magnetization. The alignment of the magnetic moments is a collective behavior that arises due to the exchange interaction between the atoms.

1.2 Quantum Simulators

1.2.1 Idea and main concepts

A simulator is a device that imitates desired properties of a given system such as an airplane, train or a physical system of quantum particles. Airplane simulator cannot fly, nor take passengers on board but provides realistic reproduction of all navigational, mechanical and electronic apparatus necessary for the efficient and safe training of the crew. Similarly, simulators of the quantum systems do not reproduce all properties of the original, simulated systems, but imitate only their specific features that are required to understand the phenomena of interest occurring in the original system. The general idea and concept of such quantum simulators (QSs) can be summarized as follows:

- There exist many interesting **quantum phenomena** with highly important applications (such as, for instance, superconductivity).
- These phenomena are often complex to describe and understand with the help of standard or even supercomputers.
- The proposal by Yu. I. Manin and R. P. Feynman [2, 3] suggests the possibility of designing another, simpler, and more controllable quantum system to

simulate, understand, and control these phenomena. Such a system would function as a quantum computer with a specific purpose, i.e., a **quantum simulator**.

Designing such a simulator, however, is not an easy task at all. The research line on QS goes back to the beginning of this century, and there are numerous valuable reviews covering the various platforms and types of QSs [4]. The practical concept of QS dates back to the proposal for simulating strongly correlated systems in optical lattices [5] and the first experiments [6]. Nowadays, QSs are commonly used for the following tasks and goals:

- **Fundamental problems of physics:** This is the most developed application, in which many achieved results are believed to reach quantum advantage; this is particularly true for the studies of quantum dynamics [7] or quantum disordered systems, such as the ones that exhibit many-body localization (MBL).

- **Quantum chemistry.** Applications of QS to quantum chemistry has only started [8, 9, 10, 11] and, although promising, it is still far from achieving the precision and accuracy of contemporary theoretical quantum chemistry. There is a growing evidence that the expect of exponential quantum advantage in quantum simulations for quantum chemistry is not such (see recent works by G.K. Chan [12], and his talks at the APS meeting in 2022).

- **Classical/quantum optimization problems for technology.** Applications of quantum NISQ devices and QS to optimization problems are also in an initial phase [13] and cannot yet compete with the classical supercomputer methods (cf. [14]).

1.2.2 Platforms and architectures

Now is the time to mention how the quantum simulators can be actually built. There are several very well developed platforms where QSs are being realized and ”practical” quantum advantage has been achieved. We should stress that QSs can be analog or digital.

In the latter case, any platform that offers tools for universal quantum computing can also be used for quantum simulation. Here comes a definitely incomplete list of already developed QS architectures:

- **Superconducting qubits**: These are the same systems as the ones used by Google [15] or D-Wave [16]. Even though in principle they allow for "noisy" but universal quantum computing, they can be and very often are used as digital QSs (cf. [17]). They can be coupled to microwave cavities, resulting into circuit QED systems [18].

- **Ultra-cold atoms**: They mostly offer the possibility for analog quantum simulation. This can be realized in the continuum or in optical lattices [19]. They are very flexible and they allow to simulate complex Hubbard models, as well as spin systems.

- **Trapped ions**: Similarly to superconducting qubits, trapped ions allow for universal quantum computing, but they can also be used as perfect analog or digital QSs [20, 21]. Similarly to superconducting qubits, they can be used to simulate spin $1/2$ systems, rather than Hubbard models. Very recently a qudit (or spin 1 and 2) quantum computer/simulator was realized with ions [22].

- **Rydberg atoms**: These are atoms where the electron has been excited to a high principal quantum number, and which are trapped in optical tweezers. They mimic spin systems with long range interactions [23, 24, 25].

- **Photonic systems**: These are typically linear optics systems which, combined with photon counting, may mimic a universal quantum computer, according to the famous paper from Knill, Laflamme, and Milburn [26]. Achieving strong non-linearity with photons is very challenging, but there are ongoing attempts and proposals [27].

- **Light and Cavity materials**: Quantum Simulators based on Cavity Quantum Electrodynamics take advantage of the coupling between quantum system and the coherent light field of the cavity, in which such system has been placed. This branch of quantum simulation is commonly named as "cavity quantum materials", since one in principle could place a many-body quantum system into a cavity and control its properties via light-matter interactions. Currently, however, the experimental studies are mainly conducted in the scope of Jaynes–Cummings and Dicke models [28]. Another research path was taken by engineering materials entirely from light with resulting photon-photon interactions[29, 30, 31, 32]. Such systems, however, require a mediator (for example Rydberg-dressed atoms) facilitating the light-light interactions.

- **Twistronics systems**: Twistronics deals with twisted bi-layer graphene or other two-dimensional materials [33, 34]. For small ”magic” angle, such systems lead to periodic Moiré patterns at a length scale much larger than the typical scale of condensed matter systems: in this sense, they can themselves be considered as condensed matter quantum simulators of condensed matter [35]. Such approach has been explained in detail in Chapter 1 of this book. Twisted bi-layer materials can, however, also be mimicked by ultra-cold atoms in a two-dimensional lattice with synthetic dimensions [36].

- **Polaritons**: Especially useful for non-equilibrium systems and quantum hydrodynamics simulation, as well as relativistic effects thanks to dual (half light half particle) nature of the polaritonic quasi-particles [37, 38, 39].

1.3 2D materials

2D materials refer to materials that are extremely thin, consisting of a single layer or a few layers of atoms arranged in a two-dimensional plane. These materials have unique properties that arise due to their reduced dimensionality, which can differ significantly from their bulk counterparts. Graphene, a single layer of carbon atoms arranged in a hexagonal lattice, is the most well-known and extensively studied 2D material.

The term ”2D material” is not limited to graphene; it encompasses a broader class of materials with different chemical compositions and structures. Below basic categories of 2D materials are listed together with their properties.

Graphene is a single layer of carbon atoms arranged in a two-dimensional hexagonal lattice. It is incredibly strong, flexible, and exhibits exceptional electrical and thermal conductivity. Due to its unique electronic properties, graphene holds promise for applications in electronics, transparent conductive coatings, energy storage devices, and sensors. It also has remarkable mechanical strength, with tensile strength about 200 times greater than steel.

Transition Metal Dichalcogenides (TMDs) are a class of 2D materials that consist of a transition metal atom (such as molybdenum or tungsten) sandwiched between two layers of chalcogen atoms (such as sulfur, selenium, or tellurium). Unlike graphene, TMDs have a bandgap, which enables them to exhibit semiconducting

properties. This property makes TMDs suitable for applications in electronics and optoelectronics, such as transistors, photodetectors, and light-emitting diodes (LEDs).

Boron Nitride (BN) is a 2D material composed of alternating boron and nitrogen atoms arranged in a hexagonal lattice, similar to graphene. It has excellent thermal and chemical stability, high electrical insulation properties, and acts as a good thermal conductor. BN is often used as a substrate for graphene and other 2D materials because it provides a clean and stable surface for their growth and preserves their unique properties.

Black phosphorus is another notable 2D material. It is composed of phosphorus atoms arranged in a layered structure. Black phosphorus exhibits a tunable bandgap, ranging from a semiconductor to a semi-metal, depending on the number of layers. This property makes it suitable for applications in electronics, optoelectronics, and photovoltaics.

Other 2D Materials: Apart from the aforementioned materials, there are various other 2D materials with distinct properties and potential applications. These include hexagonal boron nitride (hBN), which is an insulating material with a structure similar to graphene, and molybdenum diselenide (MoSe2) and tungsten disulfide (WS2), which are TMDs with unique electronic and optical properties.

The characteristics of 2D materials give rise to several unique macroscopic phenomena, such as high carrier mobility, extraordinary mechanical strength, optical transparency, and exceptional thermal conductivity.The field of 2D materials has gained significant attention in recent years due to their potential applications in various fields, including electronics, optoelectronics, energy storage, sensing, and catalysis. Researchers are actively exploring the synthesis methods, characterization techniques, and manipulation strategies to harness the properties of 2D materials and integrate them into practical devices. It's also worth noting that while graphene is a truly 2D material, many other materials considered 2D may have a small but finite thickness, consisting of a few atomic layers. Nonetheless, they still exhibit properties that are distinct from their bulk counterparts, making them valuable for technological advancements.

1.4 Supervision and authorship

The thesis is organized as follows: Chapter 2 presents the original idea of quantum simulator of twisted bi-layer materials, specifically but not limited to magic angle twisted bi-layer graphene. It proposes the experimental set-up based on ultra-cold atoms of ^{87}Sr being confined in square optical lattice. Internal magnetic degrees of freedom of ground state manifold of the atoms are used to synthetically encode two layers. Spatially varying coupling between the layers - necessary for imitating the effect of physical rotation in real systems - is performed by spatially modulated light beam imprinted onto the lattice in the perpendicular direction. Such approach eliminates the necessity of generating bi-layer lattice and, moreover, the necessity of physical rotation of one of them. Hence, twistronics without a twist. Chapter 3 expands this idea and focuses on topological properties of such quantum simulators. By implementing specific terms and adjusting experimental scheme, we energetically separate system's quasi-flat bands. Such separation allows for broad exploration of edge states, Quantum Anomalous Hall Phases etc.

Chapter 4 is the attempt to grasp the effects of band flattening in interacting systems. We have undertaken an ambitious approach of exploring all possible interaction processes happening within each synthetic rung. We focused on attractive interactions and applied Hartree-Fock-Bogoliubov mean-field approximation. As a result, we have observed strong increase of the critical temperature due to band flattening. Chapter 5 is moving away from the idea of simulating 2D materials with ultra-cold atoms. It discusses a possibility of designing systems, that can be used as quantum batteries, i.e batteries, which can be charged faster than classical batteries. In this chapter we have dug deep into evolution of quantum state, both in it's Hilbert space and it's energy eigen-space. We have defined the observables and quantities allowing for precise description of the performance of any quantum system working as a quantum battery. The proper description of the problem allowed us to formulate fundamental bound on capacity and power of the batteries, which are tighter than those resulting from Quantum Speed Limit. We have tested out approach on multiple spin systems and analyzed their potential usefulness as quantum batteries.

Chapter 6 focuses on quantum simulation of bosonic systems, which naturally have different properties, than the fermionic ones. It describes the theoretical work, which we have done to support the first realisation of the Extended Bose-Hubbard in the solid state platform, that has been proven by the detection of the

theoretically anticipated correlated phases at specific fillings.

This thesis is a result of four and a half years of my stay at ICFO, as a PhD student. Within this time I had a privilege to work with many fantastic collaborators, who were also supervising my research. Each chapter here is based on the peer-reviewed research article that the author of this thesis coauthored. The first two chapters(2-3), based on [40, 41] were supervised by Dr. Debraj Rakshit. Results presented in Chapters 4 [42] and 6 [43] were supervised by Dr. Tobias Grass and research described in Chapter 5 [44] was supervised jointly by Dr. Arnau Riera and Dr. Manabendra Bera. Dr. Ravindra Chajjlany, who appears in all publications that form this thesis, had a tremendous impact on training and can be equally considered as one of my supervisors. All of my scientific activities were financed, supervised, but most of all supported by prof. Maciej Lewenstein. I am, once again, eternally grateful to all of them.

I tried to highlight the extent of my contribution in each chapter. Theory presented in Chapter 4. was developed by all the authors with equal commitment. Regarding the exemplary models, Dickie model was calculated by Dr. Julia Farre, LMG model by me, and analytically solvable model by both of us. I present all the results together since each of them is a crucial for the discussion on potential speed-up of quantum batteries. My contribution to results presented in Chapter V is mentioned in detail in the introduction of this chapter. Shortly, I have developed the exact diagonalization code that allowed us to calculate exact values of Structure Factor, as well as exact photo luminescence spectrum. Mean Field calculations, that provided the approximated phase diagram, have been done by Dr. Utso Bhattacharya.

Chapter 2

Generation of quasi-flat band systems

Design of new crystalline materials often begins with band predicting - a process, that allows one to tailor material's energy structure in the simplest, non-interacting, scenario. This free-electron assumption provides, although incomplete, information on energy dispersion and energy gaps, which then can be used to describe the electrical and optical properties of the designed solid, such as resistivity or optical absorption. Surely, when it comes to natural materials one has very limited portfolio of tools to modify band-structure, usually limited to creating new alloys, introducing defects, applying strains or changing the temperature of the materials. Band engineering in quantum materials has slightly different meaning - novel quantum simulation platforms offer a whole palette of possibilities, such as tuning of lattice constant, modifications of hopping amplitudes and lattice geometries, spin selective processes, just to name a few only in the non-interacting approximation. Therefore with quantum simulators, one has a chance to custom design a lattice system with a desired band structure. In this context, quantum simulators do not simulate real materials, but they are rather a type of synthetic material (system), where some desired physical phenomena can occur.

New class of systems, which reveal strongly correlated phenomena are flat-band materials. They form a special sub-group of quantum materials and owe many of their collective properties to strong suppression of the kinetic energy at Fermi level, and therefore reduction of the effective mass of the electrons [45, 46, 47, 48, 49]. Besides many flat-band materials naturally existing in nature [50], twisted bi-layer graphene (TwBLG) has emerged as a prime experimental platform hosting

flat band physics. Twistronics, a term coined from twist and electronics, is commonly used nowadays to describe the physics resulting from the twist between layers of two-dimensional materials. This terminology was introduced in Ref. [51], which conducted theoretical studies on how a twist between the layers can change electronic properties of bi-layer graphene. But the history of this new area of research goes back to Ref. [52], whose authors suggested that twisted bi-layer graphene could provide a new material with unprecedented properties. Flat bands at the magic angle were discovered in 2011 [53], whereas Bistritzer and MacDonald showed that for a twisted material with a "magic angle" the free electron properties radically change [46]. More recently, two seminal experimental papers [54, 55] demonstrated that such twisted bi-layer graphene at the magic angle can host both strongly insulating Mott states and superconductivity. These impressive results triggered an avalanche of experimental and theoretical works [56, 57, 58, 59, 60, 61, 62, 63, 64, 65, 66, 67, 68, 69, 70, 71, 72, 73] (See Ref. [74] for a recent review article).

However, preparation of the TwBLG sample is a task of the highest complexity - in order to access interesting flat-band correlated phenomenology one has to generate moiré patterns by rotating one of the layers of graphene by one of the very accurate angles - so called a "magic angles" (See Fig. 2.1) [58, 59, 60, 61, 62, 63, 64, 65, 66, 67, 68, 69, 70, 71, 72, 73]. Selecting "magic angles" to obtain desired properties is not applicable only to graphene. Different schemes of stacking 2-dimensional layers have emerged as a fruitful way of modifying material properties through the design of supercell structures and opened the field of so-called Van der Waals materials [75]. The geometrical moiré patterns effectively induce spatially varying inter-layer couplings that are behind the strong modification of the band structure. As in artificial graphene systems [76], emulating the physics of twisted bi-layer graphene beyond materials research- via analog quantum simulators for example- could allow identifying key minimal ingredients that give rise to the phenomenology of TwBLG.

Quantum simulators constitute one of the four major pillars of contemporary quantum technologies [77], and can be realized with various platforms such as ultra-cold atoms, trapped ions, superconducting qubits, circuit QED, Nitrogen vacancies in diamond, or nanostructure in condensed matter (for a review see [78, 79, 80, 81, 82, 83]) Ultra-cold atoms in optical lattices [84] is one of the the most promising platforms to explore experimentally also the corresponding emerging many-body phenomena. The experimental realization of artificial graphene geometries [85, 86], lattice geometries displaying flat bands like Kagome [87] and Lieb [88,

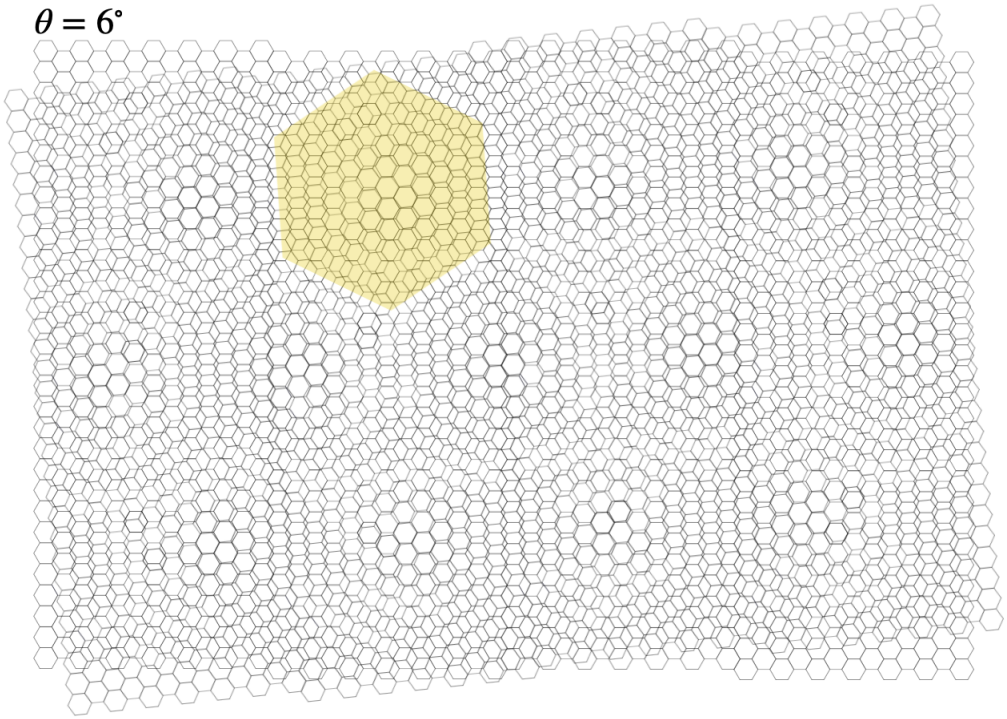

Figure 2.1: Moiré patterns of two hexagonal lattices and one rotated by approx 6 deg, with respect to the other. Size of the unit cell increases by two orders of magnitude comparing to untwisted double-layer graphene.

89], or quasi-crystal structures [90, 91, 92], provides the building blocks for such exploration.

One obvious approach to study twisted bi-layer graphene physics with ultra-cold atoms is to directly implement twisted bi-layers using two intertwined optical lattices, as recently proposed in Ref. [93]. Schemes for simulating other bi-layer heterostructures have also been put forward [94]. This direct strategy poses significant experimental challenges, as it is difficult to stabilize the two layers at relative small angles and simultaneously achieve a sufficiently large lattice containing several supercells. In this thesis, we have proposed an alternative and highly flexible experimental approach, corresponding to effectively *twisting the system without a twist*. Our scheme builds on the concept of synthetic dimensions

– reinterpreting the coherent coupling between spin states of an atom as tunneling along an artificial extra dimension [95, 96, 97]. As summarized in Fig. 3.2, we propose to realize a synthetic bi-layer structure formed by two Raman-coupled atomic states with a spatially dependent synthetic tunneling Ω in analogy to the effects of Moiré patterns of twisted bi-layer graphene. This leads to the creation of supercells with controllable sizes. By adjusting the strength, phase and spatial periodicity of Ω, this system allows engineering a broad range of band structures. In particular, *magic* values of the periodicity result in a band structure analogous to that of magic angle twisted bi-layer graphene, including Dirac cones touching a set of quasi-flat bands. Our proposal could be realized with fermionic two valence electron atoms, such as strontium or ytterbium, using available experimental techniques.

Following sections of this chapter are based on [98], where the discussed results appeared primarily.

2.1 The model

As a playground we have chosen a two-dimensional Fermi gas of neutral atoms. The gas is then loaded into a spin-independent square optical lattice of lattice spacing d, which lies in the $x - y$ plane and is characterized by a real tunneling amplitude t. In principle, as mentioned earlier, other optical lattice geometries are possible to implement, including a hexagonal lattice. Square lattice has been, however, chosen for simplicity and easiness of control. This choice will become clearer in the next section, when the twisting procedure is explained.

The concept of synthetic dimension - an additional degree of freedom acquired by control of internal states of each atom - allows one to define necessary spin states within a hyper-fine manifold of the ground states of the atoms, which plays the role of the synthetic dimension in this system. In case of presented model: two different spin states, $\sigma \pm \frac{1}{2}$ in two different layers $m = 0, 1$. four internal states will be associated as $\{m, \sigma\} = \pm 1/2$ spin states. More specifically, two states can be chosen to mimic the electron spin $\sigma = \uparrow$ - regardless the actual spin of the atom that is mimicking this electron spin. Similarly, other two sub-states work as electron spin $\sigma = \downarrow$.

In order to effectively construct a bi-layer lattice structure, spin states corresponding to the same σ are coupled in pairs. We label them by the index m, and make them play the role of a synthetic layer dimension. Since $m = 0, 1$, we obtain a bi-layer structure of synthetic layer tunneling given by the coherent coupling. In order to obtain a lattice geometry with a large supercell analogous to a Moiré pattern in twisted bi-layer graphene, the amplitude of the synthetic layer tunneling amplitude is spatially modulated according to

$$\Omega(x, y) = \Omega_0 \left[1 - \alpha(1 + \cos(2\pi x/l_x)\cos(2\pi y/l_y))\right]. \tag{2.1}$$

Here l_x (l_y) is its periodicity along the x and y axis. Of course, the presented form of inter-layer hopping $\Omega(x, y)$ (Eq. (2.1)) does not correspond to rotation - as it is in the real Twisted Bi-layer Graphene. This is because in our synthetic system we are not limited to transformations of the whole sheets of graphene. Rotation is one of the transformations one can perform with bi-layer graphene in order to modulate the inter-layer coupling, since the shape of each sheet is given. Using Spatial Light Modulator - a device allowing one to imprint desired spatial light pattern onto the lattice - we can generate any spatial pattern, not limiting ourselves to rotations.

The synthetic tunneling also induces a Peierls phase $\boldsymbol{\gamma} \cdot \mathbf{r}$, where $\boldsymbol{\gamma} = \gamma\hat{x} + \gamma\hat{y}$ and $\boldsymbol{r} = x\hat{x} + y\hat{y}$. This mimics the effect of a magnetic flux that pierces the system perpendicularly to the synthetic layer dimension [96]. As depicted in Fig. 2.2, the complete scheme represents a synthetic spinfull bi-layer structure subjected to a spatially modulated light field, that induces desired commensuration of the inter-layer hopping, denoted as $\Theta(l_x, l_y)$.

The Hamiltonian of the system is given by

$$\begin{aligned} H &= H_{\text{in}} + H_{\text{inter}} \\ &= -t \sum_{\mathbf{r},\sigma} \Big[a^{\dagger}_{0,\sigma}(\mathbf{r} + d\,\hat{x}) + a^{\dagger}_{0,\sigma}(\mathbf{r} + d\,\hat{y}) \\ &\qquad + \Omega(\mathbf{r}) \exp(-i\boldsymbol{\gamma} \cdot \mathbf{r})\, a^{\dagger}_{1,\sigma}(\mathbf{r}) \Big] a_{0,\sigma}(\mathbf{r}) + \text{H.c.}, \end{aligned} \tag{2.2}$$

where we distinguish the in-layer and the inter-layer tunnelings. To diagonalize the Hamiltonian 2.2, we combine a gauge transformation and a Fourier transform such that

$$a_{m,\sigma}(\mathbf{r}) = \sum_{\mathbf{q}} \exp\left(i(\mathbf{q} \cdot \mathbf{r} + m\boldsymbol{\gamma} \cdot \mathbf{r})\right) a_{m,\sigma}(\mathbf{q}). \tag{2.3}$$

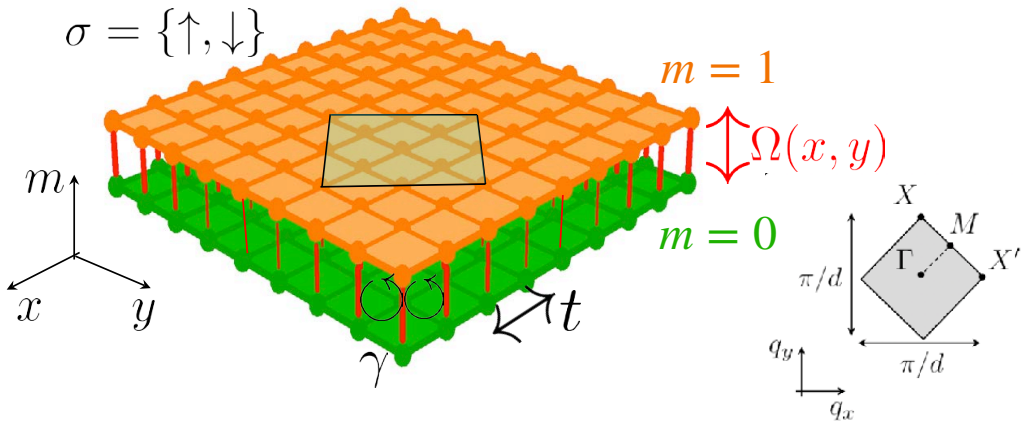

Figure 2.2: Synthetic bi-layer structure with a supercell. Real-space potential of the synthetic bi-layer. Each plane corresponds to one spin state $m = 0, 1$ (orange, green), which experiences a square lattice potential (tunneling t) and is connected to the other layer by a spatially-dependent and complex coupling $\Omega(x, y)$ (vertical red lines of variable width). A top view of the lattice indicating the unit cell of the system containing 2×8 sites for $l_x = l_y = 4d = \Theta(4, 4)$ is shown (black line).

Here, $\mathbf{q}$ is the momentum conjugated to $\mathbf{r}$. The Hamiltonian can then be rewritten as

$$H = \sum_{\mathbf{q}} H_{\mathbf{q}}, \tag{2.4}$$

where the dimension of $H_{\mathbf{q}}$ is set by the spatial periodicity of the synthetic tunneling. Fig. 2.2 sketches the Brillouin zone of the bi-layer system and a three-dimensional view of its energy spectrum for $l_x = l_y = 4d$, corresponding to $\Theta(4, 4)$, for $\gamma = 0$. In the vicinity of $E = \pm\Omega_0(1-\alpha)$, it features two quasi-flat bands and a Dirac point touching them (only one of them is represented in Fig. 2.2). This band structure is reminiscent of that of magic angle twisted bi-layer graphene.

2.2 Experimental proposal

In our studies we have focused on the cold atom based platform that realizes the quasi-flat band engineering by employing a subset of four states out of the large nuclear spin manifold $I = 9/2$ of ^{87}Sr. The choice of this specific atomic species has been made due to its wide use in experimental set-ups. The proposal could, however, be directly implemented with ^{173}Yb ($I = 5/2$) as well.

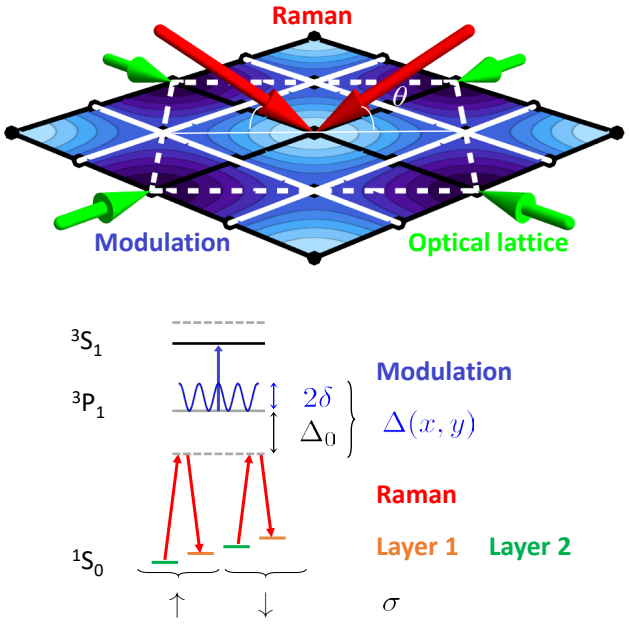

Figure 2.3: Sketch of the first Brillouin zone, indicating the position of the high-symmetry points, and three dimensional view of the energy spectrum in the vicinity of $E = -\Omega_0(1-\alpha)$ for $\Omega_0\alpha/h = 20t$ with $\alpha = 0.2$ and $\gamma = 0$. It has two quasi-flat bands intersecting a Dirac point. Note that a simple square lattice supports neither flat-bands nor Dirac cones. (c) Proposed experimental realization. Top: Two retro-reflected optical lattice beams (green) create the square lattice. Two Raman beams of opening angle θ (red) produce complex synthetic tunneling between the two layers. One "modulation laser" with a spatially varying intensity distribution (blue) modulates the amplitude of the Raman coupling. Bottom: laser beams involved in the synthetic bi-layer coupling scheme. The single-photon detuning of the Raman beams (red arrows) is spatially modulated with respect to its initial value $\Delta_0/2\pi \sim 75$ MHz using a laser beam blue detuned with respect to the $^3P_1 \rightarrow {}^3S_1$ transition (blue arrow). It produces a light shift of maximal amplitude $2\delta/2\pi \sim 30$ MHz.

Thanks to the $SU(N)$ invariant interactions characteristic of elements with two electrons in the outer shell, collisional redistribution of the atoms among the different states is inhibited. Further implications of such symmetry will be

discussed in the following sections. Two sub-levels from a ground state manifold have been arbitrarily chosen to play the role of the electron spin $\sigma = \uparrow$ in 2 accessible layers, and the other two for the spin $\sigma = \downarrow$. All the atoms are subjected to a two-dimensional spin-independent optical lattice potential, created by two counter-propagating lattice beams. We choose $\lambda_L = 813$ nm, which is commonly used because it corresponds to the magic wavelength of the clock transition ${}^1S_0 \rightarrow {}^3P_0$.

We set a lattice depth $8\,E_L$, which yields $t/h = 107$ Hz. Here, $E_L = \hbar^2 k_L^2/2m$ is the lattice recoil energy, $k_L = 2\pi/\lambda_L$, and $d = \lambda_L/2$.To create the synthetic layer tunneling, we exploit two-photon Raman transitions between spins $m = \pm 1/2$ (To suppress optical transitions to other spin states, an additional laser beam of smaller detuning and producing a large differential light shift can be used). We employ a pair of Raman beams of wavelength $\lambda_R = 689\ nm$ near-resonant to the inter-combination transition ${}^1S_0 \rightarrow {}^3P_1$, which produce a coupling of amplitude $\Omega_0 = \Omega_1\Omega_2/\Delta_0$. Here Ω_1 and Ω_2 are the individual coupling amplitudes of the Raman lasers and Δ_0 the single-photon detuning. The Raman beams propagate in a plane perpendicular to the lattice potential, are aligned along its diagonal, and form an angle θ with the lattice plane (see Fig. 2.3). This yields an in-plane momentum transfer per beam $k_R = \pm 2\pi \cos\theta/\lambda_R$, with projections $k_R/\sqrt{2}$ along the lattice axes. Therefore, the phase of the synthetic tunneling is $\boldsymbol{\gamma} \cdot \mathbf{r} = \gamma(x\hat{x} + y\hat{y})$, with $\gamma = \pm 2\pi\lambda_L/(\sqrt{2}\lambda_R)\cos\theta$. The sign is determined by the relative detuning of the Raman lasers. Experimentally, the simplest choice is to use counter propagating Raman beams ($\theta = 0°$), which yields $\gamma = 0.8 \pmod{2\pi}$. However, other magnetic fluxes can be easily realized by adjusting the value of θ.

2.3 Twisting Analogy

To implement a periodic modulation of the Raman coupling amplitude on the scale of several lattice sites, which is the key ingredient of our scheme, we propose to exploit a periodic potential created by a laser close-detuned from the excited state to excited state transition ${}^3P_1 \rightarrow {}^3S_1$ (corresponding to 688 nm [99]). This results in a large light shift of the ${}^3P_1$ excited state of amplitude δ, leading to a space-dependent detuning of the Raman beams

$$\Delta(x, y) = \Delta_0 + \delta(1 + \cos(2\pi x/l_x)\cos(2\pi y/l_y)). \tag{2.5}$$

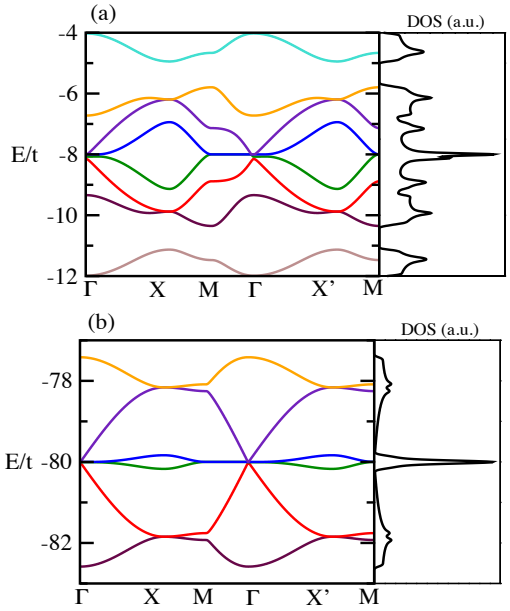

Figure 2.4: Magic configuration band structure and DOS. Band structures around energy $-\Omega_0(1-\alpha)$ and DOS (in arbitrary units) corresponding to $\Theta(4,4)$ supercell along the paths passing through the high-symmetry points $\mathbf{\Gamma}, \mathbf{X}, \mathbf{M}, \mathbf{\Gamma}, \mathbf{X}', \mathbf{M}$. Panels (a) and (b) corresponds to $\Omega_0\alpha/h = 2t$ and $20t$, respectively, with $\alpha = 0.2$ and $\gamma = 0.8$. In the evolution from panel (a) to (b) the six central bands in panel (a), denoted with colors from orange to maroon, remain close in energy (as part of one single band, see perturbative analysis in Sec. 2.4) while the remaining two bands in panel (a) (in cyan and brown) separate in energy and do not appear in panel (b).

Its effect is to modulate the Raman coupling amplitude

$$\Omega(x,y) \simeq \Omega_0[(1-\alpha) - \alpha\cos(2\pi x/l_x)\cos(2\pi y/l_y)], \tag{2.6}$$

with $\alpha = \delta/\Delta_0 \sim 0.2$ for realistic experimental parameters, see Fig. (2.4) [99, 100]. We therefore name the Raman lasers "modulation laser". Band structures analogous to the one depicted in Fig. (2.4) are obtained for large values of $\alpha\Omega_0/h \gtrsim 20t = 10.7$ kHz and spatial periodicities of the Raman coupling of several lattice sites (In this regime, the inter-layer tunneling remains smaller than the band gap between the first and second band of the real-space lattice $\Delta E/h = 13.5$ kHz). The necessary patterns could therefore be projected by combining a spatial light modulator and an optical system of moderate optical resolution, ensuring a large

flexibility.

The emerging band structures are sensitive to the spatial modulation and the strength of the laser coupling. Proper manipulations of the involved parameters can yield flat bands. Typically, a system with weak Raman coupling ($\Omega_0\alpha/h \lesssim t$) hosts a large number of extended hybridized bands. Enhanced coupling strength ($\Omega_0\alpha/h \approx 10t$) tends to foster band narrowing. Magic-angle TwBLG is characterized by flat-bands leading to a strong suppression of the Fermi velocity around the Dirac points. Analogous band structures can be realized for judicious adjustment of the Raman coupling periodicity, and as we discuss below, $\Theta(4,4)$ turns out to be the configuration with smallest moiré supercell (2×8) sites supporting a TBLG-like band structure. Fig. 1(b) illustrates spin degenerate bands around $E/t = -\Omega_0(1-\alpha)$ for an exemplary case with $\Omega_0\alpha/h = 20t$, $\alpha = 0.2$ and $\gamma = 0$. The spectrum of the system is symmetric around $E = 0$, so that we only discuss the band structure at $E < 0$. The proposed experiment considers the effect of an additional magnetic flux, set by the parameter $\gamma = 0.8$. Narrow bands are formed for sufficiently large $\Omega_0\alpha$ at the energies $-\Omega_0$, $-\Omega_0(1-\alpha)$ and $-\Omega_0(1-2\alpha)$. The bands close to the energy $-\Omega_0(1-\alpha)$ along the high-symmetry points are shown in Fig. 2 for (a) $\Omega_0\alpha/h = 2t$ and (b) $\Omega_0\alpha/h = 20t$. In this case, two near-degenerate quasi-flat bands at energy $-\Omega_0(1-\alpha)$ and two Dirac cones appear. Such values of Ω_0 and α are reachable in our setup, leading to tunable bandwidth for the quasi-flat bands. Figs. 2 also shows the associated density of states (DOS), which is given by

$$D(E) = L^{-d/2} \sum_i \left(E - E\left(\mathbf{k}_i\right)\right). \tag{2.7}$$

The central peak at the energy $-\Omega_0(1-\alpha)$ corresponds to a van-Hove singularity associated with the almost flat bands at sufficiently large Raman coupling.

Interestingly, band structures similar to the $\Theta(4,4)$ case appear when $l_x = l_y = 4\nu d$, with ν integer. This can be explained by treating the intra-layer tunneling as a perturbation to the inter-layer tunneling. As explained in the next section, the nodal lines of the periodic modulation determine a bi-layer Lieb lattice of sites. The two layers are energetically well separated with on-site energies $\pm\Omega_0(1-\alpha)$, respectively. The perturbation then induces tunnelings within the Lieb lattice topology, which at first order are composed of nearest neighbor tunneling matrix elements within a single layer. The Lieb lattice in its simplest form [101] is known to host a pair of Dirac cones intersecting at a single $\mathbf{k}$ point on a completely flat band, the Dirac point. The dispersion of the flat bands in the full model described by Eq. (2.2) originates from higher-order contributions in perturbation

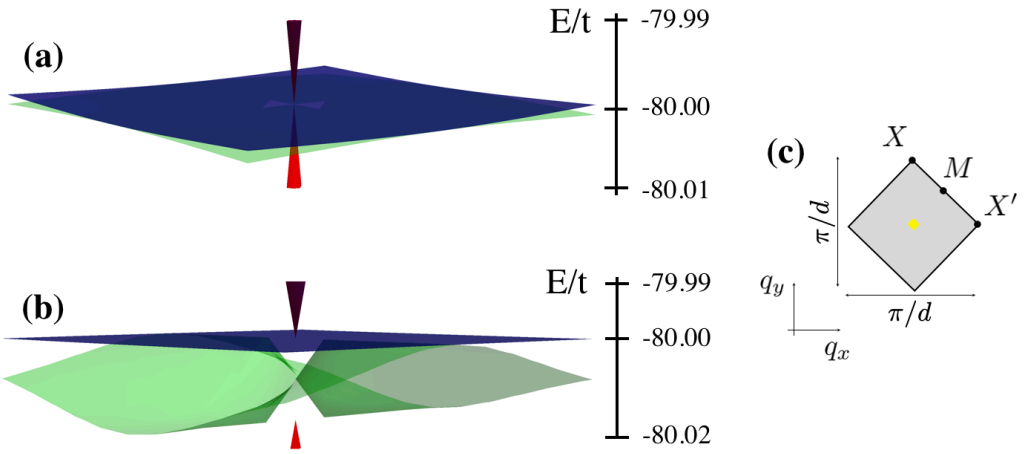

Figure 2.5: Gap opening and Dirac cone widening due to the artificial flux γ. Four bands (Dirac cones (purple and red) and quasi-flat bands (green and blue)) are shown in the vicinity of $E/t = -\Omega_0(1-\alpha) = -80$, for the $\Theta(4,4)$ system. The parameters and color scale of the bands are identical to those of Fig. 2.4(b), except for the magnetic flux that corresponds to (a) $\gamma = 0$ and (b) $\gamma = 0.8$. The energy surfaces are rotated for visibility, and only a small region centered at the $\Gamma = (0,0)$ point in the Brillouin zone (yellow area in (c), corresponding to $\sim 4\%$ of the complete Brillouin zone) is depicted.

theory. More generally, for $l_{x(y)} = 4\nu_{x(y)}$, where $\nu_{x(y)}$ are positive integers, a similar argument shows that the system can be effectively described by super-Lieb lattices with a supercell of $2(\nu_x + \nu_y) - 1$ sites. Moving away from these configurations leads generically to absence of Dirac-like physics similarly to moving away from magic angles in TwBLG.

This proposal offers a powerful setup for engineering a wide range of band structures. By manipulating the periodicity and strength of the Raman coupling, and controlling the value of the chemical potential, it is possible to drive the system from insulating to semi-metallic and then metallic-type phases, as we will show in the following sections. An additional control parameter in our system is the artificial magnetic flux γ. It affects the band structure in a number of ways. As earlier, we focus on the case $\Theta_M = \Theta(4,4)$ and the 6 bands closest to $E/t = -\Omega_0(1-\alpha)$. Increasing γ leads to strong band narrowing. More interestingly, a non-zero γ opens a gap between

the two quasi-flat bands at the $\Gamma = (0, 0)$ point in the Brillouin zone. Moreover, the lower Dirac cone detaches from the lower quasi-flat band. This is reminiscent of the effect of a staggered chemical potential in the Lieb lattice [102]. However, in our model the upper quasi-flat band remains pinned exactly at the central energy ($E/t = -\Omega_0\,(1-\alpha)$) around the Γ point, and the upper Dirac cone remains gapless. Typical band configurations for two values of γ are shown in Fig. 2.5. The flux γ also controls the Dirac velocity of the cone which tends to zero as $\gamma \to \pi$.

As already mentioned, the exact features of the spectrum can be traced *via* second order perturbation theory for large $\Omega_0(1-\alpha)$. The narrowing bandwidth and flattening of the Dirac cone are primarily driven by the same factor: the generically dominant (first order) nearest neighbour effective tunneling on the effective Lieb lattice decreases as $-t\cos(\gamma/2)$ when γ increases. On the other hand, the gap opening is driven by the tunneling modulation pattern breaking the C_4 ($\pi/2$ rotation) symmetry of the effective lattice for $\gamma \neq 0$.

2.4 Effective model

The origin of the almost flat (weakly dispersive) bands centered around energies $\pm(1-\alpha)\Omega_0$ for certain magic periodicities (multiples of 4 lattice spacings) of strong Raman coupling can be understood *via* a perturbative treatment of the Hamiltonian Eq. (2.2). For this regime $\Omega(\mathbf{r}) \gg 1$, it is fruitful to diagonalize the Raman coupling term using the operators

$$c_{\pm 1/2,\sigma}(\mathbf{r}) = \exp\Big[\mp\tfrac{i}{2}\gamma\cdot\mathbf{r}\Big](a_{1/2,\sigma}(\mathbf{r}) \pm a_{1/2,\sigma}(\mathbf{r}))/\sqrt{2}. \tag{2.8}$$

Setting the energy scale $t = 1$, the Raman inter-layer coupling then takes the form of a chemical potential

$$H_{\text{inter}} = \mp \sum_{\mathbf{r},\sigma\pm\frac{1}{2}} \Omega(\mathbf{r}) c^{\dagger}_{\pm 1/2,\sigma}(\mathbf{r}) c_{\pm 1/2,\sigma}(\mathbf{r}), \tag{2.9}$$

while the intra-layer perturbative coupling becomes

$$H_{in} = -\sum_{\mathbf{r},\hat{\mu}=\hat{x},\hat{y}} \sum_{m,m',\sigma\pm\frac{1}{2}} c^{\dagger}_{m',\sigma}(\mathbf{r}+\hat{\mu}) \left(\cos\frac{\gamma}{2}1 + i\sin\frac{\gamma}{2}\sigma^{x}\right)_{m'm} c_{m,\sigma}(\mathbf{r}) + H.c. \tag{2.10}$$

This describes a coupled bi-layer system with intra-layer tunneling $-\cos(\gamma/2)$ and inter-layer tunneling $-i\sin(\gamma/2)$. Recall that the two layers actually correspond to different internal states on a single physical layer, so the mixing term is an effective spin-orbit coupling. The two layers have different on-site chemical potentials. We choose the lower layer to host the $c_{+1/2,\sigma}$ fermions and have potential $-\Omega(\mathbf{r})$.

The perturbation is highly effective if the potential $\Omega(\mathbf{r})$ displays equipotential connected regions, i.e. if the nodes of the periodic modulation (cosines) lie on the lattice. This certainly occurs when l_x and l_y are multiples of four. For concreteness, we discuss here the case $l_x = l_y = 4$ and $0 < \alpha < 1$. In this case the nodal lines of the periodic modulation determine a Lieb lattice (see Fig. 2.6) of sites with the same on-site energy. Furthermore, we focus on the layer with $m = 1$ and determine the spectrum centered around $-(1-\alpha)\Omega_0$. Here, please note, that the $m = 0, 1$ layers are energetically well separated. At first order, the perturbation Eq. (2.10) partially lifts the degeneracy by inducing tunneling between sites on the Lieb lattice (black lines in Fig. 2.6).

Nearest neighbor tunneling on a Lieb lattice leads to a three band energy spectrum consisting of a completely flat band containing a Dirac point at which a pair of dispersive bands (with energy respectively higher and lower than the flat band) intersect. The Dirac point is located at the corner of the Brillouin zone $(\pm\pi/2, \pm\pi/2)$. This explains the origin of the band structure around energy $-\Omega_0(1-\alpha)$ (and by analogy around $\Omega_0(1-\alpha)$) as shown in the main text). However, although the Lieb lattice has a unit cell of 3 sites (1 corner and two bridge sites), our full Hamiltonian has a unit cell containing six Lieb lattice sites (one choice is shown in Fig. 2.6). This full unit cell is recovered already in second order perturbation theory. The doubling of the Lieb lattice unit cell leads to folding of the Brillouin zone. Therefore, the two Dirac cones in our system are at wave vector $\mathbf{k} = (0, 0)$. Moreover, the spectrum around $-\Omega_0(1-\alpha)$ consists of six bands. To avoid any confusion, note that in our nomenclature, the Lieb lattice spectrum (and the spectrum of our model system) has two Dirac cones – one with "positive" excitation energy and the other with "negative" excitation energy with respect to the quasi-flat band. In contrast, in literature, a shorthand notation is often used whereby the Lieb lattice is said to have a single Dirac cone. This is to distinguish it from lattices where there are two or more inequivalent Dirac points. The latter notation is also motivated by the fact that one is often interested in the (particle) excitations above the flat band. The detailed band structures, with quasi-flat bands, shown in the main text in Fig. 2.3 can be well recovered in second order

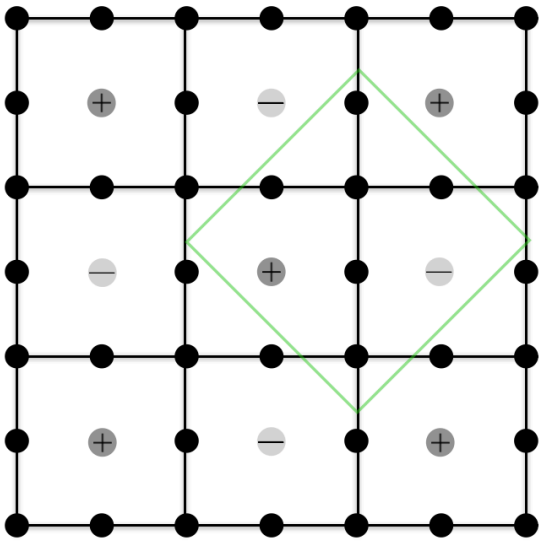

Figure 2.6: Top view of the lattice for a modulation $\Omega(x,y) \simeq \Omega_0[(1-\alpha) - \alpha\cos(2\pi x/l_x)\cos(2\pi y/l_y)]$, with $l_x, l_y = 4$. Black sites correspond to $\Omega(\mathbf{r}) = \Omega_0(1-\alpha)$, grey sites marked with $\pm$ correspond to sites with $\Omega(\mathbf{r}) = \Omega_0(1-\alpha\pm\alpha)$. The latter are energy forbidden sites. Green boundary: unit cell of the lattice. Black lines denote the tunneling between the Lieb lattice sites generated. They are responsible for the main features of the band structures centered at $\pm\Omega_0(1-\alpha)$ described in the main text: a flat band intersected by the Dirac cones. The effects of the grey sites are only taken into account in second order perturbation theory (see Fig. 2.7).

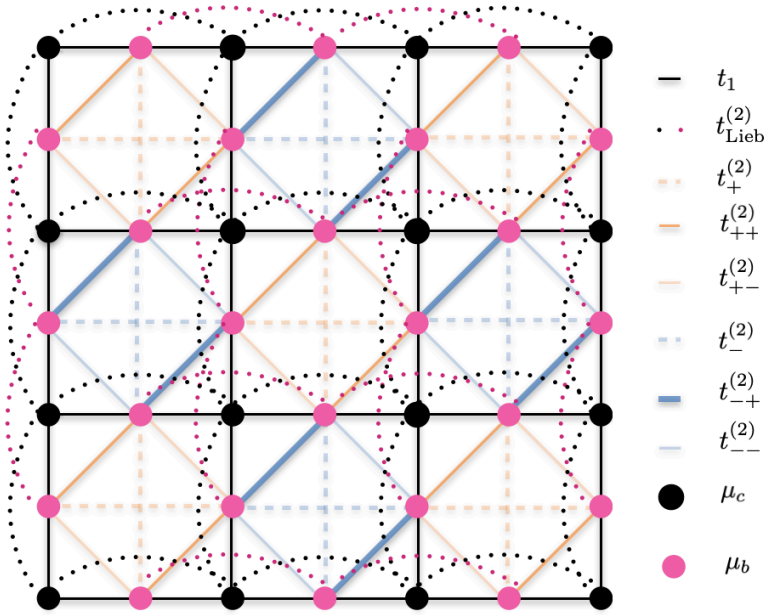

Figure 2.7: Modified effective Lieb lattice for the energy band centered at $-\Omega_0(1-\alpha)$ emerging up to second order of perturbation in the tunneling of Eq. (2.10). Black full lines are the first order effect. The second order contributions stem from virtual tunneling to forbidden energy states both within the single layer with $m = 1/2$ (grey sites in Fig. 2.6) as well as from spin-orbit coupling interaction coupling to the other $m = -1/2$ lattice (grey sites in Fig. 2.6 as well as Lieb lattice sites. As a result for $\gamma \neq 0, \pi$, the chemical potential within a layer takes two different values μ_c on corner (black) and μ_b on bridge sites (pink). Additionally a periodic pattern of next nearest and third neighbor tunneling is generated as shown by the colored lines (both full and dotted). The unit cell is that of the original lattice shown in Fig. 2.6. The values of the appropriate tunnelings are written in the text: t_1(solid black lines, first order tunneling on the Lieb lattice), $t^{(2)}_{\text{Lieb}}$ (black and pink dotted lines), horizontal and vertical tunnelings $t^{(2)}_{\pm}$ between bridge sites over forbidden sites with $\Omega(\mathbf{r}) = \Omega_0(1 - \alpha \pm \alpha)$ (dotted orange ($t^{(2)}_{+}$) and blue ($t^{(2)}_{-}$) lines). Finally, tunnelings between next neighboring bridge sites are given by $t^{(2)}_{++}$ (thick orange) and $t^{(2)}_{+-}$ (orange) and $t^{(2)}_{-+}$ (thick blue) and $t^{(2)}_{--}$ (blue).
[t!]

perturbation theory for large $\Omega_0(1-\alpha)$, as seen in Fig. 2.8. The modification of the band structure is due to an additional periodic pattern of tunnelings in the Lieb lattice of the same periodicity of the supercell $\Theta(4,4)$ generated by virtual tunneling to energy forbidden sites as shown in Fig. 2.7. The various terms described in Fig. 2.7 are gathered below.

$$t_1 = -\cos\frac{\gamma}{2}, \quad t^{(2)}_{\text{Lieb}} = \frac{\sin^2\left(\frac{\gamma}{2}\right)}{2(1-\alpha)\Omega_0} \tag{2.11}$$

$$t^{(2)}_{+} = \frac{\sin^2\left(\frac{\gamma}{2}\right)}{2(1-\alpha)\Omega_0 + \alpha\Omega_0} + \frac{t_1^2}{\alpha\Omega_0} \tag{2.12}$$

$$t^{(2)}_{++} = \frac{\sin^2\left(\frac{\gamma}{2}\right)}{2(1-\alpha)\Omega_0 + \alpha\Omega_0} + \frac{t_1^2}{\alpha\Omega_0} + t^{(2)}_{\text{Lieb}} \tag{2.13}$$

$$t^{(2)}_{+-} = -\frac{\sin^2\left(\frac{\gamma}{2}\right)}{2(1-\alpha)\Omega_0 + \alpha\Omega_0} + \frac{t_1^2}{\alpha\Omega_0} - t^{(2)}_{\text{Lieb}} \tag{2.14}$$

$$t^{(2)}_{-} = \frac{\sin^2\left(\frac{\gamma}{2}\right)}{2(1-\alpha)\Omega_0 - \alpha\Omega_0} - \frac{t_1^2}{\alpha\Omega_0} \tag{2.15}$$

$$t^{(2)}_{-+} = \frac{\sin^2\left(\frac{\gamma}{2}\right)}{2(1-\alpha)\Omega_0 - \alpha\Omega_0} - \frac{t_1^2}{\alpha\Omega_0} + t^{(2)}_{\text{Lieb}} \tag{2.16}$$

$$t^{(2)}_{--} = -\frac{\sin^2\left(\frac{\gamma}{2}\right)}{2(1-\alpha)\Omega_0 - \alpha\Omega_0} - \frac{t_1^2}{\alpha\Omega_0} - t^{(2)}_{\text{Lieb}} \tag{2.17}$$

$$\mu_c = -\frac{2\sin^2\left(\frac{\gamma}{2}\right)}{(1-\alpha)\Omega_0} \tag{2.18}$$

$$\mu_b = -\left(\frac{1}{2(1-\alpha)\Omega_0 - \alpha\Omega_0} + \frac{1}{2(1-\alpha)\Omega_0 + \alpha\Omega_0} + \frac{1}{(1-\alpha)\Omega_0}\right)\sin^2\left(\frac{\gamma}{2}\right). \tag{2.19}$$

Now, we comment on the evolution of the bands with the change of the flux γ. From Eqs. (2.11)-(2.19) we see that for $\gamma = \pi$ the effective lattice consists of two inequivalent square lattices composed of the bridge and corner sites, respectively, that are completely decoupled from each other. The corner sites form a simple square lattice structure with lattice spacing $2d$, while the bridge sites form a more

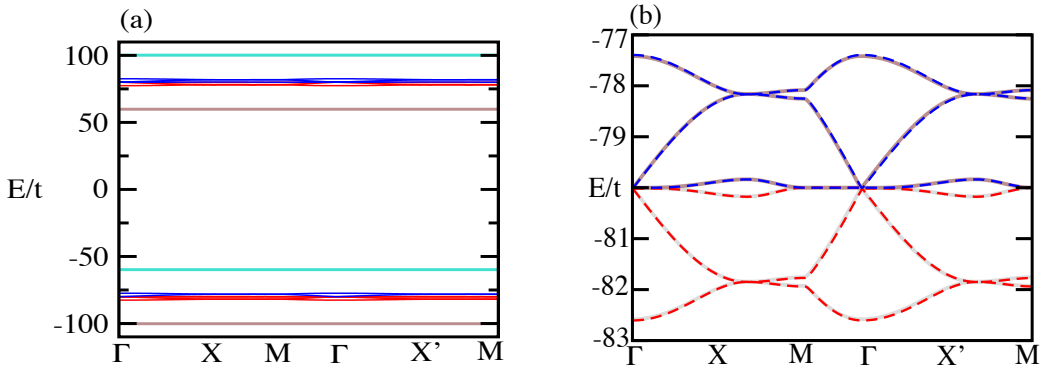

Figure 2.8: (a) Full band structure of $\Theta(4,4)$ for $\Omega_0\alpha/h = 20t$, with $\alpha = 0.2$ and $\gamma = 0.8$. (b) Zoom of the energy window around $E/t = -\Omega_0(1-\alpha) = -80$ showing the comparison of exact (solid line) and perturbative (dashed line) results.

complicated square lattice. However, neither of these support Dirac cones. These lattices have dispersive yet very narrow bands since the tunnel coupling is of the order of $0.01t$. This is distinct from the opposite limit $\gamma = 0$, which is a Lieb lattice with additional tunnelings between bridge sites. Increasing γ decreases the total bandwidth of the 6-band system due to the dependence of the dominant coupling t_1 Eq. (2.11). The flat band and Dirac cone subsystem is modified as γ is increased. In particular, the upper Dirac cone angle widens as a consequence of the decreasing bandwidth and therefore the Dirac velocity decreases. The upper flat band however exists pinned to the bare chemical potential $-\Omega_0(1-\alpha)$ at the Brillouin zone center for all γ. We have found that the behaviour of the lower Dirac cone and the opening of a gap to the upper flat band is due to the C_4 symmetry breaking modulation in tunnelling between bridge sites. Indeed, on one hand this symmetry is explicitly unbroken where there is no gap. Moreover, we have also checked that setting the other possible factor, i.e. chemical potential staggering to zero does not influence the magnitude of the gap. The unimportance of the staggered chemical potential comes from the fact that the staggering in chemical potential is two orders of magnitude smaller than the staggering in tunneling.

Finally, in the context of twistronics, it is amusing to note that the two disentangled lattices at $\gamma = \pi$ are rotated with respect to each other by $\pi/4$. By tuning γ towards 0, their coupling becomes stronger. This leads to a change in the band structure with the formation of Dirac cones that are attracted to each other at the center of the Brillouin zone towards the quasi-flat band.

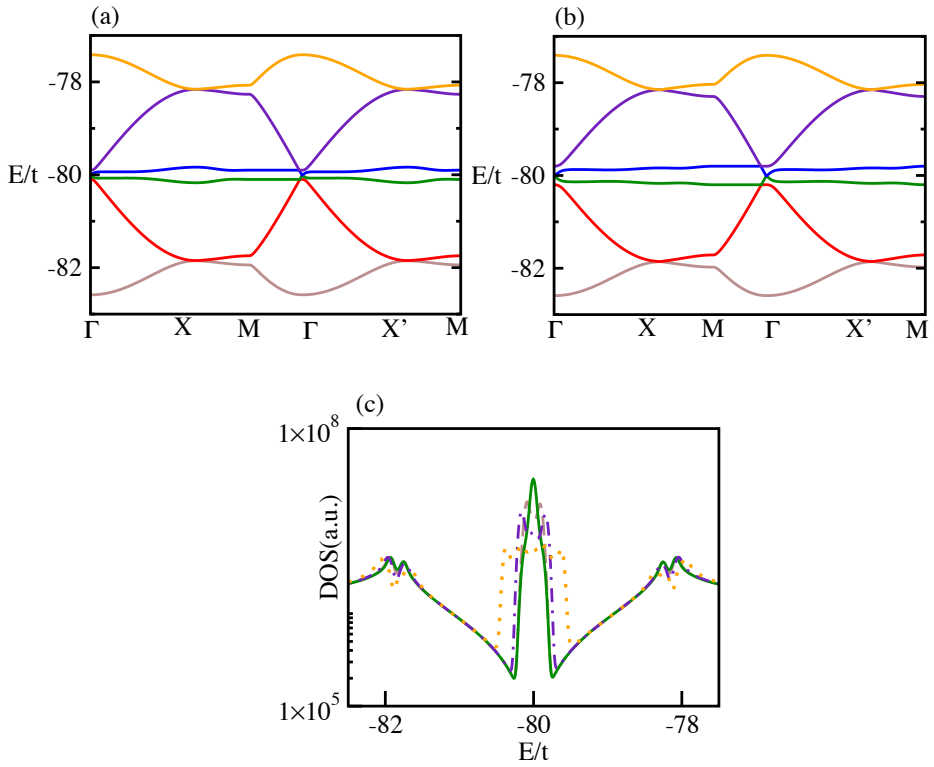

Figure 2.9: Effect of a phase shift in the spatially-dependent periodic Raman coupling. Panels (a-c) corresponds to $\Omega_0\alpha/h = 20t$, with $\alpha = 0.2$ and $\gamma = 0.8$. Single particle band calculations are shown in the vicinity of $E/t = -(1-\alpha)\Omega_0$ for $\phi_x = \phi_y = 0.005$ (a) and 0.01 (b). The DOS (in arbitrary units) for different phases are depicted in (c). The solid, dashed, dashed-dotted and dotted lines are represent the cases for $\phi_x = \phi_y = 0$, 0.005, 0.01 and 0.02, respectively. Note the logarithmic scale in (c).

2.4.1 Effect of phase shifts in the interlayer coupling

We briefly discuss the effect of allowing a phase in the spatial modulation of the synthetic layer tunneling amplitude, such that

$$\Omega(x,y) \simeq \Omega_0[(1-\alpha) - \alpha\cos(2\pi x/l_x + \phi_x)\cos(2\pi y/l_y + \phi_y)]. \tag{2.20}$$

Small phases ϕ_x and ϕ_y displace the near-degenerate quasi-flat bands at energies $\pm(1-\alpha)\Omega_0$ away from each other. As a result the central peak of the DOS splits into a double peak structure for small values of these phases. Interestingly, a

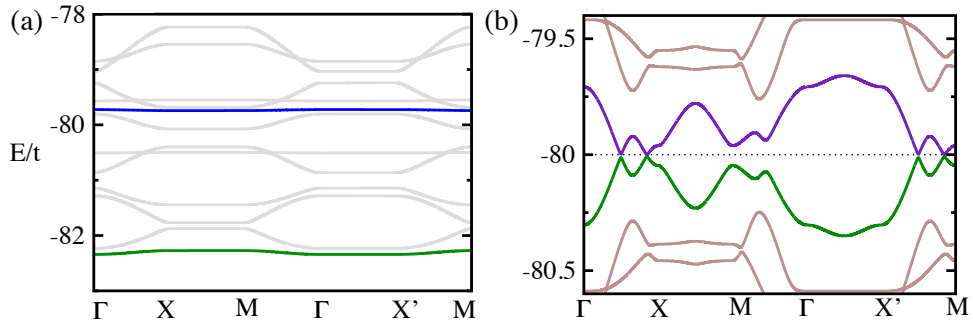

Figure 2.10: Band structures around the energy $-\Omega_0(1-\alpha)$ are depicted for (a) $\Theta(4,7)$ and (b) $\Theta(4,8)$ configuration for $\Omega_0\alpha/h = 20t$, with $\alpha = 0.2$ and $\gamma = 0.8$. The dotted line in (b) serves as a guide to the eye.

double peak structure in magic angle TwBLG has been reported in previous works [103, 104]. Associated band calculations and DOS are shown in Fig. 2.9.

2.4.2 Non-magic configurations

As already mentioned before, the proposed scheme can be exploited to engineer a broad range of band structures by simply manipulating the periodicity of the spatial modulation of the Raman lasers in the square lattice under consideration, or by modifying the lattice structure in itself, along with other parameters, such as Raman coupling strength and magnetic flux. In order to demonstrate that the band structures obtained for $\Theta(4,4)$ are not generic, we illustrate exemplary results for the configurations $\Theta(4,7)$ and $\Theta(4,8)$ in Fig. 2.10(a-b). The chosen parameters have been selected for experimental convenience. We again focus in the vicinity of $E/t = -\Omega_0(1-\alpha)$. While $\Theta(4,7)$ supports a branch of isolated or hybridised flat bands, $\Theta(4,8)$ supports semi-metallic-type bands at $E/t = -\Omega_0(1-\alpha) = -80$.

2.5 Conclusions and outlook

The basic element in the physics of TwBLG is the creation of large unit cells by rotating two layers with respect to each other. Around the magic angles, small rotations have a dramatic effect on the band structure of these systems. In this chapter, we have discussed a versatile method to create a new class of systems with controllable supercell structures for cold Fermi gases trapped in optical lattices.

The size of the supercells is easily tunable and should allow addressing whether the physics of TwBLG is uniquely related to their macroscopic periodicity or indeed can be accessed for small unit cells. An inherent advantage of our optical-lattice-based construction is the possibility to modify over a wide range the inter-layer coupling, which is controlled by a combination of optical Raman transitions and excited-state light shifts. We have shown that a square lattice synthetic bi-layer displays a band structure that can be easily engineered by modifying the spatial periodicity, strength and Peierls phase imparted by the Raman lasers. It bears analogies to TwBLG in that it supports Dirac cones and quasi-flat bands in particular energy ranges and at certain *magic* periodicities.

The existence of identical scattering lengths parameterizing interactions between the atoms in the four internal states allows simulating the effect of both intra- and inter-layer interactions in the synthetic bi-layer structure. The interacting Hamiltonian can be written as

$$H_{\mathrm{I}} = U/2 \sum_{\mathbf{r}} n(\mathbf{r})(n(\mathbf{r}) - 1), \tag{2.21}$$

where

$$n(\mathbf{r}) = \sum_{m,\sigma} a^{\dagger}_{m\sigma}(\mathbf{r}) a_{m\sigma}(\mathbf{r}), \tag{2.22}$$

is the occupation of site ($\mathbf{r}$) of the square optical lattice. The magnitude of U could be tuned by varying the transverse confinement. In particular, choosing a value of U smaller than $\Omega_0\alpha$ but much larger than the bandwidth of the quasi-flat band should allow achieving the strongly interacting regime in the latter. Projection of interactions onto the quasi-flat and hybridizing bands leads to extended Hubbard models with large on-site interactions as well as other terms, such as correlated tunneling. Probing such interacting systems at partial filling could potentially shed new light into theoretical debates on unconventional superconductivity [69, 70, 72, 105], and topological order [106, 73, 107] in TwBLG. Finally, extending our approach to other lattice structures represents an exciting perspective for future studies.

Chapter 3

Topological properties of synthetic bi-layers

3.1 Quantum Hall effects

In 1879, Edwin Hall has observed and explained electric potential difference in the conductor (let's assume x direction), that is perpendicular to the electric current (y direction) and at the same time perpendicular to the external magnetic field (z direction). The (Hall) effect stated, that the transverse (x-y) component of resistivity ρ_{xy}, is given by $\rho_{xy} = \frac{1}{ne}B$, where n is the carrier density and -e denotes the electron charge. Only few months later he observed a strong (one order of magnitude) amplification of this effect in the ferromagnetic iron - later named as Anomalous Hall Effect (AHE). This amplification was independent of the applied magnetic field and is usually proportional to the magnetization M of the sample.

While the mechanism behind the original Hall effect has readily been well understood - a Lorentz force, AHE remained a puzzle for decades. One of the soon observed properties - spontaneous Hall conductivity in ferromagnets - was indicating the independence of the terms coming from the field B and from internal magnetization M. Spontaneous Hall conductivity is an effect resulting from generation of the additional current due to intrinsic electron deflection from the direction of the original driving current. This effect was not observed in the non-magnetic materials. Although up to this day there is no full consensus over the origin of the deflection mechanism in the magnetic materials - there is an agreement that the primary mechanism is the spin-orbit interaction.

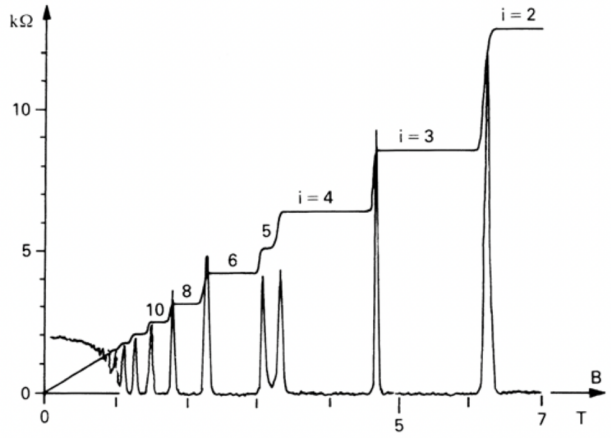

Figure 3.1: Quantum Hall Effect: Resistivity R_{xy} as a function of applied magnetic field B. The center of each plateu occures at $B = \frac{n}{\mu}\Phi_0$, where $\Phi_0 = \frac{2\pi\hbar}{e}$ is a flux quantum and n is electron density. Original plot taken from David Tong's Lectures on the Quantum Hall Effect.

The development of the Metal-Oxide-Semiconductor Field-Effect Transistor (MOSFET) opened up a new era of research into two-dimensional electron gases (2DEG), which exhibit unique electronic properties due to their confinement in a two-dimensional plane. In these systems, electrons are confined to move in two dimensions while their motion is quantized in the third dimension, leading to the formation of quantized energy levels.

When a strong magnetic field is applied to a cooled 2DEG, an intriguing phenomenon known as the Quantum Hall Effect (QHE) can be observed. Discovered by Klaus von Klitzing in 1980, the QHE is a remarkable manifestation of quantum mechanics that distinguishes it from its classical counterpart, the Hall effect. In the QHE, the Hall resistance, denoted as $R_{xy} = \frac{V_H}{I}$, becomes quantized, depending on the strength of the applied magnetic field, as shown in Fig. 3.1. The quantization is expressed as $R_{xy} = \frac{h}{e^2\nu}$, where h is the Planck constant, e is the electron charge, and ν is an integer number known as the filling factor. The filling factor represents the number of occupied cyclotron orbits or Landau levels in the 2DEG system.
Two years after von Klitzing's discovery, Tsui and Stoermer found that electronic

liquids with quantized Hall resistance can also occur at certain non-integer filling factors ν. While the existence of a gapped electron liquid at integer ν and the IQHE is understood from single-particle physics, the phenomenon at fractional filling, known as FQHE, is a consequence of a much more complex many-body effect. In general, the filling factor ν does not have to be an integer value. However, when there is an exact number of fully filled Landau levels, ν takes integer values, leading to the observation of the Integer Quantum Hall Effect (IQHE). In contrast, when the Landau levels are not completely filled, a related but distinct phenomenon known as the Fractional Quantum Hall Effect (FQHE) can be observed, where the Hall resistance becomes quantized at fractional values of the filling factor. The FQHE has led to the discovery of new forms of quantum matter and exotic quasiparticles with fractional charges, further expanding our understanding of the rich and complex behavior of 2DEG systems.

3.2 Topological properties of matter

Quantum Hall systems are insulating in longitudinal direction, and this insulating behavior arises as a consequence stemming from the topology of the magnetic field. Some materials, known as TIs, exhibit similar behavior even in the absence of a magnetic field. This unique class of materials has garnered significant interest in condensed matter physics due to their exotic electronic properties. These materials exhibit insulating behavior in their bulk while conducting electrical current on their surfaces or edges. The key to understanding the physics of topological insulators lies in the concept of topology, which is a branch of mathematics that deals with the properties of objects that remain unchanged under continuous deformations.

In the context of TIs, the term ”topological” refers to the global properties of the electronic wave functions in the material's band structure. The band structure is a representation of the energy levels of electrons in a solid as a function of their quasi-momentum. In topological insulators, the bulk band structure is characterized by a non-trivial topological invariant, which is a mathematical quantity that captures the essential topological features of the electronic wave functions. This non-trivial topological invariant leads to the emergence of conducting states on the surfaces or edges of the material.

Often, the surface states of topological insulators are protected by time-reversal symmetry, which means that the surface states cannot be removed or destroyed

by any local perturbation or impurity that preserves this symmetry. As a result, the surface states exhibit robustness against disorder and defects, allowing for the conduction of electrical current with minimal scattering or dissipation. This property has significant implications for potential applications in low-power electronics and quantum computing.

One of the remarkable features of the surface states in topological insulators is that they exhibit a unique linear dispersion relation, often resembling massless Dirac fermions. The electrons in these surface states have their spin locked to their momentum, meaning that the direction of the electron's spin is always perpendicular to its momentum. This spin-momentum locking leads to a helical arrangement of the surface states, which can give rise to a variety of interesting phenomena, such as the spin Hall effect and the potential realization of Majorana fermions.

Topological insulators can be classified into precisely ten main classes for each spatial dimension d [108]. In 2D TIs, also known as quantum spin Hall insulators, the topologically protected conducting states are found along the edges of the material, whereas in 3D TIs, the conducting states are present on the material's surfaces. Some well-known examples of topological insulators include HgTe/CdTe quantum wells (2D TIs) and Bi2Se3, Bi2Te3, and Sb2Te3 (3D TIs).

Topological order has now become a central research topic in physics, exemplified by the 2016 Nobel Prize for D. J. Thouless, F.D.M. Haldane, and J.M. Kosterlitz [109, 110]. The intimate relation between topology and condensed matter goes back to the discovery of the Integer Quantum Hall Effect (IQHE) [111]: a 2D electron gas at low temperature and under a strong magnetic field presents a quantized transverse conductivity very robust against local perturbations. It was soon realized [112] that this robustness was coming from a new paradigm: a global topological order which cannot be described by the usual Ginzburg Landau theory of phase transitions. In the particular case of the IQHE, the presence of a strong magnetic field results in the appearance of flat bands (Landau levels), each of them being characterized by a distinct topological invariant, called Chern number, and the transverse conductivity is equal to the sum of the Chern numbers of the occupied Landau levels. Soon after, F.D.M. Haldane proposed the quantum anomalous Hall effect, which presents a quantized transverse conductivity but no Landau levels [113]. Such a toy model turned out to be the crucial ingredient for the original proposal of topological insulators in graphene [114, 115] and stimulated very rapid progress of the area of topological/Chern insulators, topological superconductors, topological flat bands,

and even systems with higher-order topology [116, 117, 118, 119, 120, 121, 122, 123]. Many of recent twistronics activities discuss topological insulators in magic-angle twisted bi-layer graphene and the possibility of creating and controlling topological bands in these systems [106, 73, 107]. Recently, quantum anomalous Hall effect has been reported in Moiré heterostructures [124, 125]. One of the most challenging and still persisting questions are related to the role of interactions, in particular strong interaction and correlations [126]. Interestingly, the interactions do not always destroy the topological phases. Strong interactions in flat band topological materials can lead to the fractional quantum Hall effect [127, 128, 129] or to fractional Chern insulators [130, 131, 132, 133]. Furthermore, strong interactions can induce topology through a spontaneous symmetry breaking mechanism as it is the case in the celebrated topological Mott insulator [134, 135, 136, 137, 138, 139, 140].

Novel insights into the physics of topological order can be provided by quantum simulators. These highly flexible experimental systems are used to mimic complex quantum systems in a clean and controllable environment. Such platforms allow one to simulate diverse geometries leading to, among others, graphene-like physics in synthetic hexagonal and brickwall lattices [85, 86, 87] or flat band physics in the Lieb lattice [88, 89]. There are indeed other platform for realizing hexagonal lattices [**?**], but atoms combine additional advantages, as explained herafter. Cold atoms provide a unique playground for synthetic gauge fields [141, 142, 143], combined with time dependent lattice modulations/Floquet engineering [144, 145]. In particular, such techniques led to the experimental realization of the Hofstadter model [146, 147], the Haldane model [148, 149, 150]. Furthermore, artificial gauge fields can also be engineered with the help of synthetic dimensions which allows to engineer topological insulators on ladders with both non-trivial Chern numbers and topological edge states [95, 96, 151, 152, 153, 154, 97]. Finally, optical lattices offer possibilities to study bi-layer systems and proximity effects [94].

The rapid development of twistronics in condensed matter physics of 2D material stimulated extensive quest for quantum simulators of twistronics with ultra-cold atoms [93], and of Moiré patterns in photonic systems [155]. Our contribution to this field has been explained in the previous chapter, as well as in the original work [98]. In this chapter we again consider a single 2D optical lattice with a desired geometry (brick, or Π-flux square), and create a multi-layer system employing internal state of the atoms inserted in the lattice. These could be in the simplest case fermions with spin 1/2 or 3/2, but previously described experimental

proposal is the most realistic implementation scenario. The Moiré patterns were generated by spatial modulations of the Raman transitions coupling the internal states. Since the strength of the Raman coupling can be efficiently controlled in this system, the appearance of flat bands is expected to occur for much larger "magic" angles, or better to say for elementary cells of much more modest sizes, like unit cell consisting of only 2×4 lattice sites. In the previous chapter, we analyzed the properties of the band structure in such systems, and showed that these expectations were indeed correct.

In the present chapter we develop further the idea shown in chapter 2 and demonstrate, that such system is very flexible and can be tweaked to exhibit topological band structure in various situations. In particular, to achieve non-trivial topology we engineer artificial complex next-to-nearest neighbor tunneling analogous to the ones appearing in the Haldane model [113]. Typically, the energy bands of our interest in this system form three groups and the Chern number changes from trivial (0,0,0), to a topological phase with a trivial flat band (-1,0,1) and a topological phase with a non-tivial flat band (-1,1,0). We identify the regimes of parameters where these three situations occur, and study properties of the system with periodic and open boundary conditions. The chapter is organized as follows. In Section 3.3 we present the details of the model [98], together with modifications required for achievement of topological bands. In Section 3.4 we discuss magic configurations and quasi-flat bands. Section 3.5 is devoted to the investigations of the effects of onset of staggered hoping and appearance of topological insulators. Similar effects and topological properties are discussed for dimerized lattices in Section 3.6. Section 3.7 contains a short discussion of feasibility of experimental realization of the discussed physical effects. The conclusions and outlook are presented in Section 3.8.

3.3 Modification of the Hamiltonian

To remind the reader, we consider a system of synthetic spinfull fermions in a bi-layer material. The fermions are subjected to a synthetic magnetic field which leads to a supercell structure. Additionally to the known terms in the original Hamiltonian (2.2), here we also include next-to-nearest neighbour (NNN) hopping with staggered phase as well as on-site energy term. The importance of each

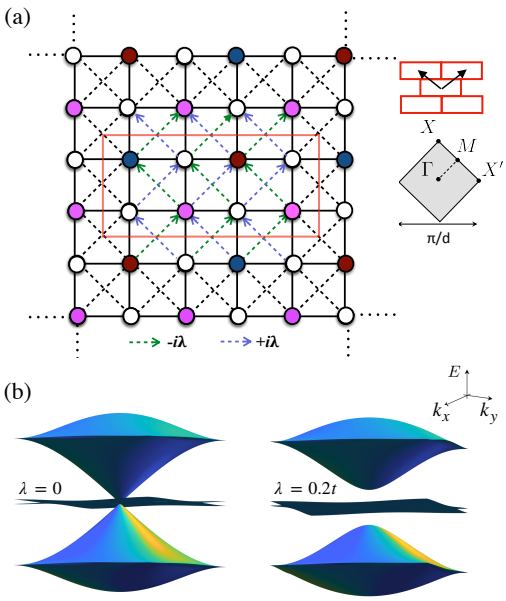

Figure 3.2: The supercell structure and effects of complex hopping. (a) The left panel illustrates a sketch of a single plane of the bi-layer structure corresponding to one of the spin states $m = \pm 1/2$. We consider square lattice potential. The maroon and dark-blue sites are Raman coupled with the second plane under the chosen spatial modulation of the synthetic tunneling. The pink sites (in both the layers) experience a onsite energies, μ. The real-space nearest-neighbor tunneling t is shown by the solid lines. The next-nearest-neighbor complex tunneling depending on directions of hopping and the position of the lattice sites is shown by staggered dotted lines. The red line shows a top view of the elementary unit cell of the system containing $2\times4\times2$(synthetic) sites for Raman periodicities $l_x = l_y = 4$, where the factor of 2 accounts for the two layers. The right top panel depicts the arrangement of elementary unit cells and the two translation vectors as arrows. This leads to the first Brillouin zone shown in the right bottom panel, indicating also the position of the high-symmetry points. (b) The three dimensional view of the six band manifold in the vicinity of $E = -\Omega_0(1-\alpha)$ for $\Omega_0\alpha/h = 40t$ with $\alpha = 0.2$, $\gamma = \pi/2$ and $\mu = 0$. The left panel shows the case, when next-nearest-neighbor complex hopping is absent, i.e., $\lambda = 0$. It has two quasi-flat bands at the Dirac points of two dispersive bands in form of Dirac cones. The right panel shows the same set of bands, but in presence of the complex tunneling, $\lambda = 0.2t$. This causes opening of a hard gap between the quasi-flat bands and the nearby dispersive bands.

term and their potential experimental realization will be explained throughout the chapter. The complete Hamiltonian reads:

$$H = H_t + H_\lambda + H_\Omega + H_\mu, \tag{3.1}$$

where

$$\begin{aligned} H_t = &- \sum_{\mathbf{r},m,\sigma} t(\mathbf{r}) \left[a^\dagger_{m,\sigma}(\mathbf{r}+\mathbf{1}_x) + a^\dagger_{m,\sigma}(\mathbf{r}+\mathbf{1}_y) \right] a_{m,\sigma}(\mathbf{r}) \\ &+ \text{h.c.} \end{aligned} \tag{3.2}$$

is the nearest neighbor hopping Hamiltonian with a real and space dependent tunneling amplitude $t(\mathbf{r})$,

$$\begin{aligned} H_\lambda = \sum_{\mathbf{r},m,\sigma} \lambda \Big[&\exp(i\phi_R(\mathbf{r})) a^\dagger_{m,\sigma}(\mathbf{r}+\mathbf{1}_x+\mathbf{1}_y) + \\ &\exp\left(i\phi_L(\mathbf{r})\right) a^\dagger_{m,\sigma}(\mathbf{r}-\mathbf{1}_x+\mathbf{1}_y) \Big] a_{m,\sigma}(\mathbf{r}) + \text{h.c.} \end{aligned} \tag{3.3}$$

is the the next-to-nearest hopping Hamiltonian with a tunneling amplitude λ and a staggered phase $\mathbf{\Phi}(\mathbf{r}) = [\phi_\mathbf{L}(\mathbf{r}), \phi_\mathbf{R}(\mathbf{r})]$,

$$H_\Omega = \sum_{\mathbf{r},m,\sigma} \Omega(\mathbf{r}) \exp(-i\boldsymbol{\gamma}\cdot\mathbf{r})\, a^\dagger_{m+1,\sigma}(\mathbf{r}) a_{m,\sigma}(\mathbf{r}) + \text{h.c.} \tag{3.4}$$

denotes the synthetic hopping Hamiltonian with a space dependent Raman coupling Ω and a phase $\boldsymbol{\gamma} = \gamma(\mathbf{1}_x + \mathbf{1}_y)$, and

$$H_\mu = \sum_{\mathbf{r},m,\sigma} \mu(\mathbf{r})\, a^\dagger_{m,\sigma}(\mathbf{r}) a_{m,\sigma}(\mathbf{r}), \tag{3.5}$$

is the onsite onsite energy Hamiltonian with an amplitude $\mu(\mathbf{r})$. Figure 3.2 provides a schematic depiction of the system under study. Moreover, we present the matrix form of the Fourier transformed Hamiltonian (3.2) in the Appendix.

The spatial modulation of the Raman coupling is chosen to be $\Omega(x,y) = \Omega_0 \left[1 - \alpha(1 + \cos(2\pi x/l_x)\cos(2\pi y/l_y))\right]$, where l_x (l_y) is its periodicity along the x (y) axis. In the following, we consider two distinct cases:

(i) Staggered complex hopping (SCH). we set $t(\mathbf{r}) = t$ and fix the phases associated with the next-nearest neighbor tunneling amplitude by setting $\phi_L(\mathbf{r}) - \phi_R(\mathbf{r}) = \pi$, where $\phi_R(\mathbf{r}) = (2\,\mathbf{r}\cdot\mathbf{1}_y + 1)\pi/2$ and $\phi_L(\mathbf{r}) = (2\,\mathbf{r}\cdot\mathbf{1}_y + 3)\pi/2$.

(ii) Dimerized lattice (DL). We consider dimerized real tunneling amplitude, such that $t(\mathbf{r})$ takes the form of t_1 and t_2 in alternative sites in the x and y directions, along with the next-nearest neighbor complex hopping, where we set $\phi_R(\mathbf{r}) = \phi_L(\mathbf{r}) = \pi/2$.

3.4 Magic configurations and quasi-flat bands

In the following, we study the Hamiltonian (3.1) under various boundary conditions: (i) periodic boundary conditions in both spatial (x and y) direction, (ii) periodic boundary condition in one of the spatial direction (here along x), and (iii) open boundary conditions in all spatial directions. We first consider the case (i), for which the quasimomentum $\mathbf{k} = (k_x, k_y)$ is a good quantum number. In this case, we can apply the Bloch theorem, along with a gauge transformation, such that $a_{m,\sigma}(\mathbf{r}) = \sum_{\mathbf{k}} \exp\left(i(\mathbf{k}\cdot\mathbf{r} + m\boldsymbol{\gamma}\cdot\mathbf{r})\right) a_{m,\sigma}(\mathbf{k})$. The Hamiltonian can then be rewritten as $H = \sum_{\mathbf{k}} H_{\mathbf{k}}$ and can be diagonalized. The spatial periodicity of the synthetic tunneling fixes the supercell dimension, and hence the dimension of $H_{\mathbf{k}}$. The notation $\Theta(l_x, l_y)$ is introduced to represent corresponding supercell configuration.

The band structure corresponding to the case with $\lambda = 0$ and $\mu = 0$ has been studied in detail in the previous chapter. Remarkably, $\Theta(4\nu, 4\nu)$ configurations, i.e., when $l_x = l_y = 4\nu d$, with ν integer, were identified as magic configurations. $\Theta(4\nu, 4\nu)$ configurations host quasi-flat bands surrounded by dispersive Dirac cone spectra with controllable Dirac velocities, and hence share certain characteristics associated with magic angle twisted bi-layer graphene. In this work we focus on the the smallest possible configuration $\Theta(4, 4)$ consisting of only 16 lattice sites. The corresponding Brillouin zone of the bi-layer system showing the high-symmetry points is depicted in Fig. 3.2(a). In the following we briefly review few consequences for the case with $\lambda = 0$ and $\mu = 0$.

In the strong Raman coupling limit $(\Omega_0\alpha) \gg t$, isolated sets of narrow spin degenerate bands appears at the energies $\pm\Omega_0$, $\pm\Omega_0(1-\alpha)$ and $\pm\Omega_0(1-2\alpha)$. The energy spectrum of the system is symmetric around zero energy, i.e. $E(\vec{q}) = -E(\vec{q})$, and therefore we restrict our discussion to the negative energy bands. A non-isolated set of six bands around the energy $E/t = -\Omega_0(1-\alpha)$ are of particular interest in this chapter. Figure 1(b) shows the energy sptectrum for a representative case with $\Omega_0\alpha/h = 40t$, $\alpha = 0.2$, $\lambda = 0$, $\mu = 0$ and the flux $\gamma = \pi/2$ (also see Fig. 3.3(a), which depicts the energy spectrum along the paths passing through the high-symmetry points). Within this six band manifold, the top and bottom three bands are symmetric around the energy $-\Omega_0(1-2\alpha)$. Noticeably, two middle bands, which are quasi-flat, are formed closest to $-\Omega_0(1-\alpha)$ and they are sandwiched between dispersive bands in form of Dirac cones. These well isolated six band manifold with a total dispersion of $\Delta_6 = 4\sqrt{2}t\cos(\gamma/2) + O(t^2/(\Omega_0\alpha))$ are

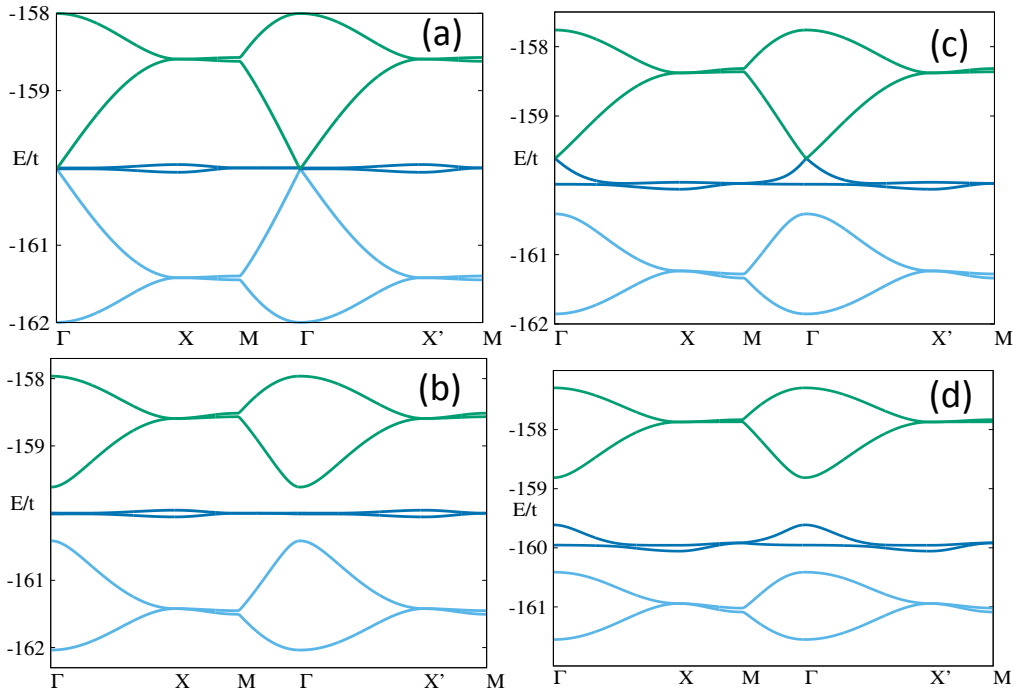

Figure 3.3: Magic configuration band structures in presence of staggered complex hopping. Band structures corresponding to $\Theta(4,4)$ supercell along the paths passing through the high-symmetry points $\mathbf{\Gamma}, \mathbf{X}, \mathbf{M}, \mathbf{\Gamma}, \mathbf{X}', \mathbf{M}$ for $\Omega_0\alpha/h = 40t$, $\alpha = 0.2$, and $\gamma = \pi/2$. Panel (a) shows the the set of six-bands around energy $-\Omega_0(1-\alpha)$ with $\lambda = 0.0$, while other bands, which are well separated (by atleast the energy of $\Omega_0\alpha$) are not shown. There is no hard gap between the two middle quasi-flat bands and adjacent dispersive Dirac cones. Panels (b-c) reveal evolution of the spectrum with respect to the onsite energy, μ. Panels (a), (b) and (c) corresponds to $\mu = 0$, $0.4t$ and $1.2t$, respectively. Finite λ induces a hard gap between the quasi-flat bands and dispersive bands. The onsite energy leads the system through a non-trivial gapped-gapless transition, given the Fermi energy is adjusted accordingly.

separated from remaining nearby bands by an energy gap of $\Omega_0\alpha$. The flatness of the quasi-flat bands (two middle bands) can be tuned precisely by adjusting the Raman coupling strength. Their approximate width can be derived within the second order perturbation theory as

$$\Delta_F = \frac{t^2\cos^2(\gamma/2)}{\Omega_0\alpha}\left(\frac{24\alpha^3 - 88\alpha^2 + 106\alpha - 32}{3\alpha^3 - 11\alpha^2 + 12\alpha - 4}\right). \tag{3.6}$$

The relative flatness of the bands is defined as $F = \Delta_F/\Delta_6$. As a result, the relatively flatter middle bands can be obtained by increasing $\Omega_0\alpha$. The parameters here are chosen from experimentally accessible regime. It is worth mentioning that the Dirac velocity is proportional to $\cos(\gamma/2)$, and hence the span of the dispersive Dirac bands can be controlled separately by tuning γ.

Within these six bands, the system has no gaps. The upper dispersive Dirac cone touches the middle quasi-flat bands at the high symmetry point Γ, i.e., $k_x = k_y = 0$. A non-zero flux, however, opens a tiny *local* gap between the lower dispersive bands and the middle quasi-flat bands at Γ. Finite flux breaks four-fold rotational symmetry (C_4) as well as time reversal symmetry(TRS) of the system. In the following we discuss strategies for opening a gap around the Dirac band touching and the resulting topological phases of matter.

3.5 Staggered complex hopping

3.5.1 Bulk properties of the system

We investigate the staggered complex hopping case [see Eq. (3.2) and Fig. 3.2(a)]. We first set $\mu = 0$ and consider periodic boundary conditions in both x and y directions. A non-zero value of λ induces a mass term at the Dirac point in the six-band subset discussed earlier. As a result, three isolated sets of bands are formed - each of them consists of two hybridized bands. The resulting band structure along the high-symmetry points is shown in Fig. 3.3(b) for $\Omega_0/h = 200t$, $\alpha = 0.2$, $\gamma = \pi/2$, and $\lambda = 0.2t$. While the quasi-flat bands remain closest to the energy $\Omega_0(1-\alpha)$, the top (bottom) dispersive bands shifts upwards (downwards). The band gaps can be controlled by tuning the value of λ. As we will see, such hopping amplitude λ drives the system into a quantum anomalous Hall phase [113].

We further investigate the influence of a non-zero staggered onsite energy μ on the system. A Finite value of μ breaks the inversion symmetry of the system and the energy spectrum is no longer exactly symmetric around the zero energy.

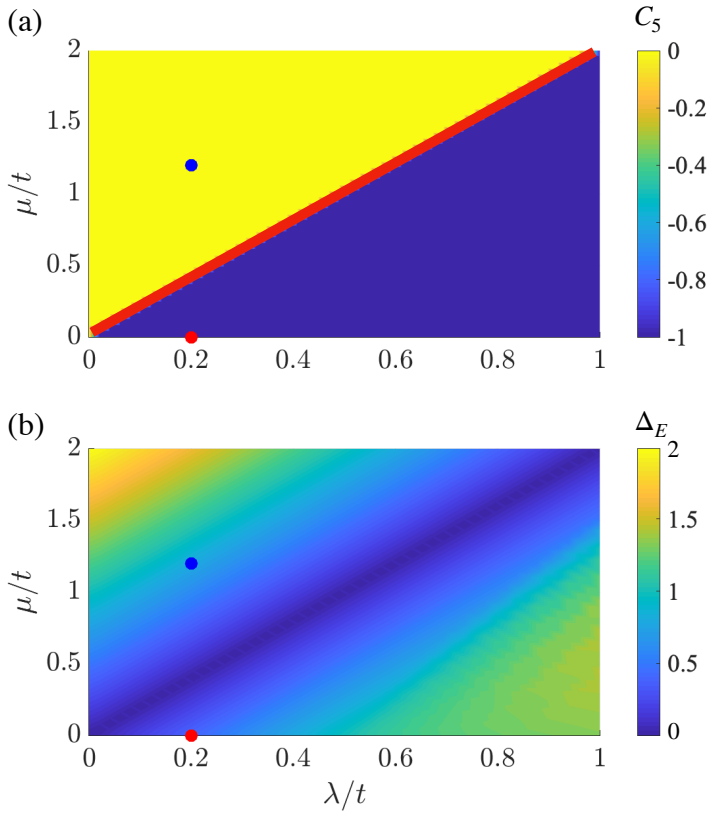

Figure 3.4: (a) Chern number of the five lowest bands as a function of system' parameters λ/t and μ/t. As seen on (b) the system is gapless for $\mu = 2\lambda$, which makes C_5 undefined in this region. The gapless region visible on (b) is marked by the red line on (a). Topological transition presented on the Fig.3.3 can be seen by looking at the vertical cross-section at $\lambda/t = 0.2$. Blue region of chern number -1 indicates the configurations at which system has standard non-trivial topology since $C_3 = -1$ and the order is $(-1, 0, 1)$, while yellow area depicts parameters' values for which non-standard topological order $(-1, 1, 0)$ can be obtained. Red and blue points mark the values of the parameters for which edge states have been plotted on Fig.3.6 (a) and (b),respectively. (b) Second band gap (energy gap between the hybridized quasi-flat middle bands and the dispersive upper band) as a function of λ/t and μ/t. Vanishing energy gaps mark a topological phase transition in the system. Meaning of red and blue points remains the same as on the panel (a).

Nevertheless, the overall qualitative features of the negative and positive energy bands remain closely similar for a value of μ smaller than the central bandgap. Moreover, this staggered onsite energy results in a significant asymmetry between the two top and two bottom bands within the six band manifold under study. As we discuss below, this staggering potential has a prominent impact on topological phases of the system. Figures 3.3 (b-d) shows the evolution of the band structure for increasing values of μ: the band gap between the top dispersive bands and the middle quasi-flat bands shrinks, and the gap closes at $\mu_c \simeq 2\lambda$. For $\mu > \mu_c$, the gap then reopens. Figure 3.4 shows the energy gap between the set of quasi-flat bands and the upper set of bands. We also observe a gap closing and reopening of the lower gap for increasing staggering potential with opposite sign. The latter is reminiscent of the interplay between the staggering potential and the imaginary next-to-nearest neighbor hopping in the Lieb lattice [156]. In fact, the system undergoes a topological phase transition. We characterize the topology of the system with the help of the Chern number C, a topological invariant for the class of Chern insulators. The Chern number of the n-th band is defined as

$$\begin{aligned} C_n &= i \int_{BZ} F_n^{xy}(\mathbf{k}) dS \\ &= i \sum_{l=1}^{N_x N_y} \int_{P_l} F_{n,l}^{xy}(\mathbf{k}) dS \end{aligned} \tag{3.7}$$

the integral of the Berry curvature $F_{n,l}^{xy}(\mathbf{k}) = \nabla_{\mathbf{k}} \times A^n(\mathbf{k})$ written in terms of the Berry connection $A^n(\mathbf{k}) = \langle u^n(\mathbf{k}) | \partial_{\mathbf{k}} | u^n(\mathbf{k}) \rangle$. In the second equality, we have rewritten this integral as a sum of integrals over the plaquettes of the discretization grid of the Brillouin Zone. For a such a discretized grid, the Berry curvature can be be computed numerically with the help of the Fukui-Hatsugai-Suzuki (FHS) algorithm [119]

$$C_n \approx \frac{1}{2\pi i} \sum_{P_l} \left(\langle u_k^n \rangle u_m^n \langle u_m^n \rangle u_o^n \langle u_o^n \rangle u_p^n \langle u_p^n \rangle u_k^n \right), \tag{3.8}$$

where P_l denotes a plaquette in the Brillouin Zone with four vertices (k, m, o, p) labeled in the anti-clockwise order with k being top left vertex and $|u_k^n\rangle$ is a Bloch function corresponding to the n-th eigenvalue at point k. The summation is performed over all plaquettes in the Brillouin Zone. We emphasize that for degenerate bands one has to use the algorithm proposed in Ref. [157] to compute the non-abelian Berry curvature. In this chapter, we use the total Chern number

defined as the sum of the Chern numbers of the i first occupied bands:

$$C_i = \sum_{j=1}^{i} C_j \tag{3.9}$$

As can be seen in Fig. 3.4(a), for $\mu < \mu_c$, The hybridized middle set of bands are topologically trivial with zero Chern number, while the bottom (top) set of dispersive band is topologically non-trivial with C =-1(1). The gap closing leads to a topological phase transition with a transfer of Chern number from the upper set of bands to the middle set of bands [158], and for $\mu > \mu_c$, the middle set of bands becomes non-trivial with $C = 1$ and the upper set of bands becomes trivial with $C = 0$. The bottom dispersive bands remain non-trivial with $C = -1$. In the following subsections, we discuss in detail the topological edge states appearing in a system with boundaries.

3.5.2 Cylindrical geometry and edge states

In order to study the topological edge states of the system, we consider a cylindrical or strip geometry. Calculations are conveniently performed using an enlarged unit cell consisting of plaquettes of size 4×4 site per layer. More specifically, we consider a bi-layer strip of finite length along the x direction and infinite length in the y direction through periodic boundary conditions. As a result k_y remains a good quantum number. The enlarged unit cell is repeated n_x times in the x direction.

Figure 3.5(a) depicts the energy spectrum for $\mu = 0$ [red dot in Fig. 3.4(b)]: The system presents three energy bands that were already present in the previous section, which we call bulk energy bands. Interestingly, the bulk energy gaps host topological edge states in accordance to the celebrated bulk-edge correspondence [157]. These topological edge modes are responsible for edge currents and their number at each edge is equal to the sum of Chern numbers of the occupied bands. Hence, setting the Fermi energy E_F at one of the two energy gaps, one finds one edge state at each edge, which is, as expected.

In the following, we fix the set of parameters as in the previous section, i.e. $\Omega_0/h = 200t$, $\alpha = 0.2$, $\gamma = \pi/2$, and $\lambda = 0.2t$, and we concentrate on the same

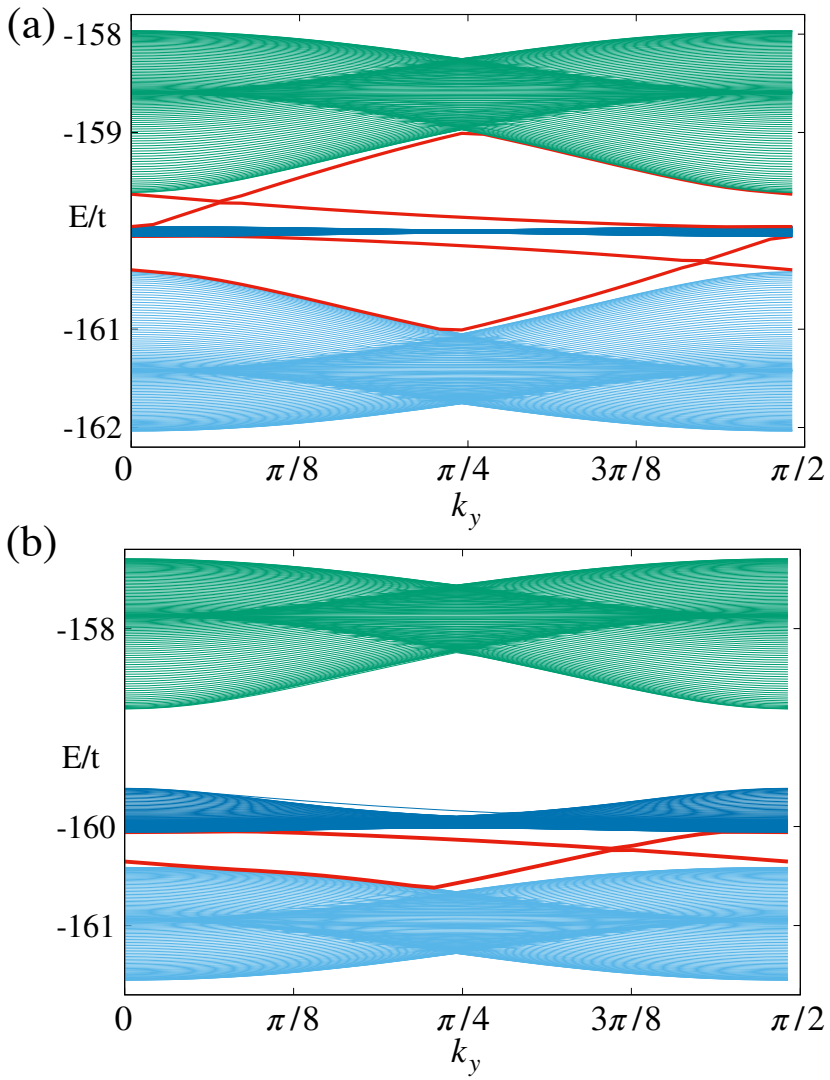

Figure 3.5: Edge and bulk dispersions for cylindrical geometry. Energy spectrum is shown to demonstrate two distinct cases with (a) $\mu = 0$ and (b) $\mu = 1.2$ for the parameters $\Omega_0\alpha/h = 40t$, $\alpha = 0.2$, $\gamma = \pi/2$, $\lambda = 0.2t$. The mid-gap states due to open boundaries along the x-axis are shown by red lines. These mid-gap states are edge states connecting the energetically separated bulk bands.

energy window close to the energy $-\Omega_0(1-\alpha)$. Figure 3.5 shows the energy spectrum as a function of the quasi momentum k_y for $n_x = 30$. Figure 3.5 (b) shows the energy spectrum for $\mu = 1.2t > \mu_c$ [blue dot in Fig. 3.4(b)]. In this case the first (bottom) energy gap supports topological edge states, while the second energy gap does not. This is again consistent with the fact that for this case the bottom band has $C = -1$, and hence there is one edge state at each edge in the first gap, while the sum of Chern numbers of bottom and middle bands is zero. Hence depending on the choice of E^F, we can have a Chern insulator insulator or a trivial insulator. In order to achieve a closer understanding of the edge states and the bulk-boundary correspondence, we further analyze a finite square lattice in the following discussion.

3.5.3 Finite square lattice and edge states

We finally consider a bi-layer finite square lattice with $2 \times L \times L$ sites. We do not impose periodic boundary condition, i.e., both the layers are open in both x and y directions. Unlike previous cases, the system can not be associated with a good quantum number due to the absence of any periodicity. We solve the Hamiltonian in Eq. (3.2) by diagonalizing the matrix with $2L^2 \times 2L^2$ entries. We again focus on the energy bands close to $-\Omega_0(1-\alpha)$ (see Figs. 3.3 and 3.5). Figure 3.6 shows the sorted eigenvalues of the Hamiltonian for a system of length $L = 40$ and for the same set of parameters of the previous subsections. We again show two different topological phases for $\mu = 0$ [Fig. 3.6(a)] and $\mu = 1.2t$ [Fig. 3.6(b)].

The appearance of the new states due to the absence of periodicity are shown by red crosses. These states are detached from the bulk states and clearly are a manifestation of the open boundaries of the layers. These are edge states and, as we demonstrate below, live on the boundaries of the layers. For $\mu < \mu_c$, the edge states appear in both energy gaps. This is consistent with the discussions for the cylindrical geometry and the computation of the bulk Chern numbers. This is illustrated in Fig. 3.6(a) as an exemplary case with $\mu = 0$. For $\mu > \mu_c$, as expected, the first energy gap hosts new states, while the second energy gap does not. Figure 3.6(b) demonstrates this via an example with $\mu = 1.2t$. The corresponding density of states (DOS) are shown in Fig. 3.8. For $\mu < \mu_c$, two regions with low density of states appear adjacent to $-\Omega_0(1-\alpha)$ under open open boundary condition. These correspond to the energies of the mid-gap states in the energy gaps of the bulk spectrum. For $\mu > \mu_c$, one of these two regions has vanishing DOS due to absence of the mid-gap states between the middle band and

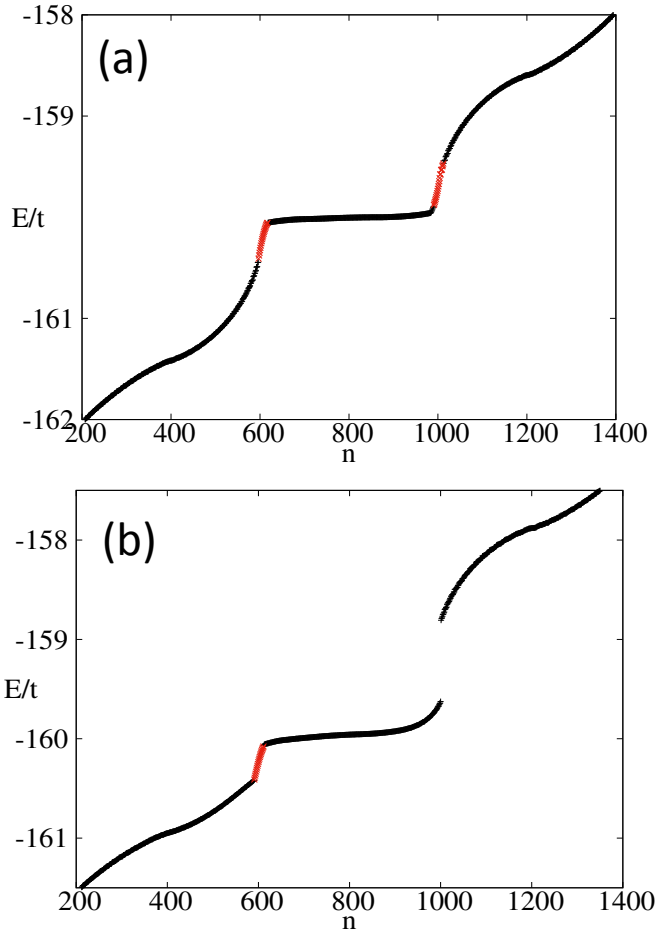

Figure 3.6: Energy spectrum of the synthetic bi-layer square lattice with 2×40×40 sites and open boundary condition for (a) $\mu = 0$ and (b) $\mu = 1.2t$ for the parameters $\Omega_0 = 200$, $\alpha = 0.2$, $\gamma = \pi/2$ and $\lambda = 0.2t$. The bulk states are shown by black plus symbols. The new mid-gap states appearing due to open boundary condition is shown by red crosses. These are the edge states. For (a)$\mu = 0$, the edge states appear in both the energy gaps. However, for $\mu > \mu_c$ (shown here (b)$\mu = 1.2t$, the edge states appear only within the first energy gap.

the upper dispersive band.

In order to characterize the edge states in real space, we define probability density of the edge state corresponding to $m = \pm 1$, $p_{\pm}(\mathbf{r}) = \left|\langle\psi_{\pm}^{E_F}(\mathbf{r})\rangle\psi_{\pm}^{E_F}(\mathbf{r})\right|^2$,

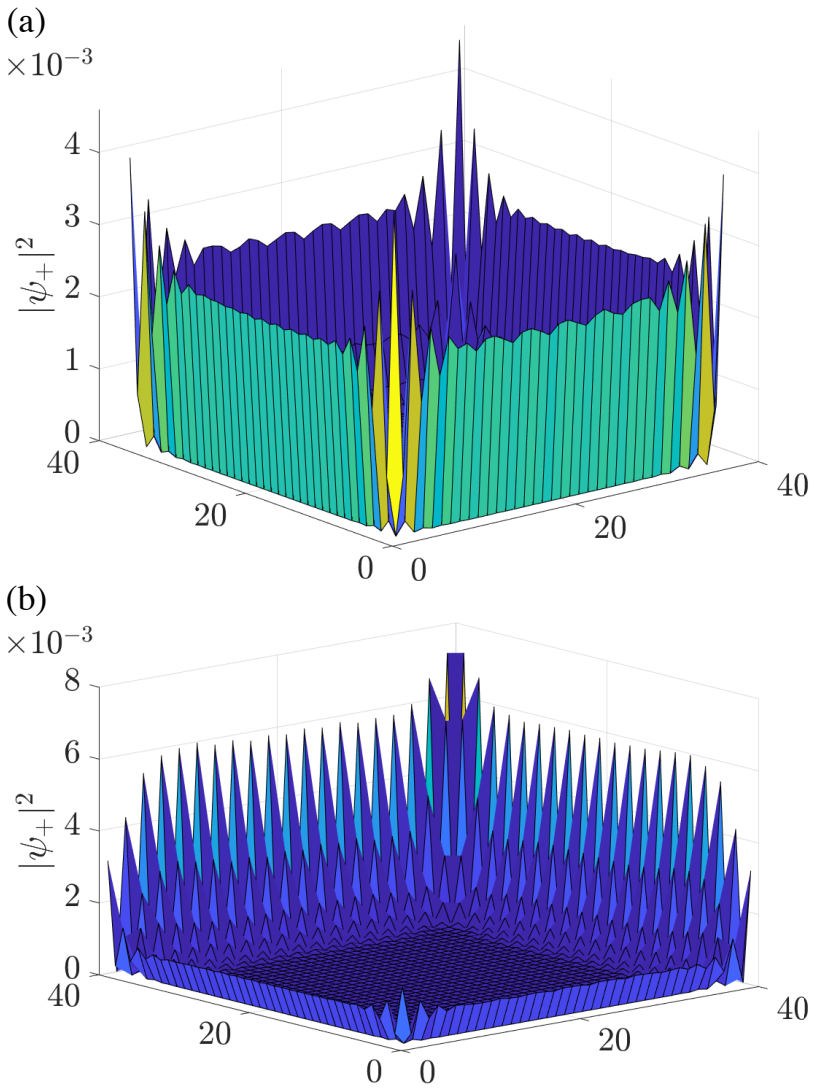

Figure 3.7: Probability density plots for an edge mode corresponding to energy $E \approx -160.28t$ for (a) and $E \approx -160.13t$ for (b). (a) The wave function is fully localized on the edges of the lattice, which in this case has a length of 39 sites. (b) The wave function is localized on two edges of the lattice which contain raman coupled sites. In this case has a length of 40 sites, commensurate with the periodicity of the unit cell.

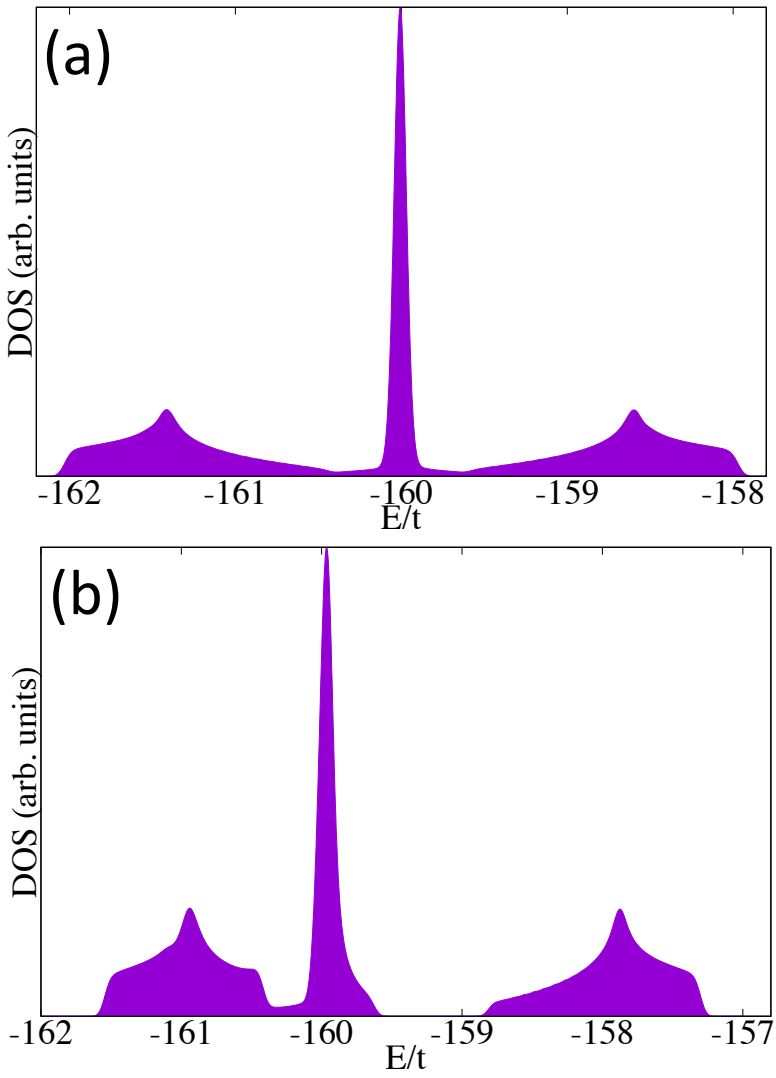

Figure 3.8: DOS (in arbitrary units) of the synthetic bi-layer square lattice with $2 \times 40 \times 40$ sites and open boundary condition for (a) $\mu = 0$ and (b) $\mu = 1.2t$ for the parameters $\Omega_0 = 200$, $\alpha = 0.2$, $\gamma = \pi/2$ and $\lambda = 0.2t$.

where $\psi_{\pm}^{E_F}(\mathbf{r})$ denotes the eigenvector whose energy is the closest to E^F the and $m = \pm 1$ denotes the projection on one of the synthetic dimensions. Interestingly, the edge states have a different real space profile depending on the commensurability of the number of sites with the supercell: lattices with the length commensurate

with the periodicity of the unit cell have two edges with Raman coupled sites and two edges that do not contain such sites [see Fig. 3.2(a)], while lattices with the length $\mod(\frac{L}{\Theta}) = \pm 1$ have all 4 edges of the same kind. Therefore to maintain the symmetry of the edges, where we expect the wave function to localize, system depicted on Fig. 3.7(a) was decreased by one site in each direction to $L_{x,y}$=39 resulting in symmetric probability distribution over all 4 edges of the lattice. On the other hand, for the lattice lengths being a integer multiple of unit cell's periodicity the edge states are also localized on the borders of the lattice, but the probability density is not equally distributed, favouring two edges, which are not Raman coupled. Such behaviour can be observed on Fig. 3.7(b), which shows the spatial density distribution, $p(\mathbf{r})$, of a typical edge states in the topologically insulating phases of the system with L=40. We have verified that $p_{-}(\mathbf{r})$ exhibits similar features. The chosen edge state is a mid-gap state in the first band gap for $\mu = 0$. The spatial distribution has an asymmetric nature, which comes from the finite size synthetic bi-layer geometry governed by the interlayer coupling pattern. The edge states are more localized at two adjacent edges of lattice corners, which host alternative sites with Raman coupled internal states, and are rather weakly localized in rest of the boundaries, where internal states in any of the sites are not subjected to such Raman coupling by construction.

3.6 Dimerized lattice

We now focus on the DL case, which is based on the alternating NN tunneling both in x and y direction and a complex NNN hopping. In particular we consider both dimerized NNN hopping, as in the SCH case as well as unstaggered NNN tunneling with $\phi_R = \phi_L$ that provides a zero net flux per palquette. First, we analyze the possibility of using dimerization as a substitute for space dependent onsite energy for obtaining the non-trivial gap between dispersive and quasi-flat sets of bands. Second, we simplify the NNN hopping leaving the dimerization untouched, since realizing constant diagonal hopping experimentally is less complicated.

The effect of the lattice dimerization has been primarily studied in Ref. [159]. The asymmetry of the hopping leads to the shift of the bands in the energy spectrum together with energy gap openings. It allows for the isolation of the set of quasi-flat bands, which originally are not separated by the global gap from the rest of the spectrum (see Fig. 3.10(a)). However, this gap opening is trivial and leads to the triplet of Chern numbers $(0, 0, 0)$.

Staggered NNN hopping The interplay of the NN dimerization and the staggered NNN hopping results in a topological phase diagram depicted Fig. 3.9. Such order was also obtained in the SCH case in absence of onsite energy. Hence, one can conclude that dimerization does not affect order-changing processes but allows one to observe the edge states of the well separated bands.

Uniform hopping We now turn our attention to a dimerized lattice with uniform next-nearest-neighbor (NNN) hopping within a single layer. As discussed in the previous paragraph, the opening of a global gap is ensured by the dimerization of nearest-neighbor (NN) hopping in this model. The role of complex NNN tunneling is somewhat more intricate to explain, since, unlike staggered NNN, it cannot be associated with a Hall phase or result in a global gap between quasi-flat and dispersive bands, as demonstrated in Fig.3.10(b).

However, similarly to the model described in Ref. [114], the net flux per plaquette in this case is zero. These observations suggest that introducing diagonal (NNN) hopping with a complex value does not necessarily confer topological non-triviality. Indeed, uniform NNN hopping does not open a global gap under any parameter configuration. Yet, in a manner akin to the effects induced by dimerization in the absence of NNN hopping, previously quasi-flat bands become dispersive with increasing λ, coinciding with a shift in the xy-plane.

All effects of the uniform complex NNN tunneling can be observed in Fig. 3.10(c). The impact of dimerized NN hopping is similar to band separation noted in staggered NNN hopping; however, the topological order of the system with uniform NNN tunneling fluctuates between trivial and standard non-trivial, eliminating the possibility of reaching non-standard topology, as presented in Fig. 3.11.

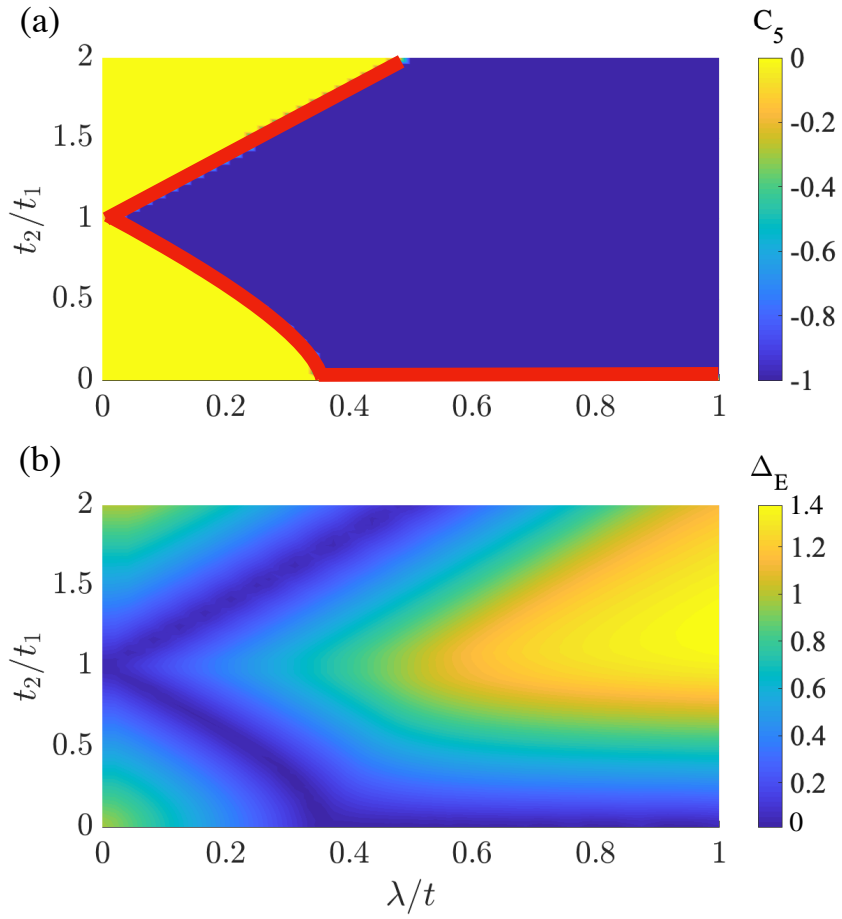

Figure 3.9: Chern number of the lower dispersive set of bands (Chern number of the set of quasi-flat bands is always 0). In the absence of the staggered NNN hopping the topology is trivial, regardless the strength of dimerization(this case is depicted by the first column of the plot). Increasing the NNN hopping causes the change of the topological order into the standard non-trivial one after reaching gapless phase, which is visible on (b) and marked by the red line on (a). The order of the signs of the Chern numbers depends on the dimerization sign. Moreover for $t_2/t_1 = 0$ discussed set of bands consists of 3 separate subsets of bands with trivial topology(this case is depicted by the lowest row of the plot). Dispersion of each of these subsets depends on the value of λ and for $\lambda = 0$ all 3 subsets are almost perfectly flat.

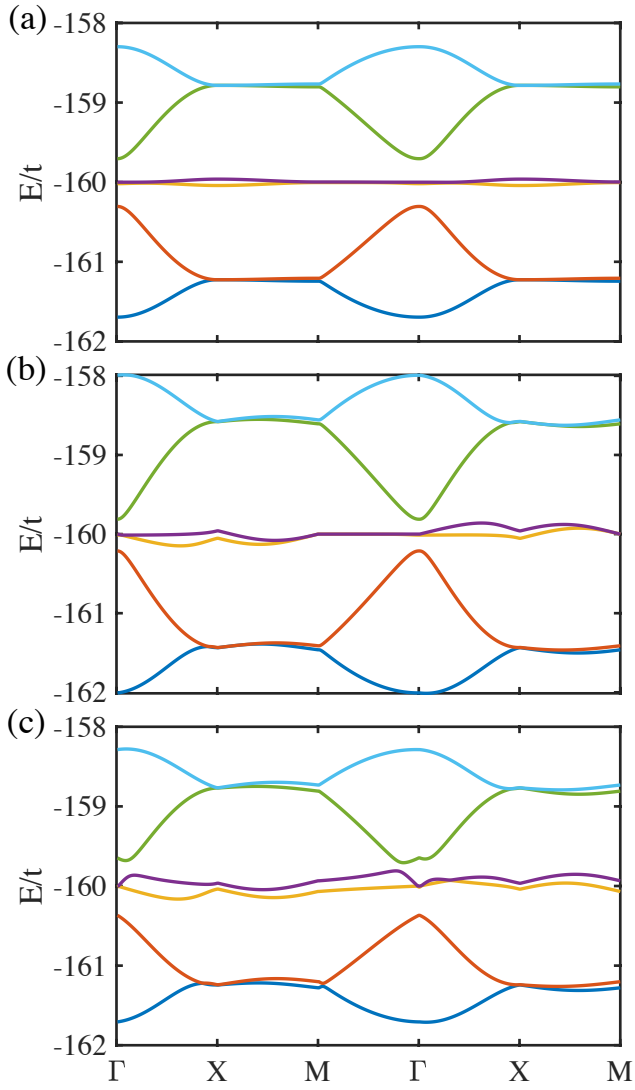

Figure 3.10: Magic configuration band structure in presence of uniform complex NNN hopping. (a) $t_2/t_1 = 0.7$ and $\lambda = 0$ shows the effect of pure dimerization of the lattice in the absence of NNN hopping resulting in vanishing Dirac cones. In comparison with Fig.3.3(b), which represents staggered NNN hopping without onsite energy one can see that dispersion of the quasi-flat bands is much bigger. (b) $t_2/t_1 = 1$ and $\lambda = 0.2$ represents the spectrum of the system with uniform NNN complex hopping generating the the increased dispersion of the quasi-flat bands and the lack of the global gap and. (c) In this case $\lambda = 0.2$ $t_2/t_1 = 0.7$. Dispersion of the quasi-flat bands is further increased but lattice dimerization provides the global gap. However, these two effects compete and the system can be gapless for different values of λ (see Fig 3.11(b)).

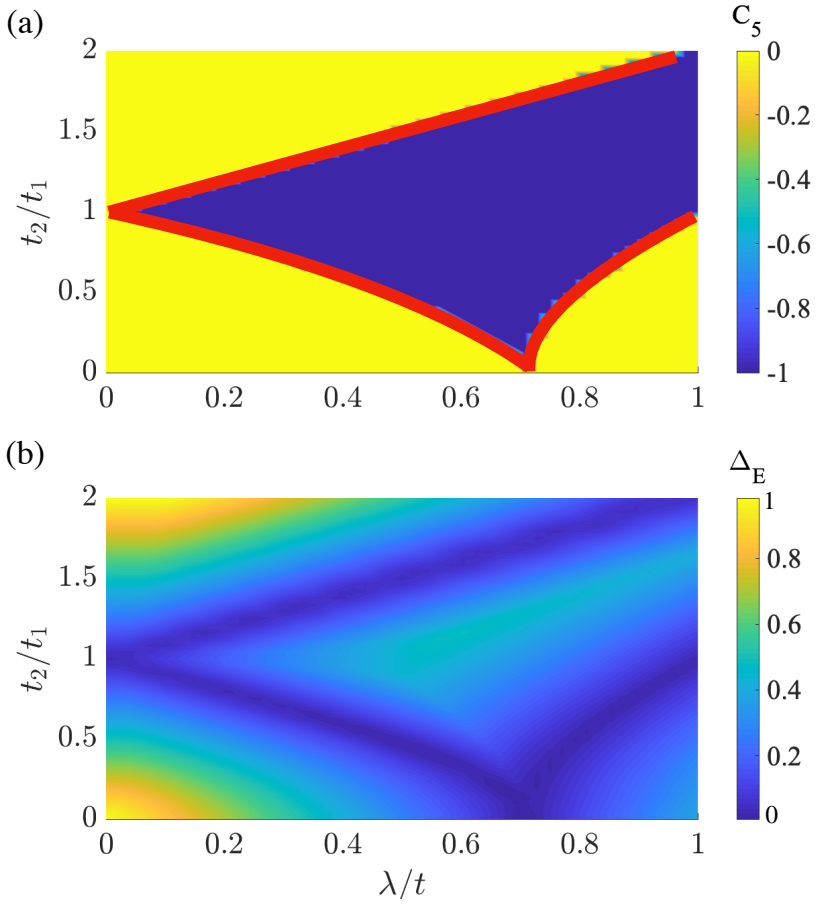

Figure 3.11: Chern number of the lower dispersive set of bands (Chern number of the set of quasi-flat bands is always 0). In the absence of the uniform NNN hopping the topology is trivial, regardless the strength of dimerization(this case is depicted by the first column of the plot). Increasing the NNN hopping causes the change of the topological order into the standard non-trivial one. However the order of the signs of the Chern numbers depends on the dimerization sign. Moreover for $t_2/t_1 = 0$ discussed set of bands consists of 3 separate subsets of bands with trivial topology(this case is depicted by the middle row of the plot). Dispersion of each of these subsets depends on the value of λ and for $\lambda = 0$ all 3 subsets are almost perfectly flat.

3.7 Potential experimental scheme

Here, a quantum simulation scheme of the system is discussee. As we will see below, all elements of the proposed scheme have been sucessfully implemented in state-of-the-art experiments. The challenge consists in combining all the necessary ingredients. We proceed in this section in steps, with the message directed mostly to the experimentalists. First, we review the basic scheme for twistronics without a twist, proposed already in Ref. [98]. Then, we discuss the necessary additional ingredients of both proposed schemes: I) Staggered complex hopping, and II) dimerized real tunnelling. We discuss possible methods that can be used to realize our schemes: i) Laser induced tunneling; ii) Floquet engineering; and iii) Superlattice and holographic potential imprinting methods. Finally, we discuss possible detection schemes of the topological properties of the model.

3.7.1 Basic experimental scheme

We proposed in Ref. [98] to use a subset of four states out of the large nuclear spin manifold $I = 9/2$ of ^{87}Sr, or ^{173}Yb ($I = 5/2$). The $SU(N)$ invariance inhibits collisional redistribution of the atoms among the different states. We select two of them to be $\sigma = \uparrow$, and the other two to be $\sigma = \downarrow$. All are subjected to a two-dimensional spin-independent optical lattice potential, created by two counter-propagating lattice beams. We choose the laser wavelength $\lambda_L = 813$ nm (corresponding to the magic wavelength of the clock transition $^1S_0 \rightarrow {}^3P_0$). We set a lattice depth to about 8 recoil energies, $8\,E_L$, which yields tunneling of order of 100 Hz. Lattice constant as usual is $d = \lambda_L/2$.

To create the synthetic layer tunneling, we exploit two-photon Raman transitions between spins $m = \pm 1/2$. A pair of Raman beams with $\lambda_R = 689$ nm near-resonant to the inter-combination transition $^1S_0 \rightarrow {}^3P_1$, produce a coupling of amplitude $\Omega_0 = \Omega_1\Omega_2/\Delta_0$. Here, Ω_1 and Ω_2 are the individual coupling amplitudes of the Raman lasers and Δ_0 the single-photon detuning. The Raman beams propagate in a plane perpendicular to the lattice potential, are aligned along its diagonal, and form an angle θ with the lattice plane (see Fig. 1 in Ref. [98]). This yields an in-plane momentum transfer per beam $k_R = \pm 2\pi \cos\theta/\lambda_R$, with projections $k_R/\sqrt{2}$ along the lattice axes. Therefore, the phase of the synthetic tunneling is $\boldsymbol{\gamma} \cdot \mathbf{r} = \gamma(x\hat{x} + y\hat{y})$, with $\gamma = \pm 2\pi \cos\theta\lambda_L/(\sqrt{2}\lambda_R)$. The sign is determined by the relative detuning of the Raman lasers. Experimentally, the simplest choice is to use counter-propagating Raman beams ($\theta = 0°$), which yields $\gamma = 0.8 \pmod{2\pi}$.

However, other values of the synthetic flux can be easily realized by adjusting the value of θ.

To implement a periodic modulation of the Raman coupling amplitude on the scale of several lattice sites, we propose to exploit a periodic potential created by a laser close-detuned from the excited state to excited state transition $^3P_1 \rightarrow {}^3S_1$ (corresponding to 688 nm [99]). This results in a large light shift of the $^3P_1$ excited state of amplitude δ, leading to a detuning of the Raman beams $\Delta(x, y) = \Delta_0 + \delta(1 + \cos(2\pi x/l_x)\cos(2\pi y/l_y))$. Its effect is to modulate the Raman coupling amplitude $\Omega(x, y) \simeq \Omega_0[(1 - \alpha) - \alpha\cos(2\pi x/l_x)\cos(2\pi y/l_y)]$, with $\alpha = \delta/\Delta_0 \sim 0.2$ for realistic experimental parameters [99, 100]. We therefore named it "modulation laser".

Note that [160] also proposed to use spatially modulated Raman couplings to generate Moiré patterns in 2D ^{87}Rb systems, originally designed by J.-W. Pan's group [161] to study robust spin-orbit coupling with bosonic atoms. In a related development, twistronic-like physics has been demonstrated in Ref. [162] in monolayer graphene undergoing a strain induced buckling transition. The buckling is associated with a periodically modulated pseudo-magnetic field that has the effect of creating a material with flat electronic bands.

3.7.2 Extensions of the basic scheme

SCH case. Here the NN tunnelling is standard and constant, $t(\mathbf{r}) = t$. The staggered onsite energy can be realized relatively easily using super-lattice or holographic potential imprinting methods. The challenging part here is relate to the phases associated with the next-nearest neighbor complex tunnelings, set to $\phi_L(\mathbf{r}) - \phi_{\mathbf{R}}(\mathbf{r}) = \pi$, where $\phi_R(\mathbf{r}) = (2\mathbf{r} \cdot \mathbf{1_y} + 1)\pi/2$. We suggest to use here laser induced tunneling or lattice shaking. For laser induced tunneling one possibility would be to to employ the clock transition from $^1S_0 \rightarrow {}^3P_0$, using appropriate polarization of the assisting laser to couple to different excited states (for instance, coupling $+3/2 \rightarrow +1/2$ via σ_- polarized light, coupling $+3/2 \rightarrow +3/2$ via π-polarized light, and $+3/2 \rightarrow +5/2$ via σ_+ polarized light). The main problem is that the clock transitions will interfere immensely with the light-shifting scheme of the $^3P_0$ state that we proposed to use to get the Moiré pattern. In fact, we should expect that the staggered complex hoppings will not only be staggered (if we design and realize the staggering well), but they will be spatially modulated as well. The period of the latter modulation should follow the period of our "Moiré" pattern i.e.

$$\lambda(\mathbf{r}) = \lambda_0 + \Delta\lambda\cos(2\pi x/l_x)\cos(2\pi y/l_y). \tag{3.10}$$

Upon conducting a meticulous study, one can discern that as long as $\Delta\lambda \sim t$, the effects of the spatial modulation of the next-nearest-neighbor (NNN) complex hopping remain minimal. In fact, they are confined to minor bandwidth corrections, which neither influence the topological order nor introduce new gaps, or close existing ones, in the system.

DL case. In Eq. (3.2), we considered dimerized real tunneling, such that $t(\mathbf{r})$ takes the form of t_1 and t_2 in alternative sites in the x and the y directions, along with the next-nearest neighbor complex hopping. Here the situation seems to be easier from the experimental point of view. The alternating tunnelling can be achieved using the super-lattice techniques (dimerization). The next-nearest neighbor complex hopping with the homogeneous phase set to $\phi_R(\mathbf{r}) = \phi_L(\mathbf{r}) = \pi/2$ shall be accessible via lattice shaking and Floquet engineering techniques.

3.7.3 State-of-the-art experimental techniques

Laser assisted tunneling: The idea of employing laser assisted tunneling for generation of synthetic gauge fields goes back to the seminal paper of Jaksch and Zoller [141]. It was generalized to non-Abelian fields in Ref. [163]. These ideas all seemed very "baroque" at that time, but finally were realized in experiments with amazing effort, but equally amazing results [164, 143, 146, 165, 147, 165].

Floquet engineering: In the context of cold atoms this technique goes back to the pioneering theory works of A. Eckardt and M. Holthaus [166], followed by experiments of E. Arimondo and O. Morsch [167]. In condensed matter the works concerned creation of topological phases in graphene [168, 169]). The possibility of generating artificial gauge field was first discussed in Ref. [144] and realized in experiments of Hamburg group [170]. This culminated with the experimental realization of arbitrary complex phases [171], and theoretical proposals combining shaking and on-site excitations [172]. In the recent years many fascinating results were obtain using shaking (cf. [173, 174], for a review see [144]). In a sense, from the perspective of the present chapter a culmination of these effort consisted in realization of the Haldane model with next nearest neighbor complex tunnelings in a brick lattice [86, 148]. Recently, the Hamburg group combined the studies of the Haldane model with the use of machine learning methods [175, 176, 149].

Super-lattice and holographic potential imprinting methods These are nowadays standard methods, developed already many years ago and described in textbooks such as [84]. They have a plethora applications ranging from designing traps of special shape, through creation of dimerized lattices, to imprinting random

potentials. All of these methods an be useful for our purposes, for instance for designing a lattice with dimerized tunneling.

3.7.4 Detection of the topological order

In cold-atom quantum simulators, the standard transport experiment techniques used to characterize the transverse conductivity in 2D materials are feasible but very demanding [177, 178], and there is, therefore, the need for other detection schemes to characterize the topology of the system. In the last decade, many detection schemes have developed for quantum simulators [142, 179], and we present here the a non-exhaustive list of techniques that could be applied to the synthetic twisted bi-layer material. The total Chern number and the Berry curvature could be measured through the anomalous velocity of the center of mass of the atomic cloud [180, 181]. This technique, already applied in recent experiments [182, 183], would require an additional optical gradient. Alternatively, the Chern number could measured through the depletion rate of the bands in the presence of heating [184]. This effect, called quantized circular dichroism, has been implemented in state-of-the-art experiment [150] and would require an additional shaking of the lattice. Finally, the topology could be characterized through the observation of the chiral edge states. The latter could be done by a suitable quench protocol [185, 186].

3.8 Conclusions - Outlook

In the present chapter we developed further the idea of "twistronics without a twist" and demonstrated that it can be used to engineer interesting topological band structures under various conditions. Focussing on a square lattice system with synthetic dimensions, we showed the appearance of an anomalous Hall phase in presence of artificial complex next-to-nearest neighbor interlayer tunneling. Moreover, we discussed the emergence of topological bands via another mechanism – lattice dimerization. In general, the bands of interest can be categorized into three groups - trivial, and two categories of topologically non-trivial bands differing by their Chern number combinations: standard non-trivial, and non-standard not-trivial.

In the next chapter we will discuss possible ways of incorporation of interaction effects. On the technical side, in the first stage, incorporation of the interaction effects can be carried out via a mean field theory at the Hartree-Fock as well as "slave boson/fractionalization" level. Moreover, as our scheme provides the

possibility of observing physics similar to magic angle twisted bi-layer graphene with an *effectively* large rotation angle, implying a much smaller supercell, performing ab-initio calculation could be possible via advanced tensor network algorithms. The pressing questions in these realm are: (i) the origins of strongly correlated phenomena in twisted materials, such as unconventional superconductivity phenomena, (ii) the coexistence of superconducting and correlated insulating states in magic-angle twisted bi-layer graphene, and their relationship, (iii) the role of topology in the interacting systems, which can be probed by altering the quasi-flat band topology. Recently, flat Chern bands have been reported from twisted bi-layer $MnBi_2Te_4$ [187].

Chapter 4

Interactions in the synthetic bi-layer

4.1 Overview of interactions in 2D materials

Electron interactions in two-dimensional (2D) materials play a crucial role in determining their electronic, magnetic, and optical properties. Unlike their three-dimensional counterparts, 2D materials, such as graphene, 2D transition metal dichalcogenides (TMDCs), and 2D topological insulators, exhibit enhanced electron correlations and quantum confinement effects due to their reduced dimensionality [188, 189]. These interactions can lead to the emergence of exotic phenomena, such as fractional Chern insulator, Mott insulators, unconventional superconductors, etc. [116, 54]. Furthermore, electron interactions in 2D materials can be influenced by external factors, such as strain, electric and magnetic fields, or proximity to other materials in heterostructures, enabling unprecedented control over their properties and potential applications in nanoscale devices [75]. Understanding the role of electron interactions in 2D materials is essential for developing new functional materials and exploiting their unique properties in next-generation electronic, spintronic, and photonic applications.

In bi-layer materials, such as twisted bi-layer graphene (TBG), various types of interactions (electron-electron, electron-carbon, carbon-carbon, etc) play a significant role in determining their electronic properties and emerging phenomena. The interplay of these interactions can lead to unique features, including flat bands, correlated insulating states, and superconductivity. The stacking of two graphene layers with a twist angle introduces a moiré superlattice, which results in a spatially periodic modulation of the interlayer tunneling energy. This modulation can be

understood in terms of the moiré potential, which governs the interlayer hopping of electrons between the layers [46].

In bi-layer materials, both intralayer and interlayer Coulomb interactions are essential. These interactions are generally repulsive, as they involve the electrostatic repulsion between electrons in the same layer or across layers. The strength of these interactions can be influenced by the dielectric environment, twist angle, and screening from other electrons, which can significantly affect the electronic properties of the system [190]. However other mechanism plays an important role in overall transport properties, namely exchange interactions, which are short-range interactions arising from the quantum mechanical requirement that the wave function of two identical fermions must be antisymmetric under particle exchange. In the context of TBG, these interactions can lead to spin-dependent effects and influence the magnetic properties of the system [191].

4.1.1 Hubbard model

In this chapter we enter the regime of interacting atoms in optical lattices. A tight-binding picture, that we have considered up to that point is now enriched by two-body contact (on-site) interactions between the fermionic atoms in the lattice. Such system can be successfully described by the (Fermi-) Hubbard model, which plays a central role in describing various aspects of the many-body physics of condensed matter systems [192, 193, 78, 194, 195, 196]. In particular, along with its variants, it is widely believed to encompass the basic ingredients required to understand high-temperature superconductivity, *e.g.* in cuprates [197, 198, 199, 200, 201]. However, it is important to note that the Hubbard model is a simplified description of the system, and more sophisticated models or numerical methods might be necessary to fully capture the rich physics emerging from the interplay of various interactions in bi-layer materials, such as twisted bi-layer graphene [202].

The Hubbard model, introduced by John Hubbard in the early 1960s, is a theoretical framework that investigates the electronic behavior of interacting particles in a lattice structure [203]. The single-band approximation is a key simplification in the Hubbard model. In real materials, there are often multiple orbitals per lattice site, and electrons can hop between different orbitals. However, the Hubbard model only considers a single orbital per site and neglects inter-orbital hopping processes. This approximation is valid when the energy scales of the other orbitals are significantly larger than the energy scales of the single orbital considered, and

when the physics of interest is primarily governed by the single orbital [204]. The Hamiltonian for the Hubbard model can be written as:

$$H_{Hubbard} = -t(\sum_{\langle i,j\rangle,\sigma} c^{\dagger}_{i,\sigma} c_{j,\sigma} + H.c) + U \sum_{i} n_{i\uparrow} n_{i\downarrow} \tag{4.1}$$

Here, the first term represents the kinetic energy of electrons, where t is the hopping amplitude, $c^{\dagger}_{i,\sigma}$, $(c_{i,\sigma})$ are the creation (annihilation) operators for an electron with spin σ at site i, and $\langle i, j\rangle$ denotes a summation over nearest neighbors. The second term accounts for the electron-electron interaction, with U being the on-site Coulomb repulsion, and $n_{i\uparrow}$ is the electron number operator for spin σ at site i [203].

4.1.2 Hubbard model for Condensed Matter Physics

Despite its simplicity, the Hubbard model has been instrumental in understanding the behavior of interacting electrons in condensed matter systems. In this short section, we discuss the critical insights it has revealed into various phenomena.

Mott Insulators: The Hubbard model helps explain Mott insulators, materials that should be metallic according to the conventional band theory but instead exhibit insulating behavior [205]. In conventional band theory, the electrical conductivity of a material is determined by the filling of its electronic bands. However, Mott insulators demonstrate that strong electron-electron interactions can lead to insulating behavior even when the band structure suggests that the material should be a metal.

By incorporating the on-site Coulomb repulsion (U) in the Hubbard model, it becomes possible to understand the insulating state in these materials. When U is large enough compared to the hopping term (t), electrons become strongly localized due to the energy cost associated with double occupancy of lattice sites. Consequently, the system exhibits an insulating state despite having a partially filled band [206]. This result highlights the importance of electron-electron interactions in determining the electronic properties of materials and demonstrates the limitations of conventional band theory in describing strongly correlated systems.

The Mott-Hubbard transition, a metal-insulator transition driven by strong correlations, has been observed in various materials. Transition metal oxides, such as V2O3

and NiO, are prototypical examples where the Mott-Hubbard transition is observed [207, 208]. In these materials, the interplay between the crystal field splitting, on-site Coulomb repulsion, and electron hopping leads to the formation of Mott insulating states. The Hubbard model has also been successful in explaining the metal-insulator transition in organic materials, such as χ-(BEDT-TTF)2Cu[N(CN)2]Br [209]. These materials offer unique opportunities to study the Mott-Hubbard transition and its associated phenomena due to their structural tunability and the possibility to control the electronic properties via chemical doping, pressure, or external fields.

The Hubbard model has been instrumental in elucidating the origin of Mott insulating behavior in various materials, providing a deeper understanding of the role of electron-electron interactions in determining their electronic properties. This insight has led to the development of new theoretical frameworks and experimental techniques to probe and control the properties of strongly correlated electron systems.

High-Temperature Superconductivity: The Hubbard model has been widely used to study the emergence of high-temperature superconductivity in copper-oxide materials (cuprates) [210]. High-T_c superconductors are a class of materials that exhibit superconductivity at temperatures much higher than conventional superconductors, with transition temperatures reaching up to 138K in $HgBa_2Ca_2Cu_3O_{8+\delta}$ [211]. Although the exact mechanism of High-$T_c$superconductivity remains an open question, the Hubbard model has provided valuable insights into the unconventional pairing symmetry and the role of strong electron correlations in these systems [212].

The parent compounds of High-T_c superconductors are antiferromagnetic Mott insulators. Upon chemical doping, the antiferromagnetic order is suppressed, and the superconducting phase emerges. The Hubbard model captures this behavior by incorporating the on-site Coulomb repulsion (U) and the electron hopping (t), allowing researchers to investigate the evolution of the electronic properties as a function of doping [213, 214]. Some of the key features of High-T_c superconductors, such as the pseudogap phase, the d-wave pairing symmetry, and the formation of charge and spin stripes, can be qualitatively understood within the framework of the Hubbard model [215, 216]. Moreover, the Hubbard model has helped unveil the relationship between doping and the superconducting phase, providing a roadmap for the search for new High-T_c superconductors [217]. By investigating the interplay between the kinetic energy and electron-electron interactions

Quantum Phase Transitions: The Hubbard model has proved instrumental in understanding quantum phase transitions (QPTs), which are continuous transitions between different ground states at zero temperature driven by quantum fluctuations [218]. QPTs are characterized by a change in a non-thermal control parameter, such as pressure, doping, or magnetic field, and are fundamentally different from classical phase transitions driven by thermal fluctuations. They often result in the emergence of new quantum phases with exotic properties, providing crucial information on the role of electron correlations in these phenomena [218].

By varying the parameters t and U in the Hubbard model, researchers can study the onset of various types of QPTs, such as magnetic ordering, superconductivity, or metal-insulator transitions. In particular, the Hubbard model has been employed to investigate the interplay between antiferromagnetism and superconductivity in heavy fermion systems, such as $CeCu_2Si_2$ and $CeIrIn_5$ [219, 220]. These materials exhibit complex phase diagrams with multiple competing phases, and the Hubbard model has provided valuable insights into the mechanisms governing the QPTs between these phases.

One prominent example of a QPT studied within the Hubbard model framework is the transition from a Mott insulator to a band insulator. This transition can be induced by applying pressure or changing the carrier concentration in the material [221]. As the system undergoes the transition, the charge gap closes at a critical value of the control parameter, giving rise to a quantum critical point. Near this point, the system exhibits unconventional behavior, such as non-Fermi liquid properties and the emergence of novel phases [222]. The Hubbard model has been a valuable tool in understanding the role of electron correlations in driving these QPTs and the associated emergent phenomena.

Another area where the Hubbard model has been applied is the study of QPTs in low-dimensional systems, such as quasi-one-dimensional organic conductors and two-dimensional electron gases at the interface of oxide heterostructures [223, 224]. In these systems, the reduced dimensionality and the enhanced role of quantum fluctuations lead to a rich variety of quantum phases and transitions. The Hubbard model provides a simple yet powerful framework for investigating the effects of electron correlations and fluctuations in these low-dimensional systems.

4.1.3 Quantum optical simulations of 2D materials

Although Hubbard models are effective simplified models of complex condensed matter systems, they can be realized with high fidelity and control in various engineered systems such as ultracold atoms in optical lattices. This, in turn, has

lead to an exciting branch of physics - quantum simulation of condensed matter phenomena [84, 225, 226, 227]. In recent years, one-, two- and three-dimensional optical lattices have been generated paving the way to studies of different quantum phases under various types of interactions [228, 229]. A distinguishing feature within the cold atom set-up is the freedom of precise tuning of microscopic system parameters, *i.e.* interactions and particle tunneling over wide ranges [230].

The control of material properties via band structure engineering has been a long standing goal in condensed matter physics. A new frontier is twistronics, where the relative rotational misalignment between layers in quasi two dimensional (2D) systems leads to Moiré patterns in real space. The Moiré patterns strongly influence the band structure and lead to enhanced collective effects induced by interactions and topology [231]. In graphene bi-layers, tuning the twist angle to so-called magic values was predicted to strongly quench the electronic kinetic energy leading to the formation of quasi-flat bands [52, **?**, 232], where small interactions can dominate the phenomenology [233]. With the successful development of fabrication methods for such devices, a series of experiments spectacularly unveiled superconductivity and correlated insulators in these materials around the magic angles [234, 235, 236].

The appearance of superconductivity originating from completely isolated or non-isolated quasi-flat bands, in particular, has turned out to be an exciting development in the search for High-$T_c$superconductivity driven by quantum geometry [237, 238, 239, 240]. These results have driven the new field of twistronics involving the study of various kinds of Van der Waals stacked heterostructures beyond bi-layer graphene [241]. The unavoidable effect of twisting 2D materials is the enlargement of the unit cell, usually by a few orders of magnitude compared to the original unit cell of a single sheet of the material [231, 242], into a so-called Moiré supercell. This emergent approximate crystal symmetry strongly complicates direct microscopic modelling and non-approximating studies of correlations in these systems. As a result direct quantum simulations of twistronics, in particular based on the promising platform of ultra cold atoms trapped in optical lattices, that allow for exquisite control of system parameters, offer an additional window to gain fundamental understanding of Moiré materials. Importantly, this approach allows to study systems without certain practical difficulties associated with materials such as the lack of control over the homogeneity of the twist angle in samples and strain effects which lead to disorder. Moreover, apart from the control of interactions, ultra cold atom systems allow for tuning of inter-layer coupling to strong values that can lead to enhanced correlation effects even for comparatively small Moiré supercells.

The interest in general 2D bi-layer systems has led to the design of multiple architectures and control schemes for bi-layer optical lattices [94, 243, 244]. Moiré systems can be generated, on one hand, by effectively performing the direct analog of material twisting in overlapping samples [245], or spin dependent optical lattices [246, 247]. A different versatile approach stems from the fact that physically the main effect of twisting is the induction of incommensurate quasi-periodic potentials and quasi-periodic inter-layer tunnelings in layered systems [248, 249, 250, 251, 40, 252, 253]. Such spatially modulated patterns can be directly imprinted on synthetic bi-layer systems [40, 41], *i.e.* a single physical optical lattice layer of atomic species with Raman coupled internal states playing the role of the additional layer degree of freedom [254, 255]. This remarkably realizes Moiré-type physics without physical twisting.

In the present chapter, we build on the idea originally presented in [40] and described in chapter 2 which uses the concept of synthetic dimensions to engineer twisted bi-layers. For such scenario, we consider attractive on-site *s*-wave interactions with full SU(4) symmetry and explore superconducting properties in such synthetic bi-layers with a chosen size and shape of the supercell. Near-flat bands with very small dispersion compared to its immediately neighboring bands can be accessed with rather small unit cells in our synthetic-dimension-based proposal, which allows us to adopt an multi-band Hartree-Fock-Bogoliubov theory [256, 257] for probing superconductivity. The analysis is performed extensively for a wide range of experimentally controllable parameters, such as inter-layer coupling and interaction strength. Our study seeks to understand and to characterize the role played by a finite dispersion of the quasi-flat band on superconductivity. In fact, the proposed setup allows to accurately control the widths of the quasi-flat bands over a broad range [40, 41].

This chapter is arranged as follows: In Sec. 4.2 we present the lattice Hamiltonian and discuss the band structure and interaction types appearing in the model. In Sec. 4.3 the detailed description of Hartree-Fock-Bogoliubov mean field decoupling is shown together with resulting Bogoliubov - de Gennes Hamiltonian and self-consistent procedure. Sec. 4.4 presents original results of our study. First, we take into account the impact of band flattening, caused by modulation of the inter-layer hopping, on the superconducting gap. Then, we consider breaking the symmetry into SU(2) $\times$ SU(2) via selectively tuning the interaction channels. We also tune one of interaction types to be of negligible amplitude to facilitate the comparison

of the obtained results with standard bi-layer Fermi-Hubbard system. Finally, conclusions are presented in Sec. 4.5.

4.2 The system

The considered cold-atom system is the same as in the first chapter 2, the Moiré lattice has a graphene-like brick-wall geometry. Its unit cell contains 8 physical sites of the original lattice, as shown in Fig. 4.1(a). Among these eight sites, we distinguish four sets of sites $\{AA, AB, B, C\}$: AA and AB denote the six black sites in Fig. 4.1(a) with two or four "black" nearest neighbours, respectively , and B and C denote the red and green sites, respectively. According to Eq. (**??**), these three sets of sites exhibit the following property:

$$\Omega(\mathbf{r}) = \begin{cases} \Omega_0(1-\alpha) & \text{if } \mathbf{r} \in AA \vee AB, \\ \Omega_0 & \text{if } \mathbf{r} \in B, \\ \Omega_0(1-2\alpha) & \text{if } \mathbf{r} \in C, \end{cases} \tag{4.2}$$

that is, the coupling strength at sites B and C is shifted by $|\alpha|$ with respect to the coupling strength at sites of type A, that is, type AA or AB.

For our choice of l_x and l_y, the spectrum of H_{kin} consists of 16 energy bands. A symmetrical arrangement of the bands with respect to $E = 0$ reflects the particle-hole symmetry in the system. At sufficiently large inter-layer tunneling, e.g., $\Omega_0 = 100t$,the spectrum is gapped, as shown on Fig. 4.1(d) for $\alpha = 0.2$ and (f) for $\alpha = 0.7$. Among these 16 bands, we focus on the subset of six bands at $E \approx \pm 80t$, i.e. we assume a Fermi energy in the vicinity of this manifold. These two manifolds are plotted in black in Fig. 4.1(d), and further analyzed in Fig. 4.1(e), where we zoom into one of the six-fold manifold. Importantly, we observe that the two central bands of this manifold are almost flat. Moreover, there are different degenercies, e.g. at the Γ-point. In addition to these quasi-flat bands, the system also exhibits isolated flat bands shown in blue and red in Fig. 4.1(d).

The impact of the twist parameter α on the structure of the whole energy spectrum is shown in Fig. 4.1(b). For $\alpha < 0.67$, the isolated bands are located above and below the six-fold manifolds, whereas for $\alpha > 0.67$ both isolated bands are above the sixfold manifold on the positive side of the spectrum, and below the

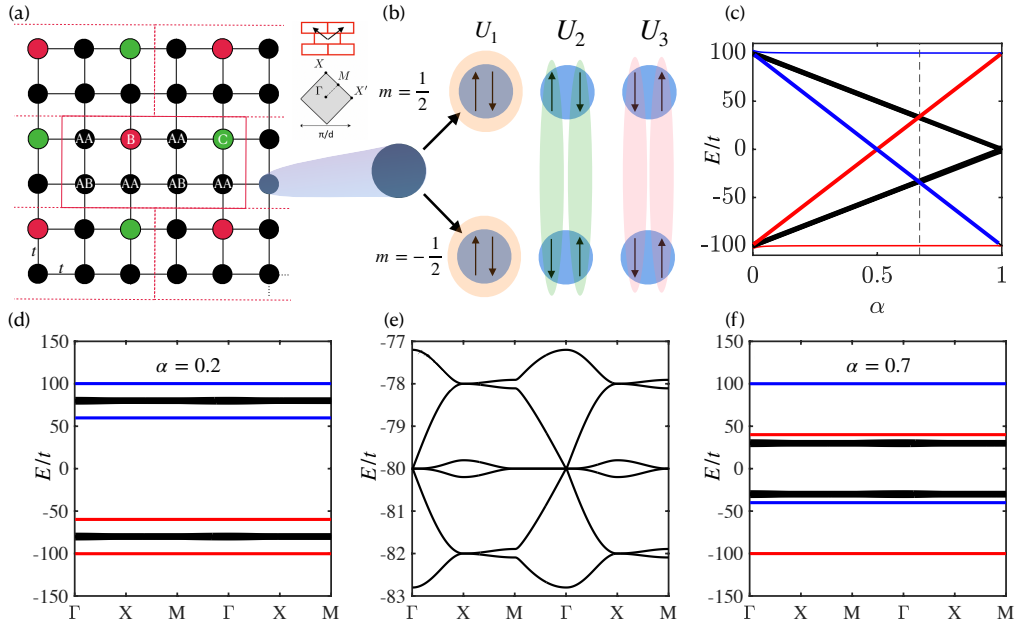

Figure 4.1: (a) Square lattice with unit cell of 8 physical sites due to synthetic coupling which is different on the black (*AA* and *AB* - depending on the amount of A-type neighbours), green (*B*), and red (*C*) sites. The lattice is covered by unit cells in a brick wall arrangement, as indicated in the inset. (b) Schematic representation of the three interaction types appearing in the system. (c) Evolution of the average energy of the bands as a function of the modulation parameter α at $\Omega_0 = 100$ (in units of t). The panel shows the outer bands (two blue lines and two read ones) of each, positive and negative manifold being shifted with respect to two the inner subsets of bands marked with black lines. At the critical value of $\alpha_c \approx 0.67$ the blue band from the upper manifold reaches lower energy than black, negative manifold. This results with change of the position of the Fermi surface. (d) Full spectrum of the system under periodic modulation $\Omega_0 = 100$ and $\alpha = 0.2$. (e) Zoomed plot of (d) highlighting the negative six-fold subset of bands including the central quasi-flat bands. (f) Spectrum of the system at $\Omega_0 = 100$ and $\alpha = 0.7$, after the flipping of the bands occurred (dashed line in panel (c)).

sixfold manifold on the negative side of the spectrum.

Within the sixfold manifold, the modulation of the inter-layer tunneling flattens the two central bands, as it mimics Moiré patterning. This implies that, for $\alpha < 0.67$, this quasi-flat band structure appears at the Fermi surface, when the filling ν of the system is 1/4 or 3/4, i.e., the lowest four or the lowest twelve bands are filled, see Fig. 4.1(d) and (e). For $\alpha > 0.67$, the quasi-flat bands are at the Fermi surface for $\nu = 5/16$ or $\nu = 11/16$, i.e., the lowest five or eleven bands are filled, see Fig. 4.1(f). In this way, the parameter α can be used to control the density of states at the Fermi surface, which will later be shown to have a strong impact on the superconducting behavior. We have defined the filling ν such that $\nu = 1$ corresponds to a lattice which is filled by 4 fermions per site. We consider only the uniform value of filling (not distinguishing the filling at each synthetic level). In the limiting case of $\alpha = 1$, twelve bands become fully degenerated at $E = 0$, as can be seen from Fig. 4.1(b).

In order to investigate the superconductivity, we consider attractive collisional Hubbard-type interactions between the atoms, i.e., local interactions in the physical lattice. We assume that the internal state of the atoms is not changed during the collision. In the most general form the interaction Hamiltonian then reads

$$H_{\text{int}} = -\sum_{\mathbf{r},m,m',\sigma,\sigma'} U^{m,m'}_{\sigma,\sigma'} n_{m,\sigma}(\mathbf{r}) n_{m',\sigma'}(\mathbf{r}), \tag{4.3}$$

where $n_{m,\sigma}(\mathbf{r}) = a^{\dagger}_{m,\sigma}(\mathbf{r}) a_{m,\sigma}(\mathbf{r})$ is the density operator of a fermion in the $\{m,\sigma\}$ state. $U^{m,m'}_{\sigma,\sigma'}$ denotes the (non-negative) interaction strength between atoms in levels $\{m,\sigma\}$ and $\{m',\sigma'\}$ and the negative sign indicates that we consider these interactions to be attractive. In general, $U^{m,m'}_{\sigma,\sigma'}$ describes 16 different kinds of interactions. Out of these, the Pauli principle excludes all diagonal interactions, i.e., $U^{m,m}_{\sigma,\sigma} = 0$. We are left with possibly twelve different non-zero interaction processes. Because of symmetry arguments, these can be further grouped into three interaction types, as illustrated in Fig. 4.1(c): The first type are the intra-layer interactions within a synthetic layer

$$U_1 \equiv U^{+,+}_{\uparrow,\downarrow} = U^{-,-}_{\uparrow,\downarrow} = U^{+,+}_{\downarrow,\uparrow} = U^{-,-}_{\downarrow,\uparrow}. \tag{4.4}$$

The second type groups the inter-layer interactions between particles of opposite spin,

$$U_2 \equiv U^{+,-}_{\uparrow,\downarrow} = U^{-,+}_{\uparrow,\downarrow} = U^{+,-}_{\downarrow,\uparrow} = U^{-,+}_{\downarrow,\uparrow}. \tag{4.5}$$

The third groups contains the interlayer interactions of particles with equal spin

$$U_3 \equiv U^{+,-}_{\uparrow,\uparrow} = U^{-,+}_{\uparrow,\uparrow} = U^{+,-}_{\downarrow,\downarrow} = U^{-,+}_{\downarrow,\downarrow}. \tag{4.6}$$

From the point of view of a realization with alkali-earth atoms, the case of $U_1 = U_2 = U_3$ is the most natural/realistic one. Interactions with nearly SU(N) symmetry are exhibited, for instance, between the internal states obtained from the nuclear spin manifolds ($I = 5/2$ and $I = 9/2$, respectively) for the fermionic isotopes ^{87}Sr and ^{173}Yb, see Ref. [258]. We also discuss the cases in which U_1 (or U_2) become the dominant interactions, which is particularly relevant from the point of view of bi-layer interpretation.

4.3 Mean-field decoupling

We apply a Hartree-Fock-Bogoliubov-de Gennes mean-field approach [259, 260] to tackle the many-body Hamiltonian $H_{\text{kin}} + H_{\text{int}}$ (see Eqs. (2.2) and (4.3)). As we consider attractive interactions, we focus only on pairing fields in the mean-field decomposition. Each on-site quadratic attractive term in Eq. (4.3) is thus decoupled as:

$$\begin{aligned} a^\dagger_{m,\sigma} a_{m,\sigma} a^\dagger_{m',\sigma'} a_{m',\sigma'} \approx\ & \langle a^\dagger_{m,\sigma} a^\dagger_{m',\sigma'} \rangle a_{m',\sigma'} a_{m,\sigma} \\ & + a^\dagger_{m,\sigma} a^\dagger_{m',\sigma'} \langle a_{m',\sigma'} a_{m,\sigma} \rangle \\ & - \langle a^\dagger_{m,\sigma} a^\dagger_{m',\sigma'} \rangle \langle a_{m',\sigma'} a_{m,\sigma} \rangle, \end{aligned} \tag{4.7}$$

where $\langle \cdot \rangle$ denotes the expectation value. The last term is a constant shift affecting the grand thermodynamic potential and is important for obtaining the self consistent equations for the order parameters via minimization of the thermodynamic potential or for assessing thermodynamic stability of different solutions. We do not display this term in the following. Combining Eqs. (4.3)-(4.7) and assuming symmetry between the layers and spins, let us explicitly write down the pairing Hamiltonian:

$$\begin{aligned} H_{\text{P}} = & \Delta_1 (a^\dagger_{+,\uparrow} a^\dagger_{+,\downarrow} + a^\dagger_{-,\uparrow} a^\dagger_{-,\downarrow}) \\ & + \Delta_2 (a^\dagger_{+,\uparrow} a^\dagger_{-,\downarrow} + a^\dagger_{+,\downarrow} a^\dagger_{-,\uparrow}) \\ & + \Delta_3 (a^\dagger_{+,\uparrow} a^\dagger_{-,\uparrow} + a^\dagger_{+,\downarrow} a^\dagger_{-,\downarrow}) + \text{h.c.} \end{aligned} \tag{4.8}$$

Here, we have defined the following superconducting order parameters

$$\Delta_1 \equiv U_1\langle a_{+,\uparrow}a_{+,\downarrow}\rangle = U_1\langle a_{-,\uparrow}a_{-,\downarrow}\rangle, \tag{4.9}$$

$$\Delta_2 \equiv U_2\langle a_{+,\uparrow}a_{-,\downarrow}\rangle = U_2\langle a_{-,\uparrow}a_{+,\downarrow}\rangle, \tag{4.10}$$

$$\Delta_3 \equiv U_3\langle a_{+,\uparrow}a_{-,\uparrow}\rangle = U_3\langle a_{+,\downarrow}a_{-,\downarrow}\rangle. \tag{4.11}$$

The value of the order parameters can, in principle, vary within each unit cell due to in-equivalence of the lattice sites and their surroundings caused by spatial modulation of the synthetic coupling, described in Eq. (**??**). As has been shown in Fig. 4.1(a) and defined in Eq. (4.2), one can differentiate the sites in the unit cell into four types. While types B and C are taken into account separately due to their different value of synthetic coupling $\Omega(\mathbf{r})$, the sites of A-type (black sites in Fig.4.1) are distinguished based on geometric reasons and divided into "bridge" (AA) and "node" (AB) sites, depending on the amount of nearest A-type neighbours (two for AA, and four for AB). A visual representation of this scheme is also shown in Fig. 4.2, where yellow sites represent "bridge" (AA) sites on panel (a) and "node" (AB) on panel (b). Therefore, distinguishing between the four different types of sites, we write the order parameter in the interaction channel $i = 1, 2, 3$ for site of type $I \in \{AA, AB, B, C\}$. For the eight sites of a unit cell, we thus have three sets of order parameters defined below:

$$\vec{\Delta_i} = (\Delta_i^{AB}, \Delta_i^{AA}, \Delta_i^{AB}, \Delta_i^{AA}, \Delta_i^{AA}, \Delta_i^{B}, \Delta_i^{AA}, \Delta_i^{C}). \tag{4.12}$$

It is also convenient to view the real-space fermionic operators $a_{m,\sigma}(\mathbf{r}_j)$ as eight-component vectors, with each component representing one site in the unit cell, and the j representing the index of unit cell within the Moiré lattice. Then, we Fourier transform the operators to quasi-momentum space, via

$$a_{m,\sigma}(\mathbf{r}_j) = \frac{1}{\sqrt{N_s}} \sum_k e^{-i\mathbf{k}\mathbf{r}_j} a_{m,\sigma}(\mathbf{k}), \tag{4.13}$$

where N_s is the number of unit cells in the lattice and $c_{m,\sigma}(\mathbf{k})$ is the eight-dimensional field operator of a fermion with quasi-momentum $\mathbf{k} = (k_x, k_y)$. The real-space hopping H_t is diagonalized as $H_t = -t\sum_{m,\sigma} a^\dagger_{m,\sigma}(\mathbf{k})H_t^m(\mathbf{k})a_{m,\sigma}(\mathbf{k})$, with $H_t^m(\mathbf{k})$ being a diagonal matrix representing the eight bands per layer index $m \in \{+, -\}$. Due to the symmetry between the synthetic layers, we have $H_t^+(\mathbf{k}) = H_t^-(\mathbf{k})$. The interlayer tunneling is also diagonal in $\mathbf{k}$, but of the form $a^\dagger_{+,\sigma}(\mathbf{k})H_\Omega(\mathbf{k})a_{-,\sigma}(\mathbf{k})$.

In order to present the full Hamiltonian, $H = H_{\text{kin}} + H_P$, containing all order

parameters of interest in the quadratic form, we define the following 8×8-dimensional Nambu spinor:

$$\Psi_{\mathbf{k}}^{\dagger} = \begin{pmatrix} a_{-,\uparrow}^{\dagger}(\mathbf{k}) \\ a_{-,\downarrow}(-\mathbf{k}) \\ a_{+,\uparrow}^{\dagger}(\mathbf{k}) \\ a_{+,\downarrow}(-\mathbf{k}) \\ a_{-,\uparrow}(\mathbf{k}) \\ a_{-,\downarrow}^{\dagger}(-\mathbf{k}) \\ a_{+,\uparrow}(\mathbf{k}) \\ a_{+,\downarrow}^{\dagger}(-\mathbf{k}) \end{pmatrix} \tag{4.14}$$

The mean field Hamiltonian in momentum space is of the Bogoliubov-de-Gennes (BdG) form and is given by

$$H(\mathbf{k}) = \Psi_{\mathbf{k}}^{\dagger} H_{\mathrm{BdG}}(\mathbf{k}) \Psi_{\mathbf{k}} - \epsilon(\mathbf{k}), \tag{4.15}$$

where $\epsilon(\mathbf{k})$ is a diagonal matrix which includes all constant values coming from the decoupling. Note that $H_{\mathrm{BdG}}(\mathbf{k})$ is a 64×64 matrix as each component of the Nambu spinor is an 8-vector yielding eight bands. The structure of this matrix is constructed as follows:

$$H_{\mathrm{BdG}}(\mathbf{k}) = \begin{pmatrix} H_F(\mathbf{k}) & J_2 \otimes \mathbf{1} \otimes \mathrm{diag}(\vec{\Delta_3}) \\ J_2 \otimes \mathbf{1} \otimes \mathrm{diag}(\vec{\Delta_3}) & H_F^*(\mathbf{k}) \end{pmatrix}, \tag{4.16}$$

where $\mathbf{1}$ is the two-dimensional unity matrix, $J_2 = [[0, 1], [1, 0]]$ is the first Pauli matrix, and $\otimes$ denotes the tensor product.

The matrix on the diagonal block has the following structure

$$H_F(\mathbf{k}) = \begin{pmatrix} H^m(\mathbf{k}) & H_R(\mathbf{k}) \\ H_R(\mathbf{k}) & H^m(\mathbf{k}) \end{pmatrix}, \tag{4.17}$$

where the four 16×16 blocks are defined as

$$H^m(\mathbf{k}) = \begin{pmatrix} H_{t\uparrow}^m(\mathbf{k}) - \mu - \frac{n}{3}(\frac{U_1}{2} + \frac{U_2}{2} + \frac{U_3}{2}) & \mathrm{diag}(\vec{\Delta_1}) \\ \mathrm{diag}(\vec{\Delta_1}) & -H_{t\downarrow}^m(-\mathbf{k}) + \mu + \frac{n}{3}(\frac{U_1}{2} + \frac{U_2}{2} + \frac{U_3}{2}) \end{pmatrix}, \tag{4.18}$$

and

$$H_R(\mathbf{k}) = \begin{pmatrix} H_\Omega(\mathbf{k}) & \mathrm{diag}(\vec{\Delta_2}) \\ \mathrm{diag}(\vec{\Delta_2}) & -H_\Omega(-\mathbf{k}) \end{pmatrix}. \tag{4.19}$$

The quadratic matrix $H(\mathbf{k})$ depends on the unknown superconducting order parameters $\vec{\Delta}_i$, which we determine self-consistently by diagonalizing $H(\mathbf{k})$ using random initial guesses of $\vec{\Delta}_i$, and subsequently updating the order parameters by the ones obtained from the diagonalization until convergence is attained. We check that this procedure leads to the same order parameters for different initial guesses, or, if this is not the case, we choose the solution with the lowest grand thermodynamic potential energy.

4.4 Results

In this section we present the original results of the pairing correlations in the system within the framework described above. While we first focus on the case of fully symmetric interactions that naturally arise in the context of the experimental proposal presented in [40], namely U_1=U_2=U_3 (see Fig. 4.1(c)), where all internal degrees of freedom of each atom are coupled to the each others with the same strength, we also study the effects of SU(4) symmetry breaking by considering the relative alteration between interaction channels U_1 and U_2 in the subsequent subsection. In this context, we set $U_3 = 0$ in all the subsequent calculations, which is justified because any pairing in the U_3 channel is strongly suppressed by the strong Raman coupling, Ω. This coupling (inter-layer hopping) energetically penalizes the state with two particles of equal pseudo-spin per site, as compared to the single-particle states formed by the antisymmetric superposition of the states with equal pseudo-spin and opposite pseudo-layer degree of freedom.

A very interesting phase diagram is found in the regime of weak interactions: superconductivity is exponentially suppressed in the symmetric case, i.e. near $U_1 = U_2$, but a significant non-zero SC gap can be again amplified if the interactions are tuned to a sufficiently non-symmetric choice. We observe the narrowing of the weakly-superconducting wedge shaped region in the phase diagram with increasing interaction strength, as well as the coexistence of both the inter and intra-layer superconducting order parameters. Techniques to tune interactions, such as Feshbach resonance or magnetic/optical field gradients [261, 262], allow in experiments for such a selective choice of a dominant interaction channel. Increase of band flattening via the tunable parameter α leads to the development of strong superconducting order for lower values of attractive interactions, in particular, as compared to the standard ($\alpha = 0$) bi-layer Fermi-Hubbard model.

Numerical calculations were performed for a system of 2×256 sites forming

a $2 \times L \times L$ bi-layer square lattice with $L = 16$. The low temperature properties were studied by choosing the temperature to $k_B T = 0.02t$.

4.4.1 Superconductivity in $SU(N)$ symmetric system

We set a strong interlayer (Raman) coupling $\Omega_0/t = 100$ in order to focus on effects in the quasi-flat band regime of our system. We investigate the influence of two main parameters, namely the modulation amplitude α and interaction strength U on the SC characteristics.

The parameter α controls the relative strength of the spatially dependent part of the synthetic hopping $\Omega(\mathbf{r})$ in eq. (**??**). The increase of α primarily results in flattening in the dispersion of the set of quasi-flat bands of our interest. Up to a value of $\alpha \approx 0.67$, the flattened bands lie exactly at Fermi energy of the system for a filling $\nu = 1/4$ (that is, one fermion per physical site). As shown in Fig. 4.1(b), the critical value of $\alpha \approx 0.67$ causes band flipping, which lifts the Fermi energy of the quarter-filled system away from quasi-flat band (see Fig. 4.1(d) and (f)). We focus on the case with $\nu = 1/4$ and $0 \leq \alpha \leq 0.67$. A large superconducting gap opens in the SU(4) symmetric system, for interaction strengths, higher than a certain, α-dependent cut-off interaction amplitude, $U > U_C(\alpha)$. We note that $U_C(\alpha)$ decreases if one considers lower temperatures.

Enhancing the density of states at the Fermi energy by increasing the band flattening through α is expected to lead to larger stability of the superconducting phase and, therefore, lower threshold values $U_C(\alpha)$. Indeed, such behaviour is markedly seen in Fig. 4.2(a,b). For an example value of $\alpha = 0.6$, the superconducting state appears above $U \sim 6.2t$. Similar effect has been observed for the critical temperature of the system with respect to modulation α. Fig. 4.2(c) depicts the growth of the critical temperature with band-flattening. We have limited the range of α in the figure such that it covers only the scenario with Fermi energy matching the energy of quasi-flat bands. Therefore, by tuning the modulation parameter α one can reach superconducting state at lower interaction values as compared to the uniform inter-layer hopping scheme. Moreover, resulting difference in critical temperature between highly modulated system at $\alpha = 0.6$ and un-modulated one is of one order of magnitude. In other words, the superconductivity near U_C is truly induced by the synthetic twist.

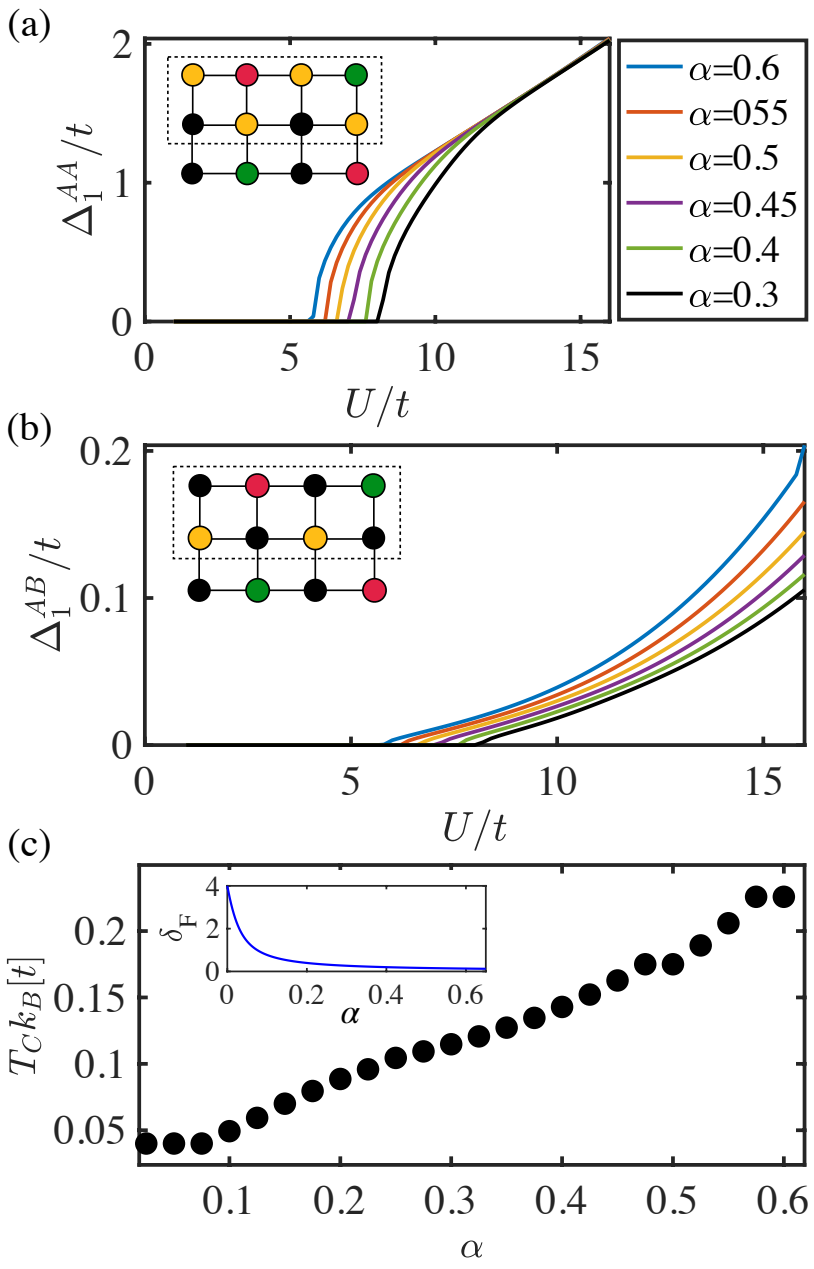

Figure 4.2: (a,b) Expansion of superconducting gaps Δ_1^{AA} and Δ_1^{AB} as a function of the $U = U_1 = U_2 \leq 16t$ under different modulation values α resulting in specific cutoff value U_c (Δ_2 has an identical behavior). (c) Critical temperature dependence on the modulation strength α at $U_{1,2,3} = 16t$. Inset plot represents the energetic width δ_F of the quasi-flat bands as a function of the modulation parameter α.

4.4.2 $SU(4)$ to $SU(2) \times SU(2)$ symmetry breaking

The $SU(N = 4)$ symmetry (spin and magnetic levels) of the system resulting from the internal structure of the atoms forbid the free tuning of the strength of each interaction type individually without an external fields applied. As shown in [263, 261], one can tune the strength of interaction types by applying an external state-dependent force that effectively separates the m_F manifold of the ground state. For atoms with two valence electrons, such as ^{87}Sr, this technique, also termed as, optical Stern-Gerlach (OSG). has already been successfully applied experimentally [263, 261]. Following the scheme of the system proposed in [40, 41], we propose to use OSG to modify the energy gaps between specific m_F states, thereby tuning the interaction strength of desired type. In this paragraph, we study the effects on the superconducting properties due to a modification of the interaction strength in such fashion. We note that the extreme scenario of $U_1 \gg U_2$ corresponds to standard spin-spin onsite only interactions widely explored in the Fermi-Hubbard model. Whereas the $SU(N)$-symmetric scenario requires a threshold value of the coupling U for the system to exhibit superconductivity, the symmetry-broken scenario allows us to observe superconducting pairing even for $U_1, U_2 < U_C$ (with one of them possibly even being zero). Interestingly, a phase where superconductivity is dominated by U_1 is separated from a U_2 dominated superconducting phase through an intermediate phase in which superconductivity g is absent, leading to the interesting re-entrance phenomena, when one of the interaction parameters is tuned.

The different phases are seen in Fig. 4.3 where the superconducting gaps $\Delta_1^{AA,AB}$ are plotted as a function of the interaction strengths U_1 and U_2, in the interval $[1, 6]$ in panels (a) and (b), and in the interval $[0, 2]$ in panels (c) and (d). Here we have chosen $\alpha = 0.$, and the corresponding U_C from the $SU(4)$ symmetric system is $U_C \approx 6$. Hence, the shown regime is below U_C everywhere, and accordingly, the system does not exhibit superconductivity along the line $U_1 = U_2$. It is seen that this non-superconducting regime, plotted in black, has a finite width, which narrows as U_1 and U_2 approach towards U_C. The width and the rate of the narrowing depends on the modulation parameter α, as indicated in the Fig. 4.4. Nevertheless, relatively small deviations from the symmetric interaction are already sufficient to open a superconducting gap. This can be understood in the following way: the superconducting pairing of each interaction type compete with each other, but breaking the symmetry favors one interaction type with respect to the other, and therefore facilitates the pairing in this channel. Although one of

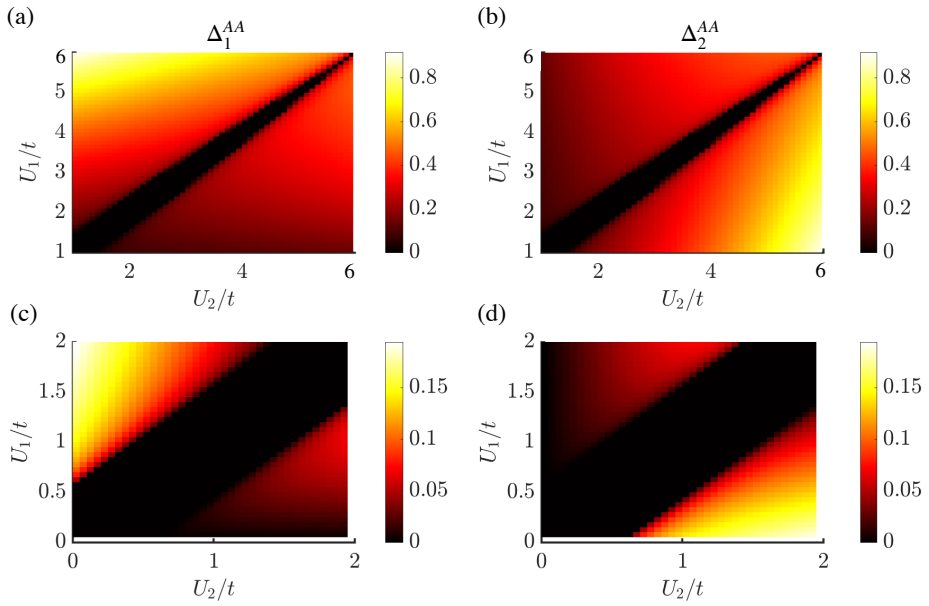

Figure 4.3: Superconducting order parameter Δ_1^{AA} (panel a and c) and Δ_2^{AA} (panel b and d) as functions of relative amplitude of U_1 and U_2 interactions at $\alpha = 0.67$. Existence of superconducting phase in this $SU(4)$ symmetric system is not present until $U = U_1 = U_2$ reaches a cut-off value U_c, at which the non-superconducting valley narrows to zero. The width of the valley as well as the critical interaction strength depends on the modulation parameter α (as shown on the Fig. 4.2). Panels (c) and (d) represent the regime of small interaction strengths that are not covered on the panels (a) and (b) due to limited colormap resolution. Sites of (AB) type reveal qualitatively identical behavior, however, with much smaller pairing amplitude (See Fig.4.4(b))

.

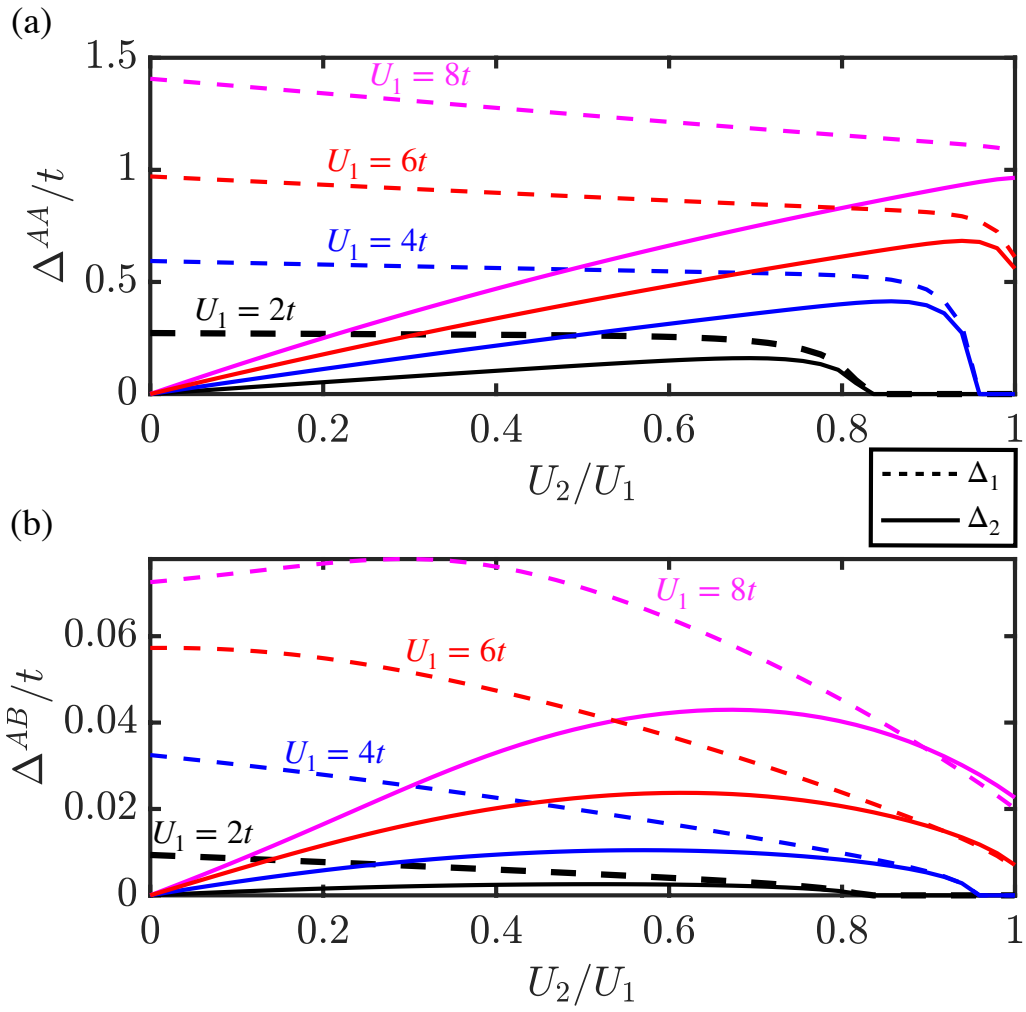

Figure 4.4: $\Delta_{AA,AB}$ (dashed) and Δ_2 (solid) as functions of U_2 (in units of U_1) for four different values of U_1 at modulation strength $\alpha = 0.67$. One can observe the shift of the superconducting gap decay towards $U_2/U_1 = 1$ with the increase of interaction strength. For $U_1 = 6t$, the decay of superconducting gap occurs at $U_2/U_1 = 1$ marking the U_C for this particular value of α.

the two different pairing channels becomes dominant, there is still coexistence of the superconducting gaps corresponding to the two channels, U_1 and U_2, for most parameter choices (unless we are in the non-superconducting regime, or one of the

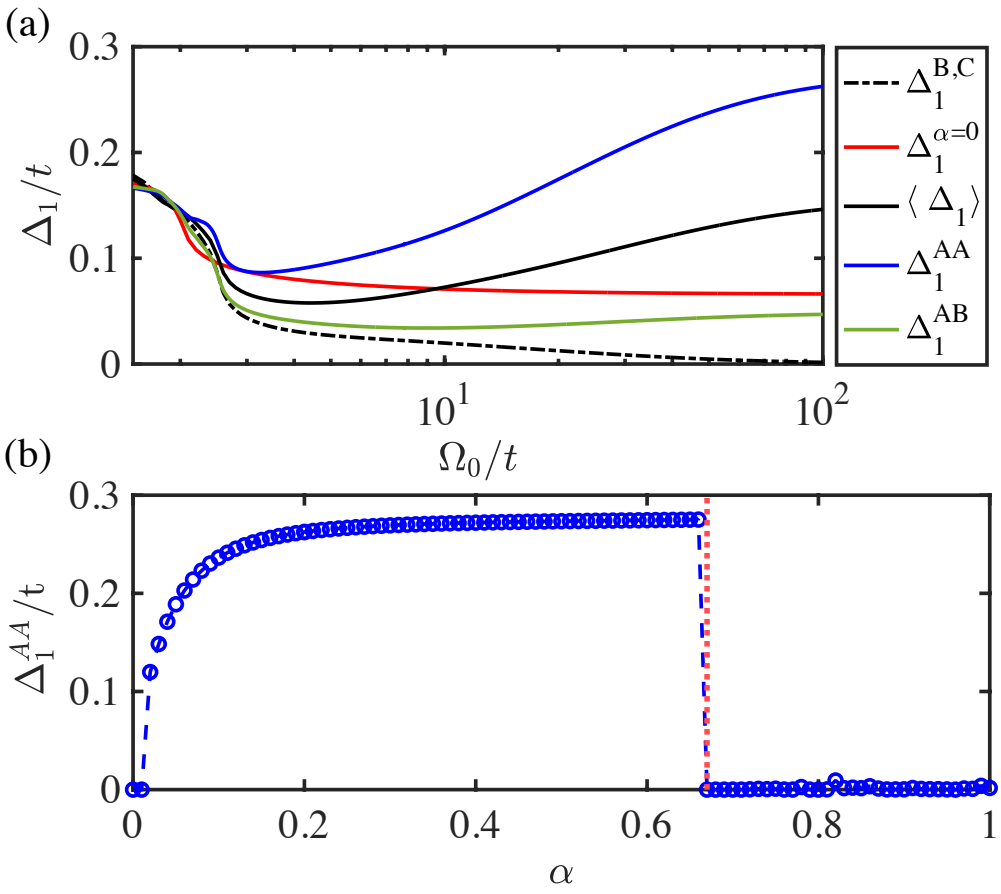

Figure 4.5: Superconducting gap in the system of $U_1 = 2t$ and $U_1 \gg U_2$. (a) The order parameter Δ_1 associated with interaction type U_1 as a function of the inter-layer hopping strength Ω_0 at $\alpha = 0.2$. We have set $U_2 = 0$ as its presence weakens the order parameter Δ_1, as shown on Fig. 4.4(b). The green line represents the situation where the $\Omega(\mathbf{r})$ is homogeneous, i.e. $\alpha = 0$. The separate plot for Δ_C has been omitted since it's behaviour is identical to Δ_B, which has been plotted. (b) Dependence of the order parameter Δ_1^{AA} on the modulation strength α for $\Omega_0 = 100t$. We have omitted the plot of Δ_1^{AB} due to its negligible amplitude. Sudden drop of pairing (marked by dashed grey line) occurs around critical value of $\alpha \approx 2/3$ at which the Fermi level does not reside at quasi-flat bands any more. Such situation has been shown on Fig. 4.1(f).

interaction parameters is zero). However, monotonicity of the size of the gap with respect to the interaction strength is not obvious. We present a closer insight to this phenomenon through the details presented in Fig. 4.4. It depicts the dependence of the superconducting order parameters on U_2 for four different values of U_1 at $\alpha = 0.67$. The decay of Δ_1^{AA} and Δ_2^{AA} as U_2 approaches $U_1 = U_2$ is the beginning of the zero-gap valley. With increasing value of U_2 the corresponding gap Δ_2^{AA} opens and keeps increasing until reaching its maximum value. In parallel, superconducting order parameter corresponding to U_1 constantly decreases.

We now consider the cases of $U_1 \gg U_2$ which can be obtained experimentally with help of OSG techniques. We would like to note that the same results have been obtained for the opposite case, i.e. $U_2 \gg U_1$. This scenario qualitatively agrees with the standard bi-layer Fermi-Hubbard model with only in-plane interactions typically considered as good approximations to describe various phenomena in condensed matter physics. Note, that in this chapter we are not aiming at direct comparison with real solid state systems. In contrast, our focus here is on a non-standard choice of parameters ($\Omega \gg t$) as it gives us access to study the effect of a flat band structure even in relatively small Moiré supercells. Such regime of parameters is accessible in cold atomic systems. We choose this regime in order to obtain a maximum possible value of the gap for a given amplitude of U. As it has been shown on the Fig. 4.4, the widest gap appears for highly unequal interaction values, i.e. $U_1 \gg U_2$. We begin by investigating the dependence on the synthetic hopping amplitude, Ω_0. In its absence the system consists of two uncoupled layers of square lattices. At finite Ω_0, we can flatten the bands through the spatial modulation provided by α, or realize the standard bi-layer model, i.e. $\alpha = 0$. Panel (a) of Fig. 4.5 depicts both of these scenarios. In particular, we have plotted separately the gap for A-type and (B,C) sites in α-modulated case, as well as the mean value of the gap averaged over all sites of the unit cell. The green line represents the size of the gap for a standard bi-layer model, that is, with $\alpha = 0$. Interestingly, with a small separation of the spectrum caused by inter-layer hopping, superconducting gaps drop. However, after a full separation of the bands into positive and negative branches, the system the size of the gap of the quasi-flat band system starts to grow, in contrast to the superconducting order parameter of the standard FH system. Panel (b) of Fig. 4.5 represent the dependence of the order parameter Δ_1 on the modulation parameter α. The plot depicts the situation where $\Omega_0/t = 100$ and therefore $\Delta_1^{B,C}$ can be neglected due to their vanishing values. The amplitudes of Δ_1 in panel (b) have been obtained for the fixed filling $n = 1/4$. Summarizing, modulation of the inter-layer hopping leads

to enhanced superconducting order parameter with respect to a non-modulated one at sufficiently high Ω_0. This effect is a result of band flattening and therefore disappears once the modulation α crosses the critical value or the Fermi energy does not match the energy of quasi-flat bands.

4.5 Conclusions

In this chapter, we have used Bogoliubov-deGennes theory to study attractive interactions of the synthetic bi-layer square lattice system. The studied model goes beyond the thoroughly explored bi-layer Hubbard models and tackles correlated phases in quasi-flat band systems emerging from the periodic modulation of inter-layer hopping. We have taken into account all possible density-density on-site interaction channels and considered properties across a wide range of experimentally accessible interaction strengths. Our system has a small Moiré unit cell for which flat band induced effects occur for large inter-layer hopping strengths. We note that similar small Moire unit cells generated at large twist angles in physical bi-layers would also require rather large inter-layer hopping to isolate the flat band regime. This could in principle be achieved by applying strong strain or pressure in the direction perpendicular to the plane of the layers in materials. However, it might be rather more easily achieved in our synthetic system where the inter-layer hopping is controlled simply by the intensity of a Raman laser coupling the internal levels that play the role of the layer degrees of freedom.

First, we have focused on the natural case of equal interaction amplitudes and observed strong dependence between the inter-layer modulation parameter α and minimal interaction strength U_C required to reach superconducting pairing at a fixed low temperature. Observed results confirm the following:

(1) Flattening of the bands in the vicinity of Fermi energy leads to opening of the superconducting gap at much lower interaction amplitudes, when compared to more dispersive systems.

(2) Band flattening causes the critical temperature scale to significantly increase in these novel synthetic-twist-induced lattices with magic configurations and thus superconductivity (paired neutral fermion superfluidity) may be potentially observable in state-of-the-art cold gas experiments.
Further results are obtained by altering relative interaction amplitudes in the system:

(3) The resulting phase diagram revealed a valley around $U_1 = U_2$ with strongly suppressed superconducting correlations. The width of this valley narrows with the growing amplitude of interactions to finally completely vanish at U_c specific for each value of α. Similar behaviour has been observed in bi-layer Hubbard square lattices with only one correlated layer [264]. There, the apparent re-entrance of the superconducting gap was a result of increasing inter-layer hopping. Here, however, we observe similar effects as a function of inter-layer interactions for large inter-layer hopping.

While the results discussed in this chapter help to form a general understanding of the effects of band flattening on superconductivity in the synthetically twisted materials, further studies can be be pursued in future, particularly, in context of topologically nontrivial bands with relatively weak dispersion, which can be obtained via more involved, but experimentally viable, means e.g., via imaginary next-to-nearest neighbor tunnelings driving the system into a quantum anomalous Hall phase [41]. In such cases, Wannier functions with algebraically decaying tails may originate from nonzero Chern number [265]. Novel understandings of the correlated phenomenon could then be obtained via incorporation of new mechanisms, such as correlated tunnelings in extended Hubbard bi-layer systems.

Chapter 5

Quantum batteries as quantum simulators

So far we have only considered the potential ability of quantum simulators to serve as a platform for analysis and generation of many-body quantum systems with high precision and control. We have argued their possible application in design of new 2D materials. Quantum simulation has, however, the second name: Special purpose quantum computer, that distinguish this approach from the universal quantum computer. Special purpose means that such a machine can perform only pre-programmed set of unitaries realizing only one algorithm. Such a scheme vastly simplifies the complexity of the hardware as well as error correction with a cost of generality.

One of the "perfect" examples of quantum simulators as special purpose quantum computers are quantum batteries. They are a result of growing interest in the study of the advantages that quantum effects could bring into the problem of energy storage [266, 267, 268, 269, 270, 271, 272, 273, 274]. This interest has been stimulated not only by scientific curiosity, but mainly as a result of the rapid growth of renewable energies, which in turn has boosted the urgency for better energy storage devices. The reasons for storing energy are two-fold. First, while energy disposal is aimed to be at will, renewable sources produce energy discontinuously, e. g. solar panels do not generate energy at night. Second, in many cases, the power provided by such sources is not enough to perform some highly consuming tasks, like running a car.

Every battery, be it classical or quantum, can be characterized by two main quantities.

The first one is the maximal amount of energy E the battery can store, called capacity. The second one is the rate(units of energy per unit of time) at which the battery can be charged and discharged, called the power of the battery, P. Charging and discharging are the two main processes of a battery. While discharging process is dependent on the external device using the energy stored in the battery, power of charging remains one of the biggest bottlenecks in their industrial development.

The field of quantum batteries is more that 10 years old, but it gained more attention in 2018, when [267] has shown the potential exponential speed-up in charging power due to global unitaries. Since then the research in this area has intensified with many seminal publications[271] and the first experimental realizations. The concept of quantum battery, principles of operations, relevant quantities, definitions and figures of merit will be explained in the following chapter. It is only slightly modified version of the original article [44], which the author of this thesis has coauthored. The chapter presents the fundamental bounds on both capacity and power of quantum batteries, that are tighter than the ones resulting from quantum speed limits. The article was written in a very didactic manner therefore is presented in this thesis in rather unchanged form.

Figure 5.1: batteries are often made-up of classical ingredients, be it chemical or cell-based, and are primary devices, where energy E can be remotely stored and accessed via charging H_C or discharging operations. Quantum battery has the same properties as classical battery. However, its charging protocols (processes) provide high-control evolution of the initial state ρ_0. The potential gains and effects of such evolutions, as well as different types and classes of charging processes are the essence of this chapter.

5.1 What are quantum batteries?

Quantum batteries are intrinsically quantum devices made of quantum-cells that can interact, and thus exploit collective quantum properties, in order to perform the task of energy storage. The study in [266], for the first time, suggested that quantum entanglement can boost the extractable stored energy from an ensemble of quantum batteries. Later, it was shown that quantum entanglement is not absolutely necessary to increase the extractable energy, and classical correlations are enough [275]. Also, the presence of correlations, in the initial and final state of a quantum battery, is detrimental to its storage capacity.

On the contrary, when looking at the power of a quantum battery, i.e., the rate at which energy can be stored or extracted, quantum correlations in the intermediate states can lead to an enhancement, usually denoted as a quantum speed up. In this line, the correspondence between quantum entanglement and the power of a quantum battery has led to many interesting studies, see for example [267, 268, 269, 270, 271, 272, 273, 274]. The role of *non-local* charging process has been studied theoretically in [267, 268], and for experimentally realizable quantum batteries in [269, 270]. More precisely, one of the features that has been explored is the achievement of a super-linear rate of charging by means of collective quantum effects. In these cases, for a battery with N quantum-cells, the total power would scale as $N\sqrt{N}$, instead of (linear) N. One trivially gets the linear scaling in the case of independent charging of the quantum-cells. A review on the recent progress can be found in [276].

In this chapter, we deem to consider all these important aspects to characterize a quantum battery, adhering to the traditional definitions of the stored energy and the power. We study the capacity of a quantum battery, i.e., a bound on the storable (extractable) energy, under entropy-preserving processes. Notice that the scenario of an entropy-constrained capacity was introduced in [277] for the study of work extraction in finite quantum systems. Here, we extend these results for the study of quantum batteries. In particular, we introduce the energy-entropy diagram for quantum states, and we show its usefulness to visualize both the limitations on extractable and storable work. We also emphasize that many of the previous works about quantum batteries assume only the expectation value of the battery Hamiltonian, i.e., the first moment. However, we know that this expectation value does not always imply accessible energy, as a non-vanishing variance implies lower usability of that energy [278]. Therefore, it is important to study higher moments of the energy, in order to properly characterize a quantum battery.

In the case of power, one of the main results is a bound on the rate at which

energy can be deposited (extracted) in a quantum battery in a charging (discharging) process, obtained by means of a quantum geometrical approach. It is valid for arbitrary charging (discharging) processes. The bound is derived in terms of the energy variance of the battery and the *Fisher information* (or speed of evolution) in the eigenspace of the battery Hamiltonian (denoted as I_E). On the one hand, the energy variance of the battery can be related to non-local properties of its quantum state, hence connecting entanglement and power. In the case of qubit-based batteries, this connection leads to another central result of this chapter, that is, a mathematical inequality bounding the power by the amount of entanglement generated between the cells. On the other hand, I_E signifies the rate of change of the battery state in the energy eigenspace. This gives a better bound on power compared to the case in which one considers the traditional speed of evolution of the battery state in Hilbert space (i.e., the *quantum Fisher Information*, I_Q). The reason is related to the fact that there can exist initial and final time-evolved states that are infinitesimal close (or identical) in energy, but orthogonal (and thus perfectly distinguishable) in Hilbert space. The speed of evolution in Hilbert space would then be non-zero, while power would be zero. Therefore, when studying power, it is necessary to consider a speed of evolution based on a notion of distinguishability between states that is directly connected to the difference in their energetic distributions.

Furthermore, we use the derived bounds for the storable energy and the power to systematically analyze the paradigmatic cases that are often studied the literature, and also more realistic models of quantum batteries, that include integrable spins chains, and two models based on the LMG and the Dicke Hamiltonian. For such a study, we restrict to charging processes in which the battery is initially in a pure quantum state. This leads to an entropy-free capacity given simply by the difference between the ground state and the highest-excited energies of the battery Hamiltonian. We then analyse which portion of this capacity is stored in the battery due to the charging dynamics, and its scaling with the number of cells N. In the case of power, we also analyze the saturation of the bound in terms of the quantities appearing in it and their scaling with N.

The main results for this part are the saturation of our bounds in the paradigmatic cases, the unveil of the role of entanglement in the power of all these models, and the challenging of the appearance of a quantum speed up in the realistic models that we consider.

The article is organized as follows. In section 5.2, we outline the important properties of a quantum battery. Section 5.3 gives the expression for capacity exploiting the energy-entropy diagram. In section 5.4, a bound on the power

of a generic battery is derived, in terms of the energy variance and the Fisher information in energy eigenspace. In the case of qubit-based quantum batteries, we introduce a bound on power in terms of the k-qubit entanglement of the battery state. Section 5.5 outlines paradigmatic spin-$\frac{1}{2}$(qubit) models that saturate the derived bounds. We study various realistic models in light of these bounds in section 5.6. Finally, we dedicate section 5.9 for conclusions.

5.2 Quantum Batteries and their properties

In this section, we make a brief outline of the properties that one needs to consider to make an assessment of a good battery. A quantum battery is a physical system, where energy can be stored for a relatively long time and extracted whenever it is convenient. It is modeled by a Hamiltonian H_B, so that its internal energy, which depends on its state ρ, is given by

$$E(\rho) \coloneqq \mathrm{Tr}(\rho H_B)\,. \tag{5.1}$$

In order to give a further insight into the problem, in this chapterwe assume that a battery is composed of independent non-interacting quantum-cells, with the Hamiltonian

$$H_B = \sum_{j=0}^{N-1} h_j, \tag{5.2}$$

where h_j is the Hamiltonian of the j-th quantum-cell, and N is the total number of them. Notice that the form of the battery Hamiltonian in Eq. (5.2) implies that we are considering an additive nature of the battery stored energy, i.e., the total energy is obtained as the sum of individual energies stored in each battery cell.

The process of charging (or discharging) a battery is a physical process Γ_t that leads to the battery state $\rho(t) \coloneqq \Gamma_t(\rho(t_0))$ at each instant of time t. The main features that we study in this chapter are the following.

Stored and extracted energy – For a given dynamical charging (discharging) process Γ_t of a quantum battery, that is initally in the state $\rho(t_0) \coloneqq \rho_0$, the stored (extracted) energy $E^s_{\rho_0}$ ($E^e_{\rho_0}$) is the maximum amount of energy that the battery absorbs (delivers). They are defined by

$$\begin{aligned} E^s_{\rho_0}[\Gamma_t] &\coloneqq \max_t E\left(\rho(t)\right) - E\left(\rho_0\right), \\ E^e_{\rho_0}[\Gamma_t] &\coloneqq E\left(\rho_0\right) - \min_t E\left(\rho(t)\right). \end{aligned} \tag{5.3}$$

Notice that, in the above definitions, the energies are a functional of the process, and the initial battery state (i.e., we do not assume that the battery is initially fully empty nor charged). Instead, we are interested in the energy change of the battery given an arbitrary initial state and a dynamical process Γ_t, belonging to a certain set $\mathcal{S}$ of control operations. Within this set, we also define the capacity $C_{\mathcal{S}}$ of the battery as its energetic amplitude, that is

$$C_{\mathcal{S}} \coloneqq \max_{\Gamma_t \in \mathcal{S}} E^s_{\rho_0}[\Gamma_t] + \max_{\Gamma_t \in \mathcal{S}} E^e_{\rho_0}[\Gamma_t]. \tag{5.4}$$

In the present chapter, we will mainly focus in entropy-preserving operations, which can be connected to unitary operations for linear maps or in the many-copy limit, as discussed in Sec. 5.3. Notice then, that the capacity $C_{\mathcal{S}}$ will depend on the initial state ρ_0 trough the initial entropy $S(\rho_0)$. Physically, this means that, while given a battery hamiltonian H_B the ideal capacity is trivially the difference between the groundstate and maximally excited state, one may not be able to bring the battery in an exact pure state, thus reducing the effective capacity under entropy-preserving/unitary operations [277].

The choice of this set of control operations is motivated by the fact that batteries are not engines that convert heat into work. Instead, they are supposed to operate in isolation from the environment and store or supply energy when demand arises. Also notice that within entropy-preserving operartions the stored energy, as defined in Eq. (5.3), coincides with the (thermodynamical) work [279]. If we go beyond this assumption, we have to consider work injection instead of internal energy, as they migh not coincide. In this context, notice that recent works directly addressed the issue of non-unitary processes by considering dissipative charging protocols [273, 274] or the impact of correlations in the extractable work from the battery [271]. It is also important the fact that even when restricting to entropy-preserving or unitary operations, we only consider the first moment of the Hamiltonian. However, a non-zero variance in the stored energy worsens its deterministic extraction, as in a discharging process it might not be possible to exactly reverse the time evolution generated during the charging.

In this chapter, we will not take this variance into account to derive our bound for storage. The reason is that for a large number of cells N the energy variance (second moment) typically scales as $1/\sqrt{N}$, and thus vanishes in the thermodynamic limit. On the contrary, we will analyze the impact of this variance when studying the charging processes of different particular models of a quantum battery. An enhanced energy variance in the battery may appear during the time evolution. In these cases, it is important to see what percentage of it remains in the final state,

and how does it decay in the large N limit.

Power – How quickly a battery can be charged (or discharged) depends on its power. It is quantified by the rate of energy flow in the battery during charging (or discharging), that is

$$P(t) \coloneqq \frac{\mathrm{d}}{\mathrm{d}t} E\left(\rho(t)\right) . \tag{5.5}$$

Notice that as in the capacity definiton, the above definition of Power coincides with the rate of Work injection only in the case of entropy-preserving transformations of the battery state, that is when we considered an input of energy in an isolated system, without heat exchange. This is also equivalent to an adiabatic process where the system undergoes a transformation without an interaction with the environment. For a given charging process of a duration $\Delta t = t_f - t_0$, the *average power* will be

$$\langle P \rangle_{\Delta t} = \frac{E(\rho(t_f)) - E(\rho(t_0))}{\Delta t} . \tag{5.6}$$

From a geometric point of view, there are two relevant properties when studying how fast a charging process can evolve a battery state from $\rho(t_0)$ to $\rho(t_f)$. Within a notion of distance (distinguishability) between quantum states, the amount of time spent in the process is affected by both the rate at which the battery state ρ changes during the time interval Δt (speed of state evolution), and how smart is the path taken, in terms of the total length (trajectory of evolution). These two aspects are illustrated in Fig. 5.2. Notice that the concepts of speed and trajectory of evolution are highly dependent on the definition of distinguishability between battery states. For instance, if one considers distinguishability of states in Hilbert space, an initial state could evolve to a perfectly distinguishable final state, but with the same energy distribution as the initial one. In this case, the speed of evolution would be non-zero, without a change in the energetic properties of the state. Instead, in this chapter we use the concept of distinguishability in the eigenspace of the battery Hamiltonian and define the speed of evolution accordingly.

In the following, we aim to understand the limits that quantum mechanics imposes on the storage, the power, and energy variance of any energy storage device. More specifically, we are interested in understanding how these quantities scale with the number of cells N. In doing so, we restrict ourselves to entropy-preserving evolutions to perform charging and discharging processes on the batteries.

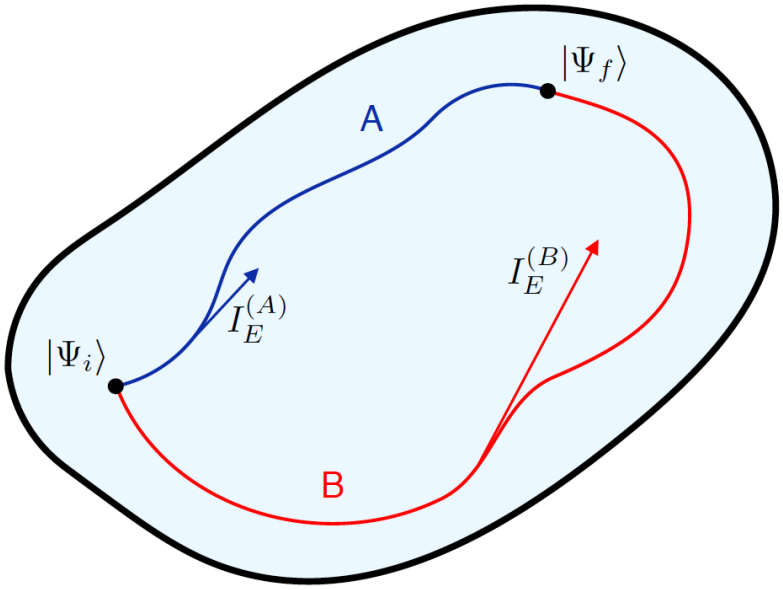

Figure 5.2: Schematic of a charging (discharging) process in the quantum state space. The trajectories represent two different charging processes A (blue) and B (red) in which the initial and final states ($|\Psi_i\rangle$ and $|\Psi_f\rangle$ respectively) coincide. The process A undergoes a path with path length L_A at a speed $I_E^{(A)}$. Similarly, the process B traverses the path length L_B and the speed $I_E^{(B)}$. The time required (t_A and t_B for the two processes) to reach to the final state, from the initial one, depends both on the path length and the speed. For instance, the charging process requires shorter time, i.e. $t_A < t_B$, although the speed of the process B is larger, $I_E^{(A)} < I_E^{(B)}$. This is because path length of B is also larger, $L_A < L_B$.

5.3 Bounds on the stored and extracted energies

Here we study the capacity of a battery, given by the maximum amount of energy that it can store or that can be extracted from it. We restrict our analysis to entropy-preserving processes, which reduce to unitary operations in the case of linear maps acting on a single copy of a state [280]. In the many-copy scenario, entropy-preserving operations are understood as effective local operations generated by a global unitary acting on asymptotically many copies of the system [281, 279] and a small ancilla η. That is, for any two states ρ and σ with equal entropies, $S(\rho) = S(\sigma)$, (here we consider the von Neumann entropy $S(\rho) = -\operatorname{tr}\rho\log\rho$) there exists an additional ancilla system of $O(\sqrt{N\log N})$ qubits and a global unitary U such

that

$$\lim_{N\to\infty} \| \mathrm{tr}_{\mathrm{anc}} \left(U\rho^{\otimes N} \otimes \eta U^{\dagger} \right) - \sigma^{\otimes N} \|_1 = 0 \,, \tag{5.7}$$

where the partial trace is performed over the ancillary qubits and $\|\cdot\|_1$ is one-norm. In the finite case, where one cannot apply the limit appearing in Eq. (5.7), we will also discuss how the operational interpretation of our analysis changes.

5.3.1 Energy-entropy diagram

In order to understand the limitations on the energy that a system can store, it is useful to introduce the *energy-entropy diagram*, as depicted in Fig. 5.3. Given a system described by a time-independent Hamiltonian H, a state ρ is represented in the energy-entropy diagram by a point with coordinates $x_\rho := (E(\rho), S(\rho))$ (see Fig. 5.3). All physical states reside in a region that is lower bounded by the horizontal axis (i.e., $S = 0$) corresponding to the pure states, and upper bounded by the convex curve $(E(\beta),\ S(\beta))$ which represents the thermal states of both positive and negative temperatures. Let us denote such a curve as the thermal boundary. The inverse temperature associated with one point of the thermal boundary is given by the slope of the tangent line in such a point, since

$$\frac{\mathrm{d}S(\beta)}{\mathrm{d}E(\beta)} = \beta \,. \tag{5.8}$$

Notice that here a thermal state with negative β corresponds to the case of population inversion, that is, the probability of finding the system in a given energy eigenstate increases with increasing energy.

Note also that a point $x_\rho := (E(\rho),\ S(\rho))$ of the energy-entropy diagram corresponds in general to several quantum states since, given a Hamilonian, there are several states with equal energies and entropies.

5.3.2 Capacity under entropy-preserving operations

Now, with the energy-entropy diagram, we derive the capacity $C(S)$ of a quantum battery. A dynamical process that changes either the energy or the entropy of a system is represented as a trajectory in the energy-entropy diagram. As we are restricted to charging (discharging) processes that are entropy-preserving, the trajectories of such a processes will be horizontal lines in the diagram, see Fig. 5.3.

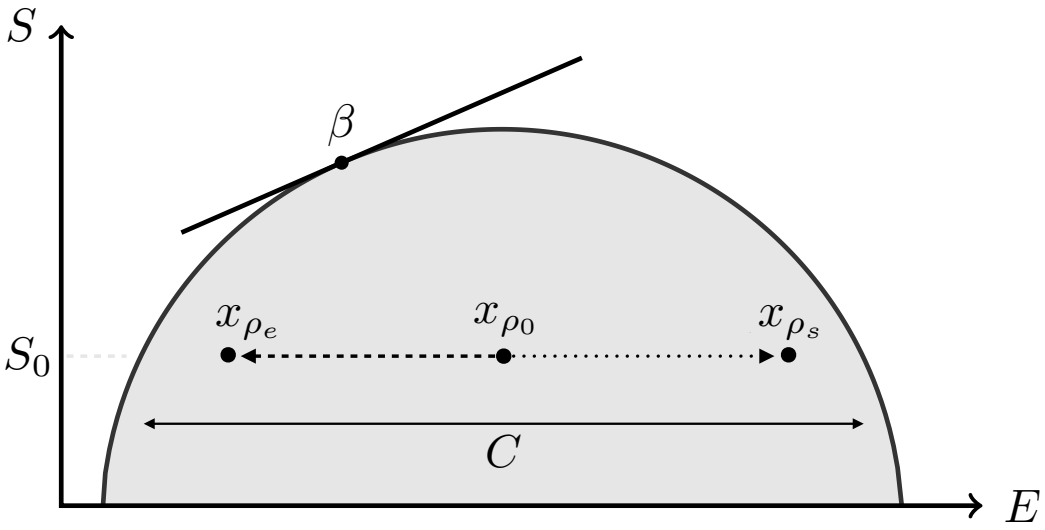

Figure 5.3: Energy-entropy diagram. Any quantum state ρ is represented in the diagram as a point with coordinates $x_\rho := (E(\rho), S(\rho))$. The point in the thermal boundary with slope β corresponds to the thermal state with inverse temprature β. The trajectory of a charging (discharging) process is represented with a dotted (dashed) line. They connect, respectively, the initial state ρ_0, with entropy S_0, and the final state ρ_s (ρ_e). The capacity C corresponds to the energetic amplitude at a given entropy.

Observation 1 (Capacity)**.** *Consider an initial battery state ρ_0 and a dynamical process Γ_t, within the set of entropy-preserving maps. The stored and extracted energies are upper bounded by*

$$\begin{aligned} E^s_{\rho_0}[\Gamma_t] &\leqslant E_{\max}(S(\rho_0)) - E(\rho_0), \\ E^e_{\rho_0}[\Gamma_t] &\leqslant E(\rho_0) - E_{\min}(S(\rho_0)). \end{aligned} \tag{5.9}$$

If we only fix the initial entropy S_0, there is a unique bound given by addition of the two above:

$$E^s_{\rho_0}[\Gamma_t] + E^e_{\rho_0}[\Gamma_t] \leqslant C(S_0) \tag{5.10}$$

where $C(S)$ is the entropy-dependent capacity of the battery

$$C(S) = E_{\max}(S) - E_{\min}(S), \tag{5.11}$$

with

$$E_{\min\,/\,\max}(S) \coloneqq \min_{\sigma:\, S(\sigma)=S} \Big/ \max_{\sigma:\, S(\sigma)=S} E(\sigma)\,. \tag{5.12}$$

Here the minimization/maximization is made over all states with entropy S. Note that the minimum/maximum in (5.12) *is achieved by thermal states with positive/negative β also called completely-passive/completely-active states [282].*

Proof. The proof is straightforward from the energy-entropy diagram and the fact that the processes are entropy-preserving. □

A first insight from the energy-entropy diagram is that inter-system correlations are not needed in order to saturate the optimal capacity of a battery. The two states that respectively minimize and maximize the energy given an entropy lie in the thermal boundary and are therefore thermal states. As thermal states of non-interacting Hamiltonians between different cells are product states, classical or quantum correlations do not provide an advantage in saturating the capacity bound.

Let us finally discuss the operational interpretation of the bounds (5.9). In the many-copy limit, for a fixed Hamiltonian and a given initial entropy, the completely-passive and completely-active states, corresponding to $E_{\min}$ and $E_{\max}$, are always reachable with the help of a small ancilla and a global unitary operation. However, this statement is not always true in the few-copy case, where unitary operations represent only a subset of entropy-preserving ones. In this latter case, even though the bounds (5.9) are still respected, it will not always be possible to saturate them when the set of control operations is limited to unitary operations [283].

5.4 Bound on power

In this section, we derive the bound on power, following geometric approaches towards quantum speed and trajectories. Although our discussion is focused on the problem of energy storage, our bound can also be applied to any other observable O, when the main goal is to increase its expectation value $\langle O(t)\rangle$ as fast as possible.

5.4.1 Speed of evolution in state space and energy eigenspace

We start by introducing a notion of distance between states in Hilbert space. At this point we deem appropriate to mention that many of the concepts that will appear in this section appear naturally in the framework of Quantum Speed Limits (QSL) (for a review, see [284]). However, here we will use them in the form crafted for the study of energy storage. Let us consider the *Bures angular distance* [285], between two quantum states ρ and σ, defined as

$$D_Q(\rho,\sigma) = \arccos\left[F(\rho,\sigma)\right], \tag{5.13}$$

where $F(\rho,\sigma) = \mathrm{tr}\left(\sqrt{\sqrt{\rho}\sigma\sqrt{\rho}}\right)$ is the Uhlmann's fidelity [286]. Now, for an evolution of a system $\rho(t) \to \rho(t+dt)$, the instantaneous speed in state space is defined as

$$v(t) \coloneqq \lim_{\delta t\to 0} \frac{D(\rho(t+\delta t),\rho(t))}{\delta t}. \tag{5.14}$$

After a straightforward calculation (see, for example, [284]), it can be rewritten as

$$v(t) = \frac{1}{2}\sqrt{I_Q(\rho(t))}, \tag{5.15}$$

where $I_Q(\rho(t))$ is the *quantum Fisher information* (QFI). For any quantum state $\rho(t) = \sum_i p_i |i\rangle\langle i|$, which is undergoing a unitary evolution driven by a Hamiltonian $H(t)$, the QFI is given by

$$I_Q(\rho(t)) = \sum_{i\neq j} \frac{(p_i - p_j)^2}{p_i + p_j} |\langle i|H(t)|j\rangle|^2. \tag{5.16}$$

The QFI, in information theory, has the interpretation of an information measure [287]. In fact, the $I_Q(\rho(t))dt^2$ quantifies the distance between states $\rho(t)$ and $\rho(t+dt)$ that are separated by an infinitesimal time dt and driven by the Hamiltonian $H(t)$. In the context of quantum metrology, a higher value of QFI indicates a

potential to result in a higher precision estimation of a parameter. For instance, $\mathcal{I}_Q(\rho(\theta)) = 0$ implies that any information about the parameter θ cannot be extracted, whereas divergent $\mathcal{I}_Q(\rho(\theta)) \to \infty$ means estimation of the parameter θ with infinite precision. We refer to the Ref. [288] for a review in the context of Quantum Information and Quantum Optics, respectively.

For the case of pure states, the Bures distance reduces to the Fubini-Study distance, which is given by

$$D(\psi, \phi) \coloneqq \arccos |\langle \phi | \psi \rangle| \,. \tag{5.17}$$

Then, the corresponding speed, for the case of a unitary time evolution driven by a Hamiltonian $H_C(t)$, becomes

$$v(t) = \sqrt{\langle \psi(t)|H_C(t)^2|\psi(t)\rangle - \langle \psi(t)|H_C(t)|\psi(t)\rangle^2} =: \Delta H_C(t) \,. \tag{5.18}$$

Hence, for pure states, the speed of the system in the Hilbert space is given by the instantaneous energy variance measured by the charging Hamiltonian $H_C(t)$ that drives the evolution of the system. Note that, in the case of a time-independent charging Hamiltonian, the energy variance does not change during the entire evolution. Once we have a notion of speed, the length of the trajectory followed for a time t_F is given by

$$L[\rho(t), t_F] = \int_0^{t_F} \mathrm{d}t \; v(t) \,. \tag{5.19}$$

When considering the Bures angle as a measure of distance, we are looking at the physical distinguishability of the system. However, when looking at systems as quantum batteries, i.e., energy storage devices, we are not interested in how fast the state changes, but in how fast its energy distribution evolves. In other words, there are orthogonal states (perfectly distinguishable) that have identical energy distributions. Thereby, although the system can be moving very fast in the state space, its change in the energy content can be negligible. From this perspective, it is useful to introduce a measure of distance between quantum states not based on their statistical distinguishability, but in their energetic distinguishability (see Fig. 5.4). To do so, let us write the battery Hamiltonian in its spectral representation

$$H_B = \sum_k E_k P_k \,, \tag{5.20}$$

where P_k is the projector onto the eigenspace associated to the eigenvalue E_k. The energy distribution of a state ρ is given by the populations

$$p_k \coloneqq \mathrm{Tr}\,(P_k \rho) \,. \tag{5.21}$$

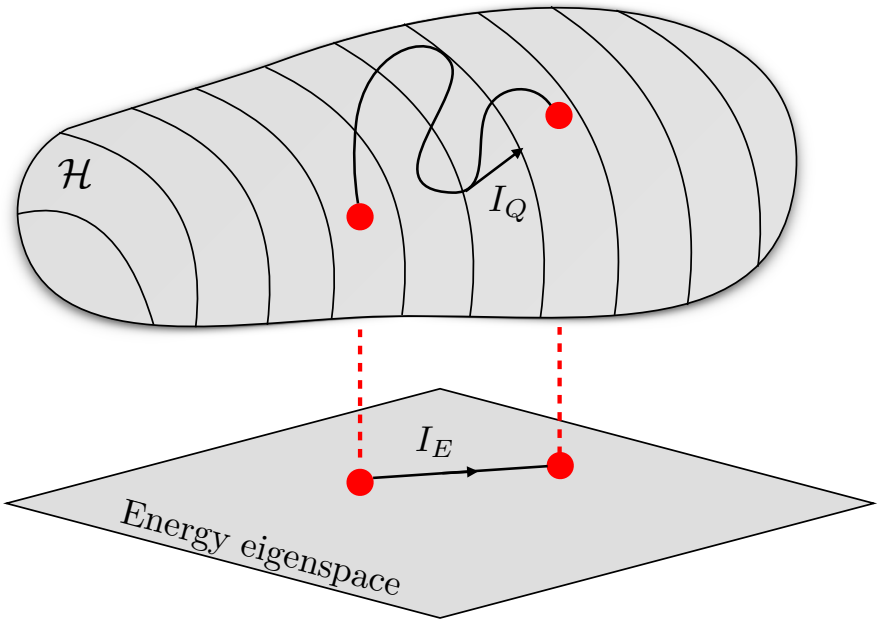

Figure 5.4: A schematic representation of speed of quantum evolution in Hilbert space (I_Q) and the speed of evolution in the energy eigenspace of the battery Hamiltonian (I_E). Notice that, in general, $I_Q \geqslant I_E$.

The speed in the energy space can then be defined as the relative entropy distance between the energy distributions in two consecutive moments of time

$$v_E(t) \coloneqq \lim_{\delta t \to 0} \frac{D_{KL}(\vec{p}(t+\delta t)\|\vec{p}(t))^{1/2}}{\delta t}\,, \tag{5.22}$$

where $D_{KL}(\vec{p},\vec{q})$ is the relative entropy or Kullback-Leibler divergence [285] between two discrete probability distributions $\vec{p}$ and $\vec{q}$. It is defined by

$$D_{KL}(\vec{p}\|\vec{q}) \coloneqq \sum_k p_k \log \frac{p_k}{q_k}\,. \tag{5.23}$$

After a straightforward calculation, one gets

$$D_{KL}\left(\vec{p}(t+\delta t)\|\vec{p}(t)\right) = \sum_k \frac{\dot{p}_k^2}{p_k}\delta t^2 + O(\delta t^3)\,, \tag{5.24}$$

where the first order contribution vanishes due to $\sum_k \dot{p}_k = 0$. This means that the right distance to define a speed is the square root of the relative entropy, which can be written in terms of the *Fisher information in the energy eigenspace* as

$$I_E(t) \coloneqq 2v_E(t)^2 = \sum_k \left(\frac{\mathrm{d}}{\mathrm{d}t}\log p_k(t)\right)^2 p_k(t)\,. \tag{5.25}$$

It is interesting to point out that the same conclusion is reached when, instead of using the Kullback-Leibler distance, one employs the angular distance $D(p,q) \coloneqq \arccos F_{\mathrm{cl}}(p,q)$, with $F_{\mathrm{cl}}(p,q) = \sum_k \sqrt{p_k q_k}$ being the classical fidelity. As the quantum fidelity reduces to the classical one in the case where the states are diagonal in the same eigenbasis, the speed in energy space can be understood as the speed in the state space of the dephased states in the energy basis

$$v_E(t) = \lim_{\delta t \to 0} \frac{D\left(\overline{\rho(t+\delta t)}, \overline{\rho(t)}\right)}{\delta t} \leqslant v(t)\,, \tag{5.26}$$

where $\bar{\rho} \coloneqq \sum_k P_k \rho P_k$ represents the dephased state in the energy eigenbasis. We refer to the Fig. 5.4 for a schematic representation. The last inequality is a consequence of the Bures distance being monotonically decreasing under quantum operations.

Note that both the I_Q and the I_E of uncorrelated and independent systems are additive. Thus, for a system composed on N identical subsystems in which each subsystem goes through the same independent evolution, the speed at which the system runs along a trajectory scales as $\sqrt{N}$. This scaling for independent subsystems will be relevant in the later discussion.

5.4.2 The bound on power

Equipped with this geometric framework, let us introduce the following result. That is an upper bound on the rate at which any dynamical process can change the mean value of a given moment of an observable.

Theorem 2. *Given an observable O, that is time-independent in the Schrödinger picture, the following inequality is satisfied*

$$\left(\frac{d}{dt}\langle O^m\rangle\right)^2 \leq \Delta(O^m)^2 I_O(t), \tag{5.27}$$

where $\Delta(O^m)^2$ is the variance of the m-th moment of the observable that captures how non-local the evolution process is, and $I_O(t)$ is the Fisher information, which corresponds to the speed of the process in the observable (O) eigenspace.

Proof. We first write the m-th power of the operator O in its spectral decomposition:

$$O^m = \sum_k O_k^m \Pi_k, \tag{5.28}$$

where O_k are the eigenvalues of O and Π_k the projectors onto the corresponding subspaces. Using this decomposition, we can write the expected value of O^m as

$$\langle O^m\rangle = \sum_k O_k^m \pi_k(t), \tag{5.29}$$

where $\pi_k(t) \coloneqq \mathrm{tr}\{(\rho(t)\Pi_k)\}$. Taking the time-derivative of the last equation we get

$$\frac{\mathrm{d}}{\mathrm{dt}}\langle O^m\rangle = \sum_k O_k^m \dot{\pi}_k(t) = \sum_k \sqrt{\pi_k(t)}\,(O_k^m - C(t))\,\frac{\dot{\pi}_k(t)}{\sqrt{\pi_k(t)}}, \tag{5.30}$$

where in the last step we have used $\sum_k \dot{\pi}_k(t) = 0$. Finally, using the Cauchy-Schwarz inequality, we get

$$\left(\frac{\mathrm{d}}{\mathrm{dt}}\langle O^m\rangle\right)^2 \leq \left[\sum_k \pi_k(t)\,(O_k^m - C(t))^2\right]\left[\sum_l \frac{\dot{\pi}_l(t)^2}{\pi_l(t)}\right]. \tag{5.31}$$

We can now identify the second factor on the right-hand side as the *Fisher information* I_O, representing the speed of evolution in the observable (O) eigenspace. Furthermore, as Eq. (5.31) is valid for any $C(t)$, a minimization over C leads to

$$C = \langle O^m\rangle, \tag{5.32}$$

which leads us to identify the first factor on the right-hand side as $\Delta(O^m)^2$, and completes the proof. □

Corollary 3 (Power)**.** *Given a process for charging (or discharging) a battery, with Hamiltonian H_B, its instantaneous power fulfills*

$$P(t)^2 \leqslant \Delta H_B(t)^2 I_E(t), \tag{5.33}$$

where $\Delta H_B(t)^2$ is the variance of the battery Hamiltonian that captures how non-local in energy the charging process is, and $I_E(t)$ is the Fisher information, which corresponds to the speed of the charging process in the energy eigenspace.

The corollary above can be seen as a special case of the Theorem 2, where the observable is the battery Hamiltonian, $O = H_B$, and $m = 1$. We can parametrize the tightness of the bound for power via an angle θ_P that satisfies

$$\cos\theta_P \coloneqq \frac{P}{\sqrt{\Delta H_B^2 I_E^2}}. \tag{5.34}$$

This angle may be used to quantify how efficient a charging process is in terms of power, if one considers ΔH_B^2 and I_E as resources that can give maximum power when $\cos(\theta_P) = 1$. Furthermore, in some cases, it could be useful to consider a time-averaged version of the bound (5.33) to eliminate the time-dependence. One possibility would be to consider the bound

$$\frac{\Delta E}{\Delta t} \leq \sqrt{\left\langle \Delta H_B^2 \right\rangle_{\Delta t} \langle I_E \rangle_{\Delta t}}\,, \tag{5.35}$$

where ΔE is the change in the battery energy during the interval Δt, and

$$\langle X \rangle_{\Delta t} \coloneqq 1/\Delta t \int_{t_0}^{t_0+\Delta t} X\, dt. \tag{5.36}$$

To show that the speed of evolution in energy eigenspace I_E is more informative than the one in Hilbert space when studying power, let us consider that the charging process is driven by a Hamiltonian evolution given by $H_C(t)$. We can derive the following inequality from Heisenberg's uncertainty principle:

$$\left(\frac{\mathrm{d}}{\mathrm{dt}} \langle H_B \rangle\right)^2 = |\langle [H_B, H_C(t)] \rangle|^2 \leq 4\Delta H_B^2 \Delta H_C(t)^2, \tag{5.37}$$

showing that our bound (5.33) is lower than the one obtained using Heisenberg's principle, as $I_E \leq 4\Delta H_C^2$. Note that this improvement is due to the fact that we

are lowering the factor $4\Delta H_C^2$, which is the speed of evolution in Hilbert space by replacing it with I_E that specifically quantifies the speed in energy space.

We also remark that, by using I_E instead of ΔH_C^2, the quantities appearing in the bound (5.33) only depend on the battery Hamiltonian H_B and the battery state $\rho(t)$. Thus, the bound is not restricted to the case of Hamiltonian evolution, but it can be used for any dynamical map. However, one should be careful with the connection between stored energy and stored work in the presence of an environment.

5.4.3 Quantum advantage in power

Once again, let us consider a battery that is made up of N identical quantum-cells, each with a Hamiltonian h_j, such that the total battery Hamiltonian reads $H_B = \sum_{j=0}^{N-1} h_j$. Now, given two charging processes, how can we meaningfully state that one of the two has a better performance in terms of power than the other? In the literature, this comparison is made in reference to the *parallel charging* case [267, 268, 269, 270]. For a battery composed of N identical quantum-cells, a parallel charging process is a unitary evolution driven by a charging Hamiltonian of the form

$$H_C^{\parallel} = \sum_{j=0}^{N-1} h_c^j \,, \tag{5.38}$$

where the Hamiltonian h_c^j locally drives the charging process of the j-th quantum-cell in the battery.

Now, to compare with any other unitary charging process, driven by a general charging Hamiltonian H_C, different quantities are chosen and normalized such that they give rise to the same scaling with the number of cells as in the parallel case. These normalization procedures impose an extensive scaling (linear in N) of the norm of the Hamiltonian $\|H_C\|$, its variance ΔH_C^2, or their time-averages in the case of time-dependent Hamiltonians, equal to the case with $H_C^{\parallel}$. Under this constraint, unnormalized and normalized Hamiltonians are related by a rescaling $H_C \to x(N)H_C$. The rescaling ensures that the total energy available to drive the charging process is always the same at order N. In the context of these normalization criteria, speed-ups in power compared to parallel charging have been theoretically explored in [267, 268]. In these works, entangled states or entangling operations are considered to be closely related with such speed ups.

There are two main issues with the aforementioned approach to compare among batteries. First, the presented normalization criteria may not correspond with the

real experimental limitations. It could very well be that the experimentalist is limited by the strength of the local interactions but not by its amount. Hence, a fair comparison will mainly depend on the experimental capabilities. A solution to this limitation can be given by our approach, in terms of the bound in (5.33), as it is derived irrespective of any normalization. There, the bound is given in terms of I_E, which may scale faster than N.

Once the speed of evolution in energy eigenspace has been properly taken into account, we focus on the second term in the bound (5.33), i.e., the energy variance $\Delta(H_B)^2_\rho$, and we analyze it from the geometrical point view. In particular, this terms encodes the information about how quantumness, such as quantum entanglement, plays an important role in enhancing the power of the battery. Below, we study its relation with quantum entanglement, and relate it with the charging power.

5.4.4 Relation of power with entanglement

Consider a battery that is made up of N identical quantum-cells, with the battery Hamiltonian $H_B = \sum_{i=0}^{N} h_i$. The variance of H_B for an arbitrary state ρ reads

$$\begin{aligned}\Delta(H_B)^2_\rho = &\sum_i \left(\mathrm{tr}\left(h_i^2\rho\right) - \mathrm{tr}(h_i\rho)^2\right) \\ &+ \sum_{i\neq j} \left(\mathrm{tr}\left(h_i h_j \rho\right) - \mathrm{tr}(h_i\rho)\,\mathrm{tr}\left(h_j\rho\right)\right) .\end{aligned} \tag{5.39}$$

Let us discuss the relation of entanglement with (5.39) for the case of pure states of the battery. The first sum corresponds to the single-cell energy variance, which we denote as $\Delta^{Loc}(H_B)^2_\rho = \sum_i \left(\mathrm{tr}\left(h_i^2\rho\right) - \mathrm{tr}(h_i\rho)^2\right)$. This quantity scales linearly with the number of cells N and coincides with $\Delta(H_B)^2_\rho$ in the case of separable states ($\rho = \bigotimes \rho_i$). As a consequence, the only way for the variance to scale faster than N is that the battery state is non-separable, and thus entangled.

Indeed, in some cases one can even bound the energy variance $\Delta(H_B)^2_\rho$ with the multipartite entanglement properties of the battery state [288, 289]. For example, let us consider linear qubit Hamiltonians, typically used as models of a quantum battery [267, 269, 270], and that will be studied in Secs. 5.5-5.6, which have the form

$$H_B = \frac{1}{2}\sum_{j=0}^{N-1} \sigma_z^j , \tag{5.40}$$

where σ_z^j is the z Pauli matrix corresponding to the j-th site of the qubit chain, and we have defined the single-cell energy spacing as the unit of energy. To characterize the multipartite entanglement of this system consisting on N qubits, one introduces the notion of a k-producible state [290, 291]: a pure state is k-producible if it is a tensor product of at most k-qubit states, that is

$$|\Psi_{k-\text{prod}}\rangle = \otimes_{l=1}^{M} |\Psi_l\rangle\,, \quad |\Psi_l\rangle = \otimes_j |\phi_j\rangle\,, \quad \#j \leqslant k\,, \tag{5.41}$$

where $|\phi_j\rangle$ is a single qubit state on the site j of the chain. A mixed state is k-producible if it is a mixture of pure k-producible states

$$\rho_{k-\text{prod}} = \sum_\alpha p_\alpha |\Psi^\alpha_{k-\text{prod}}\rangle\langle\Psi^\alpha_{k-\text{prod}}|\,, \quad \left(\sum_\alpha p_\alpha = 1\right). \tag{5.42}$$

Based on this classification of states, a state is k-qubit entangled if it is k-producible but not $(k-1)$-producible. For our purposes, a useful inequality for N-qubit k-producible states is [288, 289]

$$4\Delta(H_B)^2_\rho \leqslant rk^2 + (N - rk)^2, \tag{5.43}$$

where r is the integer part of N/k. Any state (pure or mixed) that violates the bound of Eq. (5.43) thus contains $(k+1)$-qubit entanglement. Using the above inequality, we recast the bound on power and arrive to the Corollary (4).

Corollary 4 (Power and entanglement)**.** *Given a process for charging (or discharging) a quantum battery composed of N-qubits, with a battery Hamiltonian of the form of Eq.* (5.40)*, if at time t the battery is at most k-qubit entangled, its instantaneous power fulfills*

$$P(t)^2 \leqslant \Delta H_B(t)^2 I_E(t) \leqslant \underbrace{\frac{1}{4}\left[rk^2 + (N - rk)^2\right]}_{k\text{-producibility}} \underbrace{I_E(t)}_{\substack{\text{disting. in} \\ \text{energy eig.}}}\,, \tag{5.44}$$

where r is the integer part of N/k. In the cases where r is an exact integer, the inequality reduces to

$$P(t)^2 \leqslant \frac{kN}{4} I_E(t). \tag{5.45}$$

Notice that the bound of Eq. (5.44) sets the limitations imposed in Power by the multipartite entanglement properties of the battery state and its distinguishability in the energy eigenspace, both for pure and mixed states. Thus, this bound leads to

a deeper understanding of the relation between entanglement and power in qubit-based quantum batteries. For instance, the inequality (5.43) is saturated only by a battery state which is a product of r Greenberger-Horne-Zeilinger (GHZ) states of k qubits $|\mathrm{GHZ}_k\rangle$, and another set of GHZ states of $N - rk$ qubits $|\mathrm{GHZ}_{N-rk}\rangle$[289], with

$$|\mathrm{GHZ}_k\rangle = \frac{1}{\sqrt{2}}\left(|0\rangle^{\otimes k} + |1\rangle^{\otimes k}\right). \tag{5.46}$$

An example of such a GHZ state was indeed introduced (with $k = N$) in the seminal paper [267], introducing the potential entanglement boost in quantum batteries.

Another important insight is that many-body charging Hamiltonians with a large participation number and low order of interactions will generically lead to battery states that strongly differ from the optimal GHZ ones. In that sense, we would also like to note that it is interesting to compare our bound of Eq. (5.44) with the ones derived in the work [268], where the relation of the quantum advantage in Power with the interaction order and participation number has been considered.

5.5 Paradigmatic examples

One example that has become paradigmatic in the field [267, 268, 269] is the charging of a battery composed of non-interacting cells by a time-independent Hamiltonian evolution. Once again, let us consider the battery Hamiltonian of N two-level systems with the Hamiltonian $H_B = \frac{1}{2}\sum_{j=0}^{N-1}\sigma_z^j$, which has the same form as Eq. (5.40). Initially, at $t = 0$, the battery is in its ground state $|\psi_0\rangle = |0\rangle^{\otimes N}$. Notice that the ground state has a negative energy and, as we are interested in the energy difference, hereafter we will define the stored energy at a given time as

$$E(t) := \mathrm{Tr}(|\psi(t)\rangle\langle\psi(t)|H_B) - \mathrm{Tr}(|\psi_0\rangle\langle\psi_0|H_B). \tag{5.47}$$

As the initial state is a pure state, which has zero entropy, one trivially gets that the capacity is given by $C_{S=0} = N$. In order to charge the battery, one can use different charging Hamiltonians H_C. In particular, illustrative examples are the cases of a *parallel*, *global* and *hybrid* Hamiltonians, represented by $H_C^{\|}$, $H_C^{\#}$, and

H_C^h, respectively. These Hamiltonians are given by

$$\begin{aligned} H_C^{\parallel} &= \lambda \sum_{j=0}^{N-1} \sigma_x^j, \\ H_C^{\#} &= \lambda \otimes_{j=0}^{N-1} \sigma_x^j, \\ H_C^h &= \lambda \sum_{j=0}^{q-1} \otimes_{i=1}^{r} \sigma_x^{qj+i}, \end{aligned} \tag{5.48}$$

where σ_x^j is the x Pauli matrix acting on the jth cell, and in the *hybrid* case $N = qr$. Regarding time-units, here λ represents a charging frequency, where we use the convention $\hbar = 1$. The main features of these three charging processes are outlined in the Table 5.1 below.

	Parallel	**Global**	**Hybrid**
H_C	$\lambda \sum_j \sigma_x^j$	$\lambda \otimes_j \sigma_x^j$	$\lambda \sum_{j=0}^{q-1} \otimes_{i=1}^{r} \sigma_x^{qj+i}$
$\|\|H_C\|\|$	$N\lambda$	λ	$q\lambda$
λt_F	$\pi/2$	$\pi/2$	$\pi/2$
ΔH_C^2	$N\lambda^2$	λ^2	$q\lambda^2$
I_E	$4N\lambda^2$	$4\lambda^2$	$4q\lambda^2$
$E(t)$	Np	Np	Np
$\Delta H_B(t)^2$	$Np(1-p)$	$N^2p(1-p)$	$Nrp(1-p)$
k-qubit ent.	1	N	r
$\Delta^{Ent} H_B(t)^2$	0	$Np(N-1)(1-p)$	$Np(r-1)(1-p)$
$P(t)$	$\sqrt{\Delta^2 H_B I_E}$	$\sqrt{\Delta^2 H_B I_E}$	$\sqrt{\Delta^2 H_B I_E}$

*$p = \sin^2(\lambda t)$.

**Note, at t_0 and t_f the state of the system is always a product state regardless of the form of H_C.

Table 5.1: Comparison between three different charging Hamiltonians of a battery composed of N qubit cells: the *parallel* charging, the fully interactive *global* Hamiltonian (optimal) and an *hybrid* construction where m blocks of q qubits are in parallel charged in a fully interactive way.

It is easy to see that all these Hamiltonians evolve the initial ground-state state to the highest energy state $|1\rangle^{\otimes N}$. Therefore, the stored energy coincides with the capacity at time $\lambda t_f = \pi/2$, as per Observation 1. Power is the same for all the cases, and the bound (5.33) is always saturated. Furthermore, for these cases, the evolution speed in state space and energy eigenspace coincide, as $I_E = 4\Delta H_C^2$ (see Table 5.1). Without any normalization constraints, I_E scales linearly with N in the *parallel* case, as there are many energy levels involved in the evolution. The situation is drastically different in the *global* case, where only the groundstate and

maximally excited energy levels participate, leading to an N-independent scaling of I_E. The *hybrid* case presents an intermediate behaviour.

The quantum enhancement in power in these paradigmatic examples was understood [267, 268] with the help of certain normalization criteria, as explained in Sec. 5.4.3. The approach in [268], for instance, imposes a linear scaling of ΔH_C^2 with N, and one should perform the normalization $H_C^{\#} \rightarrow \sqrt{N} H_C^{\#}$. With this criterion, the global charging is $\sqrt{N}$ times faster than the parallel one. On the other hand, under the constraint of $\|H_C\|$ scaling as N, imposed in [267], one should perform the normalization $H_C^{\#} \rightarrow N H_C^{\#}$. Within such norm rescaling, the global charging performs N times faster than the parallel one.

Instead, the approach presented in the previous sections allows us to discuss the role of the entanglement between the cells in the power of these models, without the need of relying to a normalization constrain, and in a quantitative manner. It is easy to see that the *global* (*r-hyrbid*) Hamiltonians leads to a battery state that will have $N(r)$-qubit entanglement:

$$\begin{aligned} |\Psi\rangle_{global} &= \sqrt{1-p}|0\rangle^{\otimes N} + \sqrt{p}|1\rangle^{\otimes N}, \\ |\Psi\rangle_{hybrid} &= \otimes_{j=0}^{q-1} |\Psi(t)\rangle_j, \\ |\Psi\rangle_j &= \sqrt{1-p}\, \otimes_{i=1}^{r} |0\rangle_{qj+i} + \sqrt{p}\, \otimes_{i=1}^{r} |1\rangle_{qj+i}. \end{aligned} \tag{5.49}$$

Notice (compare rows 7 ad 8 of Table 5.1) that this amount of k-qubit entanglement impacts the super-linear scaling factor of $\Delta^2 H_B$, and thus also the one of power. In the middle of the evolution, for $t = \pi/4$ the states are exactly in the GHZ form, and the bound of Eq. (5.44) is saturated.

5.6 Specific spin models

In this section, we study our previously derived bounds in specific spin-$\frac{1}{2}$ models, effectively described in terms of qubits. The models, that can in principle be realized experimentally (see, for instance, [**?**]), are *i)* integrable spin models in 1D with ultracold fermionic atoms, *ii)* the Lipkin-Meshkov-Glick (LMG) model with ultracold atoms or atoms near nanostructures, *iii)* Dicke model with ultracold ions, BEC in an optical cavity, or cavity circuit QED. While it is true that some of these spin models have already been presented in the literature [267, 269, 270] as candidates for an experimentally realizable quantum battery, we use our formalism to systematically analyze them. More specifically, for each model we discuss the impact of both the evolution speed, quantified by I_E, and the smartness

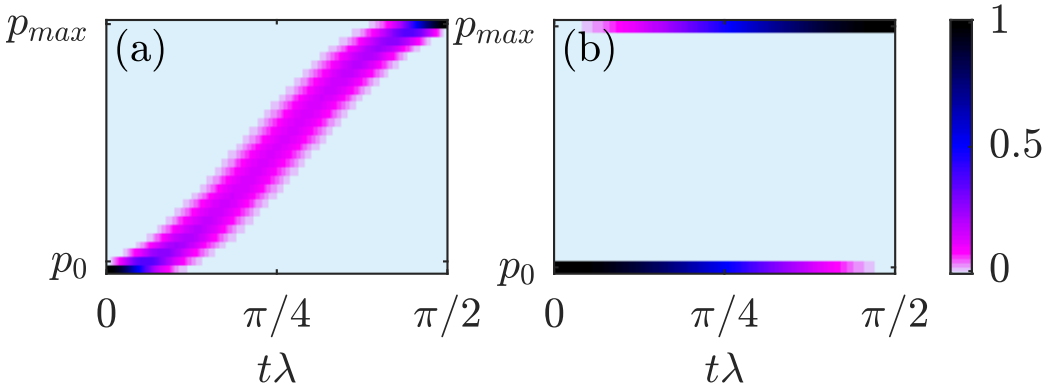

Figure 5.5: Dynamics of energy levels p_k, according to their definition (5.21), during a parallel (a) and a global (b) charging process. Here one can see the contribution of each energy level (y-axis) to the total energy, as a function of time. One can see absolute non-locality in energy space for the global case, where there is a coexistence in time of the highest and lowest energy level, and locality of the parallel one, where at a given time only levels that are close contribute to the total energy.

of the path undergone in the power of the battery, related to ΔH_B^2 and k-qubit(spin) entanglement, hence clarifying the origin of possible speed-ups. Furthermore, we also study the amount and quality of stored energy in the final battery state.

In all the cases we consider that the quantum battery is a chain of N spin-$\frac{1}{2}$ cells. We work in the local basis of Pauli matrices for each spin, i.e., any local operator acting on j-th spin can be expressed in terms of $\{\sigma_x^j, \sigma_y^j, \sigma_z^j, \mathbb{I}\}$, and define our battery Hamiltonian as

$$H_B = \frac{1}{2}\sum_{j=0}^{N-1} \sigma_z^j. \tag{5.50}$$

We consider that the spin system is initially in the ground state of the battery Hamiltonian H_B. We now look at different charging models.

5.6.1 Integrable spin models

Here we consider a general class of charging Hamiltonians in 1D of the form

$$H_{JW} = H_B + \frac{1}{2}\sum_{\substack{j=0\\m=1}}^{N-1}\Big[(\lambda_m+\gamma_m)\sigma_x^j(\otimes_{l=j+1}^{j+m-1}\sigma_z^l)\sigma_x^{j+m}+ \\ +\,(\lambda_m-\gamma_m)\sigma_y^j(\otimes_{l=j+1}^{j+m-1}\sigma_z^l)\sigma_y^{j+m}\Big], \tag{5.51}$$

that can be diagonalized exploiting the Jordan-Wigner (JW) transformation. Above, we have implicitly assumed translational invariance and periodic boundary conditions. The above family of Hamiltonians includes the 1D transverse field Ising model and XY model with a transverse field if we limit the interaction range to nearest-neighbors only. The dynamics of these spin systems, parametrized by (λ_m, γ_m), can be easily solved (for a detailed explanation, see Supplemental Information) by a mapping through the aforementioned JW transformation to a fermionic chain, followed by a Fourier transformation of the fermionic operators exploiting the translational invariance, and a final Bogoliubov transformation of the Fourier transformed fermionic operators.

What is important in our discussion of these systems, acting as quantum batteries, is that in the fermionic picture they present a local structure in momentum space due to their translational invariance. This means that the Hilbert space structure of the problem can be expressed as

$$\mathcal{H} = \bigotimes \mathcal{H}_{k,-k}, \tag{5.52}$$

where k labels the quasi-momentum, and thus these models are very similar to an *hybrid* model with $r = 2$ (see Table 5.1), which is close to the *parallel* case, as there is only 2-particle entanglement between $(k, -k)$ modes. We see this fact in that we are able to write all the relevant dynamical quantities (see App. 5.7) as a sum of independent contributions from each $(k, -k)$ subspace. For instance,

$$\begin{aligned} E(t) &= \sum_{k\in\#\mathrm{BZ}} \varepsilon_k(t), \\ P(t) &= \sum_{k\in\#\mathrm{BZ}} \dot{\varepsilon}_k(t), \\ \Delta H_B(t)^2 &= \sum_{k\in\#\mathrm{BZ}} \varepsilon_k(t)(2-\varepsilon_k(t)), \\ \Delta H_{JW}^2 &= \sum_{k\in\#\mathrm{BZ}} \sin^2(\theta_k)\omega_k^2, \end{aligned} \tag{5.53}$$

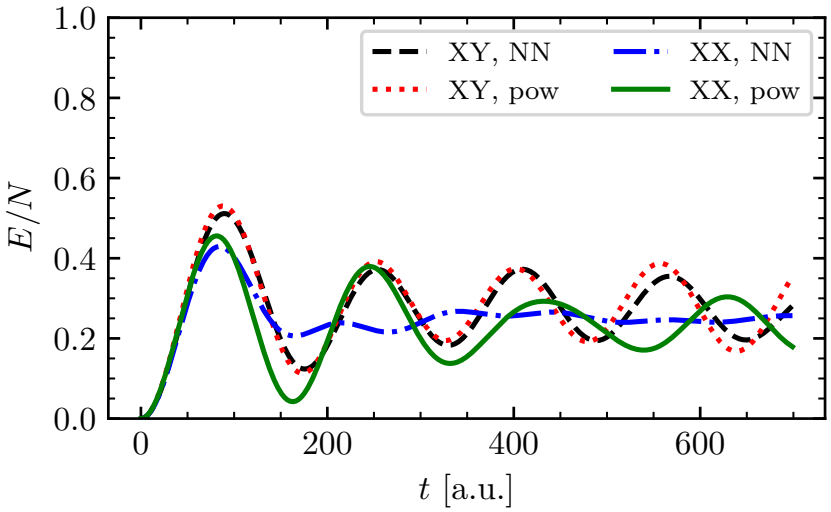

Figure 5.6: Dynamics of the stored energy for different spin integrable models described by the Hamiltonian Eq. (5.60). The legend indicates to which model corresponds each line. We have studied the XY (XX) model that correspond to $\lambda_m = 0$ ($\lambda_m = \gamma_m$). For each of these models we have studied the nearest-neighbors (NN) case, where $\gamma_1 = 1$ and $\gamma_{m\neq 1} = 0$, and also the power law (pow) case, where $\gamma_m = m^{-2}$. We have fixed the system size to $N = 20$ spins and normalized the stored energy (Y-axis) accordingly, such that it is bounded to 1. We observe that for all the models the maximum stored energy is about 50% of the total due to the desynchronization between the different modes that contribute to this quantity.

where ε_k, θ_k, and ω_k depend on the parameters of the model and $\#BZ$ refers to the reduced Brillouin zone of the fermionic chain (see the Supplemental Information). Notice that, as the size of the reduced Brillouin zone is proportional to N, the quantities appearing in Eqs. (5.70) have a natural linear scaling with N.

Comparing the *parallel* and *hybrid* rows of Table 5.1, we observe that these integrables models can present a quantum advantage by at most a factor of 2, under the criteria that the speed factor I_E is kept at a constant value. This result is in agreement with the result of [268], where it was shown that, for a fixed ΔH_{JW}^2, the maximum quantum advantage is given by the order of interaction of H_{JW}.

The only collective effect we are left with is the synchronization between independent modes (2-producible states of $(k, -k)$ particles). This phenomenon has a direct consequence: it limits the capacity and quality of stored energy, as in general the set of energies $\varepsilon_k(t)$ will not be maximized simultaneously.

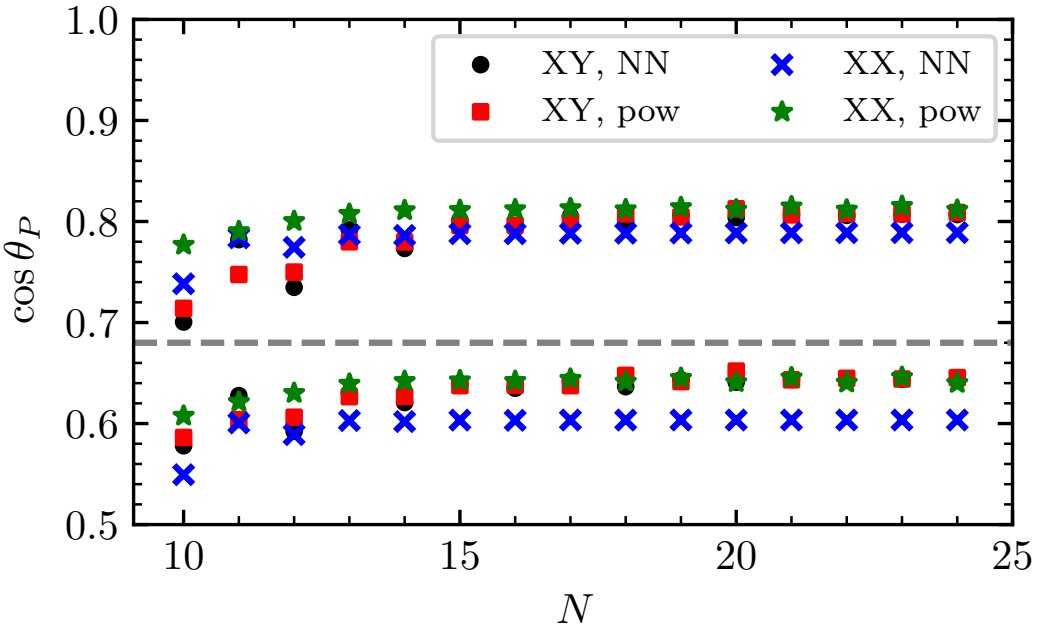

Figure 5.7: Over the grey dashed line, we plot the value of $\cos\theta_P := P/\sqrt{\langle\Delta H_B^2\rangle_{\Delta t}\langle I_E\rangle_{\Delta t}}$ as a function of the number of spins N for the models presented in Fig. 5.6. We observe a fast saturation to an approximate 0.8 value. Below the grey dashed line, we plot the same quantity but substituting $\langle I_E\rangle_{\Delta t} \to 4\Delta^2 H_{JW}$, and it saturates to an approximate 0.6 value. This shows how lower is our bound obtained using the Fisher information in energy eigenspace instead of the speed in Hilbert space for these particular models.

This feature is discussed in Fig. 5.6 for particular choices of (λ_m, γ_m). It is also important to notice that, in general, the system will not be in an energy eigenstate when it reaches maximum capacity. However, the energy uncertainty associated with the final state will be negligible in the thermodynamical limit, as $\Delta H_B(t_f)/E(t_f) \sim 1/\sqrt{N}$.

Moreover, one can compute the Fisher information in energy eigenspace for these models (see App. 5.8) to see how tight our bound is for different choices of parameters and as a function of N, a result which is shown in Fig. 5.7.

5.6.2 Lipkin-Meshkov-Glick model

Another class of charging Hamiltonians that we consider is based on the LMG model [292], which allows for two-body spin interactions with an infinite range. Namely, the charging Hamiltonian is given by

$$H_{LMG} = \frac{\lambda}{N}\sum_{i<j}(\sigma_x^i\sigma_x^j + \gamma\sigma_y^i\sigma_y^j) + \frac{1}{2}\sum_{j=0}^{N-1}\sigma_z^j, \tag{5.54}$$

where λ is the coupling strength, γ the anisotropy parameter, and the factor $\frac{1}{N}$ is included in the model in order to have a finite interaction energy per spin in the thermodynamic limit. For the infinite range Ising model ($\gamma = 0$), H_{LMG} is analog to the so-called twist-and-turn Hamiltonian [293]. There λ mimics the twisting parameter, and the linear term coming from H_B is a rotation around the z-axis. Using the components of the total spin operator $\boldsymbol{J} \coloneqq (J_x,\ J_y,\ J_z)$, with

$$J_\alpha = \sum_{j=0}^{N-1}\frac{\sigma_\alpha^j}{2}, \quad (\alpha = x,\ y,\ z), \tag{5.55}$$

the LMG Hamiltonian of Eq. (5.54) can be rewritten as

$$H_{LMG} = \frac{\lambda}{2N}\Big[(1+\gamma)\Big(J_+J_- + J_-J_+ - N\Big) + (1-\gamma)\Big(J_+^2 + J_-^2\Big)\Big] + J_z, \tag{5.56}$$

where we have introduced the ladder operators J_+ and J_-, that are related to the total spin operators by $J_x{=}\frac{1}{2}(J_+{+}J_-)$, and $J_y{=}\frac{1}{2i}(J_+{-}J_-)$. Notice that, in the total spin notation, the battery Hamiltonian reads $H_B = J_z$. Note also that $\boldsymbol{J}$ is a constant of motion, i.e., $[\mathbf{J}, H_{LMG}] = 0$, and that the initial state lies in the maximum spin sector. These properties effectively reduce the size of the Hilbert

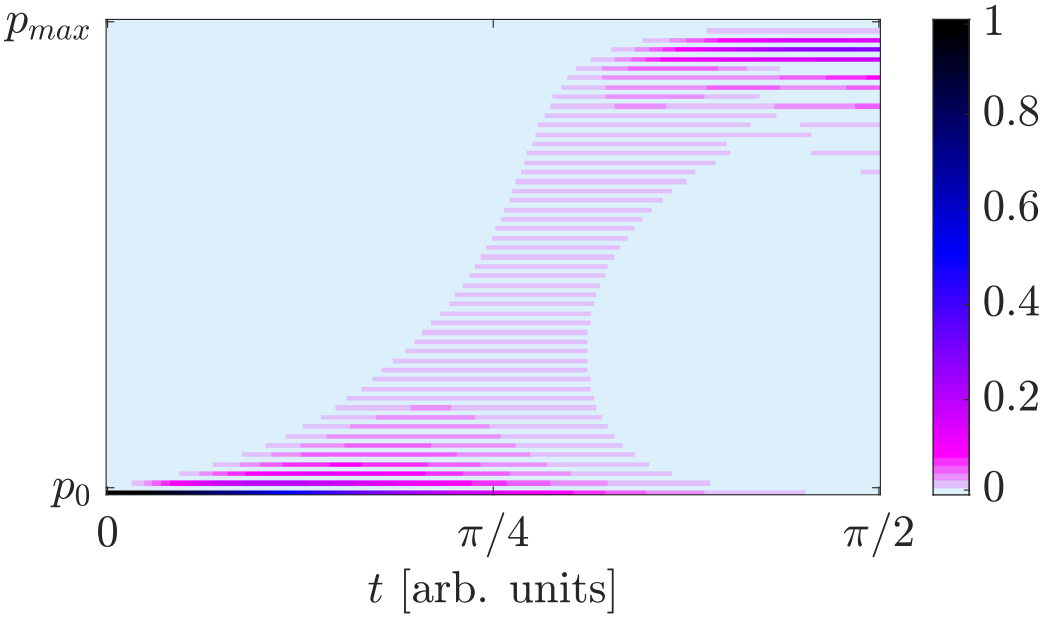

Figure 5.8: Dynamics of the energy levels during the charging process based on the LMG model for $\lambda = 5$. Due to the structure of H_{LMG}, only every second energy level starting from the initial state is occupied during the evolution.

space of the problem, that scales only linearly with N, instead of the exponential 2^N scaling of the total Hilbert space described by local Pauli matrices.

Let us first discuss some general properties of the Hamiltonian (5.56) that mainly affect the capacity properties of the LMG model. First, note that deposition of energy into the battery only occurs if $\gamma \neq 1$, and the maximum capacity is achieved for $\gamma = -1$ (see Fig. 5.10c-d). This comes from the fact that the mixed terms in the Hamiltonian (i.e. J_+J_- and J_-J_+) are diagonal operators in the energy eigenbasis, and hence they only contribute to the free evolution and not to the charging process.

Second, there are two regimes depending on the value of the parameter λ. The strong coupling regime is defined by $\lambda \geq 1$, whereas in the weak coupling regime $\lambda < 1$. In the latter, the LMG model leads to very poor charging properties, as the maximum stored energy tends to zero in the thermodynamic limit. This is due to the fact that the ground state of the battery Hamiltonian H_B (i.e., the initial state) is also an eigenstate of H_{LMG}, when $N \to \infty$ [294]. Therefore, for our discussion, we will focus on the strong coupling regime.

In studying power for LMG model, a first quantity of interest is the variance of the charging Hamiltonian

$$\Delta H^2_{LMG} = \frac{\lambda^2}{2}(1-\gamma)^2 + O\Big(\frac{1}{N}\Big). \tag{5.57}$$

We see that these variance does not scale with N, implying that I_E cannot scale with N either, as $I_E \leq 4\Delta H^2_{LMG}$. Hence, our bound (5.33) tells us that any scaling of the power with N can only be associated with ΔH^2_B. Note, the correlations are expected to be enhanced in this model due to the long-range nature of the interactions between spins, and also because it does not have any "hidden" local structure in energy, unlike the previous case of integrable spin models. Nevertheless, they are bounded to scale as N^2 at most (see Sec. 5.4.4). As a consequence, power can scale at maximum linearly with N for the LMG charging Hamiltonian, and no N-dependent speed-up is possible.

To make a quantitative analysis of the scaling of such correlations with the number of spins N, and also study the tightness of our bound on power, we have solved its dynamics for two values of the coupling strength in the strong coupling regime ($\lambda = 5,\ 20$), and a fixed value of $\gamma = -1$.

First, we would like to draw attention to Fig. 5.8, where one can visualize the evolution of the LMG battery in the eigenspace of H_B. If one compares this evolution with the ones of the paradigmatic cases (see Fig. 5.5), one observes that the LMG battery has some common properties with the global charging case, as there appears entanglement between the states that are far away in energy during evolution. This enhances the battery variance ΔH^2_B, as explained below. However, in the LMG battery, there are many energy levels involved in the charging process, contrary to what happened in the global charging case, where only the lowest and highest energy states participate.

In Fig. 5.9b, one can see the enhancement of the time-averaged energy variance ΔH^2_B in the LMG battery. Even though this variance does not saturate the bound of N^2-scaling, it definitely scales super-extensively, as $\sim N^{1.8}$. As per Eq. (5.43), this scaling means that the battery is in a highly k-qubit entangled state during the charging process. In Fig. 5.9c one observes that the Fisher information I_E does not vary with the system size, a result that is in agreement with the analytical formula of Eq. (5.57). Finally, we note that, for the LMG battery in the strong coupling regime, the bound (5.33) is tight at order N (see Fig. 5.9d), and power scales approximately linearly with N (see Fig. 5.9a), inheriting the scaling of ΔH_B. We also remark that increasing the driving parameter λ decreases the tightness of the bound.

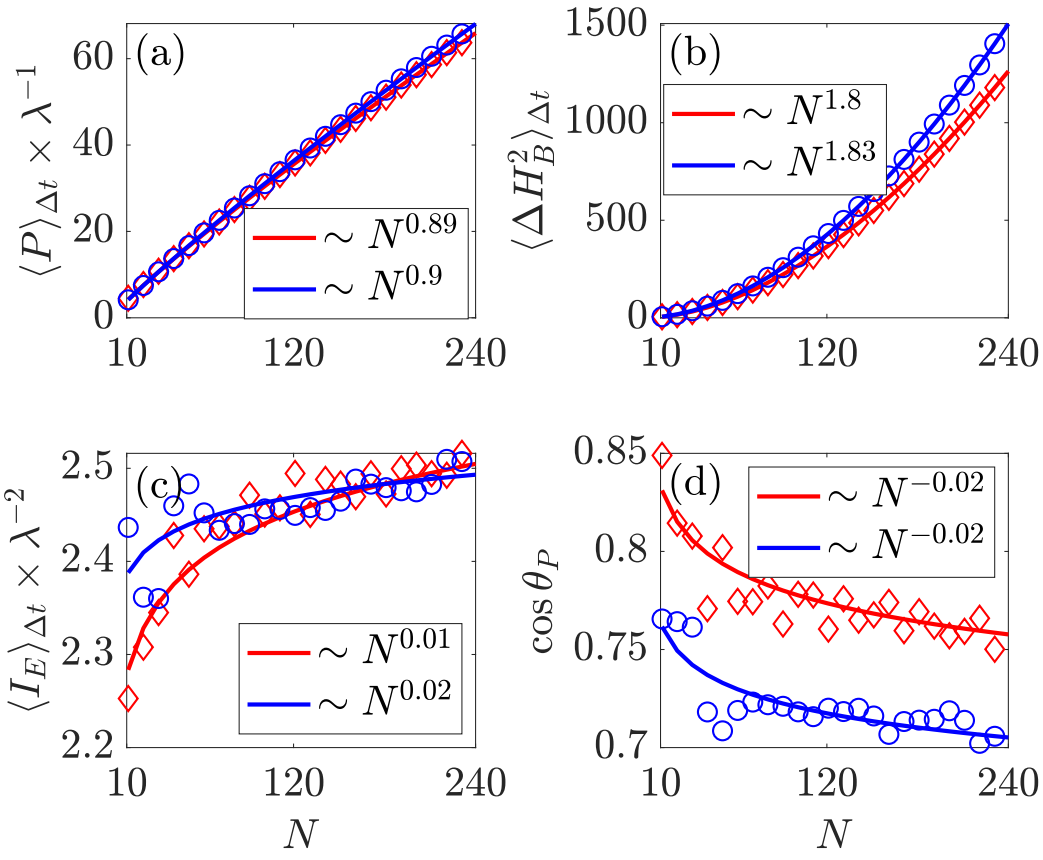

Figure 5.9: The figures consider time-averaged quantities of the LMG model, which are relevant in the study of power, as a function of the number of spins N. The final time has been chosen as the one for which the capacity is maximized. Blue color is used for $\lambda = 20$, whereas red color is used for $\lambda = 5$. Quantities that carry units of time (i.e., power and Fisher information) have been renormalized with the coupling strength λ. The legends indicate the scaling with N of the different curves.

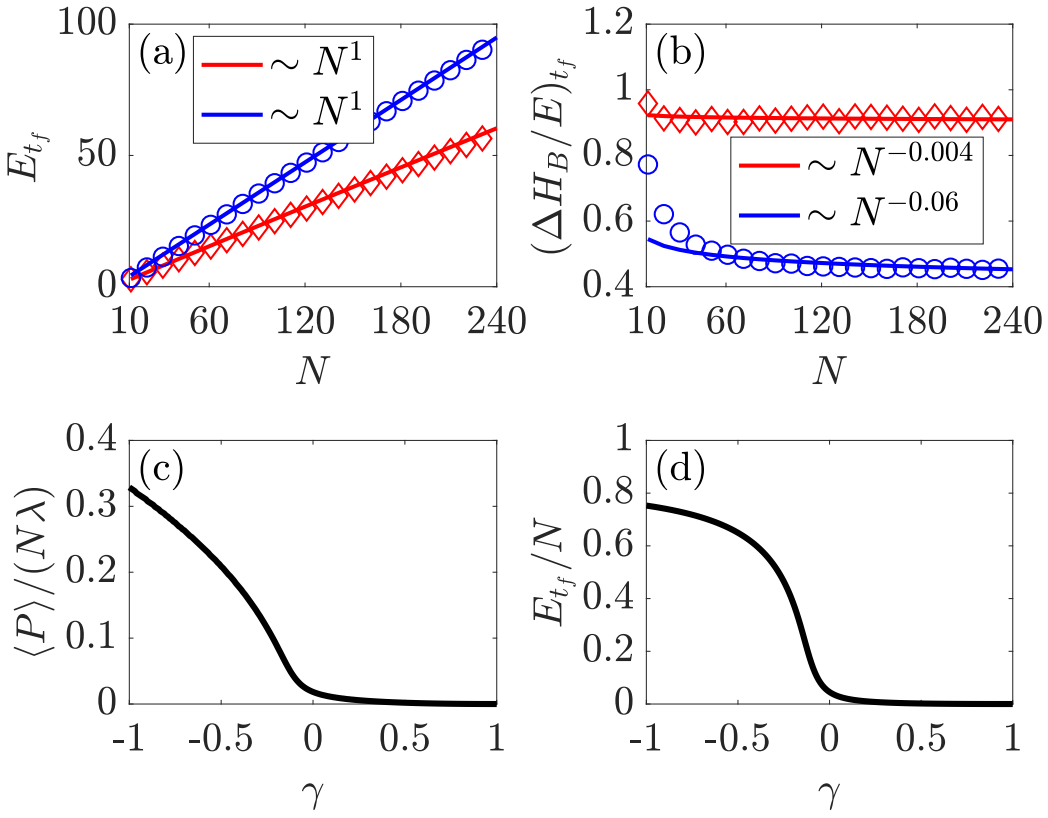

Figure 5.10: Capacity properties of the LMG battery. In figure (a) and (b) one can see the expected scaling of the capacity and the final relative energy variance as a function of the system size. The blue color is used for $\lambda = 20$, whereas red color is used for $\lambda = 5$, and the legends indicate the scaling law. In (c) we plot the dependence with the anisotropy parameter γ of both the capacity and power. For this plot, we used a system of 50 spins and set $\lambda = 5$.

At this point, it is interesting to compare the conclusions obtained for the LMG model within the scope of the bound (5.33) and the analysis on speed-ups under certain normalization criteria. In [268], it was predicted that, under a fixed linear scaling with N of ΔH_C^2, power could scale super-extensively in batteries with a large participation number, e.g. the present LMG model. In Sec. 5.4.3, we showed that if one imposes a linear scaling with N of the Fisher information I_E (and thus of ΔH_C^2), speed ups in power are directly related to the enhancement of the battery variance ΔH_B^2. We have seen that, in the LMG battery, such variance is indeed

highly enhanced and it translates into power, as the bound (5.33) is tight for this model. However, this enhancement in power does not come from the speed of evolution, as the Fisher information I_E remain invariant with the system size. Thus the normalization criterion under which such enhancement in power was predicted does not apply.

Hence, the example of the LMG model shows the importance of both ΔH_B^2 and I_E, and it stresses the two-fold origin of quantum advantage in power.

To conclude with the LMG model, let us now briefly discuss the energy capacity and its variance, quantitatively. In Fig. 5.10a, we see that in the strong coupling regime the energy stored scales linearly with the number of cells N, as expected. However, in Fig. 5.10b we see that there is no decay of the relative variance of the final stored energy in the large N limit. This presents an important problem for a deterministic extraction of the stored energy, and it means that the super extensive energy variance ΔH_B^2 that build-up during the charging process to enhance power, does not disappear in the final state.

5.6.3 Dicke model

A quantum battery can also be constructed by placing an array of spins inside an optical cavity [295]. This particular model has been studied in [269], where a collection of N spins interact with a cavity field mode. In this section, we reconsider this battery model and study it in the light of our bounds presented before. The paradigm assumed here is qualitatively different from the previous ones, as the system that provides the energy to the battery (i.e., the charging agent) is explicitly considered. The battery Hamiltonian is still given by $H_B = J_z$. The charging Hamiltonian includes the free evolution of both the spins and the cavity and a linear interaction between them. It reads

$$H_{DK} = J_z + \hat{a}^\dagger \hat{a} + \frac{2\lambda}{\sqrt{N}} J_x (\hat{a}^\dagger + \hat{a}), \tag{5.58}$$

where $\hat{a}^\dagger(\hat{a})$ are the usual creation (annihilation) operators of cavity photons, satisfying $[\hat{a}, \hat{a}^\dagger] = \mathbb{I}$, and the macro-spin notation is adopted as previously. In contrast to the convention used in [269], here we include the factor $\frac{1}{\sqrt{N}}$ in the coupling in order to have a well defined thermodynamical limit [1], for $N \to \infty$. We consider that in

[1]The thermodynamical limit is considered on the cavity-spin system as a whole. This implies that if one adds spins the cavity length L should also increase to allocate them, keeping the density N/L constant, or in other words $N \propto L$. On the other hand, the coupling term in the Hamiltonian

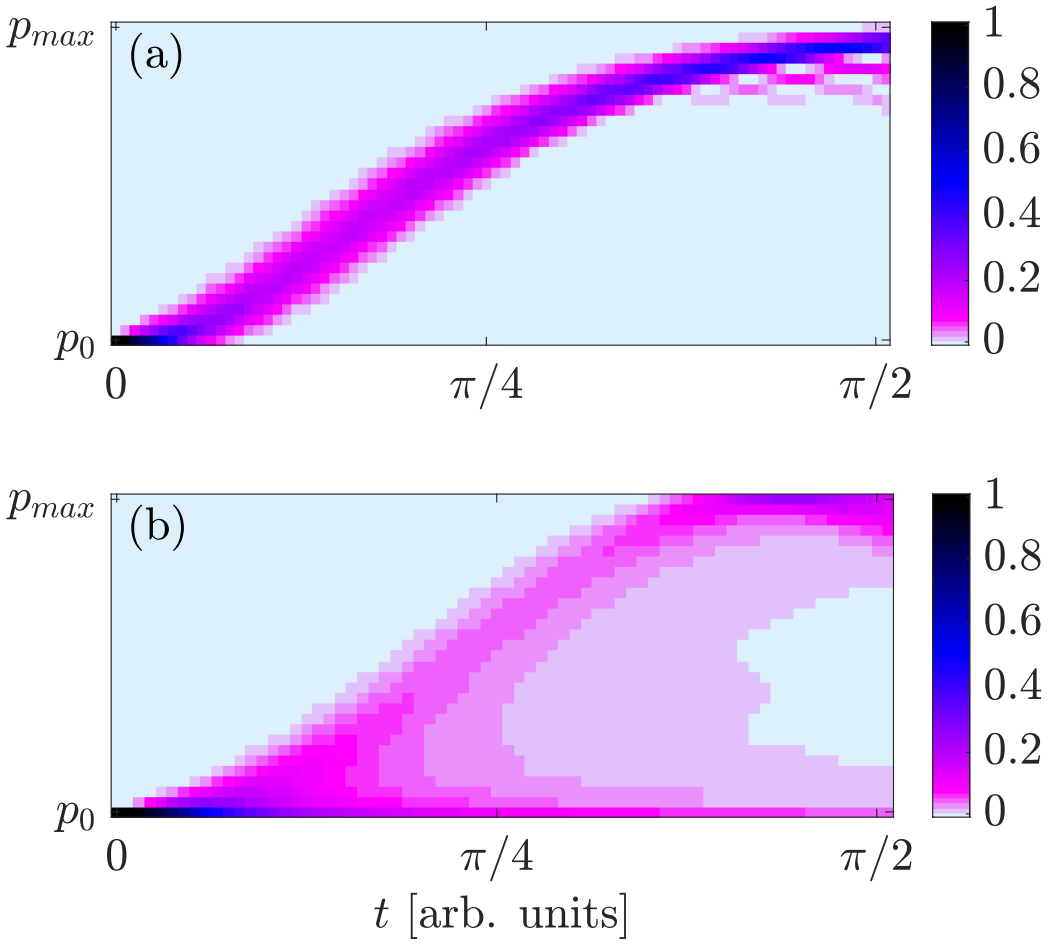

Figure 5.11: Dynamics of the energy levels p_k during the charging process based on Dicke model for λ=0.01 (a) and λ=0.5 (b). In (a) we see that for the weak coupling regime the behavior is similar to the parallel charging case. On the other hand, (b) shows an intermediate behavior between parallel and global charging.

the initial state the spins (i.e., the battery) are in the ground state of H_B, and the cavity is in the eigenstate of the photon number that contains N photons.

(5.58) has its origin in the electric-dipole interaction $\sum E_j \cdot d_j$, where d_j is the dipole of each spin, and E_j the electric field at the spin position. Of course, the individual dipole operators d_j do not carry any scaling with N, and they are simply proportional to σ_x^j, but the electric field quantized inside a cavity of length L carries a normalization factor $1/\sqrt{L}$. Thus, L and N need to be proportional.

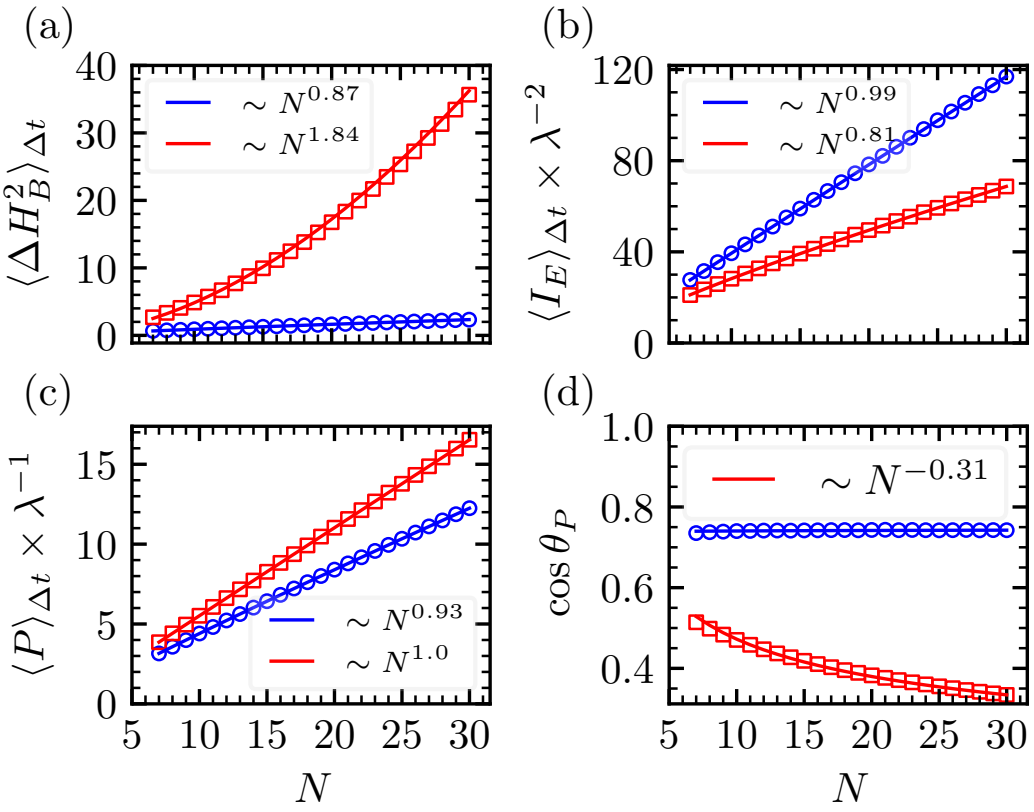

Figure 5.12: The figures consider time-averaged quantities of the Dicke model, which are relevant in the study of power, as a function of the number of spins N inside the cavity. The final time has been chosen as the one for which the capacity is maximized. The blue color (circles) is used for the weak coupling regime ($\lambda = 0.01$), whereas the red color (squares) is used for the strong coupling regime ($\lambda = 0.5$). Quantities that carry units of time (i.e., power and Fisher information) have been renormalized with the coupling strength λ. The legends indicate the scaling with N of the different curves.

A first observation is that one can analytically compute

$$\Delta H_{DK}^2 = 2\lambda^2(2N+1)\,, \tag{5.59}$$

and therefore one sees that I_E is bounded to scale linearly with N (parallel case scaling) at most. One is then left with ΔH_B^2 as the only quantity appearing in our bound (5.33) that could scale super-extensively in order to enhance the power

scaling. Notice that this is only possible if a normalized coupling $\lambda/\sqrt{N}$ is introduced. The non-normalized case, considered in [269], can be experimentally engineered [296] if one considers that N ranges from 1 to some large but finite value. In such scenario, we have $\Delta\tilde{H}^2_{DK} = 2N\lambda^2(2N+1)$. Then, the power can scale super-extensively without the need of a super-extensive scaling in of ΔH^2_B, i.e., the spins do not need to explore highly correlated subspaces. In order to be able to make stronger statements about this system, we have numerically solved the dynamics for $\lambda = 0.01$ ($\lambda = 0.5$), which are representative examples of the weak (strong) coupling regime of the Dicke model. The qualitative difference between these two regimes can be pictorially seen in Fig. 5.11, where we see that the dynamics of energy levels are very local (and thus similar to the parallel charging case) in the weak coupling regime, whereas in the strong coupling regime they exhibit highly non-local properties, with levels well separated in energy get entangled during evolution.

Let us now turn to the quantitative discussion of these two regimes. A first result (see Fig. 5.12c) is that, when including the normalization $\frac{1}{\sqrt{N}}$ in the coupling, the super-extensive behavior of power presented in [269] disappears, and linear scaling in N (as in the parallel case) is approximately recovered, both in the weak and the strong coupling regime. In contrast, when analyzed in terms of the quantities appearing in our bound, the strong coupling regime shows relevant differences with respect to a parallel charging scenario.

In Fig. 5.12b, we see that both in the weak and strong coupling regime the time-averaged Fisher information I_E scales approximately linearly with N, in agreement with the linear bound set by ΔH^2_{DK}. The differences appear when looking at the time averaged ΔH^2_B (see Fig. 5.12a). While in the weak coupling regime it scales linearly with N, in the strong coupling regime this quantity is enhanced and close to the N^2 scaling. This super-linear scaling is clearly associated to the large value of the coupling λ, that allows for cavity-mediated interactions between the spins, that explore highly-correlated subspaces. In fact, as Eq. 5.43 is also valid for mixed states, this super-linear scaling means that the spins (i.e., the battery) are in a mixture of k-qubit entangled pure states, with $k \gg 1$.

Nevertheless, the enhancement of ΔH^2_B in the strong coupling regime is not reflected in the scaling of power, as one can see in Fig. 5.12d that the bound (5.33) is far from being saturated in this regime, i.e., $\langle P\rangle_{\Delta t} \ll \sqrt{\langle \Delta H^2_B\rangle_{\Delta t}\langle I_E\rangle_{\Delta t}}$, leading to power scaling only linearly with N. Remarkably, our bound is tight at order N in the weak coupling regime.

Let us finally discuss the Dicke model in terms of storage. We observe in

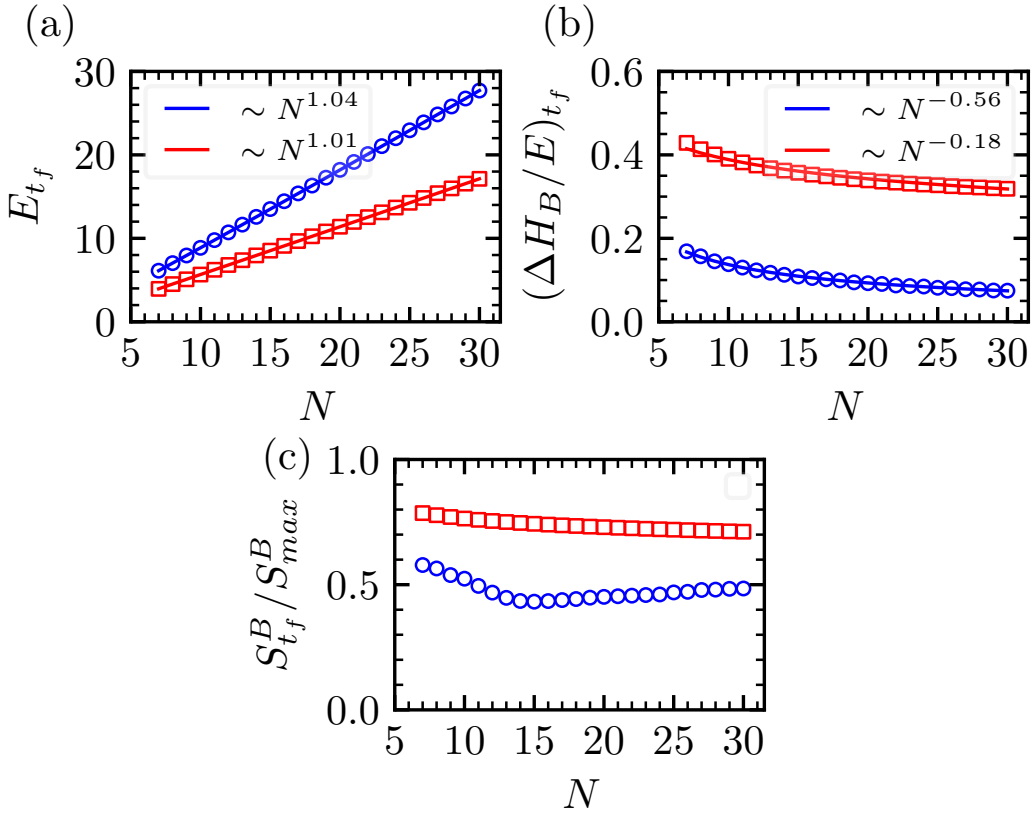

Figure 5.13: The figures show the relevant quantities for the capacity of the Dicke model evaluated at the final time t_f, as a function of the number of spins N inside the cavity. Blue color (circles) is used for the weak coupling regime ($\lambda = 0.01$), whereas red color (squares) is used for the strong coupling regime ($\lambda = 0.5$). In (c) we plot the entanglement entropy $S^B := -\mathrm{Tr}(\rho_B \log \rho_B)$ of the battery reduced density matrix, defined as $\rho_B = \mathrm{Tr}_c(\rho)$, where the trace is performed over the cavity degree of freedom. We normalize this quantity by its maximum value $S^B_{max} = \log_2(N+1)$.

Fig. 5.13 that, while in the weak coupling regime the capacity properties are similar than those of a parallel charging, in the strong coupling regime there is a worsening in the quality of the stored energy. This is because the super-extensive energy variance generated during the charging process does not disappear completely in the final state (see Fig. 5.13b), as they decay much slower than $1/\sqrt{N}$. In Fig. 5.13c we also show the significant presence of entanglement between the

final state of the battery and the source (i.e., the cavity) in this strong coupling regime.

5.7 Solution to the dynamics of the integrable spin models

Here we recast the Hamiltonian

$$\begin{aligned} H_{JW} = H_B + \frac{1}{2}\sum_{\substack{j=0\\m=1}}^{N-1}\Big[&(\lambda_m+\gamma_m)\sigma_x^j(\otimes_{l=j+1}^{j+m-1}\sigma_z^l)\sigma_x^{j+m}+\\ &+(\lambda_m-\gamma_m)\sigma_y^j(\otimes_{l=j+1}^{j+m-1}\sigma_z^l)\sigma_y^{j+m}\Big], \end{aligned} \tag{5.60}$$

To diagonalize it we start by mapping it, trough the JW transformation, to a fermionic chain with the battery and charging Hamiltonians in quadratic forms, i.e.,

$$\begin{aligned} H_B &= \sum_j f_j^\dagger f_j,\\ H_{JW} &= H_B + \sum_{\substack{j=0\\m=1}}^{N-1}\Big[\lambda_m(f_j f_{j+m}^\dagger - f_j^\dagger f_{j+m})+\\ &\quad+\gamma_m(f_j f_{j+m} - f_j^\dagger f_{j+m}^\dagger)\Big], \end{aligned} \tag{5.61}$$

where f_j ($f_j^\dagger$) are the annihilation (creation) fermionic operation at the j-th site of the chain, and we have dropped an irrelevant constant from H_B. Notice that in the fermionic picture the battery Hamiltonian is the particle number operator, and therefore a charging process occurs trough the creation of particles driven by H_{JW}, from the initial vacuum state. It is useful to perform a Fourier transformation of the fermionic operators to bring the battery and charging Hamiltonian into the following form:

$$\begin{aligned} H_B &= \sum_{k\in\#\mathrm{BZ}}(f_k^\dagger f_k + f_{-k}^\dagger f_{-k}),\\ H_{JW} &= \sum_{k\in\#\mathrm{BZ}}\Psi_k^\dagger M_k \Psi_k, \end{aligned} \tag{5.62}$$

with the definitions

$$\begin{aligned} \Psi_k &= (f_k,\ f_{-k}^\dagger)^T, \\ f_k &= \frac{1}{\sqrt{N}} \sum_j e^{-\mathrm{i}kj} f_j, \end{aligned} \tag{5.63}$$

Notice that $\#BZ$ stands for the reduced Brillouin zone, that is, the subset of positive k's from the set $k = -\pi + \frac{2\pi}{n} m$, with $m \in [0, N-1]$. M_k is a 2×2 matrix, which form depends on the parameters of the model and reads

$$M_k = \omega_k \begin{pmatrix} \cos\theta_k & \sin\theta_k e^{-i\pi/2} \\ \sin\theta_k e^{i\pi/2} & -\cos\theta_k \end{pmatrix} \tag{5.64}$$

where θ_k and ω_k are defined as

$$\begin{aligned} \omega_k &= 2\sqrt{\left[\frac{1}{2} - \sum_m \lambda_m \cos(km)\right]^2 + \left[\sum_m \gamma_m \sin(km)\right]^2}, \\ \sin\theta_k &= \frac{2\sum_m \gamma_m \sin(km)}{\omega_k}. \end{aligned} \tag{5.65}$$

The dynamics can now be solved by performing a simple Bogoliubov transformation. To do so, we define the Bogoliubov fermionic modes as $\Phi_k = U_k \Psi_k$, where U_k is a 2×2 unitary matrix. The matrix U_k is chosen such that the Hamiltonian H_{JW} in Eqs. (5.62) becomes diagonal, when rewritten in terms of the newly defined Φ_k operators (i.e., the matrix $U_k M_k U_k^\dagger$ is a diagonal matrix for all k). This matrix reads

$$U_k = \begin{pmatrix} e^{-\mathrm{i}\pi/4}\cos(\theta_k/2) & e^{-\mathrm{i}\pi/4}\sin(\theta_k/2) \\ -e^{+\mathrm{i}\pi/4}\sin(\theta_k/2) & e^{+\mathrm{i}\pi/4}\cos(\theta_k/2) \end{pmatrix}, \tag{5.66}$$

and the charging hamiltonian takes the form

$$H_{JW} = \sum_{k\in\#\mathrm{BZ}} \omega_k \Phi_k^\dagger \begin{pmatrix} 1 & 0 \\ 0 & -1 \end{pmatrix} \Phi_k. \tag{5.67}$$

From the last expression, it is easy to see that, in the Heisenberg picture, the dynamics generated by H_{JW} will lead to

$$\Phi_k(t) = \begin{pmatrix} e^{-i\omega_k} & 0 \\ 0 & e^{+i\omega_k} \end{pmatrix} \Phi_k(0). \tag{5.68}$$

Finally, one can then transform back to the Fourier transformed fermionic modes,

$$\Psi_k(t) = U_k^{\dagger} \Phi_k(t), \tag{5.69}$$

and compute all the relevant dynamical quantities of the problem.

$$\begin{aligned} E(t) &= \sum_{k \in \#\mathrm{BZ}} \varepsilon_k(t), \\ P(t) &= \sum_{k \in \#\mathrm{BZ}} \dot{\varepsilon}_k(t), \\ \Delta H_B(t)^2 &= \sum_{k \in \#\mathrm{BZ}} \varepsilon_k(t)(2 - \varepsilon_k(t)), \\ \Delta H_{JW}^2 &= \sum_{k \in \#\mathrm{BZ}} \sin^2(\theta_k)\omega_k^2, \end{aligned} \tag{5.70}$$

where $\varepsilon_k(t) = 2 \sin^2 \theta_k \sin^2 \omega_k t$.

5.8 Fisher information of integrable spin models

We want to compute the Fisher information for the Hamiltonians of integrable spin models, considered in Eq. (5.60). To do so, we first notice that in the fermionic picture the coefficient $p_l(t)$ that appears in the definition of the Fisher information is the probability of having l particles at a time t. We also notice that $p_l(t)$ will only have a non-zero value for even l, as particles need to be created in pairs $(k, -k)$ to conserve momentum. Finally, the local structure of the problem in k-space allows us to compute separately for every $(k, -k)$ subspace the probability of being in the vacuum state or in the pair state at a given instant of time. It is easy to see that

$$p_{k,-k}(t) = \frac{\varepsilon_k(t)}{2}. \tag{5.71}$$

To compute the Fisher information we use these local probabilities to determine the probability that the hole state contains l particles:

$$p_l(t) = \sum_{\{\sigma\}_l} p(\sigma_1) \dots p(\sigma_N) \tag{5.72}$$

where the sum runs over the configurations $\{\sigma\}_l$, which are binary strings, each bit representing the state of a $(k, -k)$ subspace, with 0's (1's) representing the vacuum (pair) state. These configurations are constrained to contain $l/2$ pairs (1's) and

$$p(\sigma_k) = \begin{cases} \varepsilon_k/2 & \text{if } \sigma_k = 1, \\ 1 - \varepsilon_k/2 & \text{if } \sigma_k = 0. \end{cases} \tag{5.73}$$

And the time derivative of the above probability reads

$$\dot{p}_l(t) = \sum_{\{\sigma\}_l} \sum_{\sigma_k} \frac{\dot{\varepsilon}_k}{2} (-1)^{1+\sigma_k} \prod_{\sigma_{j\neq k}} p(\sigma_j). \tag{5.74}$$

5.9 Conclusions

For a quantum battery, in which the cells are quantum in nature and the process of charging and discharging could introduce quantum correlation among them, a natural question is how to harness the quantum advantages such that it outperforms a classical battery. The aim of this chapter is to find physically meaningful quantities, in relation to the quantum nature of cells and processes, and bounds to characterize a quantum battery. The important properties of a battery are: *capacity*, i.e., the amount of energy it can store and deliver; *power*, that signifies how fast a battery can be charged or discharged; and *variance* in the stored energy, which determines the quality of the stored energy and to which extent it can be deterministically accessed. For a battery composed of many non-interacting identical quantum-cells, the capacity is additive and it is independent of the correlations present in the battery state. While in the case of power, which may not be additive, we expect to see roles of inter-cell correlations leading to certain quantum advantages.

We have derived the capacity, that is, a fundamental bound for the storage of a quantum battery, with the help of the energy-entropy diagram. For a battery with a finite number of quantum-cells and a general unitary charging and discharging process, the capacity often does not saturate. However, in the thermodynamic limit (i.e., with a considerably large number of quantum-cells) the capacity is saturated.

While studying the power of a quantum battery, we have considered the evolution of quantum states when it is projected in the eigenspace of the battery Hamiltonian. Such an approach led us to derive a lower bound on power in terms of two battery dependent quantities. One of these quantities is the Fisher information calculated after the battery state is projected in the eigenspace of the battery

Hamiltonian, and the other one is the energy variance of the battery. While both these quantities are influenced by the appearance of entanglement like correlations during charging (discharging) processes, the former signifies how fast the process takes place in the energy eigenspace and latter encodes how smart (in terms of path length) the trajectory of evolution is. This approach enables us to characterize quantum advantages arising from two different sources. Moreover, for the case of qubit-based quantum batteries, we have presented an inequality that shows the maximum charging power that a battery can exhibit when it has at most k-qubit entanglement, thus establishing a novel interrelation between entanglement and power. The fact that the k-producibility is related with the violation of Bell inequalities [297, 298] could also lead to further studies, in which the relation of power with non-locality [299] is explored.

In the light of the newly introduced bounds, we have considered several spin models of quantum batteries. A first set of paradigmatic models has served us to illustrate how the saturation of the presented bounds can be achieved, and the typical scalings with the number of cells (that is, the spins) of the relevant quantities. We have also studied a few physically realizable models. While exhibiting a reasonably good behaviour in terms of capacity, they are not able to show a super-linear scaling in power. In the case of integrable spin models, despite their interacting nature, the hidden local structure in momentum space makes them very similar to a battery in which the cells are charged independently. For the LMG model, we have shown that quantum entanglement enhances the charging power, but the reduced speed of evolution I_E leads to the same overall scaling as in the case where the cells are charged independently. Finally, we have also studied the Dicke model in two regimes. In the weak coupling regime, the model is similar to the *parallel* case, while in the strong coupling regime there is a large generation of entanglement between the spins. However, our bound is poorly staurated in this latter regime, and entanglement does not contribute in enhancing the power. That is why it exhibits the same scaling as in the *parallel* case.

As a final remark, we believe that our approach and results towards characterizing quantum batteries, in terms of bounds on storage and power, and correct identification of the origins of quantum advantages, will find important applications in its theoretical and technological aspects.

Chapter 6

Correlated phases in solid state quantum simulators

Until now we have discussed systems of fermions (Chapters 1-3) and spins (Chapter 4). The author of this thesis would like to present as well his little contribution to the field of bosonic correlated systems. Thanks to collaboration with world-leading experimental group of C. Lagoin and F. Dubin it was possible for the author of this thesis to build a theoretical model with clear experimental realization and parameters. In this chapter we briefly discuss the Extended Hubbard model, dipolar excitons as quantum simulation platform and finally experimental and theoretical techniques that, merged, allowed us to detect the strongly correlated phases in solid state 2D lattice. Theoretical framework was created depending on the provided set of experimental parameters, which we provide below. Next, two types of calculations were conducted: Exact diagonalization - which was calculated by the author of this thesis and mean-field calculations calculated by Utso Bhattacharya. In this chapter we provide both approaches to provide a complete picture, but we would like to emphasize that the contribution of Tymoteusz Salamon in this multidisciplinary and international collaboration was only ED calculations and manuscript coauthoring.

6.1 Extended Bose-Hubbard model

The Bose-Hubbard model represents a significant achievement in quantum mechanics and has paved the way for numerous advancements in the study of ultra-cold quantum gases. It's a theoretical model used to describe interacting systems of

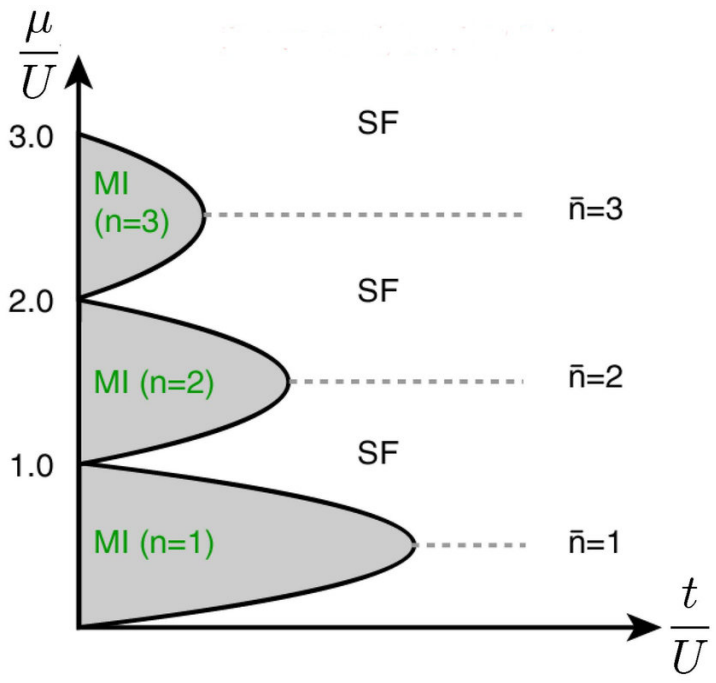

Figure 6.1: Phase diagram of Bose Hubbard model taken from [300]. It comprises two primary phases - the Mott insulator (MI) phase and the superfluid (SF) phase. In the MI phase, characterized by integer particle occupancy and a gap to particle excitations, particles are localized due to strong repulsive interactions. As the tunneling rate increases or the interaction strength decreases, a quantum phase transition occurs leading to the SF phase, where atoms can move freely across the lattice due to dominant tunneling effects.

bosonic atoms in optical lattices, and it has demonstrated profound influence in condensed matter physics, quantum optics, and quantum information science.

The model is named after Satyendra Nath Bose and John Hubbard enabling one to immediately distinguish it from original (Fermi-)Hubbard model studied in 1960s by Gersch and Knollman. BH model was studied first by Fisher Fisher Weichman in 1989 in the context of 4He, and 1998 Jaksch et al. proposed the cold atom BH simulator which made it possible to realize and probe the theoretical predictions. In 2002, researchers from the Max Planck Institute of Quantum Optics used an optical lattice to achieve a controlled transition from a superfluid to a Mott insulator, thereby confirming the Bose-Hubbard model's predictions [301]. Mathematically, the Bose-Hubbard model in its simplest scenario has a form analogical to its fermionic version presented in eq. (4.1), naturally, now with bosonic operators obeying bosonic commutation relations and is given by:

$$H_{B-H} = -t(\sum_{\langle i,j\rangle,} b_i^\dagger b_j + H.c) + U \sum_i n_i(n_i - 1) \tag{6.1}$$

The significance of the Bose-Hubbard model extends beyond just proving a theoretical concept. It is a cornerstone of many-body physics and quantum simulations, where researchers use controlled quantum systems to gain insights into the behavior of more complex, uncontrolled systems. The Bose-Hubbard model provides a simplified but non-trivial framework that allows us to understand the behavior of many-particle quantum systems. The primary achievement of the Bose-Hubbard model is its ability to capture the physics of a phase transition between a superfluid and a Mott insulator in a system of interacting bosonic particles in a periodic potential, as shown in Fig. 6.1. Superfluidity is a phase of matter where matter has $\sqrt{N}$ particle number fluctuations and long-range phase coherence. A Mott insulator, on the other hand, is a material that should conduct electricity according to conventional band theory but behaves as an insulator due to strong interactions among its particles, Moreover, MI has no/little particle number fluctuations.

Better understanding of the phase diagram of the Bose-Hubbard model has redirected much of scientific effort towards longer-range interacting model, known as Extended Bose-Hubbard (EBH) model. EBH Hamiltonian is governed by three core physical parameters. Two of them are standard BH terms: the intensity of on-site interactions denoted as U and the tunneling strength indicated as t. The third one is the interaction strength between the closest neighboring lattice sites referred to as

V:

$$H_V = V \sum_{\langle i,j \rangle} b_i^\dagger b_j^\dagger b_j b_i \tag{6.2}$$

Investigating the scenario where V predominates the many-body ground-state remains a considerable hurdle in experimental research within condensed-matter physics [302]. In this domain, theoretical research suggests that long-range interactions facilitate quantum phases that spontaneously break the lattice symmetry (see Fig. 6.2) [303, 304, 305, 306, 307, 308, 309], akin to charge density waves (CDW) exhibiting checkerboard (CB) or stripe solids. The CDW is a quantum mechanical phenomenon and it results from the interaction between the conducting electrons and the periodic potential of the lattice ions in the crystal. In a normal conductor, the electrons move freely and their density is roughly uniform, but in materials with a CDW, the electrons organize themselves into a periodic pattern, increasing in density at some points and decreasing at others These phases have been theoretically predicted and then experimentally identified in fermionic systems [310, 311, 67], while their realization for bosonic systems continues to be an enduring objective, however, with some fantastic achievements in cold atom systems [312].

6.2 Dipolar Excitons as bosons

Dipolar excitons are an intriguing field of study within condensed matter physics. They are composite particles formed from an electron and a hole that are bound together by electrostatic forces. Unlike traditional excitons, which exist within a single atomic layer or molecule, dipolar excitons possess a built-in electric dipole moment due to the spatial separation of their charge components in different layers or at different quantum well levels. This charge separation results in a number of fascinating properties. The first is their extended lifetime. In a typical exciton, the electron and hole are close together and can readily recombine to emit a photon, thus ending the exciton's life. However, in dipolar excitons, the spatial separation between the electron and the hole means they take much longer to recombine, thus leading to significantly extended lifetimes.Another significant characteristic of dipolar excitons is their strong interaction with each other. Because they possess an electric dipole moment, dipolar excitons can interact strongly with each other via the dipole-dipole interaction. This interaction can lead to novel collective phenomena that are not seen in conventional excitonic systems.

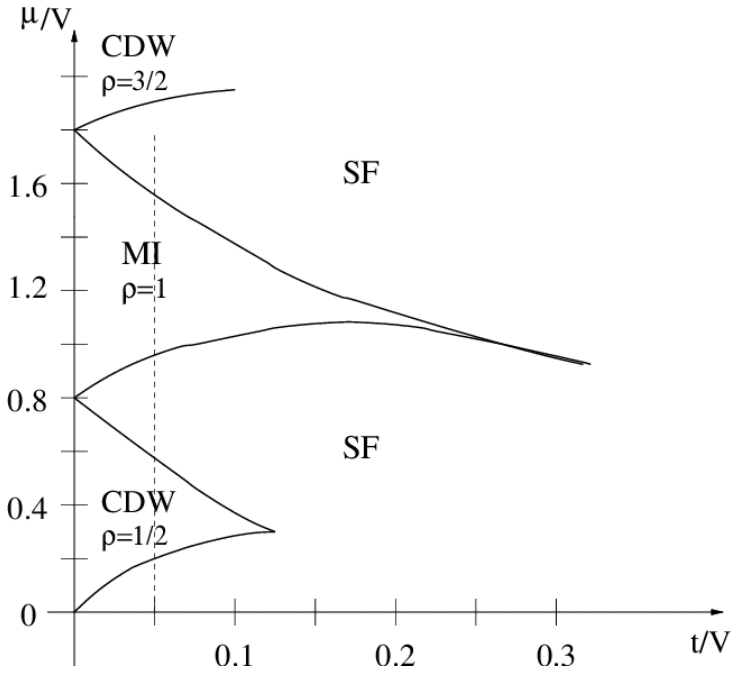

Figure 6.2: Phase diagram of 1D Bose-Hubbard with NN interactions, originally presented in [313]. Here, V=0.4t and U=1t. It shows the Mott-insulator(MI) with density $\rho = 1$, the charge density wave (CDW) phases at densities $\rho = 1/2$ and $\rho = 3/2$, and the surrounding superfluid phase(SF).

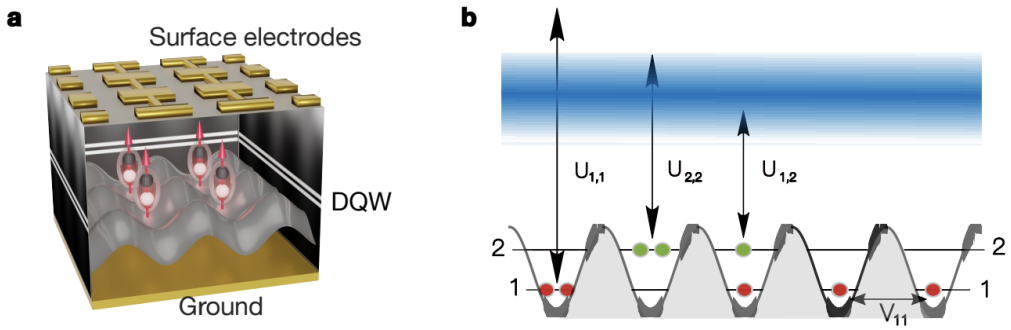

Figure 6.3: Original figure taken from [43]. Panel **a** represents the visual representation of the device with an array of polarized surface electrodes (gold) imprint a 250*nm* period 2D lattice for dipolar excitons, made by electrons (gray) and holes (white) spatially separated in a double quantum well (DQW – white layers). **b** In the lattice, dipolar excitons are confined in two Wannier states (WS) (1 and 2). $U_{1,1}$ and $U_{2,2}$ denote on-site interaction strengths for excitons in WS 1 and 2 respectively, $U_{1,2}$ for excitons in distinct WS, while V1,1 marks the strength of dipolar repulsions between NN sites for the 1st WS

Theoretical works have established that dipolar bosons in a lattice provide an ideal platform to implement the EBH model [84, 306, 307]. The article that the author of this thesis coauthored followed this path by confining dipolar excitons in a two-dimensional square lattice potential in order to observe theoretically predicted phases at half (checkerboard CDW phase) and unit filling (Mott insulator).

The natural basis for investigating the interacting dipolar excitons is Wannier basis. The backwards Fourier transformation from Bloch functions involves a unitary transformation that maps the periodic Bloch functions onto a localized basis set in a real space, called Wannier states. This transformation is not unique, and multiple sets of Wannier states can be constructed for a given system. The resulting Wannier states are orthogonal and form a complete basis that spans the same Hilbert space as the original Bloch states. Wannier states are a fundamental concept in the field of solid-state physics, serving as a powerful tool for describing the behavior of electrons in crystalline lattices. Introduced by Gregory Wannier in 1937, these states provide a localized representation of electronic wavefunctions within a solid. By localizing the electronic wavefunctions, Wannier states allow

for a more intuitive understanding of how electrons (or excitons) interact and move within the lattice.Furthermore, Wannier states enable the study of correlations and many-body effects. Their localized nature facilitates the investigation of interactions between electrons or excitons.

6.2.1 Physical parameters of the extended Bose-Hubbard Hamiltonian

The experimental set-up is based on an array of local potentials with the depth of approx. $250\mu eV$ and energy gap between two states $\Delta = 150\mu eV$. The lattice is then deep enough two confine only the first two states, while all the higher states are not confined (quantized) and, therefore, create a continuum. At low filling ($\bar{n} \lessapprox 1$), the delocalized states of the continuum are barely occupied, and, therefore, the system can be described theoretically by a two-band extended BH model. In such case, EBH Hamiltonian, described by eqs. (6.1) and (6.2) have to be expanded in order to accommodate two Wannier states at each site. Following [307]:

$$H = \sum_i h_i + \sum_{\langle i,j \rangle} h_{ij}, \tag{6.3}$$

where the on-site term has the form

$$h_i = \sum_{\alpha,\beta,\delta,\gamma} U_{\alpha\beta\delta\gamma} b^\dagger_{i\alpha} b^\dagger_{i\beta} b_{i\gamma} b_{i\delta} - \sum_\alpha \mu_\alpha n_{i\alpha}, \tag{6.4}$$

while the terms between nearest neighbour sites have the following form:

$$h_{\langle ij \rangle} = \sum_{m=1,2} -t_m (b^\dagger_{i,m} b_{j,m} + \text{h.c.}) + \sum_{m,m',m'',m'''} V_{mm'm''m'''} b^\dagger_{i,m} b^\dagger_{j,m'} b_{j,m''} b_{i,m'''} \tag{6.5}$$

Here, m denotes the Wannier state and i, j the site, $b_{i\alpha}$ ($b^\dagger_{i\alpha}$) are bosonic annihilation (creation) operators, and $n_{i\alpha} = b^\dagger_{i\alpha} b_{i\alpha}$ is a number operator.

The most influential interaction terms have been determined to be the density-density interactions, specifically, the on-site interactions labelled as $U \equiv U_{1111}$, $U_{2,2} \equiv U_{2222}$, and $U_{1,2} \equiv U_{1221} + U_{1212} + U_{2121} + U_{2112}$, as well as the nearest neighbor interactions denoted as $V \equiv V_{1111}$, $V_{2,2} \equiv V_{2222}$, and $V_{1,2} = V_{1221} + V_{2112}$. Some additional interaction terms that incorporate a mix of bands have been included into the calculations using exact diagonalization (see the subsequent section), but were omitted in the mean-field description. To quantify the influence

of the various on-site and inter-site interactions, denoted as U and V respectively, following the reference work [314], the dipolar potential was broken down into near-range and far-range components, introducing a boundary distance $r_c = 20\,\text{nm}$, which approximates twice the excitons' Bohr radius. Given the projected electric dipole moment of the excitons (d ~12-14 e.nm where e denotes the electron charge), and using the spatial distributions of the Wannier wave-functions expected for our lattice potential with a depth of 300 μeV, the sizes of on-site interactions have been projected as $U \sim 1\,\text{meV}$ and $U_{2,2} \sim 370\,\mu\text{eV}$ for the WS 1 and 2, and $U_{1,2} \sim 175\,\mu\text{eV}$. The intra-band values exceed the excitons confinement depth in the lattice and thus are not measurable. Due to the intense on-site repulsion, double occupancy of sites is significantly limited at fillings less than 1, while occupation of continuum states grows noticeably when the filling exceeds 1. For the inter-site interactions, our computations yield $V \sim 15\mu\text{eV}$, $V_{2,2} \sim 90\mu\text{eV}$, and $V_{1,2} \sim 20\mu\text{eV}$. Regarding the tunneling strength between adjacent lattice sites, we have derived $t_1 \sim 0.4\,\mu\text{eV}$ and $t_2 \sim 5\,\mu\text{eV}$ for the first and second WS correspondingly. Lastly, the band gap, expressed as $\Delta \equiv \mu_2 - \mu_1$, is roughly 150 μeV.

6.2.2 Experimental read-out of the phases

Photoluminescence spectroscopy is a widely used experimental technique for measuring dipolar excitons in various materials. The measurement process involves exciting the material with photons of sufficient energy to promote electrons from the valence band to the conduction band, creating electron-hole pairs (excitons). To measure dipolar excitons using photoluminescence, the material of interest is typically subjected to optical excitation using a laser or other light source. The energy of the excitation photons is chosen to match or exceed the band gap of the material, ensuring the creation of electron-hole pairs and the formation of excitons.

Upon absorption of photons, excitons are generated, and they subsequently undergo relaxation processes within the material. One of the relaxation mechanisms involves the recombination of the excitons, where the electron and hole recombine, releasing energy in the form of photons. These emitted photons can be detected and analyzed to obtain information about the dipolar excitons.

The emitted photons are collected and directed towards a spectrometer, which disperses the light according to its wavelength or energy. By measuring the energy (or wavelength) of the emitted photons, the photoluminescence spectrum can be obtained. The photoluminescence spectrum provides valuable information about the energy levels, distribution, and properties of the dipolar excitons within the

material.

The intensity and shape of the photoluminescence spectrum can reveal important characteristics of the dipolar excitons. For instance, the peak position of the spectrum corresponds to the energy of the emitted photons, providing information about the energy levels of the excitons. The spectral width can indicate the distribution of exciton energies, reflecting the degree of disorder or inhomogeneity in the material.

Moreover, the photoluminescence intensity can be used to study the exciton dynamics and interactions. By varying the excitation conditions, such as excitation power or temperature, the photoluminescence intensity can be measured as a function of these parameters. This allows for the investigation of exciton formation, diffusion, quenching processes, and interactions with other excitons or defects within the material.

Photo-luminescence measurement has been used to gather experimental evidence of CB and Mott phases in our system. Technical details about used parameters and lasers are beyond the scope of this thesis, however full explanation of the experimental set-up can be found in the original paper [43]. As mentioned before periodic potential generated by electrodes accommodates only two confined states, called WS1 and WS2 with the energy gap $\delta = 150\mu eV$. PL spectrum represents the the emission of the Boltzmann distribution of states at given temperature. This means that, besides the ground state, excited states will also contribute to the spectra. Naturally, the more excited the state is, the lower its probability of occurrence. Panel (a) of Fig. 6.5 represents the PL spectrum of the half filled lattice ($\langle n \rangle = 0.5$ exciton per site). In such scenario, the CB in 1WS represents the ground state with no nearest neighbour interactions. The quick look at energies of each interaction channels allows us to identify the the set of first excited states as the ones with single excitation, i.e with one of the excitons previously in the CB configuration moved to the empty site. This configuration involves interaction $V_{1,1}$ with 3 nearest neighbours, leading to the total energy cost of such configuration of $3 \times 22\mu eV = 66\mu eV$. The next set of excited states is the one with two defects, like the one explained above, and therefore with $132\mu eV$. As one can see, all the other excited states will have the energy higher than $\delta \approx 150\mu eV$, and therefore populating 2WS has to be taken into account. Panel (a) of Fig. 6.5 represents this fact with a small peak appearing shift Δ from the WS1. Naturally the amplitude of the second peak will grow with increasing temperature and therefore increasing probability of the excited states.

Panel (b) of Fig. 6.5 represents the PL spectrum at the same temperature ($330mK$)

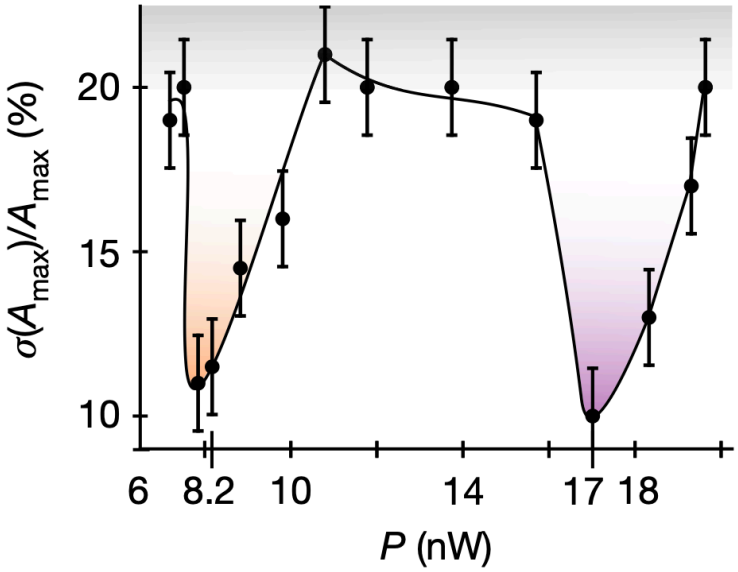

Figure 6.4: Fluctuations of the maximum of the PL spectrum proportional to compressibility κ. Two valleys can be observed at powers corresponding to half and unit fillings. Originally the figure appeared in [43].

for $\langle n \rangle = 1.0$ and therefore corresponding to the Mott insulating phase with fully filled WS1. In this case, single excitation will result with expelling the exciton to 2WS since double occupancy has energy cost of $U_{1,1} \approx 1meV$, and therefore the excited excitons prefer to cross the energy gap between the confined states. Moreover, the ground state has additional energy cost of $4\times V_{1,1}$ resulting in shifted PL spectrum to more or less half of Δ.

One of the primary properties of the bosonic Mott phase, resulting from inter-particle interactions and low mobility within the lattice, is the incompressibility and suppression of local density fluctuations. Locally, compressibility quantifies the response in the on-site density n_i to a local change of the chemical potential and is given by:

$$\kappa_i = \frac{\partial n_i}{\partial \mu_i} = \beta[\langle n_i^2 \rangle - \langle n_i \rangle^2]. \tag{6.6}$$

This relations comes from the fluctuation-dissipation theorem [315] and can be explained in the following manner. In Grand canonical ensemble the average

particle number of the system in the temperature T is given as

$$\langle N\rangle = \frac{1}{\beta}\left[\frac{\partial \ln(Z)}{\partial \mu}\right]_{T,V}, \tag{6.7}$$

where Z denotes grand canonical partition function defined as:

$$Z = \sum_i \sum_N \exp\{-\beta(E_i - \mu N)\}. \tag{6.8}$$

Here, the sum over the index i corresponds to sum over energies of all possible state configurations, each with energy E_i. Now, by calculating the system's response to the change of average particle number one gets:

$$\frac{\partial\langle N\rangle}{\partial \mu} = \frac{\partial}{\partial \mu}\Big(\frac{1}{Z}\sum_i \sum_N \beta N \exp\{-\beta(E_i - \mu N)\}\Big) \tag{6.9}$$

Making use of the Quotient rule for differentiating, one calculates the second derivative with respect to μ and gets

$$\frac{\partial\langle N\rangle}{\partial \mu} = \beta[\langle N^2\rangle - \langle N\rangle^2], \tag{6.10}$$

which is a global (in terms of the whole ensemble) form of th compressiblity given in eq. Eq. (6.6). Density fluctuations can be read out from the PL spectrum by measuring its maximum A_{max} and immediately obtaining the variance, $\sigma^2(A_{max})$. In such description, according to fluctuation-dissipation theorem [316], the compressibility takes the form $\kappa k_B T = \sigma^2(A_{max})/\bar{A}_{max}$, where the bar denotes the average. Taking into account that the excitons are loaded into the system by laser fields, observation of the PL signal depending on the loading laser power automatically provides one with the compressibilty profile as a function of exciton density. This measurement has been shown in the Fig. 6.4, which represents compressibility profile for $T = 330K$. Around 17nW, which corresponds to unit filling, one observes the vast drop of compressibility, which is widely used to identify a Mott insulating phase in bosonic systems in optical lattices [317, 318, 316]. Interestingly, similar drop has been observed around 8nW corresponding to the filling $\bar{n} = 1/2$. This observations signals the existence of the other insulating phase at half filling, which, together with theoretical calculation have given strong evidence of CB and Mott phases in the discussed system. Below we present the theoretical analysis supporting observed experimental results.

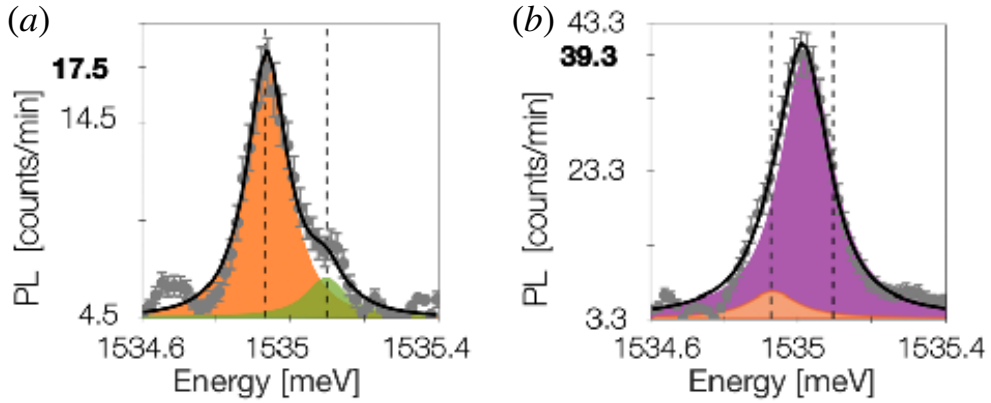

Figure 6.5: Experimental PL spectrum at $T = 330mK$ of $\langle n \rangle = 0.5$ (a) and $\langle n \rangle = 1.0$ (b) filled lattices together with theoretical simulations (ED, black solid line). The simulation assigned a 90% fraction for excitons in the 1WS (orange, violet in panel (b)) and 10% in the 2WS (green, orange in panel (b))

.

6.2.3 Exact diagonalisation calculations

For the theoretical description we have considered the extended two-band Bose-Hubbard Hamiltonian, relying on the theoretically expected parameters for t, U, and V, but with increased amplitude of density-density inter-site interactions to match the experimentally measured value of V in the first WS. Specifically, we have taken $V = 35\mu$eV, $V_{2,2} = 250\mu$eV, and $V_{1,2} = 40\mu$eV.

In order to detect CB phases we applying exact diagonalization on a supercell, spanned by $\mathbf{L}_1 = (2, 2)a$ and $\mathbf{L}_2 = (2, -2)a$, a denoting the lattice period, which contains 8 sites of the square lattice. Such unit cell is two times smaller then $4x4$ unit cell and, unlike $2x2$ cell, allows to observe CB phase. In the ED calculation, we fix the particle number to 4 excitons (half filling). From the full eigenspectrum, we calculate thermal expectation values of the observables of interest. One of such observables in a structure factor (SF), i.e Fourier transformed density-density correlation function. The peak of SF at $\mathbf{k}_{\mathrm{CB}} \equiv (\frac{\pi}{a}, \frac{\pi}{a})$ is a hallmark of CB order in the system. Since we are expecting the CB phase within the first Wannier State, we define the SF as:

$$S_1(\mathbf{k}) \sim \sum_{ij} (\langle n_{i1} n_{j,1} \rangle - \langle n_{i1} \rangle \langle n_{j1} \rangle) e^{-i\mathbf{k}\cdot\mathbf{R}_{ij}}, \tag{6.11}$$

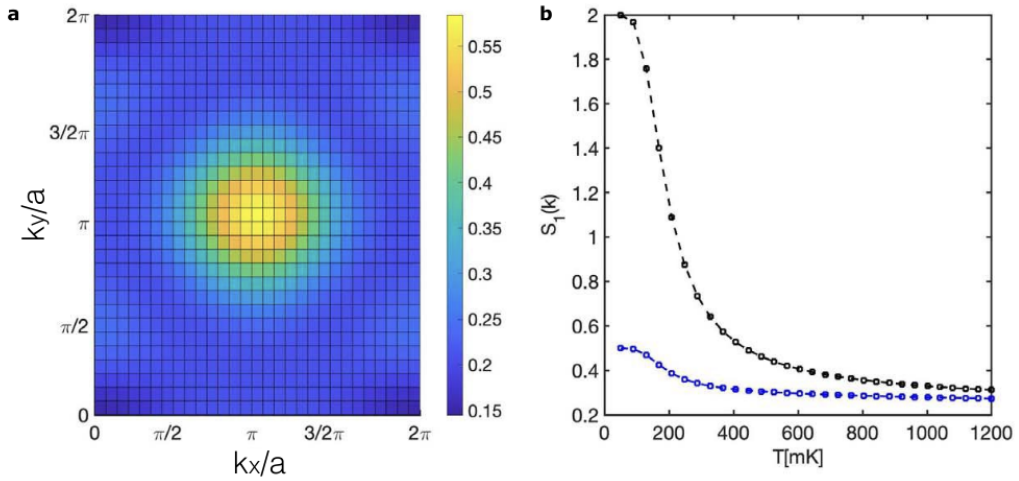

Figure 6.6: Figure originally presented in [43]Lowest band structure factor $S\,1(k)$ at $T = 100mK$ obtained by exact diagonalization of a 8 site square lattice (Betts cluster) with periodic boundary conditions. It exhibits a dominant peak at quasi-momentum $k = (\pi/a, \pi/a)$, which is a characteristic signature of CB order. A second strongly suppressed quasi-peak lies at $k = (0, 0)$ (due to finite size effects), corresponding to a homogeneous liquid without any density order. b, $|S\,1(\pi/a, \pi/a)|$ (black) and $|S\,1(0, 0)|$ (blue) are plotted versus temperature T. Up to $T \leq T_c = 420mK$, the structure factor signalling CB order remains at least twice as large as the structure factor for a homogeneous liquid.

with $\mathbf{R}_{ij}$ the lattice vector connecting sites i and j, is found to exhibit a pronounced peak at $\mathbf{k}_{\mathrm{CB}}$ (see Fig. 6.6(a)), with a value $|S_1(\mathbf{k}_{\mathrm{CB}})|$ which remains more than twice as large as any other value of $|S_1(\mathbf{k})|$ up to temperatures as large as $T \sim 400mK$ (see Fig. 6.6(b)).

6.2.4 Mean-field calculations

Larger system sizes are studied in the mean-field approximation which reduces the Hamiltonian to a sum of single-site terms, $H^{\mathrm{MF}} = \sum_i (h_i + h_i^{\mathrm{NN}})$, with

$$h_i^{\mathrm{NN}} = \sum_j [-\sum_\alpha t_\alpha (b_{i\alpha}^\dagger \langle b_{j\alpha}\rangle - \langle b_{i\alpha}^\dagger\rangle\langle b_{j\alpha}\rangle + \mathrm{h.c.}) + \sum_{\alpha,\beta} V_{\alpha\beta\beta\alpha}(n_{i\alpha}\langle n_{j\beta}\rangle - \langle n_{i\alpha}\rangle\langle n_{j\beta}\rangle]. \tag{6.12}$$

The sum in j includes all nearest neighbouring sites of i, and for simplicity we restrict ourselves to density-density interactions. On every site, the 4 mean-field values $\langle b_{i1}\rangle$, $\langle b_{i2}\rangle$, $\langle n_{i1}\rangle$, and $\langle n_{i2}\rangle$ have to be chosen such that they self-consistently match the corresponding thermal expectation values obtained from the solution of the mean-field Hamiltonian. In our numerical calculation, the self-consistency loop sweeps through a 4x4 lattice. From the solution of the self-consistent mean-field Hamiltonian, we calculate the phase diagram, shown in Fig. 6.7(b). On panel (a) of the same Figure, we provide a direct order parameter for the CB phase, namely the population mismatch $|\langle n_A - n_B\rangle|$ between the two sub-lattices A and B corresponding to two possible CB phase configurations. CB order is associated with a non-zero value of this order parameter. It is found within a finite interval of the chemical potential around the one corresponding to half filling which shrinks as the temperature is increased, and entirely vanishes at the critical temperature ($\approx$ 420 mK), in good agreement with the experimental observation and with the estimate from ED. Decay of the order parameter can be observed on Fig. 6.7(b) by looking at plots for 4 distinct temperatures: $T = 4, 125, 247, 389, 450\ mK$.

6.3 Conclusions

In this (experimentally) groundbreaking study, we realized Extended Bose-Hubbard model with a square array. The sites of an array are filled by the dipolar excitons, that are created by a flash of light, and the intensity of the light controls their density. Therefore, measuring the light emitted from this array (photo-luminescense) provides a unique fingerprint of the quantum state of the system. Through such measurements, we found that the system is characterized by two special states. First, when each site had only one quasiparticle in it, we detected a Mott insulating state, which occurs when strong interactions between electrons prevent a material from conducting electric charge. Second, when exactly half the sites in the system were occupied, the authors found that neighbouring lattice sites were alternately filled and empty, giving rise to a state resembling a chequerboard pattern. Such a pattern emerges from an exciton's ability to influence the occupancy of neighbouring sites over some distance. The resulting wave in the density of the particles is also observed in real materials, which is why this simulator might prove to be a useful tool for understanding strongly correlated behaviour in bosonic systems. ED and mean-field techniques allowed us to confront the observed phenomena with predictions of the EBH model. While mean field calculations provided, otherwise unachievable, full phase diagram, exact diagonalization gave an insight

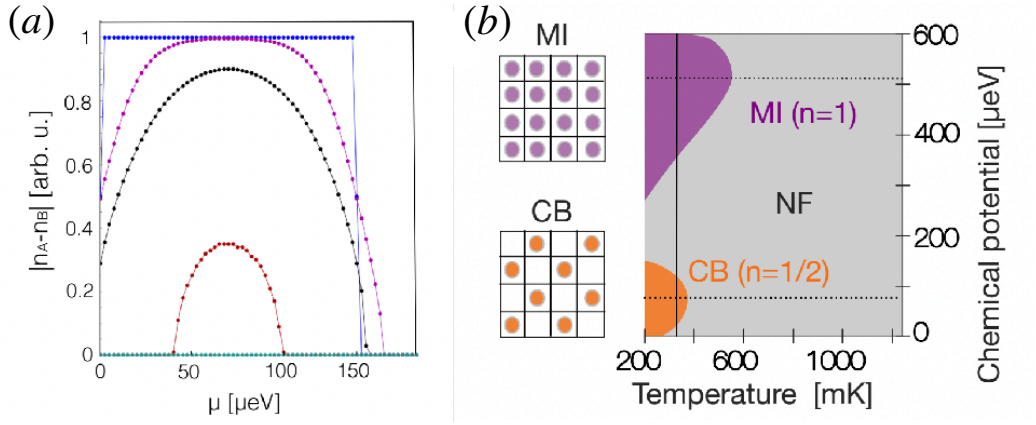

Figure 6.7: Panel (a) illustrates a graph depicting the CB (checkerboard) order parameter, deduced from mean-field calculations, as a function of the chemical potential (μ) and temperature (T). The temperatures indicated are $4, 125, 247, 389, 450$ mK in different color codes. The CB order parameter is given by the absolute difference in population $|n_A - n_B|$ between two sub-lattices, A and B, of the square lattice. The graph indicates that below around 410 mK, this population difference is significant, which manifests the presence of checkerboard (CB) order. Panel (b) presents a phase diagram, computed using a two-band mean-field model. This diagram highlights the existence of three possible phases: Checkerboard (CB), Mott insulator (MI), and Normal fluid (NF). Sketches illustrating the configurations of the CB and MI phases can be found on the left side of the diagram. A vertical line is drawn at the point of lowest bath temperature accessible in the experimental set-up.

.

into microscopic structure of the ground and excited states making it possible to calculate correlators, and therefore, extract the structure factor of the system. Appearance of the peak at the corner of the Brillouin zone for the set of experimentally obtained values of parameters was a final theoretical evidence of CB phase int the lattice.

Bibliography

[1] Fabien Alet, Aleksandra M. Walczak, and Matthew P.A. Fisher. Exotic quantum phases and phase transitions in correlated matter. *Physica A: Statistical Mechanics and its Applications*, 369(1):122–142, sep 2006.

[2] Iurii Ivanovich Manin. *Vychislimoe i nevychislimoe*. "Sov. radio, ", Moskva, 1980.

[3] Richard P Feynman. Simulating physics with computers. *International Journal of Theoretical Physics*, 21(6):467–488, June 1982.

[4] Andreas Trabesinger. Quantum simulation. *Nature Physics*, 8(4):263–263, April 2012.

[5] D. Jaksch, C. Bruder, J. I. Cirac, C. W. Gardiner, and P. Zoller. Cold bosonic atoms in optical lattices. *Phys. Rev. Lett.*, 81:3108–3111, Oct 1998.

[6] Markus Greiner, Olaf Mandel, Tilman Esslinger, Theodor W. Hänsch, and Immanuel Bloch. Quantum phase transition from a superfluid to a mott insulator in a gas of ultracold atoms. *Nature*, 415(6867):39–44, Jan 2002.

[7] Youngseok Kim, Andrew Eddins, Sajant Anand, Ken Wei, Ewout Berg, Sami Rosenblatt, Hasan Nayfeh, Yantao Wu, Michael Zaletel, Kristan Temme, and Abhinav Kandala. Evidence for the utility of quantum computing before fault tolerance. *Nature*, 618:500–505, 06 2023.

[8] William J. Huggins, Jarrod R. McClean, Nicholas C. Rubin, Zhang Jiang, Nathan Wiebe, K. Birgitta Whaley, and Ryan Babbush. Efficient and noise resilient measurements for quantum chemistry on near-term quantum computers. *npj Quantum Information*, 7(1):23, Feb 2021.

[9] Alexander J. McCaskey, Zachary P. Parks, Jacek Jakowski, Shirley V. Moore, Titus D. Morris, Travis S. Humble, and Raphael C. Pooser. Quantum chemistry as a benchmark for near-term quantum computers. *npj Quantum Information*, 5(1):99, Nov 2019.

[10] Kishor Bharti, Alba Cervera-Lierta, Thi Ha Kyaw, Tobias Haug, Sumner Alperin-Lea, Abhinav Anand, Matthias Degroote, Hermanni Heimonen, Jakob S. Kottmann, Tim Menke, Wai-Keong Mok, Sukin Sim, Leong-Chuan Kwek, and Alán Aspuru-Guzik. Noisy intermediate-scale quantum algorithms. *Rev. Mod. Phys.*, 94:015004, Feb 2022.

[11] Yudong Cao, Jonathan Romero, Jonathan P. Olson, Matthias Degroote, Peter D. Johnson, Má ria Kieferová, Ian D. Kivlichan, Tim Menke, Borja Peropadre, Nicolas P. D. Sawaya, Sukin Sim, Libor Veis, and Alán Aspuru-Guzik. Quantum chemistry in the age of quantum computing. *Chemical Reviews*, 119(19):10856–10915, aug 2019.

[12] Ruslan N. Tazhigulov, Shi-Ning Sun, Reza Haghshenas, Huanchen Zhai, Adrian T. K. Tan, Nicholas C. Rubin, Ryan Babbush, Austin J. Minnich, and Garnet Kin-Lic Chan. Simulating challenging correlated molecules and materials on the sycamore quantum processor, 2022.

[13] Nikolaj Moll, Panagiotis Barkoutsos, Lev S Bishop, Jerry M Chow, Andrew Cross, Daniel J Egger, Stefan Filipp, Andreas Fuhrer, Jay M Gambetta, Marc Ganzhorn, Abhinav Kandala, Antonio Mezzacapo, Peter Müller, Walter Riess, Gian Salis, John Smolin, Ivano Tavernelli, and Kristan Temme. Quantum optimization using variational algorithms on near-term quantum devices. *Quantum Science and Technology*, 3(3):030503, jun 2018.

[14] Daniel Stilck França and Raul García-Patrón. Limitations of optimization algorithms on noisy quantum devices. *Nature Physics*, 17(11):1221–1227, 2021.

[15] Frank Arute, Kunal Arya, Ryan Babbush, Dave Bacon, Joseph C. Bardin, Rami Barends, Rupak Biswas, Sergio Boixo, Fernando G. S. L. Brandao, David A. Buell, Brian Burkett, Yu Chen, Zijun Chen, Ben Chiaro, Roberto Collins, William Courtney, Andrew Dunsworth, Edward Farhi, Brooks Foxen, Austin Fowler, Craig Gidney, Marissa Giustina, Rob Graff, Keith Guerin, Steve Habegger, Matthew P. Harrigan, Michael J. Hartmann, Alan

Ho, Markus Hoffmann, Trent Huang, Travis S. Humble, Sergei V. Isakov, Evan Jeffrey, Zhang Jiang, Dvir Kafri, Kostyantyn Kechedzhi, Julian Kelly, Paul V. Klimov, Sergey Knysh, Alexander Korotkov, Fedor Kostritsa, David Landhuis, Mike Lindmark, Erik Lucero, Dmitry Lyakh, Salvatore Mandrà, Jarrod R. McClean, Matthew McEwen, Anthony Megrant, Xiao Mi, Kristel Michielsen, Masoud Mohseni, Josh Mutus, Ofer Naaman, Matthew Neeley, Charles Neill, Murphy Yuezhen Niu, Eric Ostby, Andre Petukhov, John C. Platt, Chris Quintana, Eleanor G. Rieffel, Pedram Roushan, Nicholas C. Rubin, Daniel Sank, Kevin J. Satzinger, Vadim Smelyanskiy, Kevin J. Sung, Matthew D. Trevithick, Amit Vainsencher, Benjamin Villalonga, Theodore White, Z. Jamie Yao, Ping Yeh, Adam Zalcman, Hartmut Neven, and John M. Martinis. Quantum supremacy using a programmable superconducting processor. *Nature*, 574(7779):505–510, 2019.

[16] James King, Sheir Yarkoni, Jack Raymond, Isil Ozfidan, Andrew D. King, Mayssam Mohammadi Nevisi, Jeremy P. Hilton, and Catherine C. McGeoch. Quantum annealing amid local ruggedness and global frustration. *Journal of the Physical Society of Japan*, 88(6):061007, 2019.

[17] G. S. Paraoanu. Recent progress in quantum simulation using superconducting circuits. *Journal of Low Temperature Physics*, 175(5-6):633–654, 2014.

[18] Alexandre Blais, Arne L. Grimsmo, S. M. Girvin, and Andreas Wallraff. Circuit quantum electrodynamics. *Rev. Mod. Phys.*, 93:025005, May 2021.

[19] Maciej Lewenstein, Anna Sanpera, and Verònica Ahufinger. *Ultracold Atoms in Optical Lattices: Simulating quantum many-body systems*. Oxford University Press, Oxford, 2012.

[20] J. Zhang, G. Pagano, P. W. Hess, A. Kyprianidis, P. Becker, H. Kaplan, A. V. Gorshkov, Z.-X. Gong, and C. Monroe. Observation of a many-body dynamical phase transition with a 53-qubit quantum simulator. *Nature*, 551(7682):601–604, nov 2017.

[21] C. Monroe, W. C. Campbell, L.-M. Duan, Z.-X. Gong, A. V. Gorshkov, P. W. Hess, R. Islam, K. Kim, N. M. Linke, G. Pagano, P. Richerme, C. Senko, and N. Y. Yao. Programmable quantum simulations of spin systems with trapped ions. *Rev. Mod. Phys.*, 93:025001, Apr 2021.

[22] Martin Ringbauer, Michael Meth, Lukas Postler, Roman Stricker, Rainer Blatt, Philipp Schindler, and Thomas Monz. A universal qudit quantum processor with trapped ions, 2021.

[23] Hannes Bernien, Sylvain Schwartz, Alexander Keesling, Harry Levine, Ahmed Omran, Hannes Pichler, Soonwon Choi, Alexander S. Zibrov, Manuel Endres, Markus Greiner, Vladan Vuletic, and Mikhail D. Lukin. Probing many-body dynamics on a 51-atom quantum simulator. *Nature*, 551:579–, November 2017.

[24] D. Bluvstein, A. Omran, H. Levine, A. Keesling, G. Semeghini, S. Ebadi, T. T. Wang, A. A. Michailidis, N. Maskara, W. W. Ho, S. Choi, M. Serbyn, M. Greiner, V. Vuletic, and M. D. Lukin. Controlling quantum many-body dynamics in driven rydberg atom arrays. *Science*, 371(6536):1355–1359, 2021.

[25] Pascal Scholl, Michael Schuler, Hannah J. Williams, Alexander A. Eberharter, Daniel Barredo, Kai-Niklas Schymik, Vincent Lienhard, Louis-Paul Henry, Thomas C. Lang, Thierry Lahaye, Andreas M. Läuchli, and Antoine Browaeys. Quantum simulation of 2d antiferromagnets with hundreds of rydberg atoms. *Nature*, 595(7866):233–238, jul 2021.

[26] E Knill, R Laflamme, and G Milburn. A scheme for efficient quantum computation with linear optics. *Nature*, 409:46–52, 02 2001.

[27] Shahaf Asban and Shaul Mukamel. Scattering-based geometric shaping of photon-photon interactions. *Phys. Rev. Lett.*, 123:260502, Dec 2019.

[28] F. Schlawin, D. M. Kennes, and M. A. Sentef. Cavity quantum materials. *Applied Physics Reviews*, 9(1):011312, mar 2022.

[29] Logan W. Clark, Nathan Schine, Claire Baum, Ningyuan Jia, and Jonathan Simon. Observation of laughlin states made of light. *Nature*, 582(7810):41–45, jun 2020.

[30] Iacopo Carusotto, Andrew Houck, Alicia Kollár, Pedram Roushan, David Schuster, and Jonathan Simon. Photonic materials in circuit quantum electrodynamics. *Nature Physics*, 16, 03 2020.

[31] Ruichao Ma, Brendan Saxberg, Clai Owens, Nelson Leung, Yao Lu, Jonathan Simon, and David I. Schuster. A dissipatively stabilized mott insulator of photons. *Nature*, 566(7742):51–57, feb 2019.

[32] Nathan Schine, Albert Ryou, Andrey Gromov, Ariel Sommer, and Jonathan Simon. Synthetic landau levels for photons. *Nature*, 534(7609):671–675, jun 2016.

[33] Yuan Cao, Daniel Rodan-Legrain, Oriol Rubies-Bigorda, Jeong Min Park, Kenji Watanabe, Takashi Taniguchi, and Pablo Jarillo-Herrero. Tunable correlated states and spin-polarized phases in twisted bilayer–bilayer graphene. *Nature*, 583(7815):215–220, may 2020.

[34] Petr Stepanov, Ipsita Das, Xiaobo Lu, Ali Fahimniya, Kenji Watanabe, Takashi Taniguchi, Frank H. L. Koppens, Johannes Lischner, Leonid Levitov, and Dmitri K. Efetov. Untying the insulating and superconducting orders in magic-angle graphene. *Nature*, 583(7816):375–378, jul 2020.

[35] Dante Kennes, Martin Claassen, Lede Xian, Antoine Georges, Andrew Millis, James Hone, Cory Dean, D. Basov, Abhay Pasupathy, and Angel Rubio. Moiré heterostructures as a condensed-matter quantum simulator. *Nature Physics*, 17:1–9, 02 2021.

[36] Tymoteusz Salamon, Alessio Celi, Ravindra W. Chhajlany, Irénée Frérot, Maciej Lewenstein, Leticia Tarruell, and Debraj Rakshit. Simulating twistronics without a twist. *Phys. Rev. Lett.*, 125:030504, Jul 2020.

[37] D. N. Basov, Ana Asenjo-Garcia, P. James Schuck, Xiaoyang Zhu, and Angel Rubio. Polariton panorama. *Nanophotonics*, 10(1):549–577, 2021.

[38] Hannes Hübener, Umberto De Giovannini, Christian Schäfer, Johan Andberger, Michael Ruggenthaler, Jerome Faist, and Angel Rubio. Engineering quantum materials with chiral optical cavities. *Nat Mater*, 20(4):438–442, April 2021.

[39] Thomas Boulier, Maxime J. Jacquet, Anne Maître, Giovanni Lerario, Ferdinand Claude, Simon Pigeon, Quentin Glorieux, Alberto Amo, Jacqueline Bloch, Alberto Bramati, and Elisabeth Giacobino. Microcavity polaritons for quantum simulation. *Advanced Quantum Technologies*, 3(11):2000052, 2020.

[40] Tymoteusz Salamon, Alessio Celi, Ravindra W. Chhajlany, Irénée Frérot, Maciej Lewenstein, Leticia Tarruell, and Debraj Rakshit. Simulating twistronics without a twist. *Phys. Rev. Lett.*, 125:030504, Jul 2020.

[41] Tymoteusz Salamon, Ravindra W. Chhajlany, Alexandre Dauphin, Maciej Lewenstein, and Debraj Rakshit. Quantum anomalous hall phase in synthetic bilayers via twistronics without a twist. *Phys. Rev. B*, 102:235126, Dec 2020.

[42] Tymoteusz Salamon, Bernhard Irsigler, Debraj Rakshit, Maciej Lewenstein, Tobias Grass, and Ravindra Chhajlany. Flat-band-induced superconductivity in synthetic bilayer optical lattices. *Phys. Rev. B*, 106:174503, Nov 2022.

[43] C. Lagoin, U. Bhattacharya, T. Grass, R. W. Chhajlany, T. Salamon, K. Baldwin, L. Pfeiffer, M. Lewenstein, M. Holzmann, and F. Dubin. Extended bose–hubbard model with dipolar excitons. *Nature*, 609(7927):485–489, sep 2022.

[44] Sergi Julià -Farré, Tymoteusz Salamon, Arnau Riera, Manabendra N. Bera, and Maciej Lewenstein. Bounds on the capacity and power of quantum batteries. *Physical Review Research*, 2(2), may 2020.

[45] E. Suá rez Morell, J. D. Correa, P. Vargas, M. Pacheco, and Z. Barticevic. Flat bands in slightly twisted bilayer graphene: Tight-binding calculations. *Physical Review B*, 82(12), sep 2010.

[46] Rafi Bistritzer and Allan H. MacDonald. Moiré bands in twisted double-layer graphene. *Proceedings of the National Academy of Sciences*, 108(30):12233–12237, 2011.

[47] J. M. B. Lopes dos Santos, N. M. R. Peres, and A. H. Castro Neto. Continuum model of the twisted graphene bilayer. *Physical Review B*, 86(15), oct 2012.

[48] Pilkyung Moon and Mikito Koshino. Energy spectrum and quantum hall effect in twisted bilayer graphene. *Physical Review B*, 85(19), may 2012.

[49] Grigory Tarnopolsky, Alex Jura Kruchkov, and Ashvin Vishwanath. Origin of magic angles in twisted bilayer graphene. *Physical Review Letters*, 122(10), mar 2019.

[50] Nicolas Regnault, Yuanfeng Xu, Ming-Rui Li, Da-Shuai Ma, Milena Jovanovic, Ali Yazdani, Stuart S. P. Parkin, Claudia Felser, Leslie M. Schoop, N. Phuan Ong, Robert J. Cava, Luis Elcoro, Zhi-Da Song, and B. Andrei Bernevig. Catalogue of flat-band stoichiometric materials. *Nature*, 603(7903):824–828, mar 2022.

[51] Stephen Carr, Daniel Massatt, Shiang Fang, Paul Cazeaux, Mitchell Luskin, and Efthimios Kaxiras. Twistronics: Manipulating the electronic properties of two-dimensional layered structures through their twist angle. *Physical Review B*, 95:075420, Feb 2017.

[52] J. M. B. Lopes dos Santos, N. M. R. Peres, and A. H. Castro Neto. Graphene bilayer with a twist: Electronic structure. *Phys. Rev. Lett.*, 99:256802, Dec 2007.

[53] E. Suárez Morell, J. D. Correa, P. Vargas, M. Pacheco, and Z. Barticevic. Flat bands in slightly twisted bilayer graphene: Tight-binding calculations. *Phys. Rev. B*, 82:121407, Sep 2010.

[54] Yuan Cao, Valla Fatemi, Shiang Fang, Kenji Watanabe, Takashi Taniguchi, Efthimios Kaxiras, and Pablo Jarillo-Herrero. Unconventional superconductivity in magic-angle graphene superlattices. *Nature*, 556(7699):43–50, mar 2018.

[55] Yuan Cao, Valla Fatemi, Ahmet Demir, Shiang Fang, Spencer L. Tomarken, Jason Luo, Javier D Sanchez-Yamagishi, Kenji Watanabe, Takashi Taniguchi, Efthimios Kaxiras, Ray Ashoori, and Pablo Jarillo-Herrero. Correlated insulator behaviour at half-filling in magic-angle graphene superlattices. *Nature*, 556:80–84, 2018.

[56] Matthew Yankowitz, Shaowen Chen, Hryhoriy Polshyn, Yuxuan Zhang, K. Watanabe, T. Taniguchi, David Graf, Andrea F. Young, and Cory R. Dean. Tuning superconductivity in twisted bilayer graphene. *Science*, 363(6431):1059–1064, 2019.

[57] Xiaobo Lu, Petr Stepanov, Wei Yang, Ming Xie, Mohammed Ali Aamir, Ipsita Das, Carles Urgell, Kenji Watanabe, Takashi Taniguchi, Guangyu Zhang, and et al. Superconductors, orbital magnets and correlated states in magic-angle bilayer graphene. *Nature*, 574(7780):653–657, Oct 2019.

[58] G. E. Volovik. Graphite, graphene, and the flat band superconductivity. *JETP Letters*, 107(8):516–517, Apr 2018.

[59] Noah F. Q. Yuan and Liang Fu. Model for the metal-insulator transition in graphene superlattices and beyond. *Phys. Rev. B*, 98:045103, Jul 2018.

[60] Mikito Koshino, Noah F. Q. Yuan, Takashi Koretsune, Masayuki Ochi, Kazuhiko Kuroki, and Liang Fu. Maximally localized wannier orbitals and the extended hubbard model for twisted bilayer graphene. *Phys. Rev. X*, 8:031087, Sep 2018.

[61] Masayuki Ochi, Mikito Koshino, and Kazuhiko Kuroki. Possible correlated insulating states in magic-angle twisted bilayer graphene under strongly competing interactions. *Phys. Rev. B*, 98:081102, Aug 2018.

[62] Liujun Zou, Hoi Chun Po, Ashvin Vishwanath, and T. Senthil. Band structure of twisted bilayer graphene: Emergent symmetries, commensurate approximants, and wannier obstructions. *Phys. Rev. B*, 98:085435, Aug 2018.

[63] Teemu J. Peltonen, Risto Ojajärvi, and Tero T. Heikkilä. Mean-field theory for superconductivity in twisted bilayer graphene. *Physical Review B*, 98(22):220504, Dec 2018.

[64] Bikash Padhi, Chandan Setty, and Philip W. Phillips. Doped twisted bilayer graphene near magic angles: Proximity to wigner crystallization, not mott insulation. *Nano Letters*, 18(10):6175–6180, Sep 2018.

[65] A. O. Sboychakov, A. V. Rozhkov, A. L. Rakhmanov, and Franco Nori. Many-body effects in twisted bilayer graphene at low twist angles. *Physical Review B*, 100(4):045111, Jul 2019.

[66] Francisco Guinea and Niels R. Walet. Electrostatic effects, band distortions, and superconductivity in twisted graphene bilayers. *Proceedings of the National Academy of Sciences*, 115(52):13174–13179, Dec 2018.

[67] Xiao Yan Xu, K. T. Law, and Patrick A. Lee. Kekulé valence bond order in an extended hubbard model on the honeycomb lattice with possible applications to twisted bilayer graphene. *Physical Review B*, 98(12):121406, Sep 2018.

[68] Fengcheng Wu, A. H. MacDonald, and Ivar Martin. Theory of phonon-mediated superconductivity in twisted bilayer graphene. *Physical Review Letters*, 121:257001, Dec 2018.

[69] Hiroki Isobe, Noah F. Q. Yuan, and Liang Fu. Unconventional superconductivity and density waves in twisted bilayer graphene. *Phys. Rev. X*, 8:041041, Dec 2018.

[70] Yi-Zhuang You and Ashvin Vishwanath. Superconductivity from valley fluctuations and approximate so (4) symmetry in a weak coupling theory of twisted bilayer graphene. *Quantum Materials*, 4(16), 2019.

[71] Biao Lian, Zhijun Wang, and B. Andrei Bernevig. Twisted bilayer graphene: A phonon-driven superconductor. *Physical Review Letters*, 122:257002, Jun 2019.

[72] Yu-Ping Lin and Rahul M. Nandkishore. Chiral twist on the high-T_c phase diagram in moiré heterostructures. *Physical Review B*, 100:085136, Aug 2019.

[73] Zhida Song, Zhijun Wang, Wujun Shi, Gang Li, Chen Fang, and B. Andrei Bernevig. All magic angles in twisted bilayer graphene are topological. *Physical Review Letters*, 123:036401, Jul 2019.

[74] Leon Balents, Cory Dean, Dmitri Efetov, and Andrea Young. Superconductivity and strong correlations in moiré flat bands. *Nature Physics*, 16:725–733, 05 2020.

[75] A. K. Geim and I. V. Grigorieva. Van der waals heterostructures. *Nature*, 499(7459):419–425, jul 2013.

[76] Marco Polini, Francisco Guinea, Maciej Lewenstein, Hari Manoharan, and Vittorio Pellegrini. Artificial graphene as a tunable dirac material. *Nature Nanotechnology*, 8:625, 04 2013.

[77] Antonio Acín, Immanuel Bloch, Harry Buhrman, Tommaso Calarco, Christopher Eichler, Jens Eisert, Daniel Esteve, Nicolas Gisin, Steffen J Glaser, Fedor Jelezko, Stefan Kuhr, Maciej Lewenstein, Max F Riedel, Piet O Schmidt, Rob Thew, Andreas Wallraff, Ian Walmsley, and Frank K Wilhelm. The quantum technologies roadmap: a european community view. *New Journal of Physics*, 20(8):080201, aug 2018.

[78] Immanuel Bloch, Jean Dalibard, and Wilhelm Zwerger. Many-body physics with ultracold gases. *Reviews of Modern Physics*, 80(3):885–964, Jul 2008.

[79] J. Cirac and Peter Zoller. Goals and opportunities in quantum simulation. *Nature Physics*, 8:264–266, 04 2012.

[80] Immanuel Bloch, Jean Dalibard, and Sylvain Nascimbène. Quantum simulations with ultracold quantum gases. *Nature Physics*, 8:267, 2012.

[81] R. Blatt and Christian Roos. Quantum simulations with trapped ions. *Nature Physics*, 8:277–284, 04 2012.

[82] Alán Aspuru-Guzik and Philip Walther. Photonic quantum simulators. *Nature Physics*, 8:285, 04 2012.

[83] Andrew Houck, Hakan Tureci, and Jens Koch. On-chip quantum simulation with superconducting circuits. *Nature Physics*, 8:292–299, 04 2012.

[84] Maciej Lewenstein, Anna Sanpera, and Verònica Ahufinger. *Ultracold Atoms in Optical Lattices: Simulating quantum many-body systems*. Oxford University Press, Oxford, 2012.

[85] P. Soltan-Panahi, J. Struck, P. Hauke, A. Bick, W. Plenkers, G. Meineke, C. Becker, P. Windpassinger, M. Lewenstein, and K. Sengstock. Multi-component quantum gases in spin-dependent hexagonal lattices. *Nature Physics*, 7(5):434–440, Feb 2011.

[86] Leticia Tarruell, Daniel Greif, Thomas Uehlinger, Gregor Jotzu, and Tilman Esslinger. Creating, moving and merging dirac points with a fermi gas in a tunable honeycomb lattice. *Nature*, 483(7389):302–305, Mar 2012.

[87] Gyu-Boong Jo, Jennie Guzman, Claire K. Thomas, Pavan Hosur, Ashvin Vishwanath, and Dan M. Stamper-Kurn. Ultracold atoms in a tunable optical kagome lattice. *Physical Review Letters*, 108(4):045305, Jan 2012.

[88] Shintaro Taie, Hideki Ozawa, Tomohiro Ichinose, Takuei Nishio, Shuta Nakajima, and Yoshiro Takahashi. Coherent driving and freezing of bosonic matter wave in an optical lieb lattice. *Science Advances*, 1:e1500854–e1500854, 11 2015.

[89] Hideki Ozawa, Shintaro Taie, Tomohiro Ichinose, and Yoshiro Takahashi. Interaction-driven shift and distortion of a flat band in an optical lieb lattice. *Physical Review Letters*, 118:175301, Apr 2017.

[90] L. Guidoni, C. Triché, P. Verkerk, and G. Grynberg. Quasiperiodic optical lattices. *Physical Review Letters*, 79:3363–3366, Nov 1997.

[91] Konrad Viebahn, Matteo Sbroscia, Edward Carter, Jr-Chiun Yu, and Ulrich Schneider. Matter-wave diffraction from a quasicrystalline optical lattice. *Physical Review Letters*, 122:110404, Mar 2019.

[92] Shankari V. Rajagopal, Toshihiko Shimasaki, Peter Dotti, Mantas Račiūnas, Ruwan Senaratne, Egidijus Anisimovas, André Eckardt, and David M. Weld. Phasonic spectroscopy of a quantum gas in a quasicrystalline lattice. *Physical Review Letters*, 123(22), Nov 2019.

[93] A. González-Tudela and J. I. Cirac. Cold atoms in twisted-bilayer optical potentials. *Physical Review A*, 100(5):053604, Nov 2019.

[94] Tobias Graß, Ravindra W Chhajlany, Leticia Tarruell, Vittorio Pellegrini, and Maciej Lewenstein. Proximity effects in cold atom artificial graphene. *2D Materials*, 4(1):015039, Dec 2016.

[95] O. Boada, A. Celi, J. I. Latorre, and M. Lewenstein. Quantum simulation of an extra dimension. *Physical Review Letters*, 108(13):133001, Mar 2012.

[96] A. Celi, P. Massignan, J. Ruseckas, N. Goldman, I. B. Spielman, G. Juzeliūnas, and M. Lewenstein. Synthetic gauge fields in synthetic dimensions. *Physical Review Letters*, 112:043001, Jan 2014.

[97] Tomoki Ozawa and Hannah M. Price. Topological quantum matter in synthetic dimensions. *Nature Reviews Physics*, 1(5):349–357, Apr 2019.

[98] Tymoteusz Salamon, Alessio Celi, Ravindra W. Chhajlany, Irénée Frérot, Maciej Lewenstein, Leticia Tarruell, and Debraj Rakshit. Simulating twistronics without a twist. *Physical Review Letters*, 125(3):030504, Jul 2020.

[99] Simon Stellmer, Benjamin Pasquiou, Rudolf Grimm, and Florian Schreck. Laser cooling to quantum degeneracy. *Physical Review Letters*, 110(26):263003, Jun 2013.

[100] Chun-Chia Chen, Shayne Bennetts, Rodrigo González Escudero, Florian Schreck, and Benjamin Pasquiou. Sisyphus optical lattice decelerator. *Physical Review A*, 100(2):023401, Aug 2019.

[101] Elliott H. Lieb. Two theorems on the hubbard model. *Phys. Rev. Lett.*, 62:1201–1204, Mar 1989.

[102] Ruohao Shen, L. Shao, Baigeng Wang, and D. Xing. Single dirac cone with a flat band touching on line-centered-square optical lattices. *Physical Review B*, 81:41410–, 01 2010.

[103] Alexander Kerelsky, Leo J. McGilly, Dante M. Kennes, Lede Xian, Matthew Yankowitz, Shaowen Chen, K. Watanabe, T. Taniguchi, James Hone, Cory Dean, Angel Rubio, and Abhay N. Pasupathy. Maximized electron interactions at the magic angle in twisted bilayer graphene. *Nature*, 572(7767):95–100, jul 2019.

[104] Noah F. Q. Yuan, Hiroki Isobe, and Liang Fu. Magic of high-order van hove singularity. *Nature Communications*, 10(1), dec 2019.

[105] J. Gonzá lez and T. Stauber. Kohn-luttinger superconductivity in twisted bilayer graphene. *Physical Review Letters*, 122(2), jan 2019.

[106] Moon Park, Youngkuk Kim, Gil Cho, and Sungbin Lee. Higher-order topological insulator in twisted bilayer graphene. *Physical Review Letters*, 123:216803, 11 2019.

[107] Chao Ma, Qiyue Wang, Scott Mills, Xiaolong Chen, Bingchen Deng, Shaofan Yuan, Cheng Li, Kenji Watanabe, Takashi Taniguchi, Du Xu, Fan Zhang, and Fengnian Xia. Discovery of high dimensional band topology in twisted bilayer graphene, 2019.

[108] Shinsei Ryu, Andreas P Schnyder, Akira Furusaki, and Andreas W W Ludwig. Topological insulators and superconductors: tenfold way and dimensional hierarchy. *New Journal of Physics*, 12(6):065010, jun 2010.

[109] John Michael Kosterlitz. Nobel lecture: Topological defects and phase transitions. *Reviews of Modern Physics*, 89:040501, 2017.

[110] F. Duncan M. Haldane. Nobel lecture: Topological quantum matter. *Reviews of Modern Physics*, 89:040502, 2017.

[111] Klaus von Klitzing. The quantized hall effect. *Reviews of Modern Physics*, 58:519, 1986.

[112] D. J. Thouless, M. Kohmoto, M. P. Nightingale, and M. den Nijs. Quantized hall conductance in a two-dimensional periodic potential. *Physical Review Letters*, 49:405, 1982.

[113] F. D. M. Haldane. Model for a quantum hall effect without landau levels: Condensed-matter realization of the "parity anomaly". *Physical Review Letters*, 61:2015, 1988.

[114] C. L. Kane and E. J. Mele. Quantum spin hall effect in graphene. *Physical Review Letters*, 95(22):226801, Nov 2005.

[115] C. L. Kane and E. J. Mele. Z_2 topological order and the quantum spin hall effect. *Physical Review Letters*, 95:146802, Sep 2005.

[116] M. Z. Hasan and C. L. Kane. Colloquium: Topological insulators. *Rev. Mod. Phys.*, 82:3045–3067, Nov 2010.

[117] Xiao-Liang Qi and Shou-Cheng Zhang. Topological insulators and superconductors. *Reviews of Modern Physics*, 83(4):1057–1110, Oct 2011.

[118] Wladimir A. Benalcazar, B. Andrei Bernevig, and Taylor L. Hughes. Quantized electric multipole insulators. *Science*, 357(6346):61–66, 2017.

[119] Takahiro Fukui, Yasuhiro Hatsugai, and Hiroshi Suzuki. Chern numbers in discretized brillouin zone: Efficient method of computing (spin) hall conductances. *Journal of the Physical Society of Japan*, 74(6):1674–1677, Jun 2005.

[120] Masatoshi Sato and Yoichi Ando. Topological superconductors: a review. *Reports on Progress in Physics*, 80(7):076501, may 2017.

[121] N. Y. Yao, C. R. Laumann, A. V. Gorshkov, S. D. Bennett, E. Demler, P. Zoller, and M. D. Lukin. Topological flat bands from dipolar spin systems. *Physical Review Letters*, 109(26):266804, Dec 2012.

[122] Yujun Deng, Yijun Yu, Meng Zhu Shi, Zhongxun Guo, Zihan Xu, Jing Wang, Xian Hui Chen, and Yuanbo Zhang. Quantum anomalous hall effect in intrinsic magnetic topological insulator mnbi2te4. *Science*, 367(6480):895–900, 2020.

[123] Cui-Zu Chang, Jinsong Zhang, Xiao Feng, Jie Shen, Zuocheng Zhang, Minghua Guo, Kang Li, Yunbo Ou, Pang Wei, Li-Li Wang, Zhong-Qing Ji, Yang Feng, Shuaihua Ji, Xi Chen, Jinfeng Jia, Xi Dai, Zhong Fang, Shou-Cheng Zhang, Ke He, Yayu Wang, Li Lu, Xu-Cun Ma, and Qi-Kun Xue. Experimental observation of the quantum anomalous hall effect in a magnetic topological insulator. *Science*, 340(6129):167–170, 2013.

[124] Guorui Chen, A. Sharpe, E. Fox, Yahui Zhang, Shaoxin Wang, L. Jiang, B. Lyu, Hongyuan Li, K. Watanabe, T. Taniguchi, Z. Shi, T. Senthil, D. Goldhaber-Gordon, Y. Zhang, and F. Wang. Tunable correlated chern insulator and ferromagnetism in a moiré superlattice. *Nature*, 579:56–61, 2020.

[125] M. Serlin, C. L. Tschirhart, H. Polshyn, Y. Zhang, J. Zhu, K. Watanabe, T. Taniguchi, L. Balents, and A. F. Young. Intrinsic quantized anomalous hall effect in a moiré heterostructure. *Science*, 367(6480):900–903, 2020.

[126] Stephan Rachel. Interacting topological insulators: a review. *Reports on Progress in Physics*, 81(11):116501, oct 2018.

[127] R. B. Laughlin. Nobel lecture: Fractional quantization. *Reviews of Modern Physics*, 71:863, 1999.

[128] Daniel C. Tsui. Nobel lecture: Interplay of disorder and interaction in two-dimensional electron gas in intense magnetic fields. *Reviews of Modern Physics*, 71:891, 1999.

[129] Horst L. Stormer. Nobel lecture: The fractional quantum hall effect. *Reviews of Modern Physics*, 71:875, 1999.

[130] N. Regnault and B. Andrei Bernevig. Fractional chern insulator. *Phys. Rev. X*, 1:021014, Dec 2011.

[131] N. Y. Yao, A. V. Gorshkov, C. R. Laumann, A. M. Läuchli, J. Ye, and M. D. Lukin. Realizing fractional chern insulators in dipolar spin systems. *Physical Review Letters*, 110:185302, 2013.

[132] Tianhan Liu, C. Repellin, B. Andrei Bernevig, and N. Regnault. Fractional chern insulators beyond laughlin states. *Physical Review B*, 87:205136, 2013.

[133] Adolfo G. Grushin, Johannes Motruk, Michael P. Zaletel, and Frank Pollmann. Characterization and stability of a fermionic $\nu = 1/3$ fractional chern insulator. *Physical Review B*, 91:035136, 2015.

[134] S. Raghu, Xiao-Liang Qi, C. Honerkamp, and Shou-Cheng Zhang. Topological mott insulators. *Physical Review Letters*, 100:156401, 2008.

[135] Kai Sun and Eduardo Fradkin. Time-reversal symmetry breaking and spontaneous anomalous hall effect in fermi fluids. *Physical Review B*, 78:245122, 2008.

[136] A. Dauphin, M. Müller, and M. A. Martin-Delgado. Rydberg-atom quantum simulation and chern-number characterization of a topological mott insulator. *Physical Review A*, 86:053618, 2012.

[137] Eduardo V. Castro, Adolfo G. Grushin, Belén Valenzuela, María A. H. Vozmediano, Alberto Cortijo, and Fernando de Juan. Topological fermi liquids from coulomb interactions in the doped honeycomb lattice. *Physical Review Letters*, 107:106402, Sep 2011.

[138] Adolfo G. Grushin, Eduardo V. Castro, Alberto Cortijo, Fernando de Juan, María A. H. Vozmediano, and Belén Valenzuela. Charge instabilities and topological phases in the extended hubbard model on the honeycomb lattice with enlarged unit cell. *Physical Review B*, 87:085136, Feb 2013.

[139] Tian-Sheng Zeng, Wei Zhu, and Donna Sheng. Tuning topological phase and quantum anomalous hall effect by interaction in quadratic band touching systems. *npj Quantum Mater.*, 3:49, 2018.

[140] Shouvik Sur, Shou-Shu Gong, Kun Yang, and Oskar Vafek. Quantum anomalous hall insulator stabilized by competing interactions. *Physical Review B*, 98:125144, 2018.

[141] D Jaksch and P Zoller. Creation of effective magnetic fields in optical lattices: the hofstadter butterfly for cold neutral atoms. *New Journal of Physics*, 5:56–56, may 2003.

[142] N. Goldman, G. Juzeliūnas, P. Öhberg, and I. B. Spielman. Light-induced gauge fields for ultracold atoms. *Reports on Progress in Physics*, 77:126401, 2014.

[143] Monika Aidelsburger, Sylvain Nascimbene, and Nathan Goldman. Artificial gauge fields in materials and engineered systems. *Comptes Rendus Physique*, 19(6):394 – 432, 2018.

[144] A. Eckardt, P. Hauke, P. Soltan-Panahi, C. Becker, K. Sengstock, and M. Lewenstein. Frustrated quantum antiferromagnetism with ultracold bosons in a triangular lattice. *Europhysics Letters*, 89(1):10010, Jan 2010.

[145] André Eckardt. Colloquium: Atomic quantum gases in periodically driven optical lattices. *Reviews of Modern Physics*, 89(1):011004, Mar 2017.

[146] M. Aidelsburger, M. Atala, S. Nascimbene, S. Trotzky, Y.-A. Chen, and I. Bloch. Experimental realization of strong effective magnetic fields in optical superlattice potentials. *Applied Physics B*, 113(1):1–11, May 2013.

[147] M. Aidelsburger, M. Atala, M. Lohse, J. T. Barreiro, B. Paredes, and I. Bloch. Realization of the hofstadter hamiltonian with ultracold atoms in optical lattices. *Physical Review Letters*, 111(18):185301, Oct 2013.

[148] Gregor Jotzu, Michael Messer, Rémi Desbuquois, Martin Lebrat, Thomas Uehlinger, Daniel Greif, and Tilman Esslinger. Experimental realization of the topological haldane model with ultracold fermions. *Nature*, 515(7526):237–240, Nov 2014.

[149] Benno S. Rem, Niklas Käming, Matthias Tarnowski, Luca Asteria, Nick Fläschner, Christoph Becker, Klaus Sengstock, and Christof Weitenberg. Identifying quantum phase transitions using artificial neural networks on experimental data. *Nature Physics*, 15(9):917–920, Jul 2019.

[150] Luca Asteria, Duc Thanh Tran, Tomoki Ozawa, Matthias Tarnowski, Benno S. Rem, Nick Fläschner, Klaus Sengstock, Nathan Goldman, and Christof Weitenberg. Measuring quantized circular dichroism in ultracold topological matter. *Nature Physics*, 15(5):449–454, 2019.

[151] B. K. Stuhl, H.-I. Lu, L. M. Aycock, D. Genkina, and I. B. Spielman. Visualizing edge states with an atomic bose gas in the quantum hall regime. *Science*, 349(6255):1514, 2015.

[152] M. Mancini, G. Pagano, G. Cappellini, L. Livi, M. Rider, J. Catani, C. Sias, P. Zoller, M. Inguscio, M. Dalmonte, and L. Fallani. Observation of

chiral edge states with neutral fermions in synthetic hall ribbons. *Science*, 349(6255):1510, 2015.

[153] Samuel Mugel, Alexandre Dauphin, Pietro Massignan, Leticia Tarruell, Maciej Lewenstein, Carlos Lobo, and Alessio Celi. Measuring chern numbers in hofstadter strips. *SciPost Physics*, 3(2):012, 2017.

[154] Dina Genkina, Lauren M Aycock, Hsin-I Lu, Mingwu Lu, Alina M Pineiro, and I B Spielman. Imaging topology of hofstadter ribbons. *New Journal of Physics*, 21(5):053021, 2019.

[155] Peng Wang, Yuanlin Zheng, Xianfeng Chen, Changming Huang, Yaroslav V. Kartashov, Lluis Torner, Vladimir V. Konotop, and Fangwei Ye. Localization and delocalization of light in photonic moiré lattices. *Nature*, 577(7788):42–46, Dec 2019.

[156] C. Weeks and M. Franz. Topological insulators on the lieb and perovskite lattices. *Physical Review B*, 82:085310, 2010.

[157] Yasuhiro Hatsugai. Edge states in the integer quantum hall effect and the riemann surface of the bloch function. *Physical Review B*, 48:11851, 1993.

[158] J Belissard. Change of the chern number at band crossings, 1995.

[159] R. C. Brown, R. Wyllie, S. B. Koller, E. A. Goldschmidt, M. Foss-Feig, and J. V. Porto. Two-dimensional superexchange-mediated magnetization dynamics in an optical lattice. *Science*, 348(6234):540–544, 2015.

[160] Yang-Zhi Chou, Yixing Fu, Justin H. Wilson, E. J. König, and J. H. Pixley. Magic-angle semimetals with chiral symmetry. *Physical Review B*, 101:235121, Jun 2020.

[161] Wei Sun, Bao-Zong Wang, Xiao-Tian Xu, Chang-Rui Yi, Long Zhang, Zhan Wu, Youjin Deng, Xiong-Jun Liu, Shuai Chen, and Jian-Wei Pan. Highly controllable and robust 2d spin-orbit coupling for quantum gases. *Physical Review Letters*, 121:150401, Oct 2018.

[162] Jinhai Mao, Slavisa P. Milovanovic, Misa Anđelkovic, Xinyuan Lai, Yang Cao, Kenji Watanabe, Takashi Taniguchi, Lucian Covaci, Francois M. Peeters, Andre K. Geim, and et al. Evidence of flat bands and correlated states in buckled graphene superlattices. *Nature*, 584(7820):215–220, Aug 2020.

[163] K. Osterloh, M. Baig, L. Santos, P. Zoller, and M. Lewenstein. Cold atoms in non-abelian gauge potentials: From the hofstadter "moth" to lattice gauge theory. *Physical Review Letters*, 95(1):010403, Jun 2005.

[164] Monika Aidelsburger. *Artificial gauge fields and topology with ultracold atoms in optical lattices*. PhD thesis, Faculty of Physics, Ludwig Maximilian University of Munich, 04 2018.

[165] Hirokazu Miyake, Georgios A. Siviloglou, Colin J. Kennedy, William Cody Burton, and Wolfgang Ketterle. Realizing the harper hamiltonian with laser-assisted tunneling in optical lattices. *Physical Review Letters*, 111:185302, Oct 2013.

[166] André Eckardt, Christoph Weiss, and Martin Holthaus. Superfluid-insulator transition in a periodically driven optical lattice. *Physical Review Letters*, 95:260404, Dec 2005.

[167] Alessandro Zenesini, Hans Lignier, Donatella Ciampini, Oliver Morsch, and Ennio Arimondo. Coherent control of dressed matter waves. *Physical Review Letters*, 102:100403, Mar 2009.

[168] Takashi Oka and Hideo Aoki. Photovoltaic hall effect in graphene. *Physical Review B*, 79:081406, Feb 2009.

[169] J. W. McIver, B. Schulte, F.-U. Stein, T. Matsuyama, G. Jotzu, G. Meier, and A. Cavalleri. Light-induced anomalous hall effect in graphene. *Nature Physics*, 16(1):38–41, Nov 2019.

[170] J. Struck, C. Olschlager, R. Le Targat, P. Soltan-Panahi, A. Eckardt, M. Lewenstein, P. Windpassinger, and K. Sengstock. Quantum simulation of frustrated classical magnetism in triangular optical lattices. *Science*, 333(6045):996–999, Jul 2011.

[171] J. Struck, C. Ölschläger, M. Weinberg, P. Hauke, J. Simonet, A. Eckardt, M. Lewenstein, K. Sengstock, and P. Windpassinger. Tunable gauge potential for neutral and spinless particles in driven optical lattices. *Physical Review Letters*, 108:225304, May 2012.

[172] Philipp Hauke, Olivier Tieleman, Alessio Celi, Christoph Ölschläger, Juliette Simonet, Julian Struck, Malte Weinberg, Patrick Windpassinger, Klaus Sengstock, Maciej Lewenstein, and et al. Non-abelian gauge fields

and topological insulators in shaken optical lattices. *Physical Review Letters*, 109(14):145301, Oct 2012.

[173] Colin V. Parker, Li-Chung Ha, and Cheng Chin. Direct observation of effective ferromagnetic domains of cold atoms in a shaken optical lattice. *Nature Physics*, 9(12):769–774, Oct 2013.

[174] Logan W. Clark, Brandon M. Anderson, Lei Feng, Anita Gaj, K. Levin, and Cheng Chin. Observation of density-dependent gauge fields in a bose-einstein condensate based on micromotion control in a shaken two-dimensional lattice. *Physical Review Letters*, 121:030402, Jul 2018.

[175] N. Flaschner, B. S. Rem, M. Tarnowski, D. Vogel, D.-S. Luhmann, K. Sengstock, and C. Weitenberg. Experimental reconstruction of the berry curvature in a floquet bloch band. *Science*, 352(6289):1091, May 2016.

[176] Matthias Tarnowski, F. Nur Ünal, Nick Fläschner, Benno S. Rem, André Eckardt, Klaus Sengstock, and Christof Weitenberg. Measuring topology from dynamics by obtaining the chern number from a linking number. *Nature Communications*, 10:1728, Apr 2019.

[177] J.-P. Brantut, J. Meineke, D. Stadler, S. Krinner, and T. Esslinger. Conduction of ultracold fermions through a mesoscopic channel. *Science*, 337:1069, 2012.

[178] S. Krinner, D. Stadler, D. Husmann, J.-P. Brantut, and T. Esslinger. Observation of quantized conductance in neutral matter. *Nature*, 517:64, 2014.

[179] Tomoki Ozawa, Hannah M. Price, Alberto Amo, Nathan Goldman, Mohammad Hafezi, Ling Lu, Mikael C. Rechtsman, David Schuster, Jonathan Simon, Oded Zilberberg, and Iacopo Carusotto. Topological photonics. *Reviews of Modern Physics*, 91:015006, 2019.

[180] H. M. Price and N. R. Cooper. Mapping the berry curvature from semiclassical dynamics in optical lattices. *Physical Review A*, 85:033620, 2012.

[181] Alexandre Dauphin and Nathan Goldman. Extracting the chern number from the dynamics of a fermi gas: Implementing a quantum hall bar for cold atoms. *Physical Review Letters*, 111:135302, 2013.

[182] M. Aidelsburger, M. Lohse, C. Schweizer, M. Atala, J. T. Barreiro, S. Nascimbène, N. R. Cooper, I. Bloch, and N. Goldman. Measuring the chern number of hofstadter bands with ultracold bosonic atoms. *Nature Physics*, 11(2):162–166, Dec 2014.

[183] Karen Wintersperger, Christoph Braun, F. Nur Ünal, André Eckardt, Marco Di Liberto, Nathan Goldman, Immanuel Bloch, and Monika Aidelsburger. Realization of an anomalous floquet topological system with ultracold atoms. *Nature Physics*, 16(10):1058–1063, Jun 2020.

[184] Duc Thanh Tran, Alexandre Dauphin, Adolfo G. Grushin, Peter Zoller, and Nathan Goldman. Probing topology by "heating": Quantized circular dichroism in ultracold atoms. *Science Advances*, 3:e1701207, 2017.

[185] N. Goldman, J. Dalibard, A. Dauphin, F. Gerbier, M. Lewenstein, P. Zoller, and I. B. Spielman. Direct imaging of topological edge states in cold-atom systems. *PNAS*, 110:6736, 2013.

[186] D.-T. Tran, A. Dauphin, N. Goldman, and P. Gaspard. Topological hofstadter insulators in a two-dimensional quasicrystal. *Physical Review B*, 91:085125, 2015.

[187] Biao Lian, Zhaochen Liu, Yuanbo Zhang, and Jing Wang. Flat chern band from twisted bilayer $mnbi_2te_4$. *Phys. Rev. Lett.*, 124:126402, Mar 2020.

[188] K. S. Novoselov, A. K. Geim, S. V. Morozov, D. Jiang, Y. Zhang, S. V. Dubonos, I. V. Grigorieva, and A. A. Firsov. Electric field effect in atomically thin carbon films. *Science*, 306(5696):666–669, 2004.

[189] Manish Chhowalla, Hyeon Shin, Goki Eda, L. Li, Kian Loh, and Hua Zhang. The chemistry of two-dimensional layered transition metal dichalcogenide nanosheets. *Nature chemistry*, 5:263–75, 04 2013.

[190] Louk Rademaker and Paula Mellado. Charge-transfer insulation in twisted bilayer graphene. *Phys. Rev. B*, 98:235158, Dec 2018.

[191] Pilkyung Moon and Mikito Koshino. Energy spectrum and quantum hall effect in twisted bilayer graphene. *Phys. Rev. B*, 85:195458, May 2012.

[192] T. Hensgens, T. Fujita, L. Janssen, Xiao Li, C. J. Van Diepen, C. Reichl, W. Wegscheider, S. Das Sarma, and L. M. K. Vandersypen. Quantum

simulation of a fermi–hubbard model using a semiconductor quantum dot array. *Nature*, 548(7665):70–73, aug 2017.

[193] Tilman Esslinger. Fermi-hubbard physics with atoms in an optical lattice. *Annu. Rev. Condens. Matter Phys.*, 1(1):129–152, 2010.

[194] Maciej Lewenstein, Anna Sanpera, Veronica Ahufinger, Bogdan Damski, Aditi Sen(De), and Ujjwal Sen. Ultracold atomic gases in optical lattices: mimicking condensed matter physics and beyond. *Adv. Phys.*, 56(2):243–379, mar 2007.

[195] Andrew G. Truscott, Kevin E. Strecker, William I. McAlexander, Guthrie B. Partridge, and Randall G. Hulet. Observation of fermi pressure in a gas of trapped atoms. *Science*, 291(5513):2570–2572, 2001.

[196] Bin-Bin Chen, Chuang Chen, Ziyu Chen, Jian Cui, Yueyang Zhai, Andreas Weichselbaum, Jan von Delft, Zi Yang Meng, and Wei Li. Quantum many-body simulations of the two-dimensional fermi-hubbard model in ultracold optical lattices. *Phys. Rev. B*, 103:L041107, Jan 2021.

[197] R. Micnas, J. Ranninger, and S. Robaszkiewicz. Superconductivity in narrow-band systems with local nonretarded attractive interactions. *Rev. Mod. Phys.*, 62:113–171, Jan 1990.

[198] Daniel P. Arovas, Erez Berg, Steven A. Kivelson, and Srinivas Raghu. The hubbard model. *Annu. Rev. Condens. Matter Phys.*, 13(1):239–274, 2022.

[199] L. F. Feiner, J. H. Jefferson, and R. Raimondi. Effective single-band models for the high-t_c cuprates. i. coulomb interactions. *Phys. Rev. B*, 53:8751–8773, Apr 1996.

[200] Erez Berg, Dror Orgad, and Steven A. Kivelson. Route to high-temperature superconductivity in composite systems. *Phys. Rev. B*, 78:094509, Sep 2008.

[201] A. Macridin, M. Jarrell, Th. Maier, and G. A. Sawatzky. Physics of cuprates with the two-band hubbard model: The validity of the one-band hubbard model. *Phys. Rev. B*, 71:134527, Apr 2005.

[202] Lede Xian, Dante M. Kennes, Nicolas Tancogne-Dejean, Massimo Altarelli, and Angel Rubio. Multiflat Bands and Strong Correlations in

Twisted Bilayer Boron Nitride: Doping-Induced Correlated Insulator and Superconductor. *Nano Letters*, 19(8):4934–4940, August 2019.

[203] J. Hubbard. Electron correlations in narrow energy bands. *Proceedings of the Royal Society of London. Series A. Mathematical and Physical Sciences*, 276:238 – 257, 1963.

[204] Antoine Georges, Gabriel Kotliar, Werner Krauth, and Marcelo J. Rozenberg. Dynamical mean-field theory of strongly correlated fermion systems and the limit of infinite dimensions. *Rev. Mod. Phys.*, 68:13–125, Jan 1996.

[205] Masatoshi Imada, Atsushi Fujimori, and Yoshinori Tokura. Metal-insulator transitions. *Rev. Mod. Phys.*, 70:1039–1263, Oct 1998.

[206] N. F. MOTT. Metal-insulator transition. *Rev. Mod. Phys.*, 40:677–683, Oct 1968.

[207] D. B. McWhan, A. Menth, J. P. Remeika, W. F. Brinkman, and T. M. Rice. Metal-insulator transitions in pure and doped v_2o_3. *Phys. Rev. B*, 7:1920–1931, Mar 1973.

[208] J. Zaanen and G. A. Sawatzky. Systematics in band gaps and optical spectra of 3D transition metal compounds. *Journal of Solid State Chemistry France*, 88(1):8–27, September 1990.

[209] Takehiko Ishiguro and Kunihiko Yamaji. *Organic Conductors*, pages 9–34. Springer Berlin Heidelberg, Berlin, Heidelberg, 1990.

[210] P. W. Anderson. The resonating valence bond state in la¡sub¿2¡/sub¿cuo¡sub¿4¡/sub¿ and superconductivity. *Science*, 235(4793):1196–1198, 1987.

[211] Andreas Schilling, Marco Cantoni, J. Guo, and H. Ott. Superconductivity above 130 k in the hg-ba-ca-cu-o system. *Nature*, 363:56–58, 05 1993.

[212] D.J. Scalapino. The case for dx2 y2 pairing in the cuprate superconductors. *Physics Reports*, 250(6):329–365, 1995.

[213] Tom Timusk and Bryan Statt. The pseudogap in high-temperature superconductors: an experimental survey. *Reports on Progress in Physics*, 62(1):61, jan 1999.

[214] Patrick A. Lee, Naoto Nagaosa, and Xiao-Gang Wen. Doping a mott insulator: Physics of high-temperature superconductivity. *Rev. Mod. Phys.*, 78:17–85, Jan 2006.

[215] John Tranquada, B. Sternlieb, John Axe, Y. Nakamura, and Shin-ichi Uchida. Tranquada, j. m., sternlieb, b. j., axe, j. d., nakamura, y. uchida, s. evidence for stripe correlations of spins and holes in copper oxide superconductors. nature 375, 561-563. *naph*, 375:561–, 06 1995.

[216] C. C. Tsuei and J. R. Kirtley. Pairing symmetry in cuprate superconductors. *Rev. Mod. Phys.*, 72:969–1016, Oct 2000.

[217] B Keimer, S Kivelson, M Norman, S Uchida, and J. Zaanen. From quantum matter to high-temperature superconductivity in copper oxides. *Nature*, 518:179–86, 02 2015.

[218] Subir Sachdev. *Quantum Phase Transitions*. Cambridge University Press, 2 edition, 2011.

[219] F. Steglich, J. Aarts, C. D. Bredl, W. Lieke, D. Meschede, W. Franz, and H. Schäfer. Superconductivity in the presence of strong pauli paramagnetism: $Cecu_2si_2$. *Phys. Rev. Lett.*, 43:1892–1896, Dec 1979.

[220] H. Hegger, C. Petrovic, E. G. Moshopoulou, M. F. Hundley, J. L. Sarrao, Z. Fisk, and J. D. Thompson. Pressure-induced superconductivity in quasi-2d $cerhin_5$. *Phys. Rev. Lett.*, 84:4986–4989, May 2000.

[221] P. Limelette, A. Georges, D. Je

rome, P. Wzietek, P. Metcalf, and J. M. Honig. Universality and critical behavior at the mott transition. *Science*, 302(5642):89–92, oct 2003.

[222] Qimiao Si, Silvio Rabello, Kevin Ingersent, and J. Lleweilun Smith. Locally critical quantum phase transitions in strongly correlated metals. *Nature*, 413(6858):804–808, oct 2001.

[223] Kazushi Kanoda and Reizo Kato. Mott physics in organic conductors with triangular lattices. *Annu. Rev. Condens. Matter Phys.*, 2:167–188, 02 2011.

[224] Akira Ohtomo and HY Hwang. Ohtomo, a. hwang, h. y. a high-mobility electron gas at the laalo3/srtio3 heterointerface. nature 427, 423-426. *Nature*, 427:423–6, 02 2004.

[225] Immanuel Bloch, Jean Dalibard, and S. Nascimbene. Quantum simulations with ultracold quantum gases. *Nat. Phys.*, 8:267–276, 2012.

[226] G. Grynberg and C. Robilliard. Cold atoms in dissipative optical lattices. *Phys. Rep.*, 355(5):335–451, 2001.

[227] W. Hofstetter, J. I. Cirac, P. Zoller, E. Demler, and M. D. Lukin. High-temperature superfluidity of fermionic atoms in optical lattices. *Phys. Rev. Lett.*, 89:220407, Nov 2002.

[228] Anton Mazurenko, Christie S. Chiu, Geoffrey Ji, Maxwell F. Parsons, Márton Kanász-Nagy, Richard Schmidt, Fabian Grusdt, Eugene Demler, Daniel Greif, and Markus Greiner. A cold-atom fermi–hubbard antiferromagnet. *Nature*, 545(7655):462–466, May 2017.

[229] U. Schneider, L. Hackermüller, S. Will, Th. Best, I. Bloch, T. A. Costi, R. W. Helmes, D. Rasch, and A. Rosch. Metallic and insulating phases of repulsively interacting fermions in a 3d optical lattice. *Science*, 322(5907):1520–1525, 2008.

[230] Cheng Chin, Rudolf Grimm, Paul Julienne, and Eite Tiesinga. Feshbach resonances in ultracold gases. *Rev. Mod. Phys.*, 82:1225–1286, Apr 2010.

[231] Eva Y. Andrei, Dmitri K. Efetov, Pablo Jarillo-Herrero, Allan H. MacDonald, Kin Fai Mak, T. Senthil, Emanuel Tutuc, Ali Yazdani, and Andrea F. Young. The marvels of moiré materials. *Nat. Rev. Mater.*, 6(3):201–206, Mar 2021.

[232] Edward McCann and Mikito Koshino. The electronic properties of bilayer graphene. *Rep. Prog. Phys.*, 76(5):056503, apr 2013.

[233] Päivi Törmä, Sebastiano Peotta, and Bogdan A Bernevig. Superconductivity, superfluidity and quantum geometry in twisted multilayer systems. *Nature Reviews Physics*, 4(8):528–542, August 2022.

[234] Yuan Cao, Valla Fatemi, Shiang Fang, Kenji Watanabe, Takashi Taniguchi, Efthimios Kaxiras, and Pablo Jarillo-Herrero. Unconventional superconductivity in magic-angle graphene superlattices. *Nature*, 556(7699):43–50, Apr 2018.

[235] Yuan Cao, Valla Fatemi, Ahmet Demir, Shiang Fang, Spencer L. Tomarken, Jason Y. Luo, Javier D. Sanchez-Yamagishi, Kenji Watanabe, Takashi Taniguchi, Efthimios Kaxiras, Ray C. Ashoori, and Pablo Jarillo-Herrero. Correlated insulator behaviour at half-filling in magic-angle graphene superlattices. *Nature*, 556(7699):80–84, Apr 2018.

[236] Lei Wang, En-Min Shih, Augusto Ghiotto, Lede Xian, Daniel A. Rhodes, Cheng Tan, Martin Claassen, Dante M. Kennes, Yusong Bai, Bumho Kim, Kenji Watanabe, Takashi Taniguchi, Xiaoyang Zhu, James Hone, Angel Rubio, Abhay N. Pasupathy, and Cory R. Dean. Correlated electronic phases in twisted bilayer transition metal dichalcogenides. *Nat. Mat.*, 19(8):861–866, Aug 2020.

[237] Aleksi Julku, Sebastiano Peotta, Tuomas I. Vanhala, Dong-Hee Kim, and Päivi Törmä. Geometric origin of superfluidity in the lieb-lattice flat band. *Phys. Rev. Lett.*, 117:045303, Jul 2016.

[238] Kukka-Emilia Huhtinen, Jonah Herzog-Arbeitman, Aaron Chew, Bogdan A. Bernevig, and Päivi Törmä. Revisiting flat band superconductivity: Dependence on minimal quantum metric and band touchings. *Phys. Rev. B*, 106:014518, Jul 2022.

[239] Xiang Hu, Timo Hyart, Dmitry I. Pikulin, and Enrico Rossi. Geometric and conventional contribution to the superfluid weight in twisted bilayer graphene. *Phys. Rev. Lett.*, 123:237002, Dec 2019.

[240] T. T. Heikkilä, N. B. Kopnin, and G. E. Volovik. Flat bands in topological media. *JETP Letters*, 94(3):233–239, oct 2011.

[241] Dante M. Kennes, Martin Claassen, Lede Xian, Antoine Georges, Andrew J. Millis, James Hone, Cory R. Dean, D. N. Basov, Abhay N. Pasupathy, and Angel Rubio. Moiré heterostructures as a condensed-matter quantum simulator. *Nat. Phys.*, 17(2):155–163, 2021.

[242] Kyounghwan Kim, Ashley DaSilva, Shengqiang Huang, Babak Fallahazad, Stefano Larentis, Takashi Taniguchi, Kenji Watanabe, Brian J. LeRoy, Allan H. MacDonald, and Emanuel Tutuc. Tunable moiré bands and strong correlations in small-twist-angle bilayer graphene. *PNAS*, 114(13):3364–3369, 2017.

[243] A. Kantian, S. Langer, and A. J. Daley. Dynamical disentangling and cooling of atoms in bilayer optical lattices. *Phys. Rev. Lett.*, 120:060401, Feb 2018.

[244] Marcell Gall, Nicola Wurz, Jens Samland, Chun Fai Chan, and Michael Köhl. Competing magnetic orders in a bilayer hubbard model with ultracold atoms. *Nature*, 589(7840):40–43, Jan 2021.

[245] A. González-Tudela and J. I. Cirac. Cold atoms in twisted-bilayer optical potentials. *Phys. Rev. A*, 100:053604, Nov 2019.

[246] Zengming Meng, Liangwei Wang, Wei Han, Fangde Liu, Kai Wen, Chao Gao, Pengjun Wang, Cheng Chin, and Jing Zhang. Atomic bose-einstein condensate in a twisted-bilayer optical lattice. 2021.

[247] Xi-Wang Luo and Chuanwei Zhang. Spin-twisted optical lattices: Tunable flat bands and larkin-ovchinnikov superfluids. *Phys. Rev. Lett.*, 126:103201, Mar 2021.

[248] Fengcheng Wu, Timothy Lovorn, Emanuel Tutuc, and A. H. MacDonald. Hubbard model physics in transition metal dichalcogenide moiré bands. *Phys. Rev. Lett.*, 121:026402, Jul 2018.

[249] Grigory Tarnopolsky, Alex Jura Kruchkov, and Ashvin Vishwanath. Origin of magic angles in twisted bilayer graphene. *Phys. Rev. Lett.*, 122:106405, Mar 2019.

[250] Yixing Fu, Elio J König, Justin H Wilson, Yang-Zhi Chou, and Jedediah H Pixley. Magic-angle semimetals. *npj Quantum Mater.*, 5(1):71, 2020.

[251] Yang-Zhi Chou, Yixing Fu, Justin H. Wilson, E. J. König, and J. H. Pixley. Magic-angle semimetals with chiral symmetry. *Phys. Rev. B*, 101:235121, Jun 2020.

[252] Junhyun Lee and J. H. Pixley. Emulating twisted double bilayer graphene with a multiorbital optical lattice. 2021.

[253] Jinjing Yi, Elio J. König, and J. H. Pixley. The low energy excitation spectrum of magic-angle semimetals. 2022.

[254] O. Boada, A. Celi, J. I. Latorre, and M. Lewenstein. Quantum simulation of an extra dimension. *Phys. Rev. Lett.*, 108:133001, Mar 2012.

[255] A. Celi, P. Massignan, J. Ruseckas, N. Goldman, I. B. Spielman, G. Juzeliūnas, and M. Lewenstein. Synthetic gauge fields in synthetic dimensions. *Phys. Rev. Lett.*, 112:043001, Jan 2014.

[256] A L Goodman. Hartree–fock–bogoliubov theory with applications to nuclei. *Adv. Nucl. Phys.; (United States)*, 11:1, 6 1979.

[257] Mathieu Lewin and Séverine Paul. A numerical perspective on Hartree-Fock-Bogoliubov theory. *ESAIM: M2AN*, 48(1):53–86, 2014.

[258] Miguel A Cazalilla and Ana Maria Rey. Ultracold fermi gases with emergent SU(n) symmetry. *Rep. Prog. Phys.*, 77(12):124401, nov 2014.

[259] Erik Koch. *2 Mean-Field Theory : Hartree-Fock and BCS*. 2016.

[260] A L Goodman. Hartree–fock–bogoliubov theory with applications to nuclei. *Adv. Nucl. Phys.; (United States)*, 11:1, 6 1979.

[261] Lindsay Sonderhouse, Christian Sanner, Ross B. Hutson, Akihisa Goban, Thomas Bilitewski, Lingfeng Yan, William R. Milner, Ana M. Rey, and Jun Ye. Thermodynamics of a deeply degenerate su(n)-symmetric fermi gas. *Nat. Phys.*, 16(12):1216–1221, Dec 2020.

[262] Giovanni I. Martone, Yun Li, and Sandro Stringari. Approach for making visible and stable stripes in a spin-orbit-coupled bose-einstein superfluid. *Phys. Rev. A*, 90:041604, Oct 2014.

[263] Simon Stellmer, Rudolf Grimm, and Florian Schreck. Detection and manipulation of nuclear spin states in fermionic strontium. *Phys. Rev. A*, 84:043611, Oct 2011.

[264] Aleksander Zujev, Richard T Scalettar, George G Batrouni, and Pinaki Sengupta. Pairing correlations in the two-layer attractive hubbard model. *New J. Phys.*, 16(1):013004, jan 2014.

[265] Sebastiano Peotta and Päivi Törmä. Superfluidity in topologically nontrivial flat bands. *Nat. Comm.*, 6(8944), Nov 2015.

[266] Robert Alicki and Mark Fannes. Entanglement boost for extractable work from ensembles of quantum batteries. *Phys. Rev. E*, 87:042123, Apr 2013.

[267] Felix C Binder, Sai Vinjanampathy, Kavan Modi, and John Goold. Quantacell: powerful charging of quantum batteries. *New Journal of Physics*, 17(7):075015, jul 2015.

[268] Francesco Campaioli, Felix A. Pollock, Felix C. Binder, Lucas Céleri, John Goold, Sai Vinjanampathy, and Kavan Modi. Enhancing the charging power of quantum batteries. *Phys. Rev. Lett.*, 118:150601, Apr 2017.

[269] Dario Ferraro, Michele Campisi, Gian Marcello Andolina, Vittorio Pellegrini, and Marco Polini. High-power collective charging of a solid-state quantum battery. *Phys. Rev. Lett.*, 120:117702, Mar 2018.

[270] Thao P. Le, Jesper Levinsen, Kavan Modi, Meera M. Parish, and Felix A. Pollock. Spin-chain model of a many-body quantum battery. *Phys. Rev. A*, 97:022106, Feb 2018.

[271] Gian Marcello Andolina, Maximilian Keck, Andrea Mari, Michele Campisi, Vittorio Giovannetti, and Marco Polini. Extractable work, the role of correlations, and asymptotic freedom in quantum batteries. *Phys. Rev. Lett.*, 122:047702, Feb 2019.

[272] Gian Marcello Andolina, Donato Farina, Andrea Mari, Vittorio Pellegrini, Vittorio Giovannetti, and Marco Polini. Charger-mediated energy transfer in exactly solvable models for quantum batteries. *Phys. Rev. B*, 98:205423, Nov 2018.

[273] Donato Farina, Gian Marcello Andolina, Andrea Mari, Marco Polini, and Vittorio Giovannetti. Charger-mediated energy transfer for quantum batteries: An open-system approach. *Phys. Rev. B*, 99:035421, Jan 2019.

[274] Felipe Barra. Dissipative charging of a quantum battery. *Phys. Rev. Lett.*, 122:210601, May 2019.

[275] Karen V. Hovhannisyan, Martí Perarnau-Llobet, Marcus Huber, and Antonio Acín. Entanglement generation is not necessary for optimal work extraction. *Phys. Rev. Lett.*, 111:240401, Dec 2013.

[276] Francesco Campaioli, Felix A. Pollock, and Sai Vinjanampathy. Quantum batteries - review chapter, 2018.

[277] A. E. Allahverdyan, R. Balian, and Th. M. Nieuwenhuizen. Maximal work extraction from finite quantum systems. *Europhysics Letters*, 67(4):565, aug 2004.

[278] Nicolai Friis and Marcus Huber. Precision and work fluctuations in gaussian battery charging. *Quantum*, 2:61, apr 2018.

[279] Manabendra Nath Bera, Arnau Riera, Maciej Lewenstein, Zahra Baghali Khanian, and Andreas Winter. Thermodynamics as a consequence of information conservation. *Quantum*, 3:121, feb 2019.

[280] Florian Hulpke, Uffe V. Poulsen, Anna Sanpera, Aditi Sen(De), Ujjwal Sen, and Maciej Lewenstein. Unitarity as preservation of entropy and entanglement in quantum systems. *Foundations of Physics*, 36(4):477–499, mar 2006.

[281] Carlo Sparaciari, Jonathan Oppenheim, and Tobias Fritz. Resource theory for work and heat. *Physical Review A*, 96(5), nov 2017.

[282] Wiesław Pusz and Stanislaw Woronowicz. Passive states and kms states for general quantum systems. *Communications in Mathematical Physics*, 58:273–290, 10 1978.

[283] Wolfgang Niedenzu, Marcus Huber, and Erez Boukobza. Concepts of work in autonomous quantum heat engines. *Quantum*, 3:195, oct 2019.

[284] Sebastian Deffner and Steve Campbell. Quantum speed limits: from heisenberg's uncertainty principle to optimal quantum control. *Journal of Physics A: Mathematical and Theoretical*, 50(45):453001, oct 2017.

[285] Ingemar Bengtsson and Karol Życzkowski. *Geometry of Quantum States: An Introduction to Quantum Entanglement*. Cambridge University Press, 2 edition, 2017.

[286] Michael A. Nielsen and Isaac L. Chuang. *Quantum Computation and Quantum Information: 10th Anniversary Edition*. Cambridge University Press, 2010.

[287] Samuel L. Braunstein and Carlton M. Caves. Statistical distance and the geometry of quantum states. *Phys. Rev. Lett.*, 72:3439–3443, May 1994.

[288] Géza Tóth and Iagoba Apellaniz. Quantum metrology from a quantum information science perspective. *Journal of Physics A: Mathematical and Theoretical*, 47(42):424006, oct 2014.

[289] Philipp Hyllus, Wiesław Laskowski, Roland Krischek, Christian Schwemmer, Witlef Wieczorek, Harald Weinfurter, Luca Pezzé, and Augusto Smerzi. Fisher information and multiparticle entanglement. *Phys. Rev. A*, 85:022321, Feb 2012.

[290] Zeqian Chen. Wigner-yanase skew information as tests for quantum entanglement. *Phys. Rev. A*, 71:052302, May 2005.

[291] Otfried Gühne, Géza Tóth, and Hans J Briegel. Multipartite entanglement in spin chains. *New Journal of Physics*, 7(1):229, nov 2005.

[292] H.J. Lipkin, N. Meshkov, and A.J. Glick. Validity of many-body approximation methods for a solvable model: (i). exact solutions and perturbation theory. *Nuclear Physics*, 62(2):188–198, 1965.

[293] W. Muessel, H. Strobel, D. Linnemann, T. Zibold, B. Juliá-Díaz, and M. K. Oberthaler. Twist-and-turn spin squeezing in bose-einstein condensates. *Phys. Rev. A*, 92:023603, Aug 2015.

[294] Julien Vidal, Guillaume Palacios, and Rémy Mosseri. Entanglement in a second-order quantum phase transition. *Phys. Rev. A*, 69:022107, Feb 2004.

[295] R. H. Dicke. Coherence in spontaneous radiation processes. *Phys. Rev.*, 93:99–110, Jan 1954.

[296] J. M. Fink, R. Bianchetti, M. Baur, M. Göppl, L. Steffen, S. Filipp, P. J. Leek, A. Blais, and A. Wallraff. Dressed collective qubit states and the tavis-cummings model in circuit qed. *Phys. Rev. Lett.*, 103:083601, Aug 2009.

[297] A. Aloy, J. Tura, F. Baccari, A. Acín, M. Lewenstein, and R. Augusiak. Device-independent witnesses of entanglement depth from two-body correlators. *Phys. Rev. Lett.*, 123:100507, Sep 2019.

[298] J. Tura, A. Aloy, F. Baccari, A. Acín, M. Lewenstein, and R. Augusiak. Optimization of device-independent witnesses of entanglement depth from two-body correlators. *Phys. Rev. A*, 100:032307, Sep 2019.

[299] J. S. Bell. On the einstein podolsky rosen paradox. *Physics Physique Fizika*, 1:195–200, Nov 1964.

[300] Bruno R. de Abreu. *Numerical quenches of disorder in the Bose-Hubbard model*. PhD thesis, 11 2018.

[301] Markus Greiner, Olaf Mandel, Tilman Esslinger, Theodor Haensch, and Immanuel Bloch. Quantum phase transition from a superfluid to a mott insulator in a gas of ultracold atoms. *Nature*, 415:39–44, 02 2002.

[302] S. Baier, M. J. Mark, D. Petter, K. Aikawa, L. Chomaz, Z. Cai, M. Baranov, P. Zoller, and F. Ferlaino. Extended bose-hubbard models with ultracold magnetic atoms. *Science*, 352(6282):201–205, apr 2016.

[303] Laura Urba, Emil Lundh, and Anders Rosengren. One-dimensional extended bose-hubbard model with a confining potential: A dmrg analysis. *Journal of Physics B: Atomic, Molecular and Optical Physics*, 39, 07 2006.

[304] G. G. Batrouni, R. T. Scalettar, G. T. Zimanyi, and A. P. Kampf. Supersolids in the bose-hubbard hamiltonian. *Phys. Rev. Lett.*, 74:2527–2530, Mar 1995.

[305] F. Hébert, G. G. Batrouni, R. T. Scalettar, G. Schmid, M. Troyer, and A. Dorneich. Quantum phase transitions in the two-dimensional hardcore boson model. *Phys. Rev. B*, 65:014513, Dec 2001.

[306] M. A. Baranov, M. Dalmonte, G. Pupillo, and P. Zoller. Condensed matter theory of dipolar quantum gases. *Chemical Reviews*, 112(9):5012–5061, aug 2012.

[307] Omjyoti Dutta, Mariusz Gajda, Philipp Hauke, Maciej Lewenstein, Dirk-Sören Lühmann, Boris A Malomed, Tomasz Sowiń ski, and Jakub Zakrzewski. Non-standard hubbard models in optical lattices: a review. *Reports on Progress in Physics*, 78(6):066001, may 2015.

[308] C Trefzger, C Menotti, B Capogrosso-Sansone, and M Lewenstein. Ultracold dipolar gases in optical lattices. *Journal of Physics B: Atomic, Molecular and Optical Physics*, 44(19):193001, sep 2011.

[309] B. Capogrosso-Sansone, C. Trefzger, M. Lewenstein, P. Zoller, and G. Pupillo. Quantum phases of cold polar molecules in 2d optical lattices. *Physical Review Letters*, 104(12), mar 2010.

[310] A. J. Leggett. Can a solid be "superfluid"? *Phys. Rev. Lett.*, 25:1543–1546, Nov 1970.

[311] L. Lackner, M. Dusel, Oleg Egorov, Bo Han, Heiko Knopf, Falk Eilenberger, Sven Schröder, K. Watanabe, T. Taniguchi, Sefaattin Tongay, C. Anton-Solanas, Sven Höfling, and César Schneider. Tunable exciton-polaritons emerging from ws2 monolayer excitons in a photonic lattice at room temperature. *Nature Communications*, 12, 08 2021.

[312] Lin Su, Alexander Douglas, Michal Szurek, Robin Groth, S. Furkan Ozturk, Aaron Krahn, Anne H. Hébert, Gregory A. Phelps, Sepehr Ebadi, Susannah Dickerson, Francesca Ferlaino, Ognjen Marković, and Markus Greiner. Dipolar quantum solids emerging in a hubbard quantum simulator, 2023.

[313] Till D. Kühner, Steven R. White, and H. Monien. One-dimensional bose-hubbard model with nearest-neighbor interaction. *Physical Review B*, 61(18):12474–12489, may 2000.

[314] Camille Lagoin, Stephan Suffit, Kirk Baldwin, Loren Pfeiffer, and François Dubin. Mott insulator of strongly interacting two-dimensional semiconductor excitons. *Nature Physics*, 18(2):149–153, dec 2021.

[315] R Kubo. The fluctuation-dissipation theorem. *Reports on Progress in Physics*, 29(1):255, jan 1966.

[316] Nathan Gemelke, Xibo Zhang, Chen-Lung Hung, and Cheng Chin. In-situ observation of incompressible mott-insulating domains of ultracold atomic gases. *Nature*, 460:995–8, 08 2009.

[317] G. G. Batrouni, V. Rousseau, R. T. Scalettar, M. Rigol, A. Muramatsu, P. J. H. Denteneer, and M. Troyer. Mott domains of bosons confined on optical lattices. *Physical Review Letters*, 89(11), aug 2002.

[318] Marcos Rigol, George G. Batrouni, Valery G. Rousseau, and Richard T. Scalettar. State diagrams for harmonically trapped bosons in optical lattices. *Physical Review A*, 79(5), may 2009.